Inner-shell photoabsorption studies in free atoms and ions isoelectronic to sodium, magnesium, aluminium and silicon.

A thesis for the degree of
Doctor of Philosophy

submitted to

Dublin City University

By

Muhammad Hassan Sayyad, M.Sc.

School of Physical Sciences
Dublin City University

Research Supervisor

Prof. Eugene T. Kennedy

August 1994

I hereby certify that this material, which I now submit for assessment on the programme of study leading to the award of Doctor of Philosophy, is entirely my own work and has not been taken from the work of others save and to the extent that such work has been cited and acknowledged within the text of my work.

Signed: M Hassan
Candidate

ID No: 89701241

Dated: 31-08-1994

This thesis is dedicated to my parents, wife (Riwana), sister (Azra) and daughter (Maryam).

CONTENTS

ABSTRACT

Using the dual laser-produced plasma technique photoabsorption studies of Mg, Al and Si plasmas have been carried out. The objective was to measure the 2p-subshell absorption in neutral and ionised species of the Na I, Mg I, Al I and Si I sequences prepared both in ground and valence-excited states. The spectra were recorded on a grazing incidence 2m Hilger stigmatic spectrograph and a 2.2m McPherson spectrometer equipped with MCP/PDA multichannel detection.

In an attempt to distinguish the origin of the various absorption features observed, and to record almost pure spectra of the species of interest, a number of time and space-resolved studies were carried out. These studies which exploit the temporal and spatial evolution of absorbing species in a laser-generated plasma plume were very successful, particularly, for neutral and singly ionised species. To facilitate the analyses of the spectra a range of *ab initio* atomic structure configuration–interaction Hartree-Fock (CIHF) calculations were carried out.

The Mg sequence in ground state absorption has been studied for atomic Mg and Mg-like ions Al^{+} and Si^{2+}. The effects of configuration-interaction in the ground and excited states have been examined in detail. Interpretation has been provided for the distribution of oscillator strength and the relative positions of observed transitions. The Mg sequence in excited state absorption is reported for Mg, Al^{+} and Si^{2+}. In order to provide insight into the dynamics of excited levels a comparison is made with the ejected-electron spectra of the corresponding atomic and ionic species arising from the autoionising and Auger transitions following electron- and photon-impact excitation/ionization.

The 2p-subshell photoabsorption study along the Al sequence in ground state has been carried out for atomic Al and Al-like ionic Si^{+}. In this work a complete analysis of these three electron systems is reported. The 2p absorption study of Al-like Si^{+} in their excited states has also been carried out.

The 2p-subshell photoabsorption spectrum of ground state atomic Si has been investigated. In addition to providing interpretation for the observed

spectrum, a comparison is made with molecular spectra.

Photoabsorption spectra of the isoelectronic species Mg^{+}, Al^{2+} and Si^{3+} both in ground and valence-excited states are presented and await analysis.

The overall results show that 2p photoabsorption of atoms and ions along the Mg I, Al I and Si I sequences in ground and excited states is dominated by the $2p^63s^a3p^b \rightarrow 2p^53s^a3p^b[(n+1)s + nd] + 2p^53s^{a-1}3p^{b+1}np$, for $n \geq 3$, and $2p^63s^{a-1}3p^{b+1} \rightarrow 2p^53s^a3p^{b+1}$ transitions respectively. In ground state absorption spectra the $2p^53s^a3p^b[(n+1)s + nd]$ Rydberg series members are strongly perturbed by the $2p^53s^{a-1}3p^{b+1}np$ doubly-excited states. In moving from neutral to ionic absorption along the sequences dramatic changes are observed. However, in the valence-excited spectra the absorption structures corresponding to the $2p^53s^a3p^{b+1}$ type configurations are observed to be unperturbed and same in appearance along the sequences.

Chapter 1

INNER-SHELL PHOTOIONIZATION STUDIES IN FREE IONS

The 2p-subshell photoabsorption spectra for a number of free many-electron systems, mostly ions, in ground and valence-excited states are reported in this thesis for the first time. The measurements and analyses of the observed spectra are given in the succeeding chapters. This chapter reviews recent experimental developments in the inner-shell photoabsorption and photoionization studies of free ions in ground and excited states.

1.1 Introduction

Even though highly ionised ions vastly predominate in the universe, very little is known experimentally on photoexcitation or photoionization of ions, because ionic species do not exist naturally on the earth. Experimental data on inner-shell photoexcitation/photoionization in neutral, singly or multiply ionised atoms are required in many areas. A knowledge of the cross section for photoionization of positively charged atomic ions is necessary in connection with plasma physics and controlled thermonuclear fusion; is relevant to upper atmospheric physics where solar radiation is absorbed by positive ions as well as neutral atoms and molecules; and finds applications in space and astrophysics to the transport of radiation through stellar atmospheres and planetary nebulae (Missavage *et al.* 1977). The calculated ionic photoionization cross sections, usually based upon simple models, are largely untested (Nasreen *et al.* 1989, Deshmukh *et al.* 1988, Daum and Kelly 1976) because very little is known about ionic photoabsorption due to the technical difficulties in producing high densities of ions suitable for photoabsorption measurements. The measured energy levels are required in connection with plasma diagnostics, XUV laser research and the identification of solar and stellar spectra. Photoabsorption studies complement many other studies carried out using ejected-electron spectroscopy following photon, electron and ion-impact excitation/ionisation, and beam-foil spectroscopy.

The studies of the ejected-electron spectra following low energy electron or ion-impact excitation/ionisation which exhibit resonances arising from the dipole allowed and optically inaccessible states often end with a number of unidentified structures (see for example Pejcev *et al.* 1977). Therefore, photoabsorption studies from ground and excited states achieved by optimising in either ground (see chapters 4, 5 and 6) or excited states (see chapter 7) are of great help for the identification of such spectra. The study of the decay dynamics of individual levels (Whitfield *et al.* 1991) following photon excitation allows the identification of transitions involving spectator decay, participator decay, shakeup or shakedown processes. These studies provide experimental evidence of the presence of various electron-interactions in a multi-electron system. Without the exact knowledge of the energy levels of the systems under consideration these studies are not possible; therefore, the measured level energies obtained through photoabsorption studies can stimulate these studies. Systematic investigations along isoelectronic or isonuclear sequences are of particular value as they provide insight into fundamental aspects of the photoionization process such as relativistic effects, correlation effects, orbital collapse (see e.g. Lucatorto *et al.* 1981, Lahiri and Manson 1988).

To date photoabsorption spectroscopy has been applied mostly to neutral species, particularly easily evaporable elements such as alkali and alkaline earth metal atoms. However, very little absorption spectroscopy has been performed for the refractory metals and ionised species in either ground or excited states. The reason is mainly due to the difficulty of producing a suitable and reproducible column of absorbing species with enough density to allow absorption measurements. These conditions can be met, however, in a pulsed regime and it is possible to perform absorption experiments of neutral and ionised species by using a pulsed background continuum source time synchronised with the transient absorbing species. For this reason the laser produced plasma (LPP) is very suitable for absorption experiments of both refractory metals and ionised species. In fact, it can be used to generate in pulsed regime, both the background continuum and the absorbing medium. Exploiting these properties of LPPs Carroll and Kennedy (1977) performed successfully an absorption experiment on the ionic species Li^+.This technique, known as dual laser-produced plasma (DLPP), is relatively well established now and has been successfully applied to atoms and ions both in ground and excited states (see chapter 3).

Fortunately, the developments in instrumentation and atomic structure

theory have gone hand in hand with the development of experimental techniques. The rapid technological developments, leading to more efficient spectrometers (Tondello 1979, Jannitti *et al.* 1979, Hopkins 1992) equipped with photoelectronic detectors (Cromer *et al.* 1985, Schwob *et al.* 1987, Jannitti *et al.* 1990, Kiernan 1994a), computer aided control, data acquisition and analysis (Shaw 1994), have opened up remarkable possibilities - it is possible now to obtain and measure absorption spectra of atoms and ions in ground and excited states for a wide variety of species. Atomic structure theory has entered a new era with the widespread availability of super computers and high performance workstations. Experimental investigations of the observed features are greatly facilitated by the theoretical results, based on *ab initio* configuration-interaction atomic structure calculations (see chapter 2). Although some theoretical approaches enable one to investigate fairly complicated mathematical models of the systems under consideration and to obtain in this way results which are in quite good agreement with the experimental measurements even then the study of some systems poses many challenging problems both for theorists and experimenters. The absorption transitions arising from the different initial states or different ionisation stages which fall in the same spectral region are very difficult to distinguish. Short-lived dipole allowed states hardly get populated (see chapter 7), therefore, it is very difficult to carry out their photoabsorption measurements. Some multiply-excited states though of great interest usually have very low cross sections and are, therefore, very difficult to observe (Kiernan *et al.* 1994b) in photoabsorption experiments. Furthermore, a reliable calculation of term energies, together with a clear physical interpretation of the oscillator strength distributions between various transitions of a many-electron atom is an extremely difficult task for any theoretical approach when more than one electron is involved in the photoexcitation process (see chapters 4, 5 and 6).

1.2 Photoionization measurements in free ions

Photoabsorption or photoionization of free atoms have long been areas of fundamental interest in atomic physics.The interaction of a photon with an atomic or ionic species (see figure 1.1) can result in valence-shell, inner-shell, one-electron or multi-electron excitations. The decay of these excited states can lead to the creation of a single or multiply charged ion and one or more ejected electrons.

Fluorescence can also be a part of the decay cascade. Hence, absorption, ion, electron, and fluorescence spectroscopies are complementry experimental methods which can be used to investigate various aspects of atomic dynamics. Because of the difficulties in producing the sufficient density of absorbing species the studies have mainly been carried out in rare gases and easily evaporable alkali and alkaline earth metals. A comprehensive review of the photoionization of rare gases by synchrotron radiation has been provided recently by Schmidt (1992). The XUV photoabsorption spectroscopy of metal atoms has been reviewed in detail by Sonntag and Zimmermann (1992).

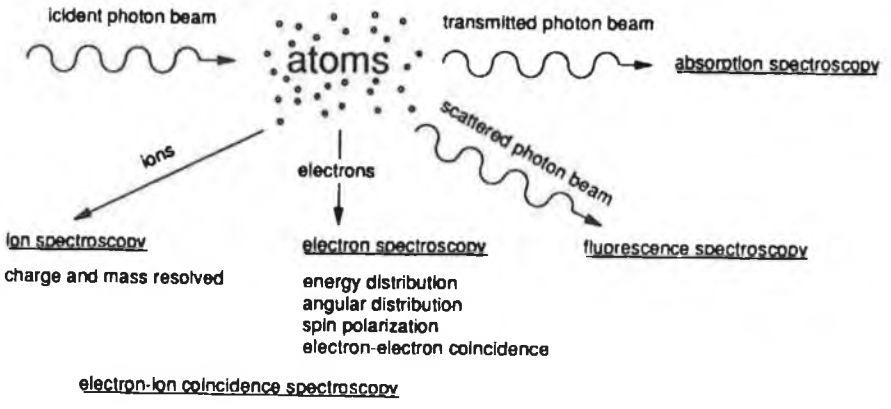

Figure 1.1

Representation of the processes which provide information about various aspects of atomic dynamics following the interaction between VUV radiation and free atomic species (from Richter 1993).

The photoabsorption in ions has been mainly studied using the resonant laser driven ionization (RLDI) and the dual laser-produced plasma (DLPP) methods. The recent experimental developments in resonant laser-driven ionization and dual laser plasma setups have been reviewed by Costello *et al.* (1991a). For the measurements of absolute photoionization cross sections the technique of merged photon–ion beam (Lyon *et al.* 1986) has been developed. More recently the first observation of the photoelectron spectra emitted in the photoionization of a singly charged beam with undulator radiation has been successfully achieved (Bizau *et al.* 1991). The various developments in the photoionization studies of ions have been described in a number of review articles by Wuilleumier (1992), Wuilleumier *et al.* (1991 and 1994) and Bizau *et al.* (1993). For the sake of

completeness a brief introduction to the various experimental techniques developed for the photoabsorption, photoion and photoelectron spectroscopy will be given.

1.2.1 Photoion spectroscopy

During the last fifteen years photoion spectrometery has been extensively applied to neutral species (Sonntag and Zimmermann 1992). Using this technique one can measure photoion yield spectra, resonance structures arising from inner-shell excitations and absolute photoionization cross sections. Its suitability for absolute photoionization ionic cross section measurements was demonstrated by Lyon *et al.* (1986) in a photon–ion merged beam experiment. The species studied in these experiments since then are shown in table 1.1.

Table 1.1. A summary of the photoionization studies in ground state ions carried out in photon–ion merged beam experiments.

Species	Regions	References
Ba^+	5p	Lyon *et al.* (1986)
Sr^+	4p	Lyon *et al.* (1987a)
Ca^+	3p	Lyon *et al.* (1987b)
Ga^+	3d	Peart *et al.* (1987)
Zn^+	3d	Peart *et al.* (1987)
K^+	3s	Peart and Lyon (1987)

The apparatus used in the first successful photon–ion merged beam experiment involving synchrotron radiation is shown in figure 1.2. A 0.1μA 2 keV singly-charged ion beam, produced in the surface ionization source S, is deflected

by the magnet M_1 into the interaction region (I) after focussing through the differential pumping region (DP). The monochromatized synchrotron radiation beam from a McPherson monochromator interacts with the ion beam along a path of about 12 cm length, photoionizing some of the ions (A^+) into doubly charged ions (A^{2+}), after separation by the second magnet M_2.

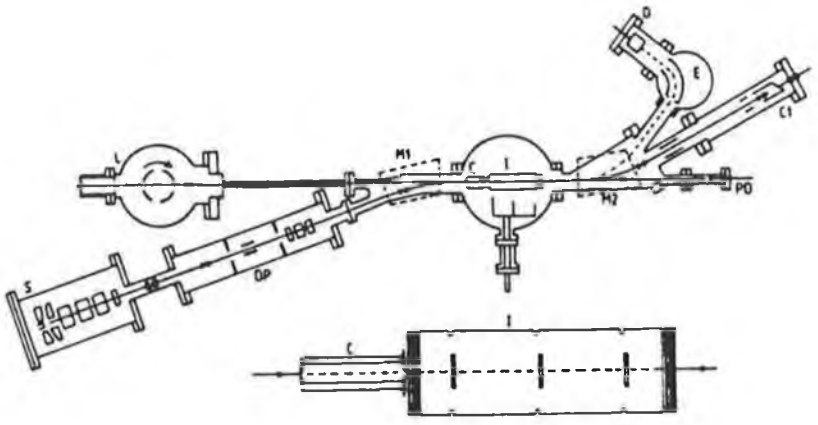

Figure 1.2

Schematic of the experimental set up for photoion spectrometry at Daresbury (from Lyon *et al.* 1986).

1.2.2 Photoelectron spectroscopy

Photoion spectrometry (Lyon *et al.* 1986, 1987a, 1987b, Peart and Lyon 1987, Peart *et al.* 1987) allows the measurement of absolute photoionization cross sections in merged photon-ion-beam experiments; however, when several channels are open into the continuum, only photoelectron spectrometry provides the detailed insight into the photoionization process by providing partial photoionization cross sections and measurement of branching ratios for the various subshells of a multielectron atom (Wuilleumier and Crause 1974, Wuilleumier 1989).

Very recently, the experimental setup shown in figure 1.3 has been developed by Bizau *et al.* (1991) for the photoelectron studies of ions. Here, a plasma discharge ion source delivers singly charged A^+ ion beams of about 20–30 μA at 10 to 20 keV kinetic energy. After magnetic and electrostatic deflections, the

ion beam is focussed into the source volume of an electron cylindrical mirror analyser (CMA), where the monochromatized photon beam from an undulator is also focussed. The electrons emitted in the interaction zone are detected with an array of channeltrons placed between the two inner cylinders around the axis of the CMA. After passing through the CMA, the A^+ and A^{2+} ions are separated by a second magnet and detected with Faraday cups. The capabilities of this technique were demonstrated by measuring the photoelectron spectra resulting from the photoionization of an ion-beam of singly ionised calcium.

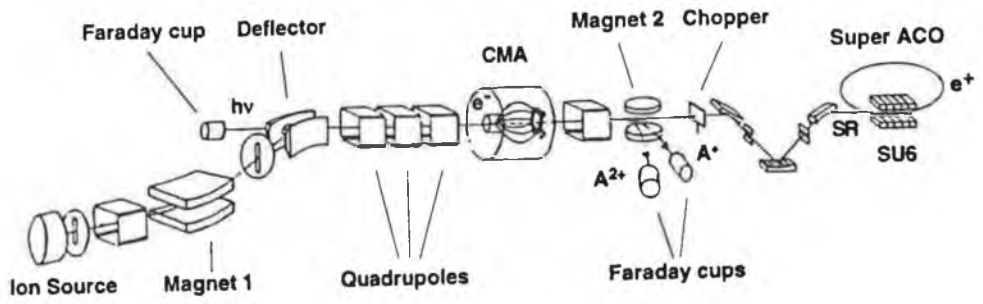

Figure 1.3

Experimental set up for the photoionization of ions with Super ACO (PISA) (from Bizau *et al.* 1991).

By combining high-power tunable lasers with synchrotron radiation, photoelectron studies have been successfully extended to optically inaccessible states in the XUV regime (Bizau *et al.* 1982, 1985, 1986, Nunnemann *et al.* 1985, Ferray *et al.* 1987, Cubaynes *et al.* 1989, Carre *et al.* 1990). The species investigated in various experiments are listed in table 1.2. The experimental arrangement used in the pioneering experiments (Bizau *et al.* 1982) is illustrated in figure 1.4. This technique was further developed by Meyer *et al.* (1987, 1990) and Baier *et al.* (1992) who took the advantage of the well defined polarisation of both radiation fields by preparing the atoms in aligned or oriented states via laser pumping and studying the dependence of the photoelectron signals on the angle between the polarisation axes of laser and synchrotron radiation.

In order to fully exploit this method a rotatable electron analyser was used for measurements of the angular distribution of photoelectrons from laser-excited aligned Li atoms by Pahler *et al.* (1992). In contrast to experiments with unpolarised atoms the study of the angular distribution of photoelectrons from

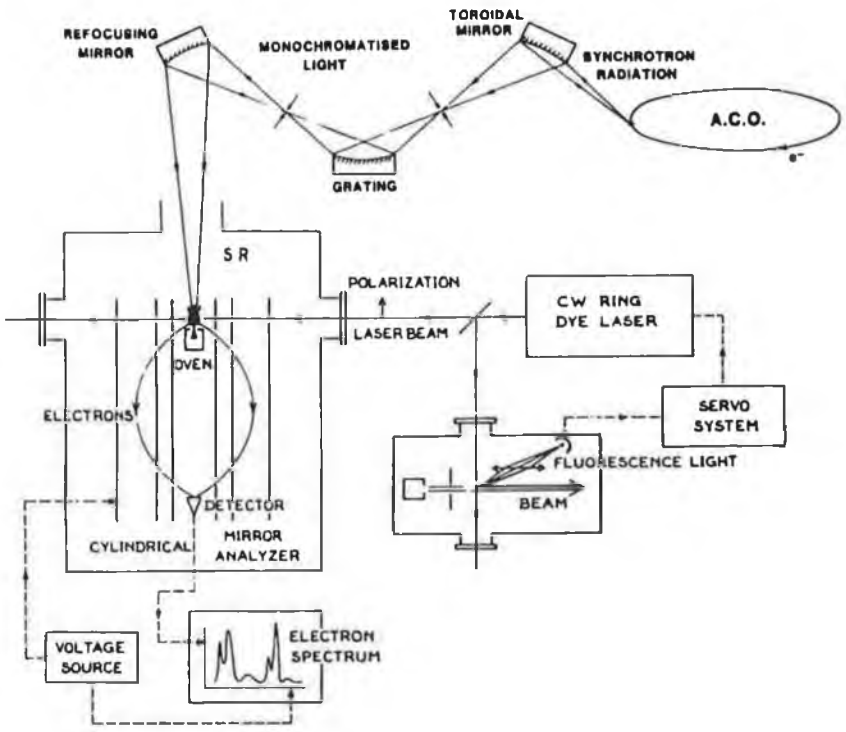

Figure 1.4

Layout of the experimental set up for the photoionization cross section studies on laser excited atoms (from Bizau *et al.* 1982).

Table 1.2. A summary of the photoelectron studies in valence-excited species carried out in combined laser–synchrotron experiments.

Species	Regions	References
Na*(3p)	2p	Bizau *et al.* (1985)
Ba*(6s5d)	5p, 4d and 5s	Bizau *et al.* (1986)
Na*(4p)	2p	Ferray *et al.* (1987)
Na*(4d)	"	"
Na*(5s)	"	"
Na*(3p)	2p	Cubaynes *et al.* (1989)

aligned or polarised atoms offers the possibility of getting additional information for the description of the photoionization process and the corresponding atomic states. As the angular distribution of the outgoing electrons critically depends on the symmetry of the core-excited state, on the alignment of the intermediate state prepared by the laser, and on the relative orientation of the polarisation vectors of the two radiation fields, one can therefore, distinguish between states of different symmetry. In the pioneering experiment (see figure 1.5) of Pahler *et al.* (1992), by measuring the angular distributions of photoelectrons, they were able to distinguish between the different symmetry character of the autoionizing ^{2}S- and ^{2}D-resonances of even parity configurations Li 1snl nℓ' which were reached by the two-step excitation Li $1s^2\ 2s\ ^2S$ (laser) $\rightarrow$ $1s^2\ 2p\ ^2P$ (SR) $\rightarrow$ 1s nl nℓ' ^{2}S, ^{2}D. In the case of Li the spin-orbit interaction is very small; fine structure splitting and doublet-quartet transitions, therefore, can be neglected and only these two types of transitions have to be considered.

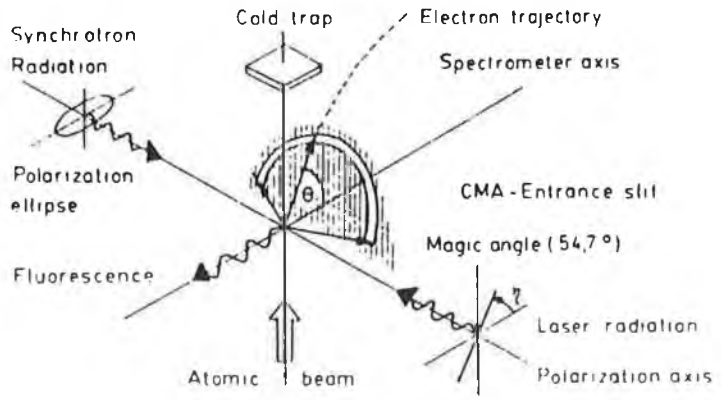

Figure 1.5

Schematic representation of the experimental set up for the two photon experiments (from Pahler *et al.* 1992).

Most recently, using this angle resolved photoelectron spectroscopy of laser aligned sodium atoms Baier *et al.* (1994) studied the $2p^5$ 3s3p resonances.

1.2.3 Photoabsorption spectroscopy

Photoabsorption measurements made on the radiation transmitted through the absorbing species can provide (i) total relative or absolute absorption cross sections, and (ii) energy level data of the resonance structures.

Progress in the field of VUV and XUV photoabsorption studies of ionic and some neutral species, other than gases and easily evaporable metallic atoms, has been hampered for many years by the lack of "small-scale" continuum sources to act as alternatives to synchrotron facilities. In addition the lack of suitable techniques for the generation of the absorbing species was a major barrier.

Esteva and Mehlman (1974) demonstrated such an experiment in which ionic absorption was measured using two synchronised electrode vacuum sparks (Mehlman-Ballofet and Esteva 1969, Esteva *et al.* 1972). One spark served as a transient source of absorbing species and the other one, termed a BRV source (Ballofet, Romand and Vodar 1961), was used to provide the background continuum. Using this technique, time-resolved photoabsorption spectra were measured for Mg, Mg^{+} and Mg^{2+} (Esteva and Mehlman 1974) and for Be^{2+} and Be^{3+} (Mehlman and Esteva 1973). This technique has not been extended to other ions.

The technique of flash-pyrolysis has been used in the photoabsorption studies of ionic Ba^{+} (Roig 1976), Li^{+} (Cantu *et al.* 1977) and neutral aluminium (Cantu *et al.* 1982). In this technique the absorbing metal is introduced in a quartz or glass tube which is surrounded by a helical flash lamp. The material in the tube is vaporised and ionised by the strong luminous flux emitted by the flash lamp. A BRV source synchronised with the flash lamp was used to provide background continuum.

This technique was only applicable to easily evaporable materials and, at most, to singly ionised species. The other drawbacks of this set up were associated with the BRV spark which has a limited repetition rate, electrode life time and operates under high vacuum environment. It provided a relatively linefree continuum but was limited to between 100-600 Å and also the pulse duration was relatively long ($\approx$ 60 ns) .

The techniques of synchronised dual vacuum spark and flash-pyrolysis were successfully employed in the time-resolved photoabsorption studies of atoms and ions but were restricted to ground state absorption studies only. Using these techniques it was not possible to selectively populate the absorbing species in

excited states.

Table 1.3. A summary of photoabsorption studies of species carried out using the technique of resonant laser-driven excitation/ionization.

Species	Regions	Detection	References
Ground state			
Na^+	2p	PG	Lucatorto and McIlrath (1976)
Li^+	1s	PG	McIlrath and Lucatorto (1977)
Ba	4d	PE	Lucatorto *et al.* (1981)
Ba^+	〃	〃	〃
Ba^{2+}	〃	〃	〃
Ba^+	5p	PG	Hill III *et al.* (1982)
Cs^+	4d		McIlrath *et al.* (1986)
Ca^+	3p		Sonntag *et al.* (1986)
Ba^+	5p	PG	Hill III *et al.* (1987)
Mn^+	3p	PE	Cooper *et al.* (1989).
Cr	〃	〃	〃
Excited state			
$Li^*(2p)$	1s & 2s	PG	McIlrath and Lucatorto (1977)
$Na^*(3p)$	2p	PG	Sugar *et al.* (1979)
$Ca^*(4s4p)$	3p	PE	Sonntag *et al.* (1986)

PG = Photographic detection, PE = Photoelectric detection.

The technique of resonant laser-driven excitation/ionization, based on the pioneering work of Bradley *et al.* (1973) and of McIlrath (1969), McIlrath and Carlsten (1973), has been used in the photoabsorption studies of the neutral, singly and doubly ionized species shown in table 1.3. In these experiments, the output of a tunable dye laser was used to ionize or selectively excite an atomic

vapour column produced in a heat pipe. To produce doubly charged species two time-synchronized tunable lasers were employed Lucatorto *et al.* (1981). One was used to convert atomic vapour in a heat pipe to a singly ionized plasma and the second to ionize it into a doubly ionized plasma. To do photoabsorption measurements a time-synchronized BRV spark or laser plasma was used as the source of background continuum.

The application of this technique, requires sufficiently high vapour densities, therefore, it is mostly suitable for easily evaporable atomic systems. Because of the lack of laser technology at shorter wavelengths this technique does not allow an extension to absorption measurements for the higher members of isoelectronic sequences although it does have the potential for selective excitation and ionization.

The technique which has enabled us to carry out absorption studies of atoms (including easily evaporable and refractory metal vapours) and ions in ground and excited states and to extend them along isoelectronic as well as isonuclear sequences is based on the pioneering works of Carillon *et al.* (1970) and Carroll and Kennedy (1977). Using the experimental set up shown in figure 1.6a, Carillon *et al.* (1970) were able to do time and space-resolved absorption studies of laser-produced plasmas. In this experiment the output of a Nd glass laser (1J, 30ns) was split into two parts. One part of this beam was utilised in producing the absorbing Al plasma and the other after an optical delay was also focused on Al to generate the probing plasma. The predominantly line radiation emitted from the probing plasma was passed through the absorbing Al plasma.

Later on Carroll and Kennedy (1977) used the XUV/VUV continuum emission from a laser generated tungsten plasma to study the photoabsorption of a lithium plasma. In this experiment (figure 1.6b) the absorbing and continuum plasmas were both generated by a single ruby laser (1.5J, 30ns). The output of this laser was split into two parts: one was focused onto the Li target to generate the absorbing plasma while the other focused on the tungsten target induced a small hot plasma which provided the background continuum. Since then, this technique, now known as dual laser-produced plasma (DLPP) where one plasma serves as a transient source of multiply ionised species and the other generates the background continuum, has been extensively applied to ionic photoabsorption studies. The species studied to date in various dual laser-produced plasma experiments are listed in table 1.4. In these experiments the two laser pulses required for generating absorbing species and background continuum were

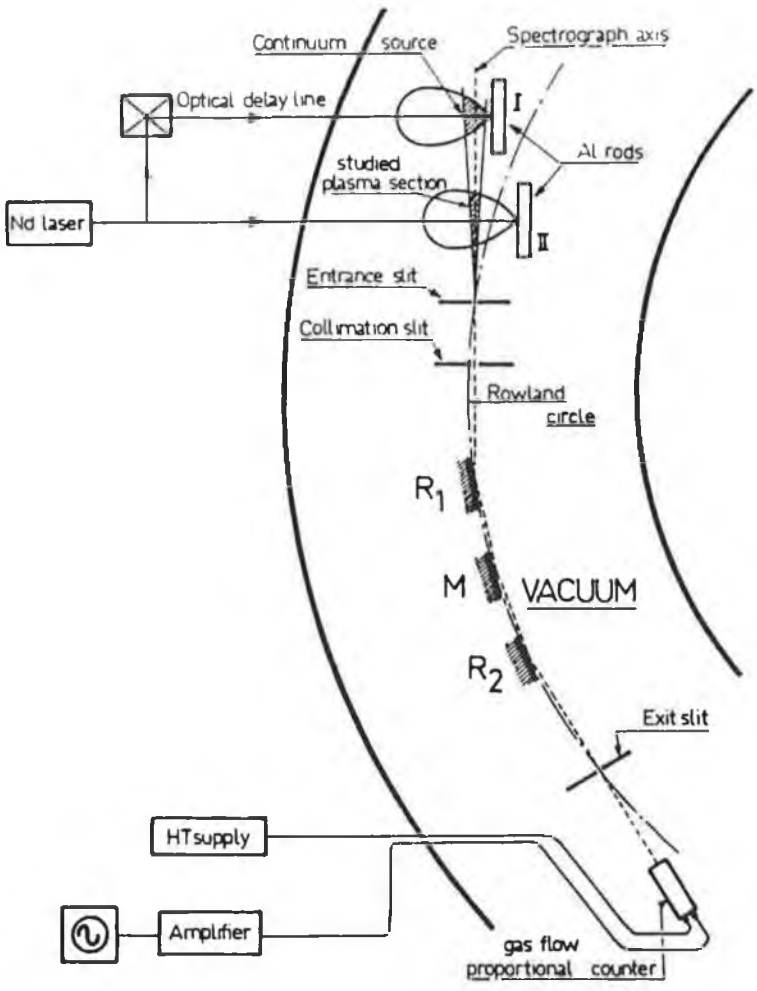

Figure 1.6(a)

The experimental setup of the dual laser-produced plasma experiment in which the radiation emitted from one aluminium plasma was used to probe the other aluminium plasma (from Carillon *et al.* 1970).

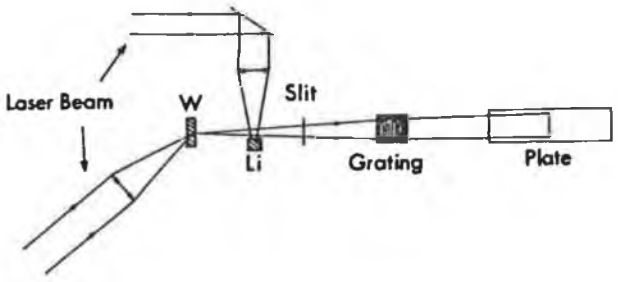

Figure 1.6(b)

Schematic of the experimental arrangement used in the first dual laser-produced plasma photoabsorption experiment in which one plasma served as a source of absorbing species and the other generated background continuum (from Carroll and Kennedy 1977).

Table 1.4. A summary of the previous photoabsorption studies in atoms and ions carried out with the dual laser-produced plasma method.

Species	Regions	Detection	References
Ground state			
Li^+	1s	PG	Carroll and Kennedy (1977)
Be^{2+}	1s	PG & PE	Jannitti *et al.* (1984a)
Be^{2+}	1s	PG & PE	Jannitti *et al.* (1984b)
Be^{3+}	1s	PG & PE	Jannitti *et al.* (1984a)
Be^+	1s	PE	Jannitti *et al.* (1985)
Be^+	1s	PE	Jannitti *et al.* (1986)
Th	5d	PG	Carroll and Costello (1986)
U	5d	PG	Carroll and Costello (1987)
Be	1s	PE	Jannitti *et al.* (1987)
Be^+	〃	〃	〃
Be^{2+}	〃	〃	〃
Be^{3+}	〃	〃	〃
Si^{3+}	2p	PG	Mosnier *et al.* (1987)
C^{4+}	1s	PE	Jannitti *et al.* (1988)
Al^{2+}	2p	PG	Brilly *et al.* (1988)
La^{3+}	4d	PG	Hansen *et al.* (1989)
C	1s	PE	Jannitti *et al.* (1990)
C^+	〃	〃	〃
C^{2+}	〃	〃	〃
C^{3+}	〃	〃	〃
Cr	3p	PE	Costello *et al.* (1991b)
Cr^+	3p	〃	〃

Continued.

Table 1.4. Continued.

Species	Regions	Detection	References
Mn	3p	PE	Costello *et al.* (1991b)
Mn^+	3p	"	"
W	4f and 5p	"	Costello *et al.* (1991c)
Pt	4f and 5p	PE	"
B	1s	PG	Lynam *et al.* (1992)
B^+	1s	PG	"
Ga^+	3p and 3d	PG	Dunne *et al.* (1993)
Excited state			
$Al^{2+*}(3p)$	2p	PG	Brilly *et al.* (1990)
$Al^{2+*}(3d)$	"	"	"
$Si^{3+*}(3p)$	"	"	"
$Si^{3+*}(3d)$	"	"	"

obtained either by splitting the output of a one laser into two parts delayed optically (Brilly *et al.* 1988) or from two separate time-synchronised lasers (Carroll and Costello 1986). Exploiting the temporal and spatial evolution of the absorbing plasma plume the spectra of the species of interest in either ground or valence-excited states were recorded photographically or photoelectrically.

As can be seen from table 1.4, most of the previous studies were carried out along either isonuclear sequences or for individual species. In the present work, with the exception of atomic silicon, photoabsorption investigations have been carried out along the isoelectronic sequences. The details of the various absorption transitions and the corresponding isoelectronic members studied are listed in table 1.5. Members of these sequences in ground state absorption have been of recent interest in theoretical photoionization studies including resonance structures. In most of these type of calculations reported so far (see, for example,

Daum and Kelly 1976, Isenberg *et al.* 1985, Altun 1989 and Ivanov *et al.* 1994) only one-electron resonances have been included. As listed in table 1.5, the members of these sequences in ground state absorption are found to exhibit strong double-electron resonances mixed with the one-electron resonances (for details see chapters 4, 5 and 6). Therefore, the data reported in this work will help in improving the theory.

Table 1.5. Details of the photoabsorption studies undertaken in this work.

Sequence studied in	Members	Transitions studied		
Ground state				
• Na I	Mg^+, Al^{2+}, and Si^{3+}	$2p^63s$	→	$2p^53snl$
			→	$2p^53pnp$
• Mg I	Mg, Al^+[a], and Si^{2+}	$2p^63s^2$	→	$2p^53s^2nl$
			→	$2p^53s3pnp$
• Al I	Al and Si^+	$2p^63s^23p$	→	$2p^53s^23pnl$
			→	$2p^53s3p^2np$
• Si I	Si	$2p^63s^23p^2$	→	$2p^53s^23p^2nl$
			→	$2p^53s3p^3np$
Excited state				
• Na I	Mg^+, Al^{2+} and Si^{3+}	$2p^63p$	→	$2p^53s3p$
• Mg I[b]	Mg, Al^+, and Si^{2+}	$2p^63s3p$	→	$2p^53s^23p$
• Al I	Si^+	$2p^63s3p^2$	→	$2p^53s^23p^2$

[a]Costello *et al.* (1992).

[b]Mosnier *et al.* (1994).

1.3 Conclusions

As can be seen from section 1.2, photoabsorption and photoionization has been studied only in few ions. Although various experimental setups have been developed, some are facing technical limitations and the remainder are passing through their testing phase. At present, only the dual laser-produced plasma technique can be applied to a wide variety of species. Although it is suitable mostly for the measurements of relative ionic cross-sections even then it can provide a testing ground for theory. The inner-shell photoabsorption technique provides measurements of descrete and continuum structures which can be compared with those predicted by theory. To date although a few calculations including resonance structures have been carried out this trend is expected to increase in the near future. It is hoped that the photoabsorption data reported in this thesis will play an important role in stimulating further theoretical studies.

1.4 References

Altun Zikri, 1989, Phys. Rev. A **40**, 4968.

Baier S, Fiedler W, Muller B R, Schulze M, Zimmermann P, Meyer M, Pahler M, Prescher T, Richter M, Ruder J and Sonntag B, 1992, J. Phys. B: At. Mol. Opt. Phys. **25**, 923.

Baier S, Schulze M, Staiger H, Zimmermann P, Lorenz C, Pahler P, Ruder J, Sonntag B, Costello J T and Kiernan L, 1994, J. Phys. B: At. Mol. Opt. Phys. **27**, 1341.

Ballofet G, Romand J and Vodar B, 1961, C.R. Acad.Sci., **252**, 4139.

Bizau J M, Wuilleumier F, Dhez P, Ederer D L, Picque J L, Gouet G L and Koch P, 1982, in *"Laser Techniques for Extreme Ultraviolet spectroscopy"*, eds. T J McIlrath and R J Freeman, AIP Conf. Proc. No. 90 (New York: American Institute of Physics) p. 331.

Bizau J M, Wuilleumier F, Ederer D L, Keller J C, LeGouet J L, Picque J L, Carre B and Koch P M, 1985, Phys. Rev. Lett. **55**, 1281.

Bizau J M, Cubaynes D, Gerard P, Wuilleumier F J, Picque J L, Ederer D L, Carre B and Wendin G, 1986, Phys. Rev. Lett. **57**, 306.

Bizau J M, Cubayne D, Richter M, Wuilleumier F J, Obert J, Putaux J-C, Morgan T J, Kallne E, Sorensen S and Damany A, 1991, Phys. Rev. Lett., **67**, 576.

Bizau J M, Cubayne D and Wuilleumier F J, 1993, in "*Vacuum Ultraviolet Radiation Physics*" , eds. Wuilleumier F J, Petroff Y and Nenner I, Proceedings of the 10th VUV conference (Singapore: World Scientific Publishing Co. Pte. Ltd.)

Bradley D J, Ewart P, Nicolas J V, Shaw J R D and Thompson D G, 1973, Phys. Rev. Lett., **31**, 263.

Brilly J, Kennedy E T and Mosnier J P, 1988, J. Phys. B, **21**, 368.

Brilly J, Kennedy E T and Mosnier J P, 1990, Physica Scripta, **41**, 30.

Cantu A M, Parkinson W H, Tondello G and Tozzi G P, 1977, J. Opt. Soc. Am., **67**, 1030.

Cantu A M, Tozzi G P and Spector N, 1982, J. Opt. Soc. Am., **72**, 729.

Carillon A, Jaegle P and Dhez P, 1970, Phys. Rev. Lett., **25**, 140.

Carre B, Oliveira P D, Ferray M, Fournier P, Gounand F, Cubaynes D, Bizau J M and Wuilleumier F J, 1990, Z. Phys. **D15**, 177.

Carroll P K and Kennedy E T, 1977, Phys. Rev. Lett., **38**, 1068.

Carroll P K and Costello J T, 1986, Phys. Rev. Lett. **57**, 1581.

Cooper J W, Clark C W, Cromer C L, Lucatorto T B, Sonntag B F, Kennedy E T and Costello J T, 1989, Phys. Rev. A **39**, 6074.

Costello J T, Mosnier J P, Kennedy E T, Carroll P K and O'Sullivan G, 1991a, *"XUV Absorption Spectroscopy with Laser-Produced Plasmas; A Review"* Physica Scripta (Proceedings of 22nd EGAS Conference), T34, 77.

Costello J T, Kennedy E T, Sonntag B F and Clarke C W, 1991b, Phys. Rev. A **43**, 1441.

Costello J T, Kennedy E T, Sonntag B F and Clarke C W, 1991c, Phys. Rev. A **43**, 1441.

Costello J T, Evans D, Hopkins R B, Kennedy E T, Kiernan L, Mansfield M W D, Mosnier J P, Sayyad M H and Sonntag B F, 1992, J. Phys. B: At. Mol. Opt. Phys. **25**, 5055.

Cromer CL, Bridges T M, Robert T R and Lucatorto T B, 1985, Appl. Opt., **24**, 2996.

Cubaynes D, Bizau J M, Wuilleumier F J, Carre B and Gounand F, 1989, Phys. Rev. Lett. **63**, 2460.

Daum R G and Kelly H P, 1976, Phys. Rev. A **13**, 715.

Deshmukh P C, Nasreen G and Manson S T, 1988, Phys. Rev. A **38**, 504.

Dunne P, O'Sullivan G and Ivanov V K, 1993, Phys. Rev. A **48**,

Esteva J M, Mehlman-Ballofet G and Romand J, 1972, J. Quant. Spectrosc. Radiat. Transfer., **12**, 291.

Esteva J M and Mehlman G, 1974, Astrophys. J., **193**, 747.

Ferray, Gounand F, Oliveira P D, Fourier P R, Cubayne D, Bizau J M, Morgan T J and Wuilleumier F J, 1987, Phys. Rev. Lett. **59**, 2040.

Hansen J E, Brilly J, Kennedy E T and O'Sullivan G, 1989, Phys. Rev. Lett., **63**, 1934.

Hill W T III, Cheng K T, Johnson W R, Lucatorto T B, McIlrath T J and Sugar J, 1982, Phys. Rev. A **49**, 1631.

Hill W T III, Sugar J, Lucatorto T B and Cheng K T, 1987, Phys. Rev. A **36**, 1200.

Hopkins R B, 1992, M.Sc. thesis, Dublin City University, unpublished.

Isenberg E M, Carter S L, Kelly H P and Salomoson S, 1985, Phys. Rev. A **32**, 1472.

Ivanov V K, West J B, Gribakin G F and Gribakina A A, 1994, Z. Phys. D **29**, 109.

Jannitti E, Nicolosi P and Tondello G, 1979, Optics Letters, **4**, 187.

Jannitti E, Nicolosi P and Tondello G, 1984a , Physica **124C**, 139.

Jannitti E, Nicolosi P and Tondello G, 1984b , Opt. Commun. **50**, 225.

Jannitti E, Mazzoni M, Nicolosi P, Tondello G and Yongchang W, 1985, J. Opt. Soc. Am. **2**, 1078.

Jannitti E, Pinzong F and Tondello G, 1986, Physica Scripta, **33**, 434.

Jannitti E, Nicolosi P and Tondello G, 1987, Physica Scripta, **36**, 93.

Jannitti E, Nicolosi P and Tondello G, 1988, Phys. Lett. A, 131, 186.

Jannitti E, Nicolosi P and Tondello G, 1990, Physica Scripta, 41, 458.

Kennedy E T and Carroll P K, 1977, Phys. Lett., **64A**, 37.

Kiernan L, 1994a, Ph.D. thesis, Dublin City University, unpublished.

Kiernan L M, Kennedy E T, Mosnier J-P, Costello J T and Sonntag B F, 1994b, Phys. Rev. Lett. **72**, 2359.

Lahiri J and Manson S T, 1988, Phys. Rev. A **37**, 1047.

Lucatorto T B and McIlrath T J, 1976, Phys. Rev. Lett., **37**, 428.

Lucatorto T B, McIlrath T J, Sugar J and Younger S M, 1981, Phys. Rev. Lett., **47**, 1124.

Lucatorto T B, McIlrath T J, Hill W T and Clark C W, 1982, AIP Conf. Proc. **94**, 584.

Lynam W G, Carroll P K, Costello J T, Evans D and O'Sullivan G, 1992, J. Phys. B. **25**, 3963.

Lyon I C, Peart B, West J B and Dolder K, 1986, J. Phys. B. 19, 4137.

Lyon I C, Peart B and Dolder K, 1987a, J. Phys. B **20**, 1925.

Lyon I C, Peart B, Dolder K and West J B, 1987b, J. Phys. B, **20**, 1471.

McIlrath T J, 1969, Appl. Phys. Lett., **15**, 41.

McIlrath T J and Carlsten J L, 1973, J. Phys. B: Atom. Molec. Phys., **6**, 697.

McIlrath T J and Lucatorto T B, 1977, Phys. Rev. Lett., **38**, 1390.

McIlrath T J, Sugar J, Kaufman V, Cooper W and Hill W T III, 1986, J. Opt. Soc. Am. B **3**, 398.

Mehlman-Balofet G and Esteva J M, 1969, Astrophys. J., **157**, 945.

Mehlman G and Esteva J M, 1973, C.R. Acad. Sci., **276**, 1973.

Meyer M, Muller B, Nunnemann A, Prescher Th, v Raven E, Richter M, Schmidt M and Zimmermann P, 1987, Phys. rev. Lett. **59**, 2963.

Meyer M, Pahler M, Prescher T, v Raven E, Richter M, Sonntag B, Baier S, Fiedler W, Muller B R, Schulze M and Zimmermann P, 1990, Physica Scripta **T31**, 28.

Missavage D W, Manson S T, and Daum G R, 1977, Phys. Rev. A **15**, 1001.

Mosnier J P, Brilly J and Kennedy E T, 1987, J. Physique, 48, C9-219.

Mosnier J P, Costello J T, Kennedy E T, Kiernan L and Sayyad M H, 1994, Phys. Rev. A **49**, 755.

Nasreen G, Manson S T and Deshmukh P C, 1989, Phys. Rev. A **40**, 6091.

Nicolosi P, Jannitti E and Tondello G, 1991, J. Physique II, **1**, C1-89.

Nunnemann A, Prescher T, Richter M, Schmidt M, Sonntag B, Wetzel H E and Zimmermann P, 1985, J. Phys. B **18**, L387.

Pahler M, Lorenz C, v Raven E, Sonntag B, Baier S, Muller B R, Schulze M, Staiger H, Zimmermann P and Kabachnik N M, 1992, Phys. Rev. Lett., **68**, 2285.

Peart B and Lyon I C, 1987, J. Phys. B: Atom. Molec. Phys., **20**, L673.

Peart B, Lyon I C, and Dolder K, 1987, J. Phys. B: Atom. Molec. Phys., **20**, 5403.

Pejcev V, Ottley T W, Rassi D and Ross K J, 1977, J. Phys. B **10**, 2389.

Richter M, 1993, in "*Vacuum Ultraviolet Radiation Physics*" , eds. Wuilleumier F J, Petroff Y and Nenner I, Proceedings of the 10th VUV conference (Singapore: World Scientific Publishing Co. Pte. Ltd.)
Roig R A, 1976, J. Opt. Soc. Am., **66**, 1400.

Schwob J L, Wouter A W and Suckewer S, 1987, Rev. Sci. Instrum., **58**, 1601.

Scmidt V, 1992, Rep. Prog. Phys., **55**, 1483.

Shaw M, 1994, M.Sc. thesis, un-finished work.

Sonntag B F, Cromer C L, Bridges J M, McIlrath T J and Lucatorto T B, 1986, "*Short Wavelength Coherent Radiation: Generation and Applications.*" (Monterey, California 1986), Proceedings of the Topical Meeting on Short Wavelength Coherent Radiation, AIP Conf. Proc. No 147 (New York: Am. Inst. Phys.) pp 412-21.

Sonntag B and Zimmermann P, 1992, Rep. Prog. Phys., 991.

Sugar J, Lucatorto T B, McIlrath T J and Weiss A W, 1979, Opt. Lett., **4**, 109.

Tondello G, 1979, Optica Acta, **26**, 357.

Wuilleumier F J, 1989, Proc. of the LURE-ESRF Workshop on Photon-Ion Interactionq, eds. Wuilleumier F J and Kallne E, (ESRF: Grenoble) pp. 5 and 231.

Whitfield S B, Caldwell C D and Krause M O, 1991, Phys. Rev. A **43**, 2338.

Wuilleumier F J and Krause M O, 1974, Phys. Rev. A **10**, 242.

Wuilleumier F J, Cubaynes D and Bizau J M, *"Atomic and Molecular Physics Third US-Mexico Symposium"*, eds. C. Cisneros, I Alvarez and T J Morgan (World Scientific Publishing Company: Singapore, 1991) p. 474.

Wuilleumier F J, 1992, *"Proceedings of Sixth Symposium on Correlations and Polarization in Electronic and Atomic Collisions and (e, 2e) Reactions"*, (Bristol: UK: Institute of Physics) p. 203.

Wuilleumier F J, Bizau J M, Cubaynes D, Rouvellou B and Journel L, 1994, Nuclear Instruments and Methods in Physics Research **B 87**, 190.

Chapter 2

SUMMARY OF ATOMIC STRUCTURE THEORY

To facilitate the analysis of measured spectra extensive atomic structure calculations have been performed with the help of a suite of atomic structure computer programs. Computed transition energies and energy level compositions were needed as an aid to identification of the observed spectral lines. To interpret line intensities, oscillator strengths were required. This chapter provides an introduction to the theory of atomic structure and an outline of the programs.

2.1 Introduction

Using the Slater-Condon theory of atomic structure (Slater 1929, 1960; Condon and Shortley 1935) *ab initio* or scaled calculations (for explanation see section 2.7.2) can be made of atomic energy levels and spectra, either in the single configuration or including configuration-interaction effects. For this purpose there are required theoretical values of: (1) the total binding energy of the spherically-averaged atom in each configuration of interest (corresponding to the centre-of-gravity energy E_{av} of all possible states of the configuration); (2) the electrostatic and spin-orbit radial integrals F^k, G^k, and ξ, in terms of which the energy splittings from E_{av} are expressible; (3) the more general Slater integrals R^k, if configuration-interaction effects are to be included; and (4) the dipole matrix elements for the transitions in question, if gf-values are to be calculated.

All of these quantities are given by familiar expressions involving various integrals of the one-electron radial wavefunction which can be obtained from the solution of the Schrodinger wave equation. The treatment provided in the following sections follows closely that given in the famous book "*The Theory of Atomic Structure and Spectra*" by R. D. Cowan (Cowan 1981).

2.2 The Schrodinger equation for a multi-electron system

The theoretical treatment of a multi-electron atom starts with the selection of a suitable Hamiltonian operator. An appropriate form may be obtained by summing the one-electron operator over all N electrons, and adding a term for the electrostatic Coulomb interactions among the electrons:

$$H = H_{kin} + H_{elec-nucl} + H_{elec-elec} + H_{s-o}, \tag{2.1}$$

or

$$H = -\sum_i \nabla_i^2 - \sum_i \frac{2Z}{r_i} + \sum_{i>} \sum_j \frac{2}{r_{ij}} + \sum_i \xi_i(r_i)(l_i.s_i), \tag{2.2}$$

where $r_i = |\mathbf{r}_i|$ is the distance of the ith electron from the nucleus, $r_{ij} = |\mathbf{r}_i - \mathbf{r}_j|$ is the distance between the ith and jth electrons and summation over $i > j$ is over all pairs of electrons. Distances are measured in Bohr units ($a_0 = 0.529177$ Å) and energy in rydbergs (13.6058 eV).

The mass-velocity and Darwin terms have not been included in the Hamiltonian (2.2). These terms depend only on $|\mathbf{r}_i|$ and have the effect only of shifting the absolute energies of a group of related levels, without affecting the energy difference among the levels. The final term of the Hamiltonian represents the sum over all electrons of the magnetic interaction energy between the spin of an electron and its own orbital motion. Unlike the mass-velocity and Darwin terms, the spin-orbit interaction involves the angular portion of the wavefunction through the operators **l** and **s**, and has a pronounced effect on energy-level structures; it is therefore necessary to retain it explicitly in the Hamiltonian. The proportionality factor ξ_i in this term is measured in rydbergs and is given by

$$\xi_i(r_i) = \frac{\alpha^2}{2} \frac{1}{r_i} \left(\frac{dV}{dr_i} \right), \tag{2.3}$$

where V(r) is an appropriate potential energy function for an electron in a multi-electron atom and α is the fine structure constant.

The Schrodinger equation for the Hamiltonian (2.1) can be written as

$$H\Psi^k = E^k\Psi^k. \tag{2.4}$$

Solving this equation one can obtain the wavefunction Ψ^k and the energy E^k of the atom for every stationary state k of interest. The total wavefunction is a function of 4N variables: three space and one spin co-ordinate for each electron. For N > 1, exact solutions cannot be obtained at all and approximations of one sort or another are required. The method to be described here was first developed by Slater (1929), and later extended by Condon and Shortley (1935). The basic procedure consists of expanding the unknown wavefunction Ψ^k in terms of a set of known orthonormal basis functions Ψ_b :

$$\Psi = \sum_b y_b^k \Psi_b . \tag{2.5}$$

This basis set has an infinite number of members. In practice, it is necessary to truncate the series to a finite number of terms. Substitution of (2.5) into (2.4) gives

$$\sum_{b'=1}^{M} H\, y_{b'}^k \Psi_{b'} = E^k \sum_{b'=1}^{M} y_{b'}^k \Psi_{b'} . \tag{2.6}$$

Multiplying this from the left by Y_b and integrating over all 3N space co-ordinates, we have

$$\sum_{b'=1}^{M} H_{bb'} y_{b'}^k = E^k \sum_{b'=1}^{M} y_{b'}^k \langle \Psi_b | \Psi_{b'} \rangle$$

$$= E^k\, y_b^k, \qquad 1 \le b \le M, \tag{2.7}$$

where

$$H_{bb'} \equiv \langle \Psi_b | H | \Psi_{b'} \rangle . \tag{2.8}$$

The relations (2.7) represent a set of M simultaneous linear equations in the M unknowns $y_{b'}^k$. This set of equations has a non-trivial solution only if the determinant of the matrix $(H_{bb'} - E^k \delta_{bb'})$ is zero:

$$\left| H - E^k I \right| = 0 . \tag{2.9}$$

where I is the identity matrix. When this determinant is expanded into a polynomial of degree M in E^k, its zeroes represent M different possible energy levels of the atom. Each of these values of E^k, substituted back into (2.7), gives $M-1$ independent equations for the $M-1$ ratios

$$y_b^k / y_i^b, \qquad b \neq i;$$

the value of y_i^b is chosen such that

$$\sum_{b=1}^{M} |y_b^k|^2 = 1, \tag{2.10}$$

so that Ψ^k is normalized:

$$\langle \Psi^k | \Psi^k \rangle = \langle \sum_b y_b^k \Psi_b | \sum_{b'} y_{b'}^k \Psi_{b'} \rangle = \sum_b \sum_{b'} (y_b^k)^* y_{b'}^k \langle \Psi_b | \Psi_{b'} \rangle = \sum_b |y_b^k|^2 .$$

For M no greater than 2 or 3, the above procedure is feasible, either numerically or analytically. For appreciably larger M, the Hamiltonian matrix $H \equiv (H_{bb'})$ is diagonalized numerically. If the set of expansion coefficients is written in the form of a column vector

$$Y^k = \begin{pmatrix} y_1^k \\ y_2^k \\ y_3^k \\ \cdot \\ \cdot \\ \cdot \\ y_M^k \end{pmatrix}, \tag{2.11}$$

then equations (2.7) may be written as the single matrix equation

$$HY^k = E^k Y^k , \tag{2.12}$$

and the problem is to find the M eigenvalues E^k of the matrix H, together with the corresponding eigenvectors $\mathbf{Y}^k$. To achieve this numerical values of the matrix elements $H_{bb'}$ are supplied to a computer, and a matrix T is found that can diagonalize H. The kth diagonal element of the diagonalized Hamiltonian matrix is the eigenvalue E^k,

$$T^{-1}HT = (E^k \delta_{kb}). \tag{2.13}$$

In summary, once the Hamiltonian matrix elements $H_{bb'}$ are computed, the energy levels of an atom can be calculated. The computing of H is the most

difficult task. It involves setting up suitable basis functions required to evaluate the matrix elements.

2.3 Choosing the basis functions

In a multi-electron atom any given electron i can be assumed to move independently of the others in the electrostatic field of the nucleus and the other N-1 electrons (Independent particle model). This field is assumed to be time-averaged over the motion of the N-1 electrons, and therefore to be spherical symmetric. In this central field, the probability distribution of electron i can be described by a one-electron wavefunction (also called spin-orbital):

$$\varphi_i(r_i) = \frac{1}{r} P_{n_i l_i}(r_i).Y_{l_i m_{l_i}}(\theta_i, \phi_i).\sigma_{m_{s_i}}(s_{i_z}) , \tag{2.14}$$

where r_i denotes position (r, θ, ϕ) with respect to the nucleus and also the spin orientation s. This function differs from the hydrogenic one only in the radial part P_{nl}. As the potential energy V(r) in a multi-electron atom is no longer a simple Coulomb function; exact analytical solution of the differential equation is therefore not possible. Numerical procedures are required for the calculation of P_{nl}. The orthonormality of the spin-orbital yields

$$\langle \varphi_{nlm_l m_s} | \varphi_{n'l'm'_l m'_s} \rangle = \delta_{nn'}.\delta_{ll'}.\delta_{m_l m'_l}\delta_{m_s m'_s} , \tag{2.15}$$

or

$$\langle \varphi_i | \varphi_j \rangle = \delta_{ij} . \tag{2.16}$$

From the one-electron spin-orbitals one can construct the basis function for the entire atom. The probability that an electron lies at r_i from the nucleus is $|\varphi_i(r_i)|^2$ so the probability distribution of all the N electrons is $\Pi_{i=1}^{N}|\varphi_i(r_i)|^2$. This shows that for a multi-electron atom the basis function can be written as a product of spin-orbitals

$$\psi = \varphi_1(r_1)\varphi_2(r_2)\varphi_3(r_3)\cdots\varphi_N(r_N) . \tag{2.17}$$

The drawback of this product function is that it does not obey the Pauli exclusion principle. However, this can be rectified by using a wavefunction that is antisymmetric upon interchange of any two electron co-ordinates. Such a

wavefunction can be formed by taking the following linear combination of product functions:

$$\Psi = (N!)^{-1/2} \sum_{P} (-1)^{P} \varphi_1(r_1)\varphi_2(r_2)\varphi_3(r_3)\cdots\varphi_N(r_N). \qquad (2.18)$$

This antisymmetrized function may be written in the form of a determinant

$$\Psi = \frac{1}{N!^{1/2}} \begin{vmatrix} \varphi_1(r_1) & \varphi_1(r_2) & \varphi_1(r_3) & \cdots & \varphi_1(r_N) \\ \varphi_2(r_1) & \varphi_2(r_2) & \varphi_2(r_3) & \cdots & \varphi_2(r_N) \\ \varphi_3(r_1) & \varphi_3(r_2) & \varphi_3(r_3) & \cdots & \varphi_3(r_N) \\ \cdot & \cdot & \cdot & \cdots & \cdot \\ \cdot & \cdot & \cdot & \cdots & \cdot \\ \cdot & \cdot & \cdot & \cdots & \cdot \\ \varphi_N(r_1) & \varphi_N(r_2) & \varphi_N(r_3) & \cdots & \varphi_N(r_N) \end{vmatrix}, \qquad (2.19)$$

and is therefore referred to as a determinantal function or a Slater determinant (Slater 1929). The physical significance of this choice is clear from the well known properties of determinants. The interchanging of two columns in this determinant is equivalent to changing the co-ordinates of any two electrons. A determinant is zero if its two rows or columns are identical. Two orbitals having the same quantum numbers are reflected by two identical rows while the two electrons being in the same location are shown by two identical columns.

This determinantal form of a basis function Y exhibits almost all the required features for a basis vector. Although the basis functions can be chosen arbitrarily it is convenient to chose them to be as close as possible to the eigenfunctions of the Hamiltonian. Such a choice is important to have desired accuracy from ab initio calculations.

2.4 Matrix elements for determinantal basis functions

In the Hamiltonian operator given by

$$H = -\sum_i \nabla_i^2 - \sum_i \frac{2Z}{r_i} + \sum_i \xi_i(r_i)(l_i.s_i) + \sum_{i>} \sum_j \frac{2}{r_{ij}}, \qquad (2.20)$$

the first three terms are one-electron operators of the form

$$\sum_{i=1}^{N} f_i \equiv \sum_i f(r_i) \ , \tag{2.21}$$

symmetric in the spatial-plus-spin co-ordinates r_i of all N electrons, and the last term is a two-electron operator of the form

$$\sum_{i=2}^{N}\sum_{j=1}^{i-1} g_{ij} \equiv \sum_{i>}\sum_{j} g(r_i, r_j) \ , \tag{2.22}$$

symmetric in all N(N - 1)/2 pairs of co-ordinates. For a determinantal basis function it can be shown that

$$\langle \Psi | \sum_i f_i | \Psi \rangle = \sum_i \langle i | f_i | i \rangle , \tag{2.23}$$

$$\langle \Psi | \sum_{i>}\sum_{j} g_{ij} | \Psi \rangle = \sum_{i>}\sum_{j} [\langle ij | g | ij \rangle - \langle ij | g | ji \rangle . \tag{2.24}$$

In equation (2.24), the first terms on the right are the direct terms and they represent the energy due to mutual electrostatic repulsion for an uncorrelated spatial distribution of electrons. The second terms are the exchange terms and they represent the decrease in the repulsion energy that results when one includes the positional correlation of parallel-spin electrons.

2.5 One-electron and total atom binding energies

With the aid of the above results for determinantal basis functions, we can derive expressions for the centre-of-gravity energy of atomic states corresponding to an arbitrary electron configuration. It represents the energy of the spherically averaged atom, and is given by

$$E_{av} = \langle b | H | b \rangle_{av} , \tag{2.25}$$

where the average is to be carried out over all basis functions b belonging to the configuration in question. The simple form of this average is when all basis functions are given equal weight:

$$E_{av} = \frac{\sum_b \langle b|H|b\rangle}{\text{number of basis functions}}. \qquad (2.26)$$

Since the trace of a matrix is invariant under all orthogonal transformations (2.13) which diagonalizes H, (2.26) may also be written in the form

$$E_{av} = \frac{\sum_{\text{states}} E^k}{\text{number of states}}. \qquad (2.27)$$

where the summation is over all eigen states k of the configuration, having corresponding eigen value E^k. Since each energy level has a (2J + 1)-fold degeneracy, we may also write

$$E_{av} = \frac{\sum_{\text{levels}} (2J+1)E^J}{\sum_{\text{levels}} (2J+1)}. \qquad (2.28)$$

From this expression one may calculate an experimental value of E_{av}, using the observed energies of the levels belonging to the configuration in question. For example, for the configuration p^2 having LS terms ^3P, ^1D and ^1S,

$$E_{av} = \frac{1}{15}\left[E(^3P_0) + 3E(^3P_1) + 5E(^3P_2) + 5E(^3D_2) + E(^1S_0)\right].$$

The value of the centre-of-gravity energy given by the above expression is significant only to the extent that configuration-interaction perturbations are small.

The theoretical expressions for E_{av} can be obtained by substituting (2.23) and (2.24) in (2.25):

$$E_{av} = \sum_i \langle i|-\nabla^2|i\rangle_{av} + \sum_i \langle i|-\frac{2Z}{r_1}|i\rangle_{av} + \sum_{i>} \sum_j [\langle ij|\frac{2}{r_{12}}|ij\rangle_{av} - \langle ij|\frac{2}{r_{12}}|ji\rangle_{av}]. \qquad (2.29)$$

For the spin-orbit term the matrix elements cancel out (see Cowan 1981); thus the spin-orbit contribution to E_{av} is zero.

In expression (2.29), the first and second terms represent the kinetic (E_k) and electron-nuclear (E_n) energies while the last terms represent the electron-

electron Coulomb energies. The configuration-average binding energy of an electron in an orbital $n_i l_i$ is

$$E^i = E_k{}^i + E_n{}^i + \sum_{j \neq i} E^{ij}. \tag{2.30}$$

and the configuration-average total binding energy of all N electrons may be written in any of the equivalent forms

$$E_{av} = \sum_i E_k{}^i + \sum_i E_n{}^i + \sum_{i>} \sum_j E^{ij}. \tag{2.31}$$

or

$$E_{av} = \sum_i \left(E_k{}^i + E_n{}^i + \frac{1}{2} \sum_{j \neq i} E^{ij} \right), \tag{2.32}$$

or

$$E_{av} = \sum_i \left(E^i - \frac{1}{2} \sum_{j \neq i} E^{ij} \right), \tag{2.33}$$

or

$$E_{av} = \frac{1}{2} \sum_i (E_k{}^i + E_n{}^i + E^i). \tag{2.34}$$

Making use of the spin-orbitals (2.14) the values of the different terms - involved in the expressions for one-electron and total-atom binding energies - can be evaluated using the following expressions:

$$E_k{}^i \equiv \langle i|-\nabla^2|i\rangle_{av} = \int_0^\infty P^*_{n_i l_i}(r) \left[-\frac{d^2}{dr^2} + \frac{l_i(l_i+1)}{r^2} \right] P_{n_i l_i}(r) dr, \tag{2.35}$$

$$E_n{}^i \equiv \langle i|-\frac{2Z}{r_1}|i\rangle = \int_0^\infty (-\frac{2Z}{r})|P_i(r)|^2 dr, \tag{2.36}$$

The general expression for the matrix elements of $(1/r_{12})$ between the two-electron product functions is given by

$$\langle ij|2/r_{12}|tu\rangle = \delta_{m_{s_i} m_{s_t}} \delta_{m_{s_j} m_{s_u}} \sum_{k=0}^{\infty} R^k(ij,tu)$$

$$\times \sum_{q=-k}^{k} \delta_{q, m_{l_i} - m_{l_t}} \delta_{q, m_{l_j} - m_{l_u}} (-1)^q c^k(l_i m_{l_i}, l_t m_{l_t}) c^k(l_j m_{l_j}, l_u m_{l_u}), \tag{2.37}$$

where

$$R^k(ij,tu) \equiv \int_0^\infty \int_0^\infty \frac{2r_<^k}{r_>^{k+1}} P_i^*(r_1) P_j^*(r_2) P_t(r_1) P_u(r_2) dr_1 dr_2 \,. \qquad (2.38)$$

The electron-electron matrix elements involved in the expression (2.29) for E_{av} are the special cases of (2.32). For the direct contribution we obtain

$$\langle ij|2/r_{12}|ij\rangle = \sum_{k=0}^{\infty} F^k(ij) c^k(l_i m_{li}, l_i m_{li}) c^k(l_j m_{lj}, l_j m_{lj}), \qquad (2.39)$$

where

$$F^k(ij) \equiv R^k(ij,ij) = \int_0^\infty \int_0^\infty \frac{2r_<^k}{r_>^{k+1}} |P_i(r_1)|^2 |P_j(r_2)|^2 dr_1 dr_2, \qquad (2.40)$$

the contribution due to the exchange term is given by

$$-\langle ij|2/r_{12}|ji\rangle = -\delta_{m_{si} m_{sj}} \sum_{k=0}^{\infty} G^k(ij) [c^k(l_i m_{li}, l_j m_{lj})]^2, \qquad (2.41)$$

where

$$G^k(ij) \equiv R^k(ij,ji) = \int_0^\infty \int_0^\infty \frac{2r_<^k}{r_>^{k+1}} P_i^*(r_1) P_j^*(r_2) P_j(r_1) P_i(r_2) dr_1 dr_2. \qquad (2.42)$$

The radial integrals F^k and G^k (or more generally, R^k) are called the Slater integrals . The c^k's are the angular co-efficients and can be represented by analytical expressions (see Cowan 1981).

2.6 Calculation of level structure

The calculation of the level structure of an atom or ion involves the (i) determination of the detailed shape of the functions $P_{nl}(r)$ that form the radial factors of the one-electron spin-orbitals (2.14), and (ii) calculation of the energy matrix elements $H_{bb'} \equiv \langle b|H|b'\rangle$ [using as basis functions Ψ_b either the uncoupled determinental functions (2.14) or functions constructed according to any desired coupling scheme (see Cowan 1981)] and diagonalization of the energy matrix as described in section 2.2.

2.6.1 Determination of radial functions

The radial wavefunctions are the solutions of the radial part of the Schrodinger wave equation. For a multi-electron system no analytical solution is possible for this equation, however, this many body problem can be solved through approximations. As already stated, each electron can be assumed to be moving independently in an average potential formed by the Coulomb forces of the nucleus and other electrons (Independent Particle Model). Within the framework of this approximation, similar to hydrogen atom, each electron can be described by a spin-orbital

$$\varphi_i(r_i) = \frac{1}{r} PY\sigma. \tag{2.43}$$

The state wavefunction can be obtained from an antisymmetric linear combination of these spin-orbital products.

Each spin-orbital must satisfy the eigenvalue equation. Thus we get a set of N equations of the form,

$$H_i\varphi_i(r_i) = \varepsilon_i\varphi_i(r_i)\ , \tag{2.44}$$

called the Hartree equations. The radial part of these equations to be solved is of the form

$$\left[-\frac{d^2}{dr^2} + \frac{l_i(l_i+1)}{r^2} + V^i(r)\right]P_i(r) = \varepsilon_i P_i(r), \tag{2.45}$$

where $V^i(r)$ is the potential-energy function for the field in which the ith electron moves. Once the $P_i(r)$ are found for each configuration, the centre-of-gravity energy E_{av} and F^k, G^k, ξ and R^k can easily be calculated. These quantities when combined with the angular coefficients give the energies of the various levels in the configuration.

The differential equations (2.45) each have exactly the same form as the hydrogenic Schrodinger equation but $V^i(r)$ is different. In these equations the $V^i(r)$ depends on the radial functions $P_i(r)$, therefore, they are solved numerically by the self-consistent field (SCF) method. The net potential $V^i(r)$ experienced by the ith electron - initially unknown - can be found by going through a self-consistent treatment.

The calculation is started with the aid of an appropriate potential-energy function $V_o(r)$, scaled to $-2Z/r$ at small radii and to $-2(Z - N + 1)/r$ at large radii. This provides an initial potential $V^i(r)$ in which to calculate trial functions

$P_i^{(1)}(r)$ for all orbitals $n_i l_i$ on the first cycle of the SCF iteration (m = 1). Therefore, the potential-energy function $V^i(r)$ for cycle m is computed for the desired method (H, HFS, HX, or HS) (see section 2.7.1), using the functions $P_j(r)$ from cycle $m-1$. The value of e_i is adjusted so that $P_i^{(m)}(r))$ satisfy the boundary conditions

$$P_i(0) = 0, \text{ and} \tag{2.46}$$

$$\lim_{r\to\infty} P_i(r) = 0. \tag{2.47}$$

The condition (2.46) is required to keep the electron density finite at r = 0 and the condition (2.47) is required for the wavefunction of a bound electron. The $P_i^{(m)}(r)$ obtained is normalized and used to calculate $V^i(r)$ which in the next cycle yield $P_i^{(m)}(r)$. This procedure is repeated until the $P_i^{(q)}(r)$ found at the end of a cycle is essentially the same as that used at the beginning.

2.6.2 Calculation of energy levels

The energy levels of an atom or ion can be computed using a single or multi-configuration basis set.

In the single-configuration approximation of the Slater-Condon theory of atomic structure the energies of the various states of the field free atom are given by the eigenvalues of the matrix

$$\begin{pmatrix} H_{11} & H_{12} & H_{13} & \cdot & \cdot & \cdot \\ H_{21} & H_{22} & H_{23} & \cdot & \cdot & \cdot \\ H_{31} & H_{32} & H_{33} & \cdot & \cdot & \cdot \\ \cdot & \cdot & \cdot & & & \\ \cdot & \cdot & \cdot & & & \\ \cdot & \cdot & \cdot & & & \end{pmatrix}, \tag{2.48}$$

(one matrix for each possible value of total angular momentum) of the Hamiltonian operator. The matrix elements of the Hamiltonian

$$H = -\sum_i \nabla_i^2 - \sum_i \frac{2Z}{r_i} + \sum_i \xi_i(r_i)(l_i.s_i) + \sum_{i>} \sum_j \frac{2}{r_{ij}}, \tag{2.49}$$

connecting states b and b' may be written in the form

$$H_{bb'} = E_{av}\delta_{bb'} + \sum_{ijk}\left[f_k F^k(l_i,l_j) + g_k G^k(l_i,l_j)\right] + \sum_i d_i \xi(r_i)\,, \qquad (2.50)$$

if only the most important interactions are included and are evaluated using the coupled, antisymmetric basis functions (see Cowan 1981). Here l_i and l_j are orbital angular-momentum quantum numbers of electrons of a configuration

$$l_1^{n_1} l_2^{n_2} l_3^{n_3} \cdots l_q^{n_q}\,, \qquad (2.51)$$

of incompletely filled subshells. E_{av} is the average energy of all states (not levels) of the configuration. The parameters F^k and G^k are the same as defined by equations (2.40) and (2.42). The term $d_i\xi_i$ is defined by

$$\langle n_i l_i j_i m_i | \xi_i \cdot (l_i \cdot s_i) | n_i l_i j_i' m_i' \rangle = \xi_i \langle n_i l_i j_i m_i | (l_i \cdot s_i) | n_i l_i j_i' m_i' \rangle \equiv d_i \xi_i, \quad (2.52)$$

where

$$\xi_i(l_i) \equiv \xi_{n_i l_i} = \frac{\alpha^2}{2}\int_0^\infty \frac{1}{r}\left(\frac{dV^i}{dr}\right) |P_{n_i l_i}(r)|^2\, dr. \qquad (2.53)$$

The parameter coefficients f_k, g_k, d_i in equation (2.50) depend on the angular quantum numbers of the basis sates b and b′of the configuration (2.51) in the chosen representation, but are independent of the radial wavefunctions and therefore of the particular atom or ion which exhibits this configuration. Their values can be computed with the help of general analytical formulas (see Cowan 1968).

In the case of interacting configurations, accurate calculations cannot be made within the limitations of a single-configuration basis set. It is then necessary to use a multi-configuration approximation, in which the basis set includes wavefunctions from two or more configurations. Each computed eigenfunction Ψ will in general then be a mixture of basis functions from all configurations included in the calculation - a result referred to as *configuration mixing*. Correspondingly, the computed energies will be different from the values that would have been given by a set a single-configuration calculations - a result referred to as *configuration-interaction perturbations*. The wavefunction-mixing and energy-level and energy-level-perturbation aspects jointly are referred to simply as *configuration-interaction*.

Similar to the calculations performed for a single configuration, the CI calculations involve the setting up the matrix the of Hamiltonian operator. For two configurations (c_1 and c_2) the Hamiltonian matrix can be written in the form:

$$\begin{pmatrix} c_1 & c_1 - c_2 \\ c_2 - c_1 & c_2 \end{pmatrix}. \qquad (2.54)$$

It is made up of four different submatrix blocks. The two diagonal blocks (c_1 and c_2) are always square, and are identical with the energy matrices that we would have had for the two configurations c_1 and c_2 when considered separately. In either block, each matrix consists of sums of terms E_{av}, $f_k F^k(ij)$, $g_k G^k(ij)$, and $d_i \xi_i$. However, the numerical value of E_{av} that appears in the diagonal elements of the block c_1 will be different from that in c_2. Likewise, the radial integrals $F^k(ij)$, etc., for the block c_1 will normally be computed from radial wavefunctions $P_i(r)$ and $P_j(r)$ obtained from a Hartree-Fock (or HX, HFS, etc.) calculation for the configuration c_1 whereas the radial integrals appearing within c_2 will be computed via a HF calculation for c_2.

The off-diagonal blocks (blocks $c_1 - c_2$ and $c_2 - c_1$) represent configuration-interaction elements, They are in general rectangular rather than square, and one block is just the transpose of the other because the total matrix is symmetric. The configuration-interaction (CI) matrix elements are calculated exactly as were the single-configuration matrix elements [$H_{bb'} \equiv \langle b|H|b' \rangle$] but $\langle b$ and $b' \rangle$ now belong to different configurations. In place of the single-configuration direct and exchange radial integrals F^k and G^k, the electron-electron Coulomb operator gives CI radial integrals R_d^k and R_e^k. The general forms of these integrals are given by

$$R_d^k(l_i l_j, l_{i'} l_{j'}) \equiv \int_0^\infty \int_0^\infty \frac{2r_<^{\,k}}{r_>^{\,k+1}} P_i^*(r_1) P_j^*(r_2) P_{i'}(r_1) P_{j'}(r_2) dr_1 dr_2 , \qquad (2.55)$$

and

$$R_e^k(l_i l_j, l_{i'} l_{j'}) \equiv R_d^k(l_i l_j, l_{j'} l_{i'})$$

$$= \int_0^\infty \int_0^\infty \frac{2r_<^{\,k}}{r_>^{\,k+1}} P_i^*(r_1) P_j^*(r_2) P_{j'}(r_1) P_i(r_2) dr_1 dr_2 . \qquad (2.56)$$

Note that unlike F^k and G^k, R^k is not necessarily positive. Analogous to the single-configuration direct and exchange angular coefficients f_k and g_k, CI integrals have their own coefficients r_d^k and r_e^k, respectively, and are defined by general analytical formulas (see Cowan 1981). There are also configuration-interaction spin-orbit matrix elements but their contribution is usually very small.

Requirements and consequences of configuration-interactions.

1. The Hamiltonian operator has even parity, and so the CI matrix elements are zero unless the bra and ket functions have a common parity. Thus the configurations included in the calculations should have the same parity.

2. The Hamiltonian involves only one- and two-electron operators, so that interactions can occur only between two configurations that differ in at most two orbitals. For example, interactions may occur between any two of the configurations d^3s^2, d^4s, d^5, d^3p^2 and d^2sp^2, except for d^5-d^2sp^2.

3. The matrix of the Coulomb operator in an LS representation is (just in the single-configuration case) diagonal in the quantum numbers LSJM. Therefore, non-zero Coulomb CI matrix elements exist only if each configuration contains a basis state with some common value of LS. For example, sp and sf do not interact, because the former contains only $^{1,3}P^o$ terms whereas the latter contains only $^{1,3}F^o$.

4. The non-zero Coulomb matrix element that connects basis functions $|b\rangle$ and $|b'\rangle$ of two configurations c and c′ causes each eigenstate to be a mixture of the two basis states. Because of the spin-orbit mixing present within each configuration separately, each eigenstate of the two-configuration calculation indirectly becomes a mixture of all basis states (of given J) of both configurations. Similarly, a three-configuration calculation for $d^5 + d^3s^2 + d^2sp^2$ will give eigenstates each of which is a mixture of basis functions of all three configurations, even though d^5 and d^2sp^2 do not interact directly.

5. Configuration-interaction effects tend to be largest between configurations whose centre-of-gravity energies E_{av} are not greatly different, and/or for cases in which the Coulomb matrix elements $r^kR^k(ij,i'j')$ are large in magnitude. Large values of $|R^k|$ tend to occur when the two configurations belong to the same complex (*i.e.* configurations having the same n values such as configurations $2p^63s3p$, $2p^53s^23d$, $2p^53s3p^2$, $2p^53d3p^2$ belong to the same complex) because the various radial wavefunctions then tend to have maximum overlap. Thus, particularly in high ionisation stages where E_{av} depends primarily

on the principal quantum numbers and relatively weakly on the orbital angular momenta, the largest interactions tend to occur among the configurations within a complex, such as $3s^23p^w$-$3p^{w+2}$ or $3s3p^{w+1}$ -$3s^23p^{w-1}3d$ interaction remains strong throughout the isoelectronic sequence. However, the interaction $3s3p^{w+1}$ - $3s^23p^{w-1}nd$ is notoriously strong in neutral atoms for all values of n. Consequently, it results in the strong perturbation of all nd Rydberg states.

2.6.3 Calculation of statistically-weighted oscillator strength (gf-value)

When XUV radiation is passed through an atomic or ionic vapour its absorption due to various excitation and ionization processes results in the attenuation of the incident beam. The relation between the transmitted and incident radiation at some discrete frequency ν is given by the expression

$$I = I_o e^{-k_\nu L}, \tag{2.57}$$

which is also known as the Lambert-Beer law and k_ν is termed as the absorption co-efficient. I and I_o are the initial and final intensities of radiation of frequency ν passed through the absorbing column of length L.

In the case of discrete atomic absorption the oscillator strength (f) is often used to quantify the strength of an observed transition and it can be shown (Kirkbright and Sargent 1974) that

$$f_{ij} = \frac{mc}{n\pi\varepsilon^2}\int k_\nu d\nu \ , \tag{2.58}$$

where m, e, c and n are the electron mass, electron charge, velocity of light and the number of absorbing species per unit volume. The integral $\int k_\nu d\nu$ is the integrated absorption co-efficient.

The photoabsorption spectra reported in this work are obtained by plotting $\ln(I_o/I)$ versus energy. I_o represents the intensity of the backlighting continuum and I the intensity transmitted through the absorbing column (see chapter 3 for further details). It has been shown (Kiernan 1994) that for optically thin cases this provides a good representation of the relative absorption co-efficient as a function of energy. To facilitate the analysis visual comparisons are made between the relative absorption spectra and stick diagrams based on

calculated gf-values for the atomic or ionic transitions (for example, see chapter 4).

The oscillator strength (f) of a transition can be written in terms of its gf-value by the expression

$$f_{i\to f} = \frac{gf_{i\to f}}{2J_i + 1}\,. \tag{2.59}$$

The theoretical expression for the gf-value for a transition from some lower level "i" to a higher level "j" is given by

$$gf = \frac{1}{3}(E_j - E_i)S, \tag{2.60}$$

where $E_j - E_i$ is the transition energy in rydbergs. The quantity S is called the line strength and its square root is defined by the expression

$$S^{1/2} = \langle \Psi_i \| \mathbf{P}^{(1)} \| \Psi_f \rangle, \tag{2.61}$$

or

$$S^{1/2} = (-1)^{l_i}(2l_i+1)^{1/2}(2l_f+1)^{1/2}\begin{pmatrix} l_i & 1 & l_f \\ 0 & 0 & 0 \end{pmatrix} \times \int P_{nl_f}(r)\ er\ P_{nl_i}(r)dr, \tag{2.62}$$

where $\mathbf{P}^{(1)} \equiv er$, is the electric dipole operator.

The above expressions show that calculation of the gf-value for a transition involves the computation of the corresponding line strength or that of its square root

$$S^{1/2} = \langle \Psi_i \| \mathbf{P}^{(1)} \| \Psi_f \rangle = \langle \gamma J_i \| \mathbf{P}^{(1)} \| \gamma J_f \rangle. \tag{2.63}$$

In real calculations the wavefunctions $|\gamma J_i\rangle$ and $|\gamma J_f\rangle$ usually do not involve only the single terms, therefore, they are expanded in terms of their suitable basis functions of the form

$$|\gamma_i J_i\rangle = \sum_{\beta_i} y^{\gamma_i}_{\beta_i J_i} |\beta_i J_i\rangle, \text{ and} \tag{2.64}$$

$$|\gamma_f J_f\rangle = \sum_{\beta_f} y^{\gamma_f}_{\beta_f J_f} |\beta_f J_f\rangle. \tag{2.65}$$

Substitution of (2.64) and (2.65) in (2.63) gives

$$S^{1/2} = \sum_{\beta_i} \sum_{\beta_f} y^{\gamma_i}_{\beta_i J_i} \langle \beta_i J_i || \mathbf{P}^{(1)} || \beta_f J_f \rangle y^{\gamma_f}_{\beta_f J_f} . \qquad (2.66)$$

In the case of neutral atoms having complex configurations errors in the computed gf-values - ranging from 50 or 100 percent to one or more orders of magnitude - can be observed. The deviations between observed and calculated values usually arise as a result of cancellation effects of one sort or another. Some of these effects described below can be explained on the basis of expressions (2.61) and (2.66).

Intermediate coupling. The line strengths are generally computed in terms of single-configuration, pure-coupling basis functions. The quantum states in real atoms (especially with Z and N greater than 5) do not usually closely approximate pure basis functions. Therefore, computed line strengths usually involve evaluating the sum of several terms, because of intermediate-coupling and configuration-interaction mixing of basis states. As is clear from expression (2.64) this sum represents a mixing of amplitudes rather than of line strengths themselves. Consequently, the effect of mixing is not necessarily a tendency to average out the various line strengths. The destructive effects could occur frequently and cause a weak line to become still weaker, or even cause an otherwise strong line to essentially disappear - a situation observed in the 2p-subshell photoabsorption spectra of neutral Al and Si.

Radial-integral cancellation. Another type of cancellation may occur which is completely different from the angular effects produced by intermediate-coupling mixing of basis states. Such a situation arises from the destructive-interference effect in the radial portion (rather than the angular portion) of $S^{1/2}$. In extreme cases, the cancellation effect may be almost 100%. This more or less completely wipes out an entire transition array (Cowan 1981).

Configuration-interaction effects. The computed line strengths are very sensitive to the composition of a level, so configuration-interaction while not affecting greatly the energy of a level may have a considerable effect on the line strengths. This situation is very common in the case of core-valence interactions (see chapters 4). As the total line strength is always conserved: cancellation effects in one line are always counterbalanced by increased line strengths elsewhere. In this way, configuration-interaction effects quite commonly result in the net transfer of line strength from one transition array to another (also see chapter 4).

2.7 *Ab initio* calculations with Cowan's code

In order to analyse the measured spectra reported in this work a range of ab initio scaled as well as unscaled Configuration-Interaction Hartree-Fock (CIHF) atomic structure calculations were carried out with the help of a suite of computer programs (Cowan 1981) based on the preceeding theory. The calculations requiring limited basis states were performed on the DCU VAX while the ones involving large expansions were performed on the Cray XMP/48 at the Rutherford Appleton Laboratory (UK). The results obtained from these calculations, particularly the computed transition energies are highly accurate with the exception of a few multi-electron transitions and is clearly evident from the comparison made between the computed and measured transition energies (see chapters 4, 5 and 6). For the study of photoabsorption spectra from excited states (see chapter 7) the ab initio unscaled calculations were found in agreement with the measured spectra, therefore, the assignment of the spectra were straightforward (for discussion see section 2.7.2). In the case of absorption from ground states (see chapters 4, 5 and 6) the desired accuracy was achieved partly by suitably scaling the various radial integrals (for discussion see section 2.7.2). This suite consisted of the programs RCN35, RCN2, and RCG10. The roles played by each of these programs are given in the flow diagrams shown in figures 2.1 and 2.2. The primary information is always to RCN, and each program automatically provides information to the succeeding program of the chain.

2.7.1 RCN35

Program RCN35 calculates the single-configuration wavefunctions $P_{nl}(r)$ for a spherically symmetrized atom via any one of the following methods - each is an approximation to the true Hartree-Fock Method (Cowan 1981) -

1. Hartree (H),
2. Hartree-Fock-Slater (HFS),
3. Hartree-plus-statistical-exchange (HX), and
4. Hartree-Slater.

The difference in these approaches lies in the form of assumed central field potential (for details see Cowan 1981). Normally the HX method is used since it is computationally the most efficient. It also serves as a starting point for

the other methods. The calculations can be made either within the framework of centre-of-gravity energy of the configuration or for the energy of a specific LS term of the configuration (LSD-HF) provided there exists only one term having that value of LS.

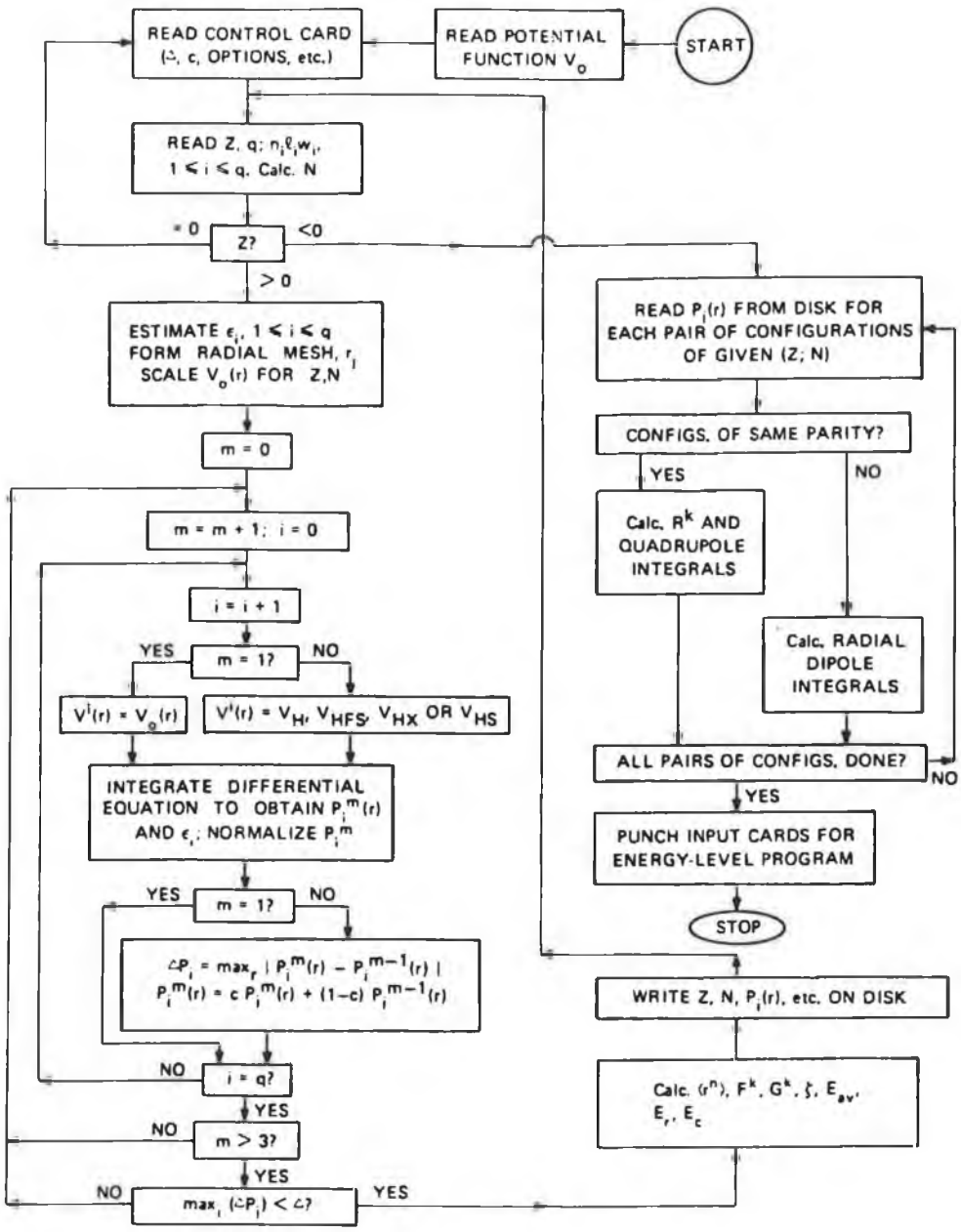

Figure 2.1

Simplified flow diagram of computer program RCN for the calculation of radial wavefunctions and radial integrals for an electron configuration via the H, HFS, HFSL, HX or HS method (from Cowan 1981).

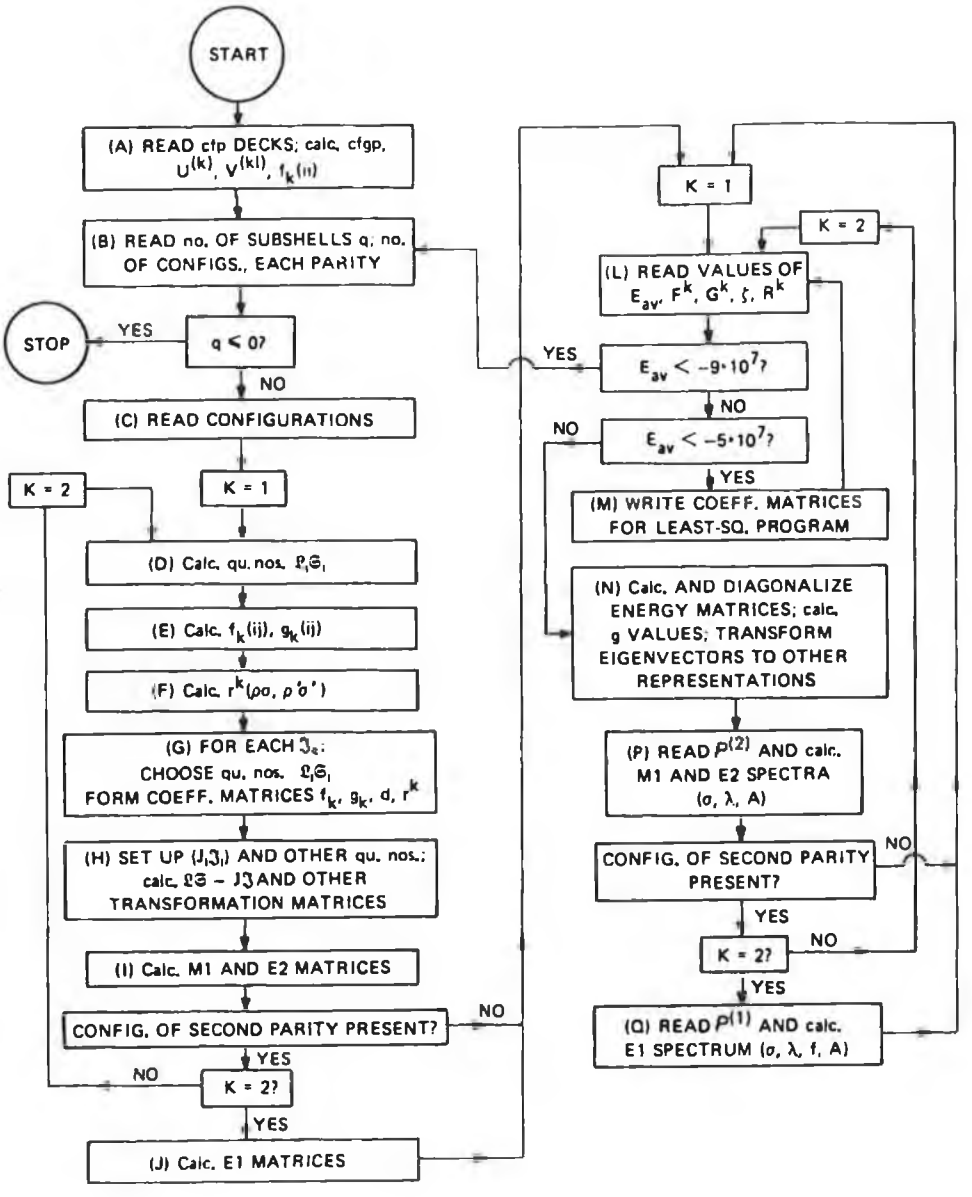

Figure 2.2

Simplified flow diagram of computer program RCG. The left-hand column represents the calculation of angular coefficient matrices; the right-hand column represents the calculation of atomic energy levels and spectra for given values of various radial integrals. K =1 and 2 represents the first and second parities, respectively (from Cowan 1981).

The computed radial wavefunctions are used to calculate the single-configuration radial integrals $\langle r^m \rangle$, F^k, G^k, ξ and E_{av} of the system for each

electron configuration involved in the calculation. Relativistic effects on the total binding energies and radial wavefunctions become appreciable for Z as small as 10 and 30, respectively. In this program these effects are incorporated as perturbations to the Hartree Method (see Cowan 1981). Proper treatment of relativistic effects leads to what may be called the Dirac-Fock (DF) or Dirac-Hartree-Fock (DHF) equations (Grant 1970, Desclaux 1975). However, these are considerably more complex than the HF equations. Also the achievement of convergence of the SCF (Self-Consistent-Field) procedure becomes more difficult when Dirac-Fock equations are used.

It has been found (Cowan 1981 and references therein) that theoretical values of E_{av} agree well with the experiment (at least in simple cases), provided that relativistic and correlation corrections are included. Spin-orbit effects are usually predicted with good accuracy, provided that values of ξ are computed via the Blume-Watson theory (see Cowan 1981) using HF radial functions. Within the framework of the configuration-average approach, the computed energy-level splitting resulting from electron-electron Coulomb interactions are generally larger than observed by ten to fifty percent. This is a consequence of the neglect of the LS-term dependence of electron correlation.

2.7.2 RCN2

Program RCN2 accepts radial wavefunctions from the RCN program and calculates various multiple-configuration radial integrals: overlap integrals $\langle P|P'\rangle$, configuration-interaction Coulomb integrals R^k and spin-orbit integrals ξ_{nl}, and radial electric-dipole integrals. At this stage, it is also possible to scale down the various radial integrals, if desired.

In the ab initio HF method (or any of the approximations thereto), electrons are considered to move independently of each other. In reality, the electron movements are spatially correlated, primarily by virtue of the simple Coulomb repulsion between them. The effects of these corrections can only be taken into account approximately, because exact analytical solutions are not known for non-hydrogenic systems. The single-configuration ab initio methods such as Hartree-X and and Hartree-Fock do contain approximate allowances for correllations; and by specifically including configuration mixings, better approximations to reality are obtained. However, in any practicable calculation of atomic structure, relatively few configurations can be included directly. Beyond about 40 simple configurations or 2 or 3 very complex ones, the

combination of computer time and storage requirements soon become prohibitive on even the largest computers.

In situations, where configurations are widely separated in energy or else are only linked by very small R^k, it is found that good agreement with the observed energy level separations can be obtained by direct inclusion of only a few of the most significant interactions (see chapter 7). In some cases, even the single configuration approximation is good enough. However, as fewer and fewer mixings are directly treated, so it becomes more and more important to allow for omitted weak mixings in some way. Even if as many as 40 or more configurations are explicitly in the calculation, it is still very often necessary to allow for the infinity of mixings with far-off configurations, and indeed for mixing with the continuum of unbound states. In short, the spatial correlation between electrons may be fairly well represented by the inclusion of some nearby configurations, but it is not completely so.

However, with calculations performed including only the most significant interactions better agreement with experiment can be obtained by decreasing the ab initio values of various radial integrals by suitable amounts (see chapters 4, 5 and 6). This scaling is used to account for the electron-electron correlation effects not properly modelled in the *ab initio* calculations (Cowan and Wilson 1988). The required values of scale factors depend on the system under investigation. For the systems which exhibit very small electron-correlation effects - a situation observed in energy levels closest to being hydrogenic (e.g., in highly ionised atoms, configurations involving highly excited states or excited configurations arising from the valence-excited states) scaling factors have been observed as almost unity (see chapter 7).

2.7.3 RCG10

This program employing Racah-algebra techniques generates the coefficients of fractional parentage required to remove ambiguity in the similarly labelled LS levels and the various angular coefficients needed to construct the Hamiltonian energy matrices from the radial integrals supplied by the RCN35/RCN2 programs. By diagonalizing the energy matrices it yields energy levels and eigenvector compositions. From these energy levels and eigenvector compositions data, and the supplied electric-dipole integrals it computes the statistically weighted transition rates (gA) and oscillator strengths (gf).

2.8 References

Condon E U and Shortley G H, 1935, The Theory of Atomic Spectra (Cambrigde University Press.).

Cowan R D, 1968, J. Opt. Soc. Am. **58**, 808.

Cowan R D, 1981, The Theory of Atomic Structure and Spectra (Uinversity of California Press).

Cowan R D and Wilson M, 1988, J. Phys. B: At. Mol. Phys. **21**, L275.

Desclaux J P, 1975, Comput. Phys. Commun. **9**, 31.

Grant I P, 1970, Adv. Phys. **19**, 747.

Kiernan L, 1994, Ph.D. thesis, Dublin City University.

Kirkbright G F and Sargent M, 1974, Atomic Absorption and Fluorescence Spectroscopy (Academic Press London).

Slater J C, 1929, Phys. Rev. **34**, 1293.

Slater J C, 1960, Quantum Theory of Atomic Structure (McGrawHill Book Co., New York.) 2 Vols.

Chapter 3

EXPERIMENTAL METHOD AND RESULTS

In order to record photoabsorption spectra of the species of interest and distinguish the features arising from different ionization stages or from different initial states belonging to the same species, a range of time and space-resolved studies were carried out. The purpose of this chapter is to (i) describe the experimental method used in the photoabsorption measurements and the experimental systems employed for this purpose, and (ii) exhibit some of the results obtained. Detailed interpretation is provided in succeeding chapters.

3.1 Experimental method

Figure 3.1 shows the schematic diagram of the experimental method used for carrying out the time and space-resolved photoabsorption measurements of laser-produced plasmas. Two plasmas were generated in an evacuated target chamber in front of the slit of a grazing incidence spectrograph and on the optical axis of the spectrograph. One generated at $t = 0$, called the absorbing plasma, was used to provide the absorbing species. The second plasma generated after a time delay Δt, called the probing plasma, was used for providing the background continuum. The transmitted radiation was collected by the toroidal mirror and focused on the slit of a grazing incidence spectrograph/spectrometer.

When a laser pulse is focused onto a solid target in vacuo the leading edge of the pulse causes vaporisation and ionization of the target surface and creates a low temperature plasma expanding away from the target surface with velocities up to 10^7 cm s^{-1}. The expanding plasma thus produced strongly absorbs the remainder of the laser pulse and results in the rise of plasma temperature as well as the degree of ionization of the absorbing plasma. To conserve momentum, a shock wave moves into the solid. Heat transported through the plasma vaporises more target material thus replenishing the plasma lost from the focal volume due to

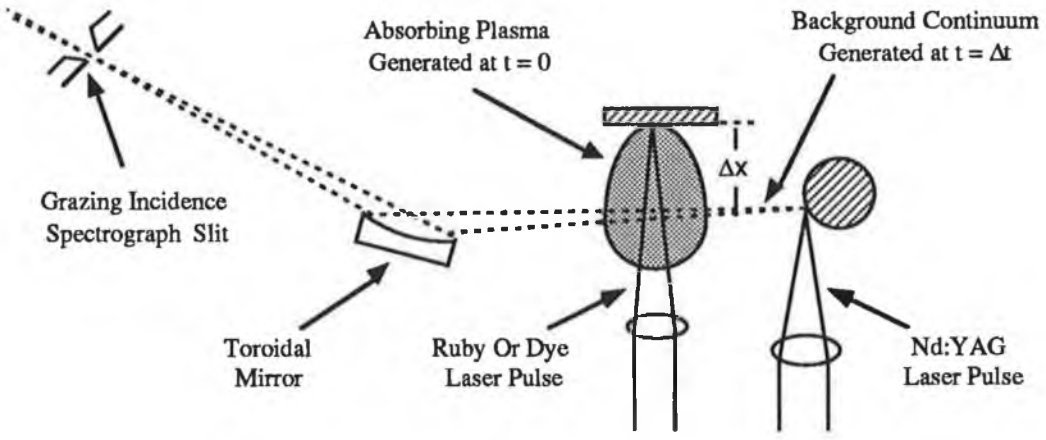

Figure 3.1

Schematic of the dual laser-produced plasma technique used to carry out the time and space-resolved photoabsorption studies of laser-produced plasmas.

hydrodynamic expansion. At the end of the laser pulse, the plasma temperature rises to its maximum value and leaves the plasma in different ionization stages having temporal and spatial distributions in the plasma plume.The most highly ionised atoms appear at the front of the plasma expanding away from the target and the highest degree of ionization can be controlled by laser irradiance on the target surface.

In time-resolved studies, which exploit the temporal evolution of absorbing species in the laser generated plasma, a particular region of the absorbing plasma plume, at a fixed distance Δx from the target surface as shown in figure 3.1, was probed after different inter-plasma time delays. Because of the limitations of the experimental system used, measurements were made only during the cooling phase of the laser plasma. In space-resolved studies, which exploit the spatial evolution of absorbing species, different regions of the plasma plume, almost normal to the target surface, were probed at a fixed time delay.

3.2 Experimental systems

The results of the photoabsorption experiments presented in the following sections were obtained using both photographic and photoelectric systems. The different parts of the systems used in the photoabsorption studies carried out can be divided

into three main blocks:

(a) photographic system,

(b) photoelectric system, and

(c) synchronised lasers.

The details of the development and assessment of the photographic system including a stigmatic 2m grazing incidence spectrograph, toroidal optics, target chamber, target holders, focusing optics, vacuum system and the system alignment has been described by Hopkins (1992).

The development, characterisation and assessment of the photoelectric system, using a 2.2m McPherson grazing incidence spectrometer equipped with MCP/PDA type multichannel detection, has been the subject of the Ph.D. thesis of Kiernan (1994). The synchronisation of the lasers used was achieved as part of the M.Sc. work of Evans (1991). In the photoelectric system the firing of the lasers and data acquisition was conducted through an IBM PC based OMA system. The software used and various details of the data capturing and processing have been described by Shaw (1994). For the sake of completeness, the systems will be very briefly introduced in this section.

3.2.1 Photographic system

Figure 3.2 shows the layout of the photographic system which employed the dual laser-produced plasma technique (Carroll and Kennedy 1977, Carroll and Costello 1986) and a stigmatic grazing incidence spectrograph (Tondello 1979, Hopkins 1992). The absorbing plasma was produced using the output of either a Q-switched ruby laser (1.5J, 30ns) or a dye laser (2J, 800ns). The focusing was via either a spherical lens or a cylindrical lens. The probing plasma was generated by tightly focusing the output of a time synchronised Q-switched Nd:YAG laser (1J, 10ns) on the cylindrical surface of a tantalum or tungsten target. A multichannel digital delay system providing delays in the range 0-999.99 μs was used for the synchronisation of the lasers. Firing of the lasers was either through an IBM PC or manually. The jitter between the two laser pulses was about ± 30ns.

The spectra were recorded on KODAK-SWR (Short Wavelength Radiation) plates by means of a 2m stigmatic grazing incidence Rank and Hilger spectrograph equipped with a 1200 lines/mm concave grating; the entrance slit of

spectrograph was kept at 10 μm. The dispersion of the spectrograph was 1 Å/mm at 120 Å. The theory and construction of the spectrograph can be found in an excellent book by Samson (1967). The various details of the spectrograph used and development of the plates has been described by Brilly (1990a).

In a typical photoabsorption experiment carried out using this system 10 - 20 shots were enough to produce adequate plate blackening; this is much less than required in earlier experiments employing astigmatic spectrographs (Brilly *et al.* 1988). In measuring the plates well known emission lines of Al and O ions listed by Kelly (1987) were used as external wavelength standards in addition to the internal absorption lines of Al^{2+} reported by Brilly *et al.* (1988, 1990) and Al and Al^{+} listed by Cantu *et al.* (1982). The external references were obtained by recording emission spectra of point plasmas formed on aluminium and aluminium oxide targets with tightly focused laser beams. The plates were measured on a photoelectric comparator in the Physics Department at University College Dublin.

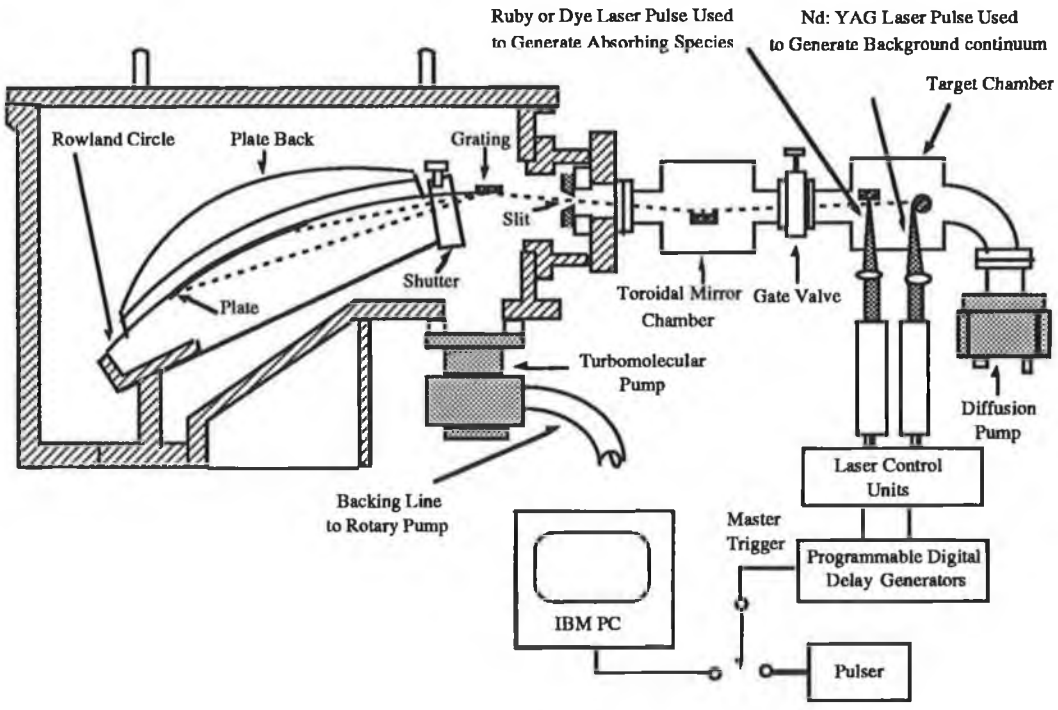

Figure 3.2

Layout of the photographic system used in the XUV photoabsorption studies of atoms and ions.

This instrument is operated by hand and essentially allows the accurate

determination of the position of spectral lines along the photographic plate. To compute final wavelength values for the unknown features a third order polynomial fitting was applied to the known reference lines. The measured errors were within ± 0.02 eV.

This system was employed only in photoabsorption studies of Al plasmas. In an attempt to measure the 2p- absorption spectrum of Al^+ a time-resolved study of Al plasma was carried out and time-resolved absorption spectra of Al^{2+}, Al^+ and Al were recorded on a single plate (see Costello *et al.* 1992). All other photoabsorption studies were carried out photoelectrically.

3.2.2 Photoelectric system

The photoelectric system employed is shown in figure 3.3. The spectra were recorded on a 2.2m McPherson grazing incidence spectrometer equipped with a 1200 lines/mm grating, operated with a slit width of 10 μm and MCP/PDA multichannel detection. The technology behind this method of detection and the various applications together with examples of spectra obtained have been given by Wiza (1979), Cromer *et al.* (1985), Schwob *et al.* (1987), Colcott *et al.* (1988) and Kiernan *et al.* (1994).

In a photoabsorption experiment, the background continuum (I_o) and transmitted (I) radiations were captured with the help of OMA system using a 1024 pixels photodiode array (PDA). To obtain I_0, the YAG laser was fired on the continuum generating target and to obtain I both the lasers were fired. Typically 20 such single shot spectra were acquired both for I and I_0 and numerically averaged to improve the signal to noise ratio. The relative cross section was obtained by computing the quantity $-\ln(I/I_0)$. For each setting of the array detector, a wavelength reference emission spectrum of Al and O ions was also taken. A standard third order polynomial fitting procedure was applied to the reference spectrum in order to provide calibrated energy scales for the photoabsorption data.The spectral resolution of the system is ≈ 1500 and measurements obtained from this instrument carry a typical error of ± 0.05 eV.

The synchronised lasers were the same as used in the photographic system. The firing of the lasers and data acquisition was through an OMA system. In order to monitor on a single shot basis the video output of the photodiode array was connected to a digital Hewlett Packard oscilloscope. In order to monitor the

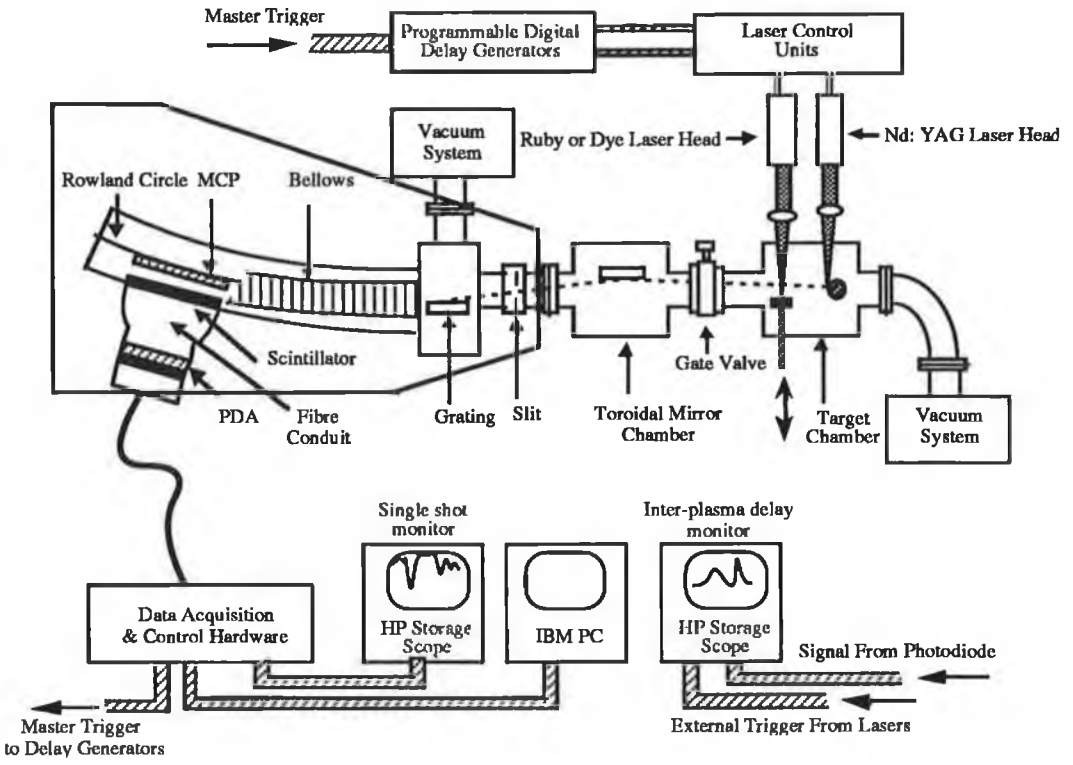

Figure 3.3

Layout of the multi-laser, multichannel spectrometer used in the time and space-resolved photoabsorption studies of laser plasmas.

shot to shot delay of the lasers, scattered light from the targets was detected with a photodiode the output of which was sent to a second digital HP oscilloscope.

3.3 Photoabsorption of Mg laser plasmas

Photoabsorption studies of Mg plasmas were carried out in the 2p-subshell regions of (i) atomic Mg in ground and excited states, and (ii) Na-like ionic Mg^+ in excited states.

3.3.1 Atomic magnesium in ground state absorption

Figure 3.4 shows the time-resolved photoabsorption spectra of atomic

magnesium in the ground state. The absorption measurements of dye laser generated line plasmas were made after inter-plasma time delays of 200 ns, 250 ns, 350 ns and 450 ns at a distance of 0.1 mm from the target surface.

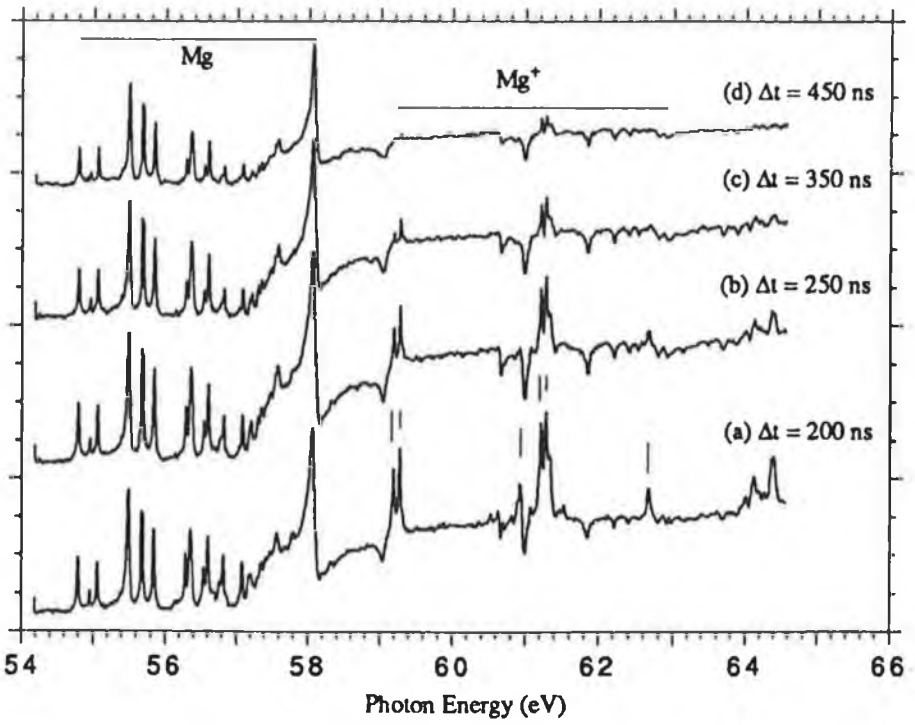

Figure 3.4

Time-resolved photoabsorption spectra of dye laser generated Mg line plasmas recorded in the 2p-subshell region of atomic Mg in the ground state. The plasmas were probed 0.1 mm from the target surface after inter-plasma time delays of 200 ns, 250 ns, 350 ns and 450 ns.

Fortunately, the spectral identification of neutral Mg does not pose any serious problem as its features are observed well separated from Na-like ionic Mg^+ absorption. The 2p absorption due to Mg^+ is observed above the 2p limits of neutral Mg (see figure 3.4) except for $2p^63s\ ^2S \rightarrow 2p^53s^2\ ^2P$ resonances which appear at 49.90 eV and 50.17 eV and also do not fall in the region of 2p absorption of ground state Mg.

3.3.2 Atomic magnesium in excited state absorption

Figure 3.5 exhibits the results of photoabsorption measurements of ruby laser generated line plasmas probed at a fixed distance of 0.1 mm from the target

surface under two different laser irradiances. At the lower laser power density corresponding to a flash lamp voltage of 1.9 kV the measurements were made at time delays of 105 ns (Figure 2.5a) and 130 ns (Figure 2.5b). At a higher flash lamp voltage of 2 kV, the time delays were 105 ns (Figure 2.5c) and 150 ns (Figure 2.5d). In both cases significant absorption is observed from the $2p^63s3p$ ^3P metastable states but absorption from the $2p^63s3p$ ^1P states is very weak.

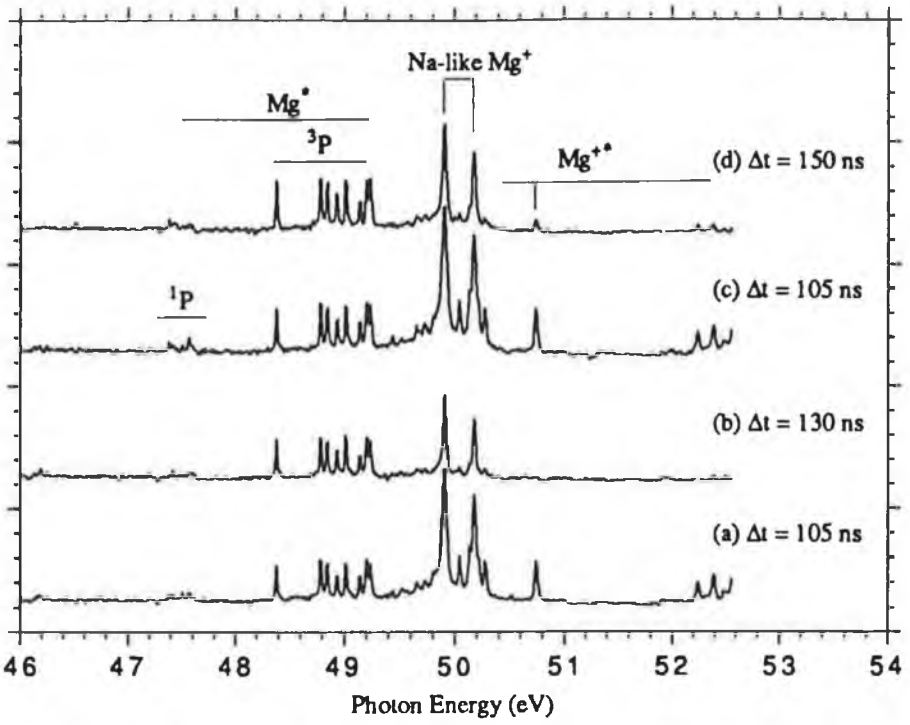

Figure 3.5.

Time-resolved photoabsorption spectra of ruby laser generated Mg line plasmas recorded in the 2p-subshell region of atomic Mg in excited states using two different laser irradiances but probed at a fixed distance from of 0.1 mm from the target surface. In the cases of (a) and (b) the ruby flash lamp voltage was 1.9 kV. For (c) and (d) it was increased to 2 kV.

3.3.3 Na-like magnesium in excited state absorption

In order to make absorption measurements for Na-like Mg^+ in excited states a time-resolved study of ruby generated Mg line plasmas was carried out. The results are shown in figure 3.6. The absorbing plasma was probed 0.1 mm

from the target surface after inter-plasma time delays of 60 ns, 80 ns, 100 ns and 125 ns.

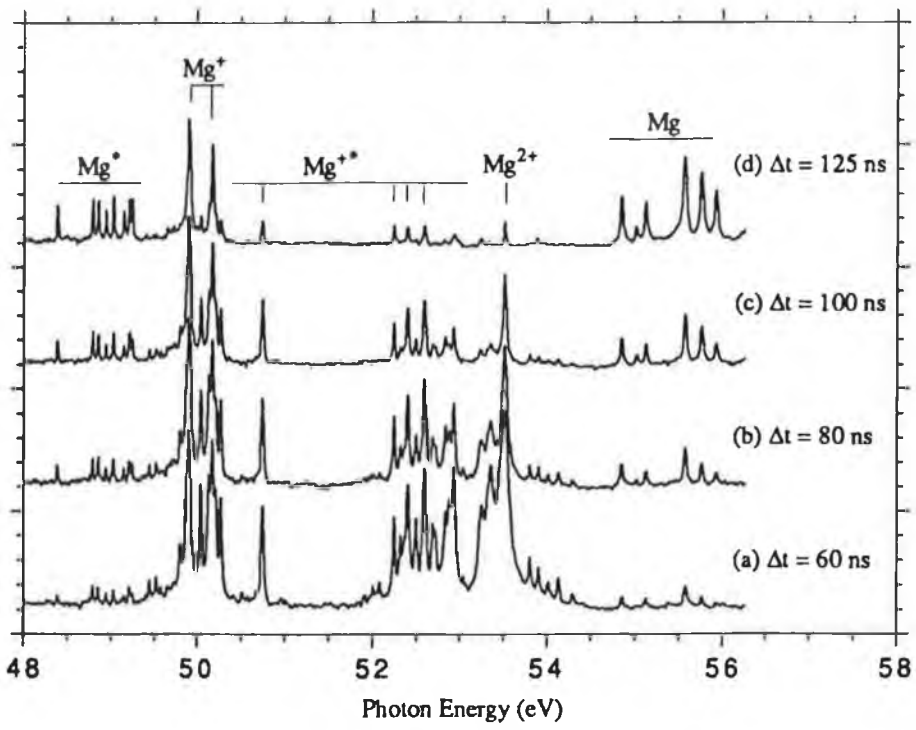

Figure 3.6

Time-resolved photoabsorption spectra of ruby laser generated Mg line plasmas recorded in the 2p-subshell region of Na-like Mg^+ in excited states. The plasmas were probed 0.1 mm from the target surface after inter-plasma time delays of 60 ns, 80 ns, 100 ns and 125 ns.

It is clearly evident from the photoabsorption study shown in figure 3.6 that when the plasma conditions are optimised for Mg, Mg^+ and Mg^{2+} the abundance of the Mg^+ ions in ground states almost remains the same whether the absorption is dominated by Mg (observed at 125 ns) or Mg^{2+} (observed at 60 ns). A similar situation has been observed in the case of the Al and Si plasmas reported in sections 5 and 6 of this chapter. In general, when the plasma conditions are optimised for three different ionization stages the abundance of the intermediate ions in ground states almost remains the same whether the absorption is dominated by higher or lower ionization stages and is in agreement with the results of the collisional radiative equilibrium model (Colombant and Tonon 1973). Therefore, in order to record a pure spectrum of some intermediate ionic species in ground state the optimisation of laser plasma for that particular ion stage is essential.

However, in the photoabsorption measurements of species in excited states the situation is different. The strong absorption from absorbing species of interest in excited states is observed only when the plasma conditions are optimised for the absorbing species of interest and its higher ionization stage. In the case of excited state absorption from Na-like Mg^+ this is evident from the time-resolved spectra shown in figure 3.6. At 60 ns delay where the Mg^+ and Mg^{2+} ions dominate in the absorbing plasma strong absorption is observed from the valence-excited states of Mg^+. With increasing delay as the relative abundance of Mg^{2+} ions decreases the absorption from the valence-excited states of Mg^+ also decreases.

3.4 Photoabsorption of Al laser plasmas

Photoabsorption measurements of aluminium plasmas were made for (i) atomic Al in ground and excited states, (ii) Mg-like Al^+ in ground and excited states, and (iii) Na-like Al^{2+} in excited states. The absorbing plasmas were generated using both dye and ruby lasers.

3.4.1 Atomic Al in ground state absorption

In order to record the 2p-subshell absorption spectrum of atomic aluminium in the ground states a time-resolved study of ruby laser generated Al plasmas was carried out. The plasma was probed 0.2 mm from the target surface after inter-plasma time delays of 150 ns, 200 ns and 250 ns. The results of this time-resolved study are shown in figure 3.7. At 150 ns, absorption is due to Al^{2+} in the ground state and Al^+ in both ground and excited states. At 200 ns, the absorption is mainly due to Al^+ in ground state. At a time delay of 250 ns strong absorption takes place due to neutral Al along with relatively weak absorption due to Al^+. As the absorption due to Al^+ does not overlap with that of neutral Al its presence does not cause any serious problem for the spectral analysis of the neutral.

The abundance of Al^+, an intermediate stage between neutral Al and Al^{2+}, remains very significant whether the plasma conditions are favourable for the

absorption of Al^{2+} or neutral Al. This is similar to the photoabsorption spectra of Mg plasma shown in figure 2.6. Furthermore, similar to figure 2.6, the spectra shown in figure 2.7 clearly demonstrate that significant absorption from valence

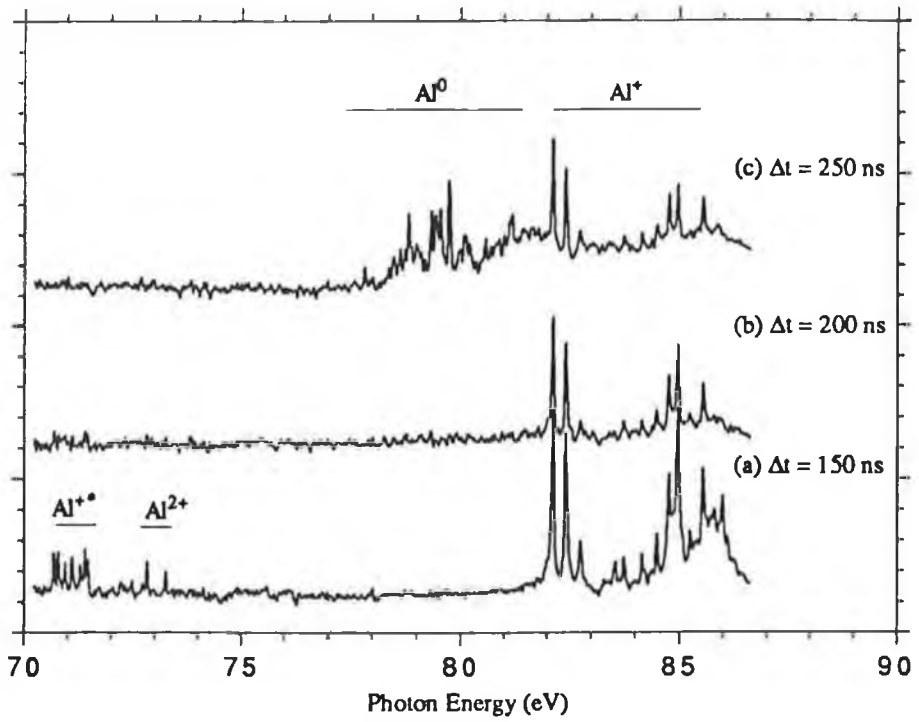

Figure 3.7

Time-resolved photoabsorption spectra of ruby laser generated Al point plasmas measured in the 2p-subshell regions of atomic Al. The plasmas were probed 0.2 mm from the target surface after inter plasma time delays 150 ns, 200 ns and 250 ns.

excited states takes place only when the plasma conditions are optimised for that particular stage and the corresponding higher ionization stage in ground states.

3.4.2 Mg-like Al^+ in ground state absorption

To distinguish the 2p absorption of Al^+ from the other observed spectral features (particularly due to Al^{2+}) and record its pure spectrum a number of time and space-resolved studies were carried out. Figure 3.8 shows a time-resolved photoabsorption spectra of ruby laser generated Al plasmas. The absorption

measurements were made at inter-plasma time delays of 80 ns, 110 ns, 150 ns, 180 ns and 220 ns, and the plasma was probed 1.2 mm from the target surface.

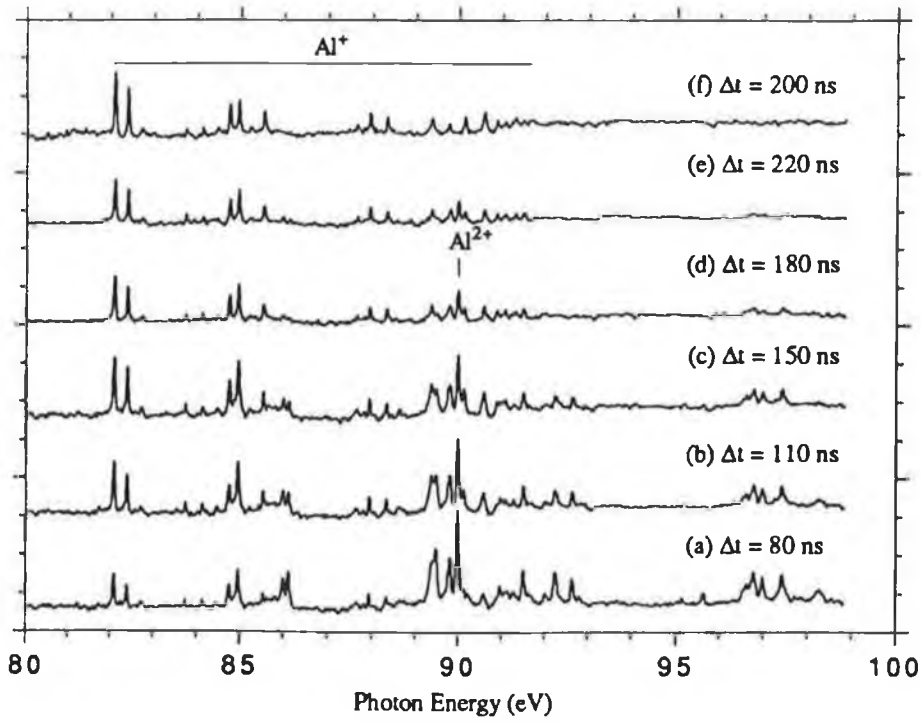

Figure 3.8

Time-resolved photoabsorption spectra of ruby laser generated Al plasmas recorded in the 2p-subshell region of Mg-like Al^+ in ground state. In figures (a) - (e) the plasmas were probed 1.2 mm from the target surface after inter plasma delays of 80 ns, 110 ns, 150 ns, 180 ns and 220 ns. In figure (f) it was probed at 0.15 mm from the target surface after inter-plasma delay of 200 ns.

At a time delay of 80 ns, the absorption is due to Al^+ and Al^{2+} but is dominated by Al^{2+} absorption. In moving from 80 ns to 220 ns as the relatively fast moving Al^{2+} ions leave the region probed by XUV radiation and more slowly moving Al^+ ions arrive in this region the relative absorption due to Al^+ increases. Consequently, at higher delays these ions become almost time-resolved in this region. At 220 ns only the strongest features of Al^{2+} are observed. In an other experiment (figure 3.8f) where the Al plasma, generated under the same conditions of laser-irradiance and focusing, was probed at a distance of 0.15 mm from the target surface after an inter-plasma time delay of 200 ns the Al^+ and Al^{2+} ions

were found to be relatively more time-resolved. This enabled the relatively weak higher Rydbergs which overlap with the strongest features of Al^{2+} to be unambiguously identified.

3.4.3 Neutral Al in excited state absorption

Unfortunately, no specific time or space-resolved study was carried out with the intention to obtain an absorption spectrum from the valence excited states of Al. However, in a photoabsorption experiment carried out to measure the absorption spectrum of valence excited Al^{+}, the absorption from the valence excited states of neutral Al was also observed. The results of this experiment in which the absorbing plasma was probed 0.1 mm from the target surface after a delay of 50 ns seconds are shown in figure 3.9. The absorption from the valence excited neutral Al is relatively weak as the absorbing plasma was dominated by Al^{+} and Al^{2+}.

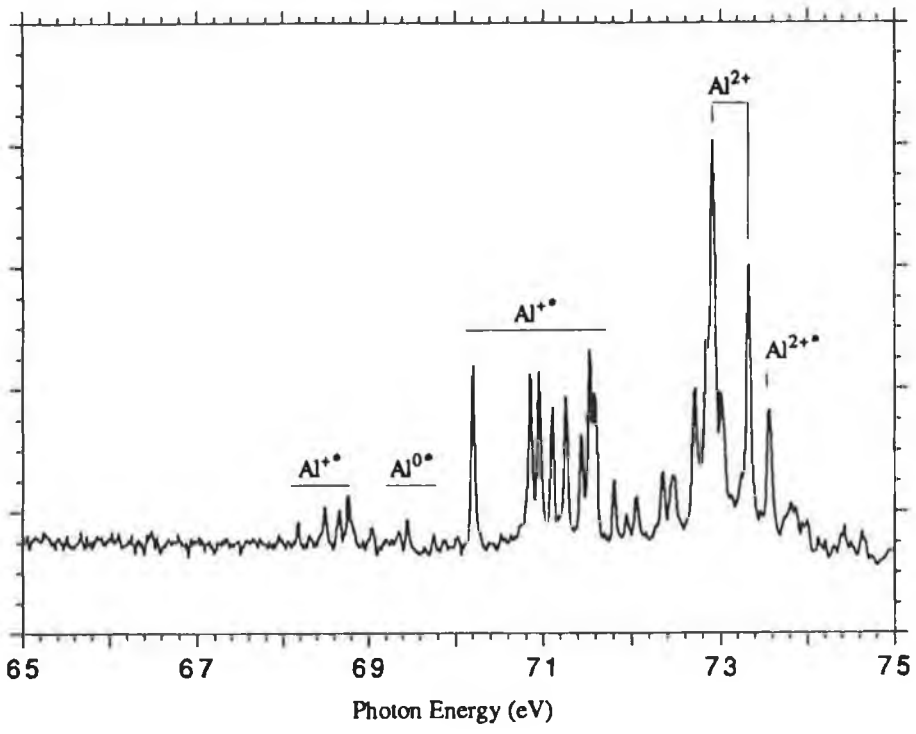

Figure 3.9

The 2p-subshell photoabsorption spectrum of neutral Al in valence excited state.

3.4.4 Mg-like Al^+ excited state absorption

Figure 3.10 shows the results of a time-resolved study in which the ruby laser generated Al point plasmas were probed 0.1 mm from the target surface after inter-plasma time delays of 20 ns and 50 ns. At 20 ns strong absorption is observed due to Al^{2+*}. However, at a longer delay of 50 ns, as the plasma cools the relative absorption due to the valence-excited states of Al^+ is increased.

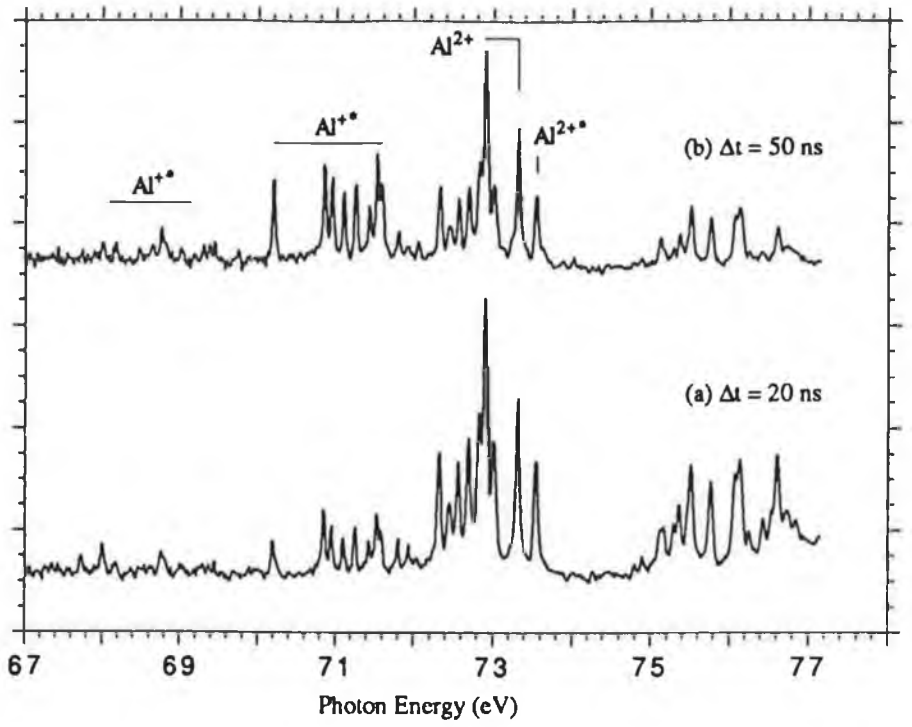

Figure 3.10

Time-resolved photoabsorption spectra of a ruby laser generated Al plasmas recorded in the 2p-subshell region of Mg-like Al^+ in excited states. The plasmas were probed 0.1 mm from the target surface after an inter plasma delays of 20 ns and 50 ns.

3.4.3 Na-like Al^{2+} excited state absorption

The photoabsorption spectrum of Al^{2+} in valence-excited states was recorded in an experiment where the absorbing plasma was probed 0.3 mm from

the target surface after an inter-plasma time delay of 50 ns. The results are shown in figure 3.11. The absorbing plasma was optimised for Al^{2+} and Al^{3+}.

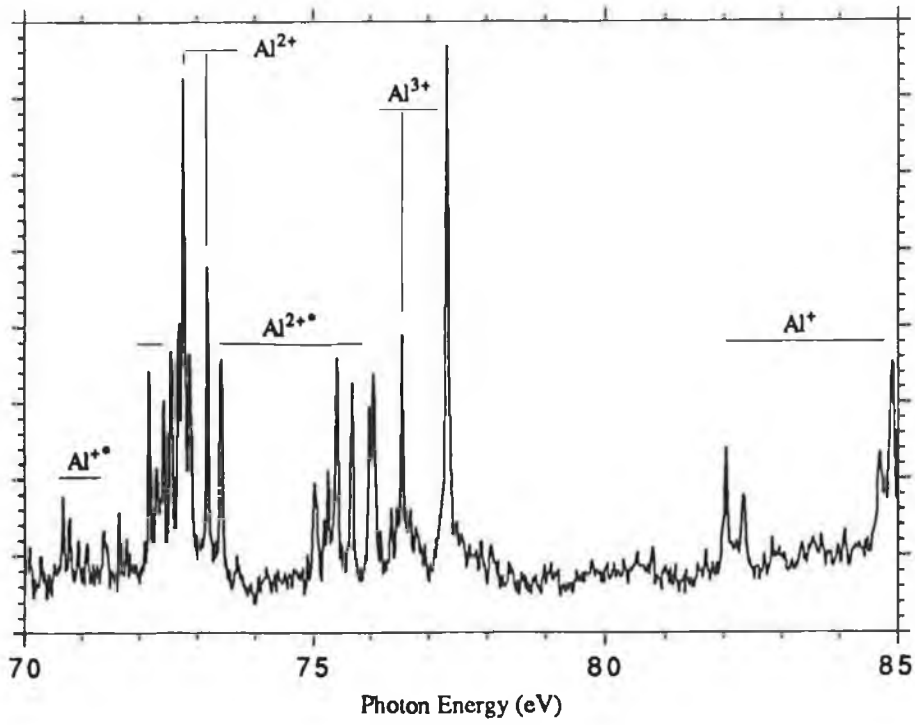

Figure 3.11

Photoabsorption spectra of ruby laser generated Al plasmas recorded in the 2p-subshell region of Al^{2+} in excited states. The plasmas were probed at a distance of 0.3 mm from the target surface after a delay of 50 ns.

3.5 Photoabsorption of Si laser plasmas

Photoabsorption measurements of Si plasmas were made for (i) atomic silicon in ground state, (ii) Al-like Si^{+} in ground and excited states, (iii) Mg-like Si^{2+} in ground and excited states, and (iv) Na-like Si in ground and excited states. The absorbing plasmas were generated with the ruby laser.

3.5.1 Neutral and singly ionised silicon ground state absorption

The absorption measurements of neutral and singly ionised species did not pose any serious problems. By controlling the laser irradiance one can produce laser plasma containing at the highest only singly ionised species. Such a plasma when probed close to the target surface at relatively shorter delays yielded absorption due to only the singly ionised species. The measurements made after longer delays should exhibit absorption due to neutrals. Also, the 2p absorption spectra of neutrals and singly ionised species, often, do not overlap as was the case in Mg and Al. Therefore, one can easily distinguish among the absorption structures arising from neutrals and singly ionised species.

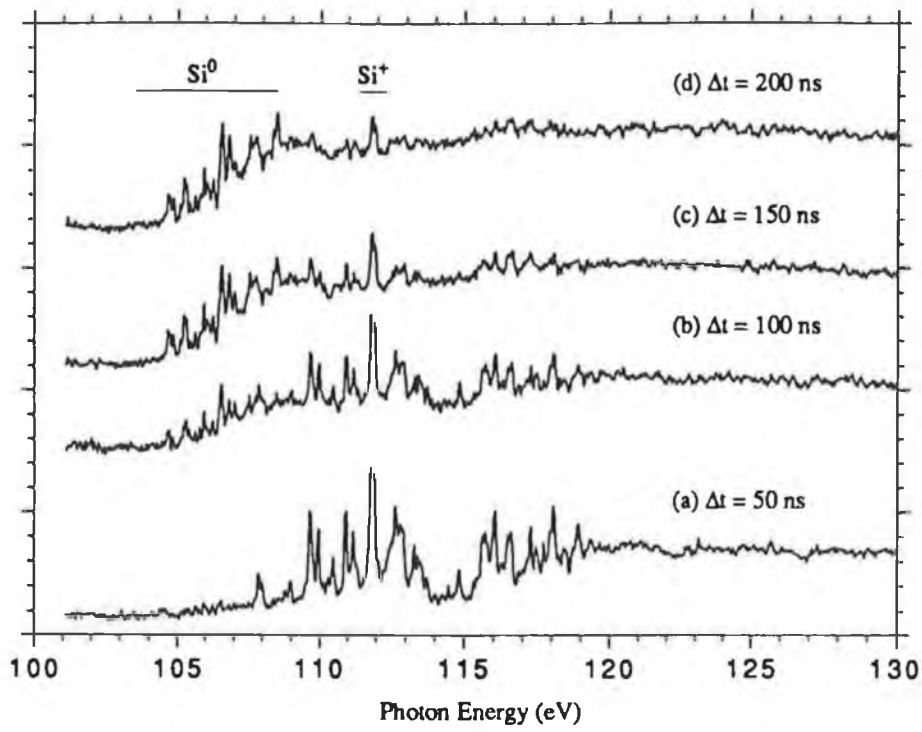

Figure 3.12

Time-resolved photoabsorption spectra of a ruby laser generated Si plasmas recorded in the 2p-subshell regions of Si neutral and Si^+ in ground states.

In order to record the 2p absorption of neutral and singly ionised silicon in

ground states the silicon plasmas were generated in such a way that Si^+ was the highest ionization stage. Time-resolved measurements were made in order to record the spectra of Si^+ and neutral Si. The results of these measurements are shown in figure 3.12. The absorbing plasma was probed 0.1 mm from the target surface after inter-plasma time delays of 50 ns, 100 ns, 150 ns and 200 ns.

At 50 ns delay absorption is only due to Si^+. At 100 ns, as the plasma cools relatively weak absorption from neutrals also takes place. Along with the increasing time delay the absorption due to Si^+ gradually falls. At 200 ns, only the strongest features of Si^+ are observed and the absorption is dominated by the neutral silicon features.

3.5.2 Mg-like Si^{2+} in ground state absorption

As the degree of ionization increases absorption measurements for the Mg-like ion stage become more difficult because of overlapping of spectral features with lower and higher ionization stages. In Si^{2+} the features on the lower energy side overlap with ground state absorption of Si^+ and excited state absorption of Si^{2+} arising from the $2p^63s3p \rightarrow 2p^53s3p3d$ transition array. The higher energy region overlaps with that of Na-like silicon. In contrast to Na-like Al^{2+} the strongest features of Si^{3+} which arise from $2p \rightarrow 3d$ transitions are well separated from the absorption features due to Si^{2+}, therefore, their weak presence, which could be observed even when the plasma conditions are optimised for Si^{2+}, does not cause any serious problem for the spectral analysis of higher Rydbergs. The absorption structures on the lower energy region can be separated from Si^+ absorption in a photoabsorption experiment in which the highest degree of ionization of the laser plasma is optimised for Si^{2+}.

In figure 3.13, a space-resolved absorption study of Si plasma is shown in which the plasma was optimised for Si^{2+} as the highest degree of ionization. The plasma was probed at 0.5 mm, 1.5 mm, 2.5 mm, 3.5 mm and 4.5 mm positions from the target surface after a fixed inter-plasma delay of 200 ns. At 0.5 mm, the spectrum exhibits strong absorption due to Si^+ and very weak absorption due to

Si^{2+}. With increasing distance from the target surface, the relatively slow Si^{+} ions lag behind Si^{2+}; consequently, the relative absorption due to Si^{2+} increases. The plasma probed at 4.5 mm exhibits absorption only due to Si^{2+}.

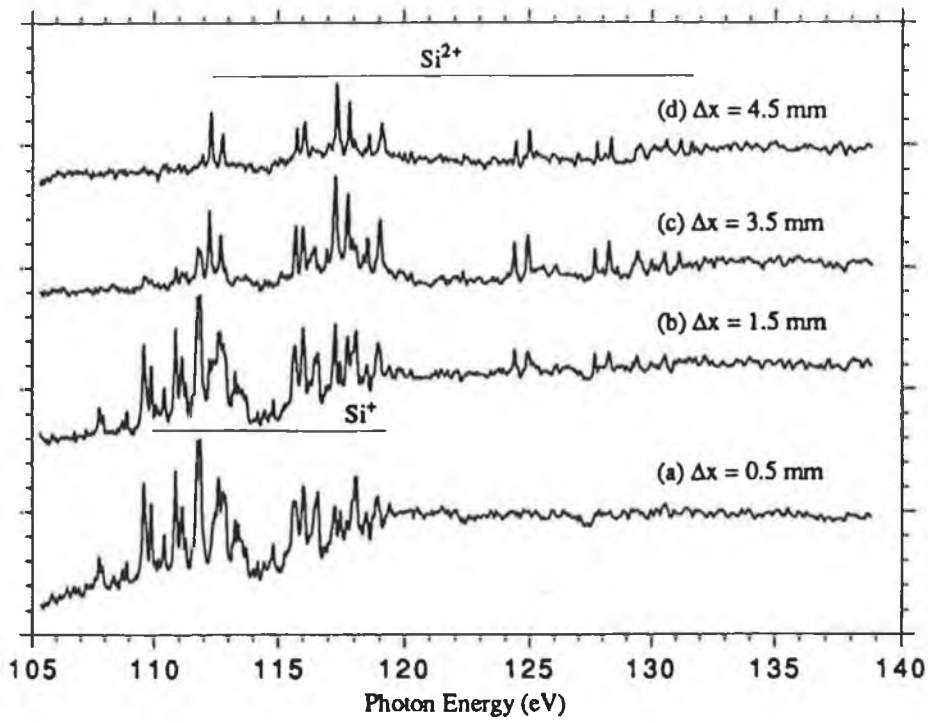

Figure 3.13

Space-resolved photoabsorption spectra of a ruby laser generated Si plasma measured in the 2p-subshell region of ground state Si^{2+}.

3.5.4 Si^{3+}, Si^{2+} and Si^{+} in excited state absorption

In order to record the 2p absorption of Si^{3+}, Si^{2+} and Si^{+} a time-resolved study of ruby laser generated Si plasmas, with Si^{4+} as the highest degree of ionization was carried out. The absorbing plasma was probed at a fixed distance of 0.3 mm from the target surface after inter-plasma time delays of 30 ns, 40 ns, 60 ns and 80 ns. The results of this study are shown in figure 3.14. The temporal evolution and expansion geometry of the ions is well exhibited.

At a delay of 30 ns the absorption is due to Si^{4+}, Si^{3+} and Si^{2+} in ground

states and Si^{3+} in excited states as the ground state absorption is dominated by Ne-like Si^{4+} absorption.

At 40 ns, the absorption is still due to Si^{4+}, Si^{3+}, Si^{2+} and Si^{+} in ground states, however, it is dominated by Na-like Si^{3+}. The relative absorption due to the fast moving Si^{4+} ions decreases as the majority of them leave the region probed by the XUV continuum. The absorption in excited states is observed only due Si^{3+} and Si^{2+} and is dominated by Si^{3+} absorption.

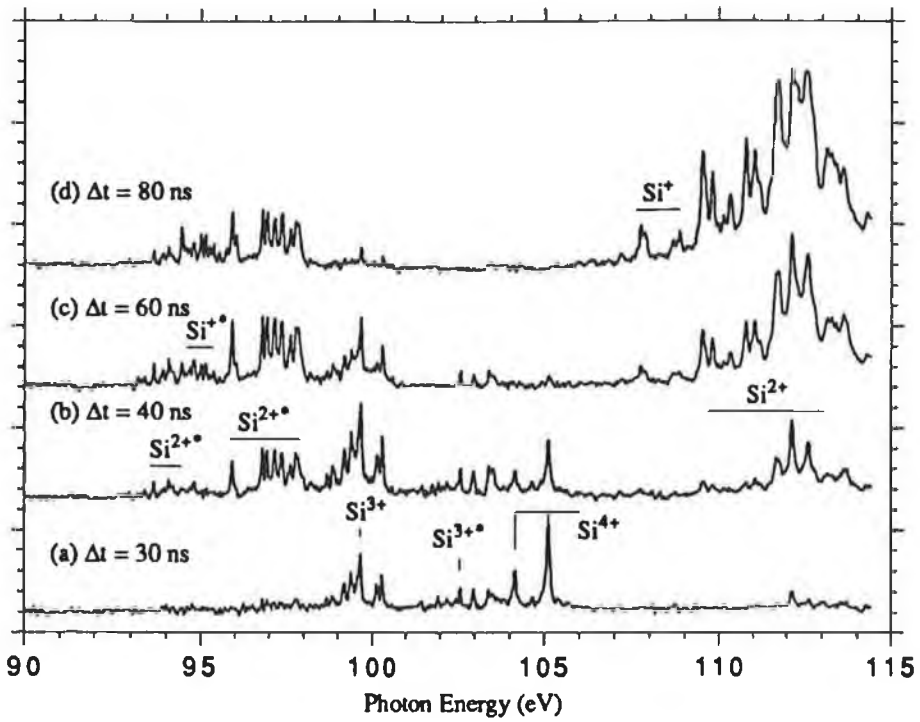

Figure 3.14

Time-resolved photoabsorption spectra of a ruby laser generated Si plasma measured in the 2p-subshell region of Si^{3+}, Si^{2+} and Si^{+} in excited states.

At 60 ns, all the Si^{4+} ions have left this region and absorption is only observed due to Si^{3+}, Si^{2+} and Si^{+} in ground states. It is dominated by Mg-like Si^{2+} and Si^{3+}, Si^{2+} and Si^{+} in excited states. The excited state absorption is dominated by the $2p^6 3s3p\ ^3P \rightarrow 2p^5 3s^2 3p\ ^{1,3}L$ transitions of Si^{2+}. The absorption from the valence excited $2p^6 3s3p\ ^1P$ dipole allowed states remains relatively very weak.

At 80 ns, the absorption is due to Si^{3+}, Si^{2+} and Si^{+} in ground states and is dominated by Si^{2+} and Si^{+}. The weak absorption observed due to Si^{3+} shows that they are slower than Si^{4+}. The valence excited absorption is observed in Si^{2+} and Si^{+}.

3.6 Conclusions

The way time- and space-resolved studies of laser plasmas help us to distinguish the absorption features arising from different species is demonstrated. These studies show that in the case of ground state absorption by probing the plasma close to the target surface just after the end of the laser pulse almost pure spectra of the ion stage of interest can be obtained when the highest degree of ionization in the plasma is equal to the ion stage of interest. If the degree of ionization is higher a relatively longer delay is required. However, in the case of excited states the strong absorption from species of interest can be obtained only when the plasma conditions are optimised for the absorbing species of interest and its higher ionization stage.

3.7 References

Brilly J, Kennedy E T and Mosnier J P, 1988, J. Phys. B, **21**, 368.

Brilly J, 1990, Ph.D. thesis, Dublin City University, unpublished.

Brilly J, Kennedy E T and Mosnier J P, 1990, Physica Scripta, **41**, 30.

Callcott T A, Tsang K-L and Zhang C H, 1988, Nucl. Instrum. Methods, **A262**, 578.

Cantu A M, Tozzi G P and Spector N, 1982, J. Opt. Soc. Am., **72**, 729.

Carroll P K and Kennedy E T, 1977, Phys. Rev. Lett., **38**, 1068.

Carroll P K and Costello J T, 1986, Phys. Rev. Lett., **57**, 1581.

Colombant D and Tonon G F, 1973, J. Appl. Phys., **44**, 8.

Cromer C L, Brigdes T M, Robert T R and Lucatorto T B, 1985, Appl. opt., **24**, 2996.

Dave D, 1991, M.Sc. thesis, Dublin City University, unpublished.

Hopkins R B, 1992, M.Sc. thesis, Dublin City University, unpublished.

Jannitti E, Nicolosi P and Tondello G, 1979, Optics Letters, **4**, 187.

Kelly R P, 1987, J. Phys. Chem. Ref. Data, **16**, Supp. 1.

Kiernan L, 1994, Ph.D. thesis, Dublin City University, unpublished.

Samson J A, 1967, *"Techniques of Vacuum Ultraviolet Spectroscopy."* , (Wiley & Sons).

Schwob J L, Wouter A W and Suckewer S, 1987, Rev. Sci. Instrum., **58**, 1601.

Shaw M, 1994, M.Sc. thesis, Dublin City University, unpublished.

Tondello G, 1979, Optica Acta, **26**, 357.

Wize J L, 1979, Nucl. Instrum. Methods, **162**, 587.

Chapter 4

MAGNESIUM ISOELECTRONIC SEQUENCE IN GROUND STATE ABSORPTION

Photoabsorption investigations of isoelectronic species Mg, Al^+ and Si^{2+} in their ground states have been carried out in their 2p-subshell regions. The effects of configuration-interactions on the relative distribution of gf-values and term energies both in the ground and excited states have been examined in detail for Al^+ and Si^{2+}. A revised term analysis is given for Al^+ and a complete assignment of the Si^{2+} spectrum is given for the first time. General features of the spectra are discussed and a comparison is made with the corresponding valence-shell spectra.

4.1 Previous work

2p-subshell excitation/ionization along the Mg isoelectronic sequence in the ground state continues to be the subject of both theoretical and experimental studies. Atomic magnesium, because of its rather simple structure (Kämmerling *et al.* 1992) and dynamics (Hausmann *et al.* 1988, Whitfield *et al.* 1991), has been an ideal candidate for 2p photoionization studies. The 2p-subshell excitation/ionization of neutral magnesium has been studied experimentally using a variety of techniques. The resonance structures were measured in photoabsorption experiments by Newsom (1971), Esteva and Mehlman (1974) and Ederer *et al.* (1979). Detailed term analyses have been made on the basis of quantum defect (Newsom 1971) and multiconfiguration atomic structure calculations (Mansfield and Connerade 1972, Esteva and Mehlman 1974). Experimental photoionization studies were carried out by Hausmann *et al.* (1988) and Kämmerling *et al.* (1992). Decay of the autoionizing states has been the subject of ejected-electron (Pegg *et al.* 1975, Pejcev *et al.* 1977), electron-impact (Breuckmann *et al.* 1976) and photoemission (Whitfield *et al.* 1991) studies.

Photoionization of atomic Mg has been studied using different theoretical approaches. Using the relativistic random-phase approximation (RRPA),

Deshmukh and Manson (1983) performed cross section calculations covering the energy region from the 3s threshold to 270 eV but included only the single-electron resonances due to the $2s \rightarrow np$ ($n \geq 6$) and $2p \rightarrow nd$ (ms) ($n \geq 8$, $m \geq 10$) excitations. Using the many-body perturbation theory (MBPT), Altun (1989) carried out detailed calculations of the photoionization cross section of magnesium for photon energies ranging from the 3s threshold to 300 eV. In these calculations he included both $2s \rightarrow np$ ($n \geq 3$), $2p \rightarrow nd$ (ms) ($n \geq 3$, $m \geq 4$) single-electron resonances and $3s^2 \rightarrow 3pnd$ (ms) ($n \geq 3$, $m \geq 4$) double-electron resonances.

Inner-shell ionization studies of Mg-like ions have been carried out in connection with their importance in laboratory and astrophysical plasmas where ionization takes place through direct and indirect processes. In the direct-ionization process either a valence electron or any of the inner-shell electrons are knocked out from the ion by photon or electron-impact. The indirect-ionization proceeds through the excitation of an inner-shell electron followed by autoionization. These excitation-autoionization processes have recently been of great interest both in photoionization (Peart *et al.* 1989) and electron-impact (Howald *et al.* 1986) studies as they result in the dramatic enhancement of ionization cross sections. Absolute electron-impact ionization cross sections for the Mg-like ions S^{4+}, Cl^{5+}, and Ar^{6+} were measured in a crossed-beam experiment from threshold to 1500 eV by Howald *et al.* (1986). The relative magnitude of the indirect ionization process was found to be increased dramatically in comparison with the direct process along the sequence. Excitation-autoionization contributions to the electron-impact ionization of the Mg-like ions S^{4+}, Cl^{5+}, and Ar^{6+} were calculated in the distorted-wave approximation by Pindzola *et al.* (1986). The calculated cross sections were in very good agreement with the experimental measurements of Howald *et al.* (1986). Using the R-matrix method Tayyal and Henry (1986) carried out calculations for Mg-like ions Al^{+}, S^{4+}, Cl^{5+} and Ar^{6+}. The ground $3s^2\ {}^1S$ state together with the autoionizing states arising from the $2p^53s^23p$, $2p^53s^23d$, $2p^53s^24s$, $2s2p^63s^23p$, $2s2p^63s^23d$, and $2s2p^63s^24s$ configurations were included in the R-matrix expansion. In the case of Al^{+} a comparison was made with the experimental data of Montague and Harrison (1983). The calculated cross sections for S^{4+}, Cl^{5+} and Ar^{6+} were compared with the crossed-beam experimental data of

Howald *et al.* (1986). Although the $2p^5 3s 3p^2$ configuration, which is strongly mixed with the $2p^5 3s^2 3d$ configuration, was not included in the calculations even then the calculated and measured cross sections were in excellent agreement. In both calculations the largest contributions predicted were due to the $2p \rightarrow 3p$ monopole and $2p \rightarrow 3d$ dipole excitations.

Theoretical investigations of the electron-correlations involving the valence shells in the magnesium sequence are numerous. The two-electron excitations, both below and above the first ionization limits, which lead to resonances and series perturbers are of great interest in computation (Chang 1986a, 1986b, 1987). A theoretical study of the $2p^6 3s^2\ ^1S \rightarrow 2p^6[3p(n+1)s + 3pnd,\ n \geq 3]\ ^1P$ doubly excited states, which lie above the first-ionization threshold of magnesium, has been reported by Chang (1986b). Good agreement was found between the experimental and calculated energy values of these doubly excited states. The importance of the configuration-interaction between the doubly excited perturber and the singly excited $2p^6 3snl$ series has been examined quantitatively using superposition of configuration calculations (Chang 1986a). The entire 3snd series was found perturbed by the $3pn(\geq 3)p$ configuration series. In particular the entire 3snd series was shifted due to the strong interaction with the $3p^2$ configuration. The effects of configuration-interaction on the term values and oscillator strengths of the $2p^6 3snl\ ^1L$ singly excited states of the Mg atom below the first-ionization threshold have also been examined in detail by Chang (1987). A theoretical study of configuration-interaction between bound singly excited $(3snl)\ ^{1,3}L$ and doubly excited $(n_1 l_1,\ n_2 l_2)^{1,3}L$ states below the first ionization threshold of the Mg-like ions Al^+ and Si^{2+} has been published by Chang and Wang (1987). The study viewed the problem from the perspective of the doubly excited state as the perturber of each one electron Rydberg series $3s^2 \rightarrow 3snl$. The effect of each doubly excited state on term energies and gf values for each Rydberg member was examined in detail. Recently Chang and Wang (1991) have extended their study on the effect of configuration-interaction to the energy levels, the oscillator strengths and the radiative lifetimes of the bound excited states to the Mg-like ions P^{3+} and S^{4+}. The Al^+ and Si^{2+} ions were also included in this study. O'Mahony (1985) using a combination of R-matrix and hyperspherical coordinate techniques studied the effects of electron correlation in atomic valence-shells. The $2p^6 3snd$-$2p^6 3p^2$

mixing in Mg was analysed in detail and its relevance to the s^2p^nd-sp^{n+2} interactions throughout the row was indicated by a study of the $2p^63s^2nd$-$2p^63s3p^2$ mixing in Al. The $2p^63s3p^2$ configuration was found strongly mixed throughout the $2p^63s^2nd$ Rydberg series and into the $3s^2\varepsilon d$ continuum. The $2p^63s^2ns$ Rydberg were not perturbed to any great extent by the $2p^63s3p^2$ configuration.

4.2 Present work

The spectrum of Mg has previously been studied in some detail (Ederer *et al.* 1979) while we have published recently measurements and analysis of the 2p photoabsorption spectrum of Al^+ (Costello *et al.* 1992). More recently we have extended these studies to Si^{2+}. The 2p subshell photoabsorption spectra of atomic magnesium, singly ionised aluminium and doubly ionised silicon going to the $2p^53s^2$ ($^2P_{3/2,1/2}$) limits are shown in figure 4.1. The limits indicated in this figure were obtained by adding the first ionization potential of each species as given by Martin and Zalubas (1979, 1980, 1983) to the $2p^63s$ ($^2S_{1/2}$) $\rightarrow$ $2p^53s^2$ ($^2P_{3/2,\ 1/2}$) transition energies of Mg^+ (Esteva and Mehlman 1974), Al^{2+} (Brilly *et al.* 1988) and Si^{3+} (Mosnier *et al.* 1987). The spectra along this sequence are dominated by the $2p^63s^2\ ^1S \rightarrow 2p^53s^2nl\ ^{1,3}L$ one-electron excitations and $2p^63s^2\ ^1S \rightarrow 2p^53s3pnp\ ^{1,3}L$ two-electron excitations.

In order to provide interpretation for the observed spectra of Si^{2+} and gain a more complete understanding of the level structure of this sequence, atomic structure configuration-interaction calculations have been performed for Al^+ and Si^{2+}.

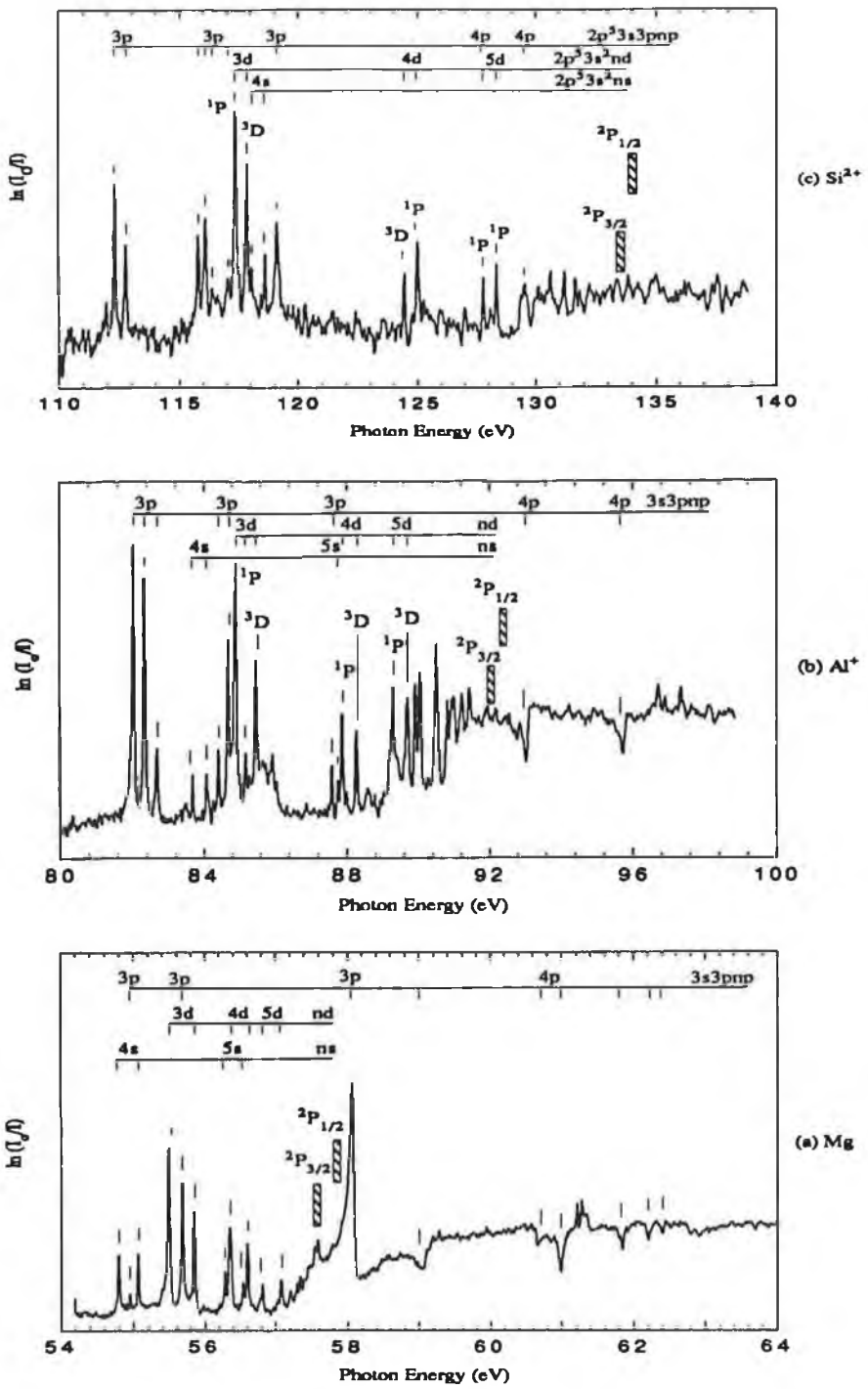

Figure 4.1

The 2p-subshell ground state photoabsorption spectra of (a) Mg , (b) Al^+ and (c) Si^{2+} obtained using the DLPP technique. The labelling shown for Mg is from Ederer *et al.* (1979) while for Al^+ and Si^{2+} is based on the present investigations (see tables 4.1 and 4.2). The positions of the $^2P_{3/2}$ and $^2P_{1/2}$ thresholds indicated in the figure are at 57.55 and 57.81 eV foe Mg, 91.76 and 92.18 eV for Al^+, and 133.32 and 133.84 eV for Si^{2+} respectively.

4.3 Effects of CI on the ground and excited states

The effects of configuration-interaction (CI) both on the ground and excited states have been examined in detail for Al^+ and Si^{2+}. A qualitative comparison with the experimental results is also provided. The effects of configuration-interaction on the term energies and oscillator strength of excited states will be discussed in section 4.3.1 while the role of electron correlations in the ground state will be assessed in section 4.3.2.

4.3.1 CI effects on the excited states

In order to investigate the configuration-interaction (CI) effects on the excited states a series of scaled atomic structure calculations were performed with a fixed basis states expansion for the ground states while adding successively the odd parity configurations to the excited states expansion including only the Rydberg series members. Throughout this study the computed and observed relative transition energies and oscillator strengths were compared as each new configuration was added.

First of all, the calculated level structure obtained for the unperturbed Rydberg series members, referred to as SA, is discussed then the effects of the $2p^53s3p^2$ and $2p^53s3p4p$ the doubly excited perturbers are investigated. Finally the effects of the $2s2p^63s^23p$, $2p^63s3p$ and $2p^63p3d$ configurations, which account for the core-valence interactions, are examined on the energies and oscillator strengths of both the Rydberg series members and the doubly excited states. The results of these scaled calculations, where the direct and exchange integrals were reduced by 20%, configuration-interaction integrals by 30% and spin orbit integrals by 10%, are shown in figure 4.2 both for Al^+ and Si^{2+}. In this figure the gf-values have been plotted against the calculated term energies for each expansion.

$$\mathbf{SA = 2p^6(3s^2+3p^2) \rightarrow 2p^5 3s^2(n+1)s + 2p^5 3s^2 nd,\ [n = 3,..10]}$$

Apart from overestimating the transition energies by $\leq$ 0.3 eV, this

expansion provides a reasonable fit to the $2p \rightarrow nl$, ($n \geq 4$) Rydberg series. It also clearly demonstrates that some of the strongest features in this spectrum must arise from multiply excited transitions and hence correlation effects play a major role in Al^+ and Si^{2+} just as they do in Mg.

The relative positions and intensities of ^1P and ^3D terms, belonging to the 3d (lines 4 and 5), 4d (lines 7 and 8) and 5d (lines 9 and 10) configurations in Al^+, predicted by these calculations are in accordance with the observed spectra (Figure 4.2a). In Si^{2+}, the calculated positions of ^1P and ^3D in 3d configuration (lines 3 and 4) are not in agreement with experiment (Figure 4.2b).

$$\mathbf{SB = SA + 2p^5 3s 3p^2}$$

The origin of the three prominent features, in the Al^+ spectrum, in the 81.5 $\rightarrow$ 83.0 eV range becomes clear as oscillator strength is transferred from the $2p \rightarrow 3d$ array to $2p \rightarrow 3s3p^2$ transitions leading to a substantial redistribution of oscillator strength between these two arrays. Compared to the 3d ^1P term more oscillator strength is sucked from the 3d ^3D term.

The inversion of ^1P and ^3D (lines 3 and 4 respectively) as observed in the Si^{2+} spectrum is also evident from expansion SB when compared with expansion SA (Figure 4.2b). In the Si^{2+} spectrum the ^3D term of the 3d configuration is strongly perturbed by the $2p^53s3p^2$ configuration and is pushed to higher energy region while the ^1P term remains unperturbed in energy. In the case of Al^+, both the ^1P and ^3D are strongly perturbed in energy (Figure 4.2a SA and SB) but their relative positions remain the same.

The $2p^53s^23d$ and $2p^53s3p^2$ configurations were found strongly mixed with each other both in Al^+ and Si^{2+}. On the other hand, no significant effect has been seen on the higher Rydberg series members belonging to the nd series as well as the entire ns series.

SC = SB + $2p^5 3s3p4p$

The inclusion of $2p^5 3s3p4p$, which mixes with higher nd states, leads to slight energy and oscillator strength corrections to the 2p → nd transitions both in Al^+ and Si^{2+}.

The expansion SC yields good values for the Rydberg transition energies and oscillator strengths and is almost sufficient for the purposes of spectral identification. The calculated term energies of the $2p^5 3s3p^2$ and $2p^5 3s^2 3d$ configurations are found to be in quite good agreement with the observed energies, except for a few doubly excited terms. However, the higher Rydberg series members although they have a good distribution of the oscillator strength their energies need a constant shifting of ≈ 0.2 eV towards the lower energy region.

Hence, as far as the distribution of oscillator strength and term energies are concerned this expansion is very satisfactory both for Al^+ and Si^{2+} ions. In particular the predicted relative strengths of the nd Rydberg series members seems in reasonable agreement with the measurements. The relative distribution of gf-values within the doubly excited states however is not justified by the calculations. In order to better reconcile the calculated and observed spectra an attempt was made to include the extra effects due to (i) penetration of the core region by outer shell electrons via inclusion of valence excited configurations, (ii) core polarisation in the ground state by opening up the 2p-subshell and (iii) core polarisation in the excited state by opening up the 2s-subshell.

SD = SC + $2s2p^6 3s^2 3p$

The inclusion of the $2s2p^6 3s^2 3p$ configuration in the CI calculations leads to a better oscillator strength division between the lowest two doubly excited transitions, $2p^6 3s^2(^1S_0) \rightarrow 2p^5 3s(^3P)3p^2(^1D)^3D_1$ and $2p^5 3s(^1P)3p^2(^1D)^1P_1$ (Lines 1 and 2, respectively, in figure 4.2b) . Particularly, in Si^{2+}, the inclusion of this configuration leads to changes in the compositions of the $(^1D)^1P$ and $(^1D)^3D$ terms which in turn brings the results in better visual agreement with the experiment (Figure 4.2b SD).

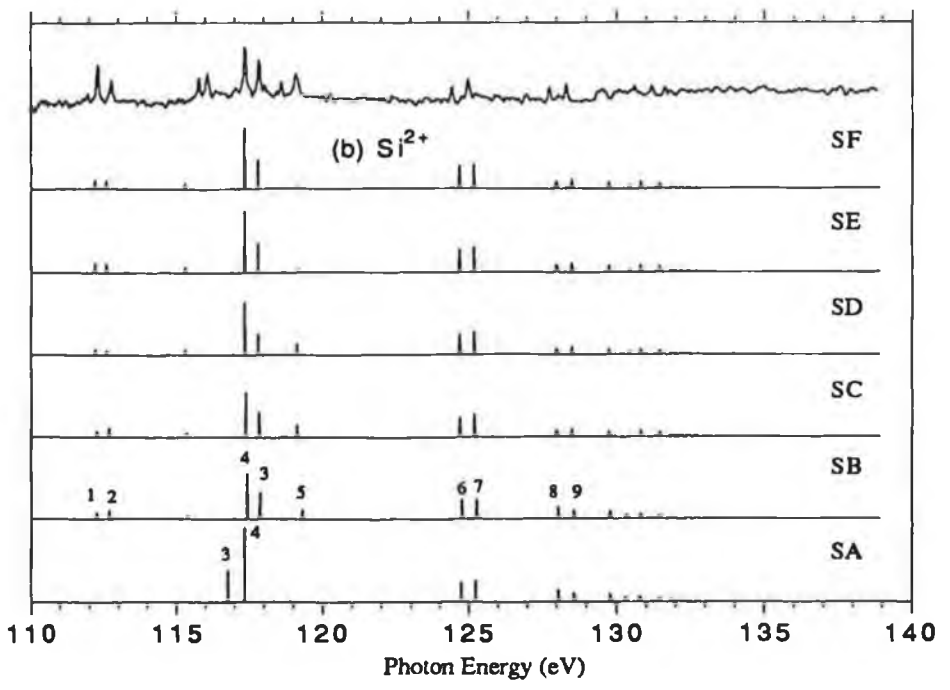

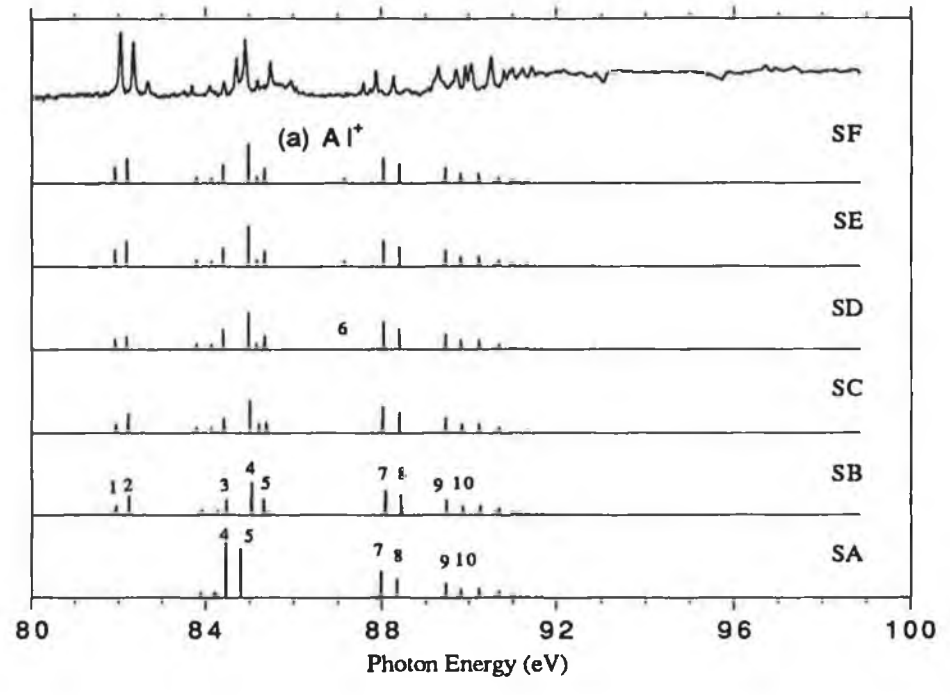

Figure 4.2

Configuration-interaction effects on the excited states in the 2p photoabsorption spectra of (a) Al^+ and (b) Si^{2+}.

4.3.2 CI effects on the ground state

The ground state of the magnesium sequence shows strong electron-correlation effects (Robb 1974). Recently the electron-correlations in the ground state of Mg-like ions Al^{+} and Si^{2+} have been investigated in detail by Serrao (1991, 1991). In this study which used the configuration interaction method where the electronic orbitals were generated by means of Thomas-Fermi-Dirac-Amaldi (TFDA) potentials, the most important contribution to the ground state wavefunction was reported to be made by the doubly excited states ($2p^6 3pnp\ ^1S$).

In order to assess the effect of electron-correlations in the ground state, a series of calculations were carried out with a fixed configuration expansion for the excited states (which includes the $2p^5 3s^2(n+1)s + 2p^5 3s^2 nd$, [n = 3,4...10] + $2p^5 3s 3p^2 + 2p^5 3s 3p 4p + 2s 2p^6 3s^2 3p + 2p^6 3s 3p + 2p^6 3d 3p$ basis states) while adding successively even parity configurations to the ground state. The results of the first set of calculations, named as SG, carried out for the $2p^6 3s^2 \rightarrow 2p^5 3s^2(n+1)s + 2p^5 3s^2 nd$, [n = 3,4...10] + $2p^5 3s 3p^2 + 2p^5 3s 3p 4p + 2s 2p^6 3s^2 3p + 2p^6(3s 3p + 3d 3p)$ are shown in figure 4.3a.

$$\mathbf{SH = SG + 2p^6 3p^2}$$

The addition of the $2p^6 3p^2$ configuration which is known to mix strongly with the $2p^6 3s^2$ ground state (Serrao, 1991, 1991) leads to an overall weakening of most of the $2p^6 3s^2\ ^1S_0 \rightarrow 2p^5 3s 3p^2\ ^{1,3}L$ array with the exception of $2p^6 3s^2\ ^1S_0 \rightarrow 2p^5 3s(^1P)3p^2\ (^1S)^1P_1$ (line 3 both in Al^{+} and Si^{2+}, figure 4.3) which is strengthened. The effect of $2p^6 3p^2$ configuration on the term energies is evident from the comparison of expansions SG and SH (Figure 4.3).

In the magnesium 2p absorption spectrum the strongest asymmetric resonance at 58.07 eV has been identified as the $2p^6 3s^2(^1S_0) \rightarrow 2p^5 3s(^1P)3p^2(^1S)^1P_1$ transition (Ederer *et al.* 1979). The reason for this feature to be the strongest was described as the mixing of the ^1S term of the $2p^6 3p^2$ configuration with the normal $2p^6 3s^2\ ^1S_0$ ground state. The present results along

the Mg-like ions agree with this proposition (see figure 4.3), the predicted enhancement is by no means as great. Also, this term (line 3) is not among the strongest features in the Al^+ and Si^{2+} spectra. One other interesting point about this particular resonance is that it is surprisingly not observed in the ejected-electron data of Pejcev *et al.* (1977). The following explanation is proposed for this. It should be noted that the Mg feature at 58.07 eV is observed above the $^2P_{3/2,\ 1/2}$ limits thereby opening up the possibility both for direct and resonant 2p photoionization via the process $2p^63s^2+h\nu \rightarrow 2p^53s3p^2(^1S)^1P \rightarrow 2p^5\ (^2P_{3/2})3s^2\varepsilon l$. Such a process can both lead to an enhancement in the strength of this feature in phoexcitation and will also result in an Auger electron of an energy of less than 1 eV compared to the 41.5 → 50.4 eV expected by Pejcev and co-workers who searched for its decay into the $2p^63s$, 3p or 3d + εl channels.

$$\mathbf{SI = SH + 2p^5 3s^2 3p}$$

The $2p^53s^23p$ configuration has been included in order to account for core polarisation in the ground state. Although not affecting the energy distribution of the computed spectrum it certainly does lead to a significant enhancement in the strength of the singly excited 2p → nl transitions while leaving transitions to doubly excited states largely unaffected with the exception of the $2p^53s3p^2(^3P)^1P$ term (Line 6 both in Al^+ and Si^{2+}, figure 4.3). The strength of this term was enhanced in Si^{2+} and decreased in Al^+.

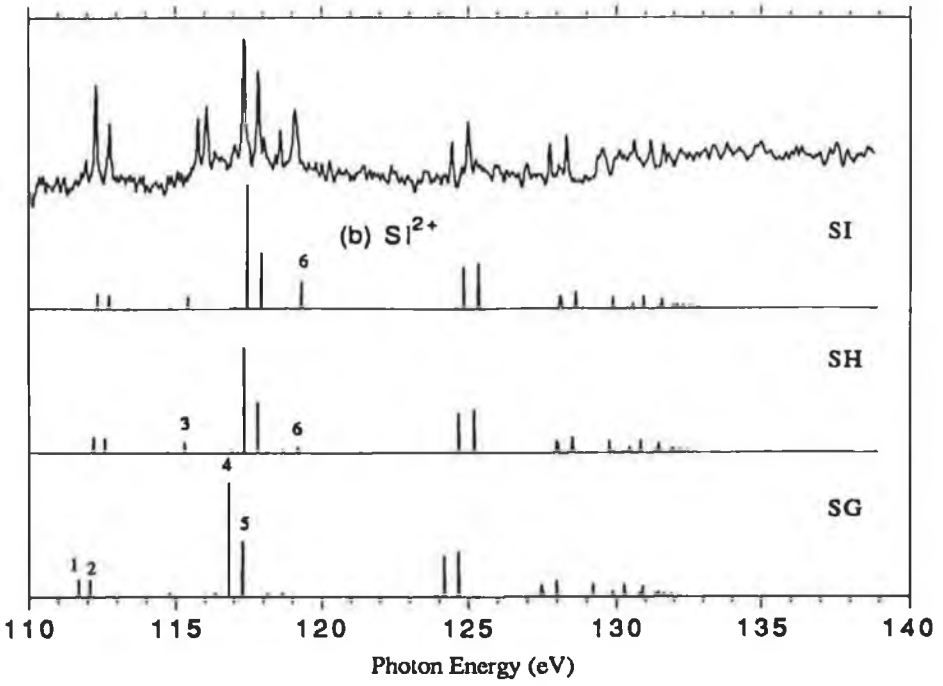

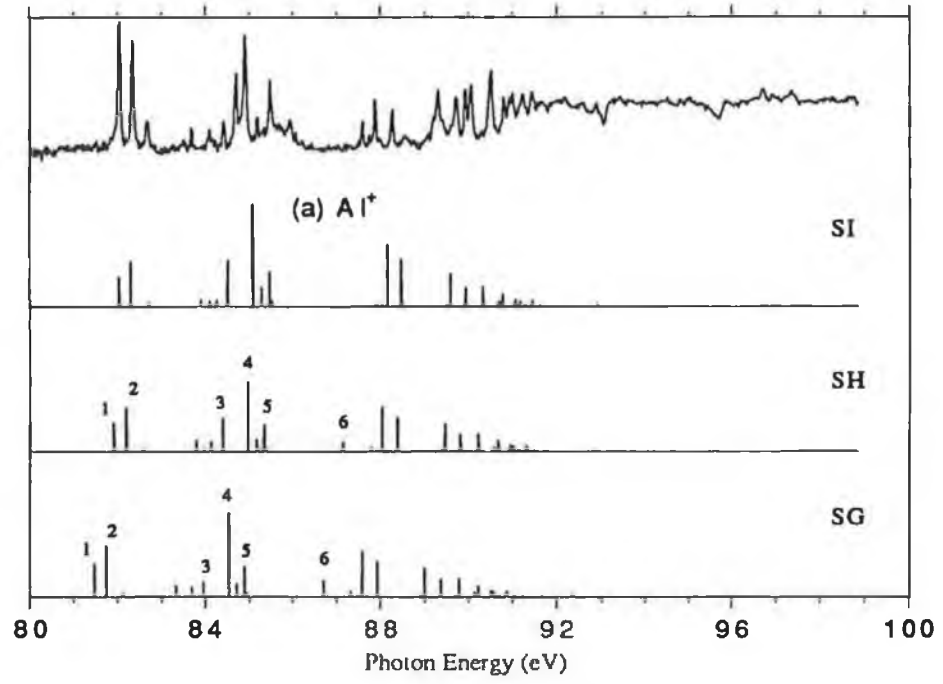

Figure 4.3

Configuration-interaction effects on the ground state in the 2p photoabsorption spectra of (a) Al^{+} and (b) Si^{2+}.

4.4 Term analyses

The analyses of measured level structure becomes extremely difficult when more than one electron is involved in the photoexcitation process. The unscaled and scaled atomic structure calculations performed using the same set of basis states including extensive interactions differ widely in the calculated term energies and gf-values and make the line identification more complicated and confusing. The different approximations give the same term energies but differ in the distribution of oscillator strengths in a very dramatic way such as a feature predicted as strongest by one approximation is shown with negligible gf-values using some other approximation.

In the approach adopted, with only the most significant interactions included in both the ground and excited states, the different expansions give almost the same term energies but slightly differ in the distribution of gf-values. A comparison of figures 4.2 and 4.3 shows that the calculated positions of the energy levels obtained using expansions SC, SD, SE, SF, SG = SE, SH and SI are almost the same. However, in going from one expansion to other slight changes in the distribution of oscillator strength are observed. The expansion SE which includes only the most significant interactions in the initial and final state expansions gives a better qualitative as well as quantitative agreement with the experiment. The level energies and gf-values of both the Al^+ and Si^{2+} computed using expansion SE are listed in tables 4.1 and 4.2. In table 4.1 a comparison of the levels belonging to the $2p^5 3s 3p^2$ and $2p^5 3s^2 3d$ configurations is made with the calculated energies. The experimental and theoretical level energies of the higher Rydberg series members are compared in table 2. With the exception of a few doubly excited states, the results are in reasonable agreement with the measured spectra.

The assignments for Al^+ have already been reported by our group (Costello *et al.* 1991). In that work along with the basis states included in expansion SE although basis states $2p^6 3d^2$ for ground state expansion and $2p^5 3p^2 3d$, $2p^5 3s 3d^2$ and $2p^5 3p^2 4s$ for the excited state expansion were also included.

In the assignment of the observed features at 84.78 eV, 84.99 eV and 85.36 eV the present investigation differs from the earlier study of Al^+ (Costello *et al.* 1991) where they were assigned to the 3d ^3P, ^3D and ^1P levels. According to the present study ^3P terms in the whole nd series both in Al^+ and Si^{2+} show

negligible gf-values and, therefore, should not be observed. The ^1P and ^3D terms are predicted strong and weak, respectively, throughout the nd series both in Al^+ and Si^{2+} which is in agreement with the experiment. In the earlier assignment the strong and weak levels of the 3d configuration were assigned to the ^3D and ^1P terms respectively. The present assignment is more reliable because calculated term energies of these resonances along with the distribution of gf-values are in agreement with the experiment which was not the case in earlier studies.

In the case of Si^{2+}, the lines predicted at 115.32 eV and 116.01 eV which are assigned to the features at 115.81 eV and 116.07 eV could only be identified tentatively because they do not follow the rules, adopted in the assignments given, which are: (i) a strong line should be predicted as a strong line and vice versa, (ii) the splitting of the predicted term energies -at least- within a configuration should be equal to the measured splitting of the corresponding terms, and (iii) measured and calculated energies should fall in the same energy region. Also we are not sure about the origin of the features measured at 115.81 eV and 116.07 eV. These features could be due to the $2p^63s3p \rightarrow 2p^53s3p3d$ transitions which are predicted in this region by our calculations, performed during the study of $2p^63s3p \rightarrow 2p^53s23p + 2p^63s3p3d$ transitions (Mosnier *et al.* 1994). In atomic Mg the $2p^63s3p \rightarrow 2p^53s3p3d$ transitions have not been observed. In Al^+, the $2p^53s3p3d$ transition array has been observed but features were very weak and unresolvable. In moving from atomic Mg to Si^{2+}, with the increase in the overlap of 2p and 3d orbitals, which is evident from the increase in the relative strength of $2p \rightarrow 3d$ transitions (Figure 4.1), the $2p^63s3p \rightarrow 2p^53s3p3d$ transitions should be stronger than in Al^+. There is another possibility that these features could be due to some impurities which we were not able to identify in this spectrum. By extending photoabsorption studies to the higher isoelectronic species the identification of these features could be solved. With continuous increase in the overlap of 2p and 3d orbitals along this sequence if they are associated with the $2p^63s3p \rightarrow 2p^53s3p3d$ transitions they should appear stronger.

Table 4.1. Comparison of calculated and observed term energies (in eV) for $2p^6 3s^2\ ^1S \rightarrow 2p^5(3s^2 3d + 3s3p^2)\ ^{1,3}L$ transitions of Al^+ and Si^{2+}. The F and G integrals were reduced by 20%, the configuration interaction integrals by 30% and the spin-orbit integrals by 10%.

	Al^+				Si^{2+}		
Config./term	$E_{cal.}$	$E_{obs.}$	gf	Config./term	$E_{cal.}$	$E_{obs.}$	gf
$2p^5 3s(^3P)3p^2\ (^1D)^3D_1$	81.92	82.15	0.0396	$2p^5 3s(^3P)3p^2\ (^1D)^3D_1$	112.23	112.30	0.0542
$2p^5 3s(^1P)3p^2\ (^1D)]^1P_1$	82.91	82.45	0.0607	$2p^5 3s(^1P)3p^2\ (^1D)]^1P_1$	112.62	112.80	0.0502
$2p^5 3s(^3P)3p^2\ (^1D)^3P_1$	82.58	82.77	0.0052	$2p^5 3s(^3P)3p^2\ (^1D)^3P_1$	113.27	-------	0.0037
$2p^5 3s(^3P)3p^2\ (^1S)^3P_1$	83.98	84.50	0.0054	$2p^5 3s(^3P)3p^2\ (^1S)^3P_1$	114.74	-------	0.0066
$2p^5 3s(^1P)3p^2\ (^1S)^1P_1$	84.40	84.78	0.0455	$2p^5 3s(^1P)3p^2\ (^1S)^1P_1$	115.32	115.81	0.0348
$2p^5 3s^2(^2P)3d\ ^3P_1$	84.77	------	0.0009	$2p^5 3s(^3P)3p^2\ (^3P)^3P_1$	116.01	116.07	0.0001
$2p^5 3s^2(^2P)3d\ ^1P_1$	84.98	84.99	0.0967	$2p^5 3s(^3P)3p^2\ (^3P)^3D_1$	116.46	-------	0.0009
$2p^5 3s(^3P)3p^2\ (^3P)^3P_1$	85.17	85.26	0.0172	$2p^5 3s(^3P)3p^2\ (^3P)^3S_1$	116.93	-------	0.0124
$2p^5 3s^2(^2P)3d\ ^3D_1$	85.34	85.36	0.0362	$2p^5 3s^2(^2P)3d\ ^3P_1$	117.14	-------	0.0018
$2p^5 3s(^3P)3p^2\ (^3P)^3D_1$	85.40	85.36	0.0055	$2p^5 3s^2(^2P)3d\ ^1P_1$	117.37	117.34	0.3679
$2p^5 3s(^3P)3p^2\ (^3P)^3S_1$	85.74	------	0.0001	$2p^5 3s^2(^2P)3d\ ^3D_1$	117.83	117.88	0.1761
$2p^5 3s3p^2\ (^3P)^1P_1$	87.14	87.65	0.0132	$2p^5 3s3p^2\ (^3P)^1P_1$	119.22	119.12	0.0195

Table 4.2. Comparison of calculated and observed term energies (in eV) for $2p^63s^2\ {}^1S \rightarrow$ nd, (n+1)s [n≥4] transitions of Al^+ and Si^{2+}.The F and G integrals were reduced by 20%, the R integrals by 30% and the spin-orbit integrals by 10%.

Config./term	Al^+ $E_{cal.}$	Al^+ $E_{obs.}$	gf		Si^{2+} $E_{cal.}$	Si^{2+} $E_{obs.}$	gf
$4s[3/2,1/2]_1/(^1P)$	83.78	83.77	0.0156	$4s[3/2,1/2]_1/(^1P)$	118.19	118.09	0.0058
$4s[1/2,1/2]_1/(^3P)$	84.14	84.17	0.0135	$4s[1/2,1/2]_1/(^3P)$	118.71	118.63	0.0115
$5s[3/2,1/2]_1/(^1P)$	87.78	87.80	0.0066	$5s[3/2,1/2]_1/(^1P)$	125.33	------	0.0006
$5s[1/2,1/2]_1/(^3P)$	88.15	88.05	0.0014	$5s[1/2,1/2]_1/(^3P)$	125.87	------	0.0026
$6s[3/2,1/2]_1/(^1P)$	89.36	89.26	0.0029	$6s[3/2,1/2]_1/(^1P)$	128.35	------	0.0028
$6s[1/2,1/2]_1/(^3P)$	89.74	89.62	0.0011	$6s[1/2,1/2]_1/(^3P)$	128.88	------	
$4d[3/2,5/2]_1/(^1P)$	88.04	87.93	0.0616	$4d[1/2,3/2]_1/(^3D)$	124.72	124.47	0.1355
$4d[1/2,3/2]_1/(^3D)$	88.39	88.31	0.0475	$4d[3/2,5/2]_1/(^1P)$	125.34	125.02	0.1493
$5d[3/2,5/2]_1/(^1P)$	89.46	89.33	0.0383	$5d[3/2,5/2]_1/(^1P)$	128.02	127.78	0.0411
$5d[1/2,3/2]_1/(^3D)$	89.82	89.73	0.0230	$5d[3/2,5/2]o_1/(^1P)$	128.53	128.35	0.0534
$6d[3/2,5/2]_1/(^1P)$	90.22	90.10	0.0242	$6d[3/2,5/2]_1/(^1P)$	129.72	129.53	0.0409
$6d[1/2,3/2]_1/(^3D)$	90.60	90.52	0.0068	$6d[1/2,3/2]_1/(^3D)$	130.24	130.10	0.0038
$7d[3/2,5/2]_1/(^1P)$	90.67	90.52	0.0149	$7d[3/2,5/2]_1/(^1P)$	130.83	130.62	0.0420
$7d[1/2,3/2]_1/(^3D)$	91.04	90.95	0.0075	$7d[1/2,3/2]_1/(^3D)$	131.34	131.24	0.0126
$8d[3/2,5/2]_1/(^1P)$	90.96	90.83	0.0086	$8d[3/2,5/2]_1/(^1P)$	131.47	131.24	0.0336
$8d[1/2,3/2]_1/(^3D)$	91.33	91.25	0.0080	$8d[1/2,3/2]_1/(^3D)$	132.00	131.73	0.0174
$9d[3/2,5/2]_1/(^1P)$	91.15	91.05	0.0036	$9d[3/2,5/2]_1/(^1P)$	131.90	------	0.0143
$9d[1/2,3/2]_1/(^3D)$	91.56	91.46	0.0012	$9d[1/2,3/2]_1/(^3D)$	132.43	------	0.0111

4.5 Conclusions regarding the general behaviour along the isoelectronic sequence

On the basis of the assignments given in section 4.4 and a study of the eigenvector compositions of the observed transitions a number of general remarks may be made.

With the increase in Z along the isoelectronic sequence the spectrum restructures itself and shows changes in the distribution of oscillator strength and the relative positions of singlets and triplets. As we move along the sequence to Si^{2+} the transitions to $2p^5 3s3p^2$ (which are the strongest features in the Mg and Al^+ spectra) weaken considerably as the 3d orbital contracts and $2p \rightarrow 3d$ transitions become the dominant features of the Si^{2+} 2p - subshell absorption spectra. In Al^+ the ^1P terms belonging to the 3d, 4d and 5d configurations are observed lower in energy than the corresponding ^3D terms (Figure 4.1b). In the case of Si^{2+} such a situation is observed only in 3d configuration (Figure 4.1c).

In Al^+ and Si^{2+} the centres of gravity of the $2p^5 3s3p^2$ and $2p^5 3s3p4p$ configurations shift downwards in energy with respect to the E_{av} of the $2p^5 3s^2 nl$ Rydberg series members. All terms of the $2p^5 3s3p^2$ configuration drop below the limit for Al^+ and Si^{2+} and are strongly mixed with the $2p^5 3s^2 3d$ configuration. Some features belonging to the $2p^5 3s3p4p$ configuration are also observed below the series limit where they are mixed with higher Rydberg series members.

Level crossing within the $2p^5 3s^2 ns$ and $2p^5 3s^2 nd$ Rydberg series is evident from these spectra. In particular the 3d drops below the 4s on going from Al^+ to Si^{2+}. Clearly 3d contraction is also responsible for this 3d/4s level crossing observed in Si^{2+}. The 4d and 5s energies become almost degenerate.

Level crossing within the $2p^5 3s^2 nl$ and $2p^5 3s3pnp$ configurations is also observed along this sequence. This occurs in an isoelectronic sequence whenever "plunging" configurations are present (Froese Fisher, 1980). These are the configurations whose energies lie above the ionization limit in neutral atoms and are present both in the valence and inner-shell spectra. In the valence-shell spectra they could be the doubly excited states (such as, $3s^2 \rightarrow 3pn(\geq 3)d$ or $3s^2 \rightarrow 3pm(\geq 4)s$ transitions in magnesium) or the singly-excited states where the inner-

valence electron is excited (such as, $3s^23p \rightarrow 3s3pn(\geq 3)p$, transitions in aluminium). In the inner-shell spectra these are the multi-electron excitations, such as the doubly excited states belonging to the $2p^53s3p^2$ configuration in the ground state 2p absorption in magnesium. As the nuclear charge increases, the energy levels of the plunging configurations drop below the limit where they appear as discrete features mixed with the Rydberg series members in the case of valence-shell spectra while in the inner-shell spectra, in addition to the strong mixing with the Rydberg series members, they are also coupled to the background continuum channel (Conneely *et al.* 1992).

In neutral Mg the $2p^53s3p^2$ configuration acts as a strong perturber for the whole $2p^53s^2nd$ Rydberg series. However, along the magnesium isoelectronic sequence the $2p^53s^2n(\geq 4)d$-$2p^53s3p^2$ interaction is "short-range" in nature (Froese Fisher 1980) as in proceeding from neutral magnesium to the Mg-like ions Al^+ and Si^{2+} it is not observed. The reason is that in magnesium the $2p^53s3p^2$ configuration is smeared out over the entire Rydberg series including the $2p^53s^2\varepsilon l$ continuum while in going from the neutral to ions all its levels lie below the 4d. On the other hand, $2p^53s^23d$-$2p^53s3p^2$ interaction acts as a "long-range" interaction along the magnesium sequence as it remains strong throughout the sequence. This is because the two configurations belong to the same complex. It is due to this long-range interaction that the $^{1,3}L$ terms of the $2p^53s^23d$ configuration remain strongly perturbed in the magnesium sequence.

The $2p^53s^2nd$-$2p^53s3p^2$ interaction among the core-excited configurations of neutral magnesium is analogous to that of the $2p^63s^23p^n3d$-$2p^63s3p^{n+2}$ interaction along the period which could be seen from the $2p^63s^2nd$-$2p^63s3p^2$ and $2p^63s^23pnd$-$2p^63s3p^3$ interactions described for atomic aluminium (Weiss 1974, Lin 1974, O'Mahony 1985) and silicon (Tatewaki 1978) respectively. The core-excited states in Mg sequence are perturbed by the doubly excited states while the perturbers in the outer-shell spectra of neutral Al and Si are singly excited states. The doubly excited states belonging to the $2p^53s3p4p$ configuration in neutral magnesium all are observed above the 2p-limit which is again similar to the $2p^63s3p4p$ and $2p^63s3p^24p$ configurations along the period in Al (Martin and Zalubas 1979) and Si (Martin and Zalubas 1983) respectively.

4.6 References

Altun Z, 1989, Phys. Rev. A **40**, 4968.

Breuckmann B, Schmidt V and Schmitz W, 1976, J. Phys. B **9**, 3037.

Brilly J, Kennedy E T and Mosnier J P, 1988, J. Phys. B: At. Mol. Opt. Phys. **21**, 3685.

Chang T N, 1986a, Phys. Rev. A **34**, 4550.

Chang T N, 1986b, Phys. Rev. A **34**, 4554.

Chang T N, 1987, Phys. Rev. A **36**, 447.

Chang T N and Wong Rong-Qi, 1987, Phys. Rev. A **36**, 3535.

Chang T N and Wong Rong-Qi, 1991, Phys. Rev. A **44**, 80.

Conneely M J, Lipsky L and Russek A, 1992, Phys. Rev. A **46**, 4012.

Costello J T, Evans D, Hopkins R B, Kennedy E T, Kiernan L, Mansfield M W D, Mosnier J-P, Sayyad M H and Sonntag B F, 1992, J. Phys. B: At. Mol. Opt. Phys., **25**, 5055.

Cowan R D, 1981, *"The Theory of Atomic Structure and Spectra"*, (University of California Press, Berkeley).

Deshmukh P C and Manson S T, 1983, phys. Rev. A **28**, 209.

Deshmukh P C, Nasreen G and Manson S T, 1988, phys. Rev. A **38**, 504.

Ederer D L, Lucatorto T B and Mehlman G, 1979, J. Opt. Soc. Am., **69**, 520.
Esteva J M and Mehlman G, 1974, Astrophys. J. **193**, 747.

Froese Fisher C, 1980, Phys. Rev. A **22**, 551.

Hameed S, Herzenberg A and James M G, 1968, J. Phys. B **1**, 822.

Hameed S, Phys. Rev., 1969, **179**, 16.

Haussmann A, Kämmerling B, Kossmann H and Schmidt V, 1988, Phys. Rev. Lett., **61**, 2669.

Hibbert A, Physica Scripta , 1989, **39**, 574.

Howald A M, Gregory D C, Meyer F W, Phaneuf R A, Müller A, Djuric N and Dunn G H, 1986, Phys. Rev. A **33**, 3779.

Kämmerling B, Haussmann A, La..uger J and Schmidt V, 1992, J. Phys. B **25**, 4773.

Lin C D, (1974), Astrophys. J. **187**, 385.

Mansfield M W D and Connerade J P, 1972, Physica Scripta **6**, 191.

Martin W C and R. Zalubas R, 1979, J. Phys. Chem. Ref. Data, **8**, 817.

Martin W C and R. Zalubas R, 1980, J. Phys. Chem. Ref. Data, **9**, 1.

Martin W C and R. Zalubas R, 1983, J. Phys. Chem. Ref. Data, **12**, 323.

Montague R G and Harrison M F A, 1983, J. Phys. B **16**, 3045.

Mosnier J P, Brilly J and Kennedy E T, 1987, J. Physique, **C-9**, 219.

Nasreen G, Manson S T and Deshmukh P C, 1989, Phys. Rev. A **40**, 6091.

Newsom G H, 1971, Astrophys. J. **166**, 243.

O'Mahony P F, 1985, Phys. Rev. A **32**, 908.

Pindzola M S, Griffin D C and Bottcher C, 1986, Phys. Rev. A **33**, 3787.

Peart B, Underwood J R A and Dolder K, 1989, J. Phys. B: At. Mol. Opt. Phys. **22**, 1679.

Pegg D J, Haselton H H, Thoe R S, Griffin P M, Brown M D and Sellin I A, 1975, Phys. Rev. A **12**, 1330.

Pejcev V, Ottley T W, Rassi D and Ross K J, 1977, J. Phys. **B 10**, 2389.

Robb W D, 1974, J. Phys. B **7**, 1837.

Serrao J M P, 1991a, J. Quant. Spectrosc. Radiat. Transfer, **45**, 121.

Serrao J M P, 1991b, J. Quant. Spectrosc. Radiat. Transfer, **45**, 349.

Tatewaki H and Sasaki F, 1978, Phys. Rev. A **18**, 1837.

Tayyal S S and Henry R T W, 1986, Phys. Rev. A **33**, 3825.

Weisheit J C, 1972, Phys. Rev. A **5**, 1621.

Wiess A W, 1974, Phys. Rev. A **9**, 1524.

Whitfield S B, Caldwell C D and Krause M O, 1991, Phys. Rev. A **43**, 233.

Chapter 5

ALUMINIUM ISOELECTRONIC SEQUENCE IN GROUND STATE ABSORPTION

Photoabsorption investigations of atomic Al and Si^+ in ground states have been carried out in their 2p subshell regions. To provide interpretation for the observed spectra a comprehensive analysis of this three-electron system, based on configuration interaction calculations, has been carried out. The objective of this chapter is to describe the previous work done along the Al sequence in ground state absorption and report the present investigations carried out.

5.1 Previous work

Aluminium is placed among the 15 most abundant cosmic elements (Martinson, 1989). A large number of aluminium lines are present in the solar spectrum. For a long time its atomic properties have been measured and calculated whenever new techniques promised improved results.

The transitions that involve the excitation of the outer shell 3p or 3s electrons have been extensively studied both theoretically and experimentally; a summary of this work has been published by Cantu *et al.* (1982), and Tayal and Burke (1987). Only a few investigations have been carried out on the transitions involving the excitation of an inner-shell 2p-electron. Among them the Auger decay following 2p ionisation/excitation processes by electron impact, as studied by Aksela (1984) and Messmer (1984), has been mentioned by Malutzki *et al.* (1987) as part of their private communication. Ejected-electron spectra of atomic Al following 2p excitation/photoionization have been measured at selected photon energies by Malutzki *et al.* (1987). At photon energies higher than the 2p ionisation of Al, they have observed decay due to the $2p^5 3s^2 3p$ configuration of Al^+. At 79 eV photon energy - below the 2p limit of Al - autoionization decay due to the levels of $2p^5 3s^2 3pnl$ configurations of atomic Al has been reported. In their work the authors have provided almost complete interpretation for the observed Auger

spectra of Al^+. However, in their experiment because of the broad bandpass of the exciting photons (Malutzki *et al.* 1987) a detailed discussion of the structures arising from the autoionising decay of atomic Al was not possible. The 2p absorption spectrum of neutral aluminium, obtained with a flash-pyrolysis technique combined with a BRV source, has been reported by Cantu *et al.* (1982).

Like aluminium, silicon is also among the 15 most abundant cosmic elements (Martinson, 1989). The astrophysical importance of silicon is well known (Dufton *et al.* 1992 and references therein). Knowledge of oscillator strength and photoionization cross sections of astrophysical important elements such as silicon are necessary for calculations of stellar abundances, opacity, electron density and other properties (Daum and Kelly 1976). Experimental measurement of the photoionization cross section of ionic silicon is quite difficult because of the recombination effects (Daum and Kelly 1976) as well as the difficulties associated with the production of enough ionic silicon. As far as we know no experimental study of ionic Si^+, involving the excitation of a 2p electron, has been carried out. However, on the theoretical side, photoionization cross section calculations of Si^+ have been reported (Daum and Kelly 1976) from threshold to 1 KeV. In their calculations, which were performed using the technique of many body perturbation theory, resonances from the 3s3pnp, $2p^53s^23pns$, $2p^53s^23pnd$, and $2s2p^63s^23pnp$ configurations were also included. Correlations among the 2p, 3s, and 3p electrons were shown to have a large effect on the cross section.

5.2 Present work

We have undertaken a comprehensive new analysis of the aluminium 2p photoabsorption spectrum which we have recorded using the dual laser plasma technique. Furthermore, we have extended this photoabsorption study to the aluminium like silicon spectrum which we have recorded for the first time. To elucidate the observed features, configuration-interaction calculations were performed with Cowan's code (see chapter 2).

In the photoinduced 2p Auger spectra of atomic Al (Malutzki *et al.* 1987) some difficulties associated with the production of an atomic Al vapour were mentioned. In particular, the aluminium oxide layer, which is always present, and the high reactivity of the hot Al liquid, made the production of an atomic Al vapour

very difficult. After a number of failures they were able to produce almost pure aluminium vapour. Fortunately, we have not faced any such failure; by firing a few shots on the target surface before making absorption measurements one can eliminate the effects of any oxide layer.

Atomic aluminium demonstrates strong configuration interaction effects among the excited states arising both from L and M-shell excitations. A number of studies have been carried out of the electron-correlations among the excited states involving the M-shell electrons. However, as far as we know, no investigation has been carried out of the electron-correlations among the excited states involving 2p excitation. Compared to the relatively simple two electron case (Costello *et al.* 1992, chapter 4) this system with three electrons outside the 2p-core not only yields an extensive number of terms but also makes the accurate calculations of the term structures significantly more difficult. Some of the observed features in the 2p absorption spectrum of neutral aluminium (Cantu *et al.*1982) were explained using the semi-empirical Racah-Slater method. The calculations were carried out only for the $2p \rightarrow 4s$ transitions and almost all of the strongest features were assigned to these transitions.

5.3 Results and analysis

The 2p-subshell photoabsorption spectra of neutral aluminium and singly ionised silicon going to the $2p^5 3s^2 3p$ (^{3}L) limits are shown in figure 5.1. The energies of the $2p^5 3s^2 3p$ (^{3}L) terms have been taken from chapter 7. The relevant optical energies have been taken from Martin and Zalubas (1979, 1983). In these spectra the absorption structures exhibit the $2p^6 3s^2 3p\ ^2P \rightarrow 2p^5 3s^2 3pnl\ ^{2,4}L$ and $2p^6 3s^2 3p \rightarrow 2p^5 3s 3p^3\ ^{2,4}L$ one and two-electron excitations respectively. Transitions to the doublet terms are expected to appear strongly; however, departures from LS-coupling will also allow transitions to the quartet terms.

In the 2p-subshell photoabsorption study along the magnesium sequence in the ground state, as presented in chapter 4, the magnesium spectrum was found to be more complicated than the corresponding ionic spectra of Al^+ and Si^{2+}. This was because of the strong perturbation caused by the doubly excited configuration $2p^5 3s 3p^2$ which in the case of neutral magnesium was very strong throughout the Rydberg series members. However, in the case of ions the perturbing doubly

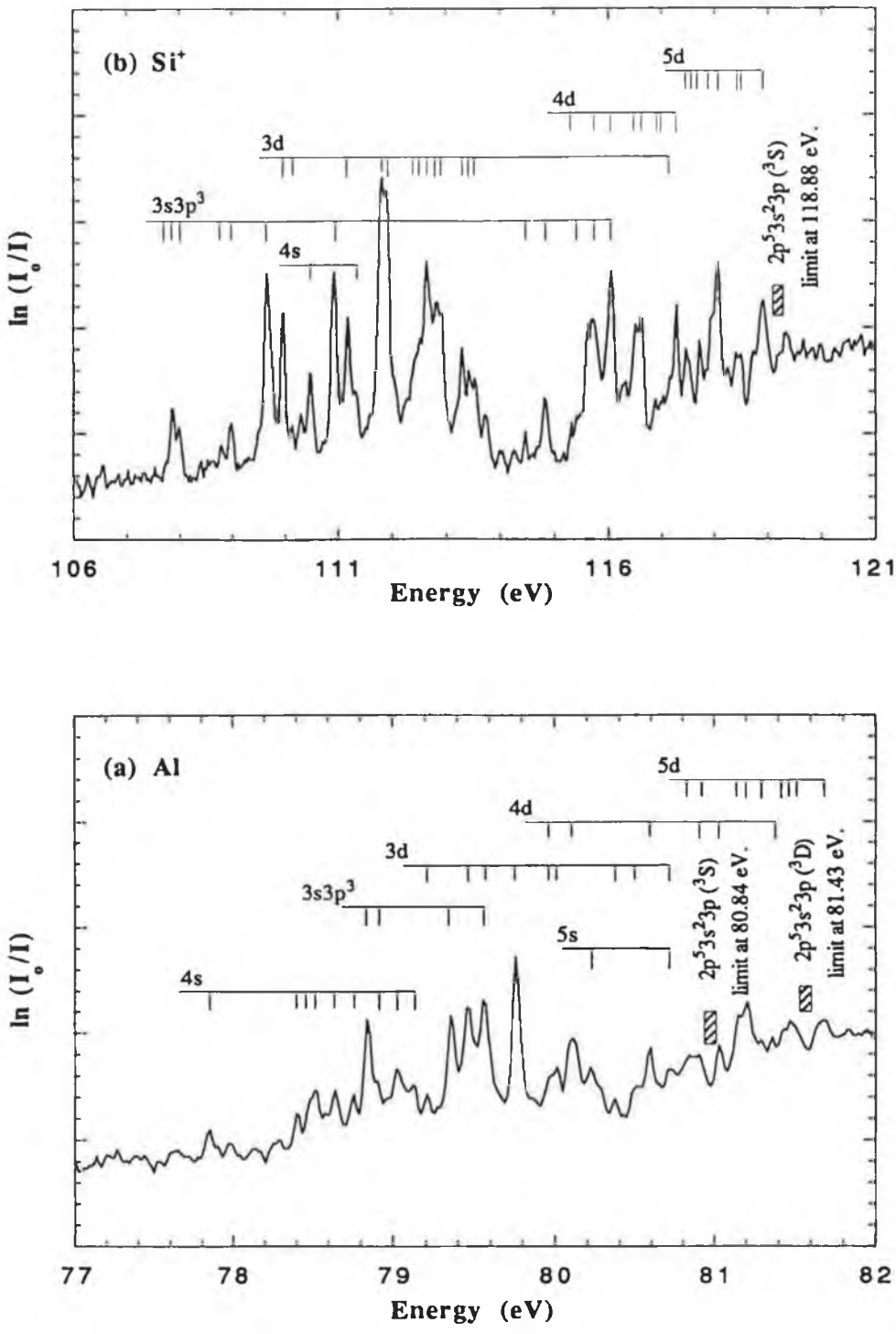

Figure 5.1

The 2p-subshell absorption in (a) atomic Al, and (b) Si^{+}. The spectra exhibit the $2p^{6}3s^{2}3p \rightarrow 2p^{5}3s^{2}3p[(n+1)s + nd] + 2p^{5}3s3p^{3}$ transitions.

excited states were only found mixed with the $2p^53s^23d$ configuration. In the 2p absorption along the aluminium sequence the situation looks quite the opposite. The spectrum of ionic Si^+ seems to be more perturbed than the corresponding spectrum of atomic aluminium. We believe that in Al I most of the doubly excited states belonging to the $2p^53s3p^3$ configuration are above the 2p threshold which is at 80.84 eV for the $2p^53s^23pnl$ resonances and only a few are present below this threshold. When we move to Si^+ more members of the doubly excited states drop below the limit which is at 118.88 eV in Si^+ and mix with the $2p^53s^23pnl$ Rydberg series members resulting in strong perturbation.

To provide an interpretation for the measured spectra we have performed scaled atomic structure calculations. The calculations, performed with the Cowan's code (chapter 2), include the $2p^63s^23p$ and $2p^63p^3$ basis states for the ground state expansion while the $2p^53s^23p[ms+nd,\ m = 4,\ 5;\ n = 3,\ 4,\ 5.]$, $2p^53s3p^3$, $2p^63s^23d$, $2p^63s3p^2$ and $2s2p^63s^23p^2$ basis states are included for the excited state expansion. To give reasonable agreement with the measured level energies the HF radial integrals $F^k(i, i)$, $F^k(i, j)$, $G^k(i, j)$, $R^k(i, j)$ and ξ_i were scaled down by 15%, 15%, 15%, 25% and 10% respectively. The results of these calculations are listed in tables 5.1-5.6.

5.3.1 The $2p^53s^23pns$ series

The configurations of the type $2p^53s^23pns$ give rise to 30 possible transitions (see table 5.1). In most of the transitions the same upper level is connected to the two lower $^2P_{1/2,3/2}$ levels. Due to the small splitting between the $^2P_{1/2}$ and $^2P_{3/2}$ levels, the transitions connecting the two ^2P levels to the same upper level are not resolvable. Out of the 30 possible transitions 26 constitute such unresolvable double transitions and the remaining four are of the type $^2P_{3/2} \rightarrow {}^{2,4}L_{5/2}$ single transitions.

In the $2p^53s^23p4s$ array, out of the 13 doubles the two doubles associated with the $(^3S)\ ^4S_{3/2}$ and $(^3D)\ ^4D_{1/2}$ terms are not allowed as they are almost pure LS-coupled both in Al and Si^+. Among the remaining 11 doubles, in aluminium

the 4 doubles associated with the $(^1P)\ ^2P_{1/2}$, $(^3P)\ ^4P_{1/2}$, $(^3P)\ ^2P_{1/2}$ and $(^1S)\ ^2S_{1/2}$ terms show negligible gf-values. Also there is a single $^2P_{3/2} \rightarrow (^3P)\ ^4P_{5/2}$ transition which shows a negligible gf-value. Therefore, we are left with 7 doubles and 3 single transitions having non-negligible gf-values. A comparison of the predicted and measured spectra are listed in table 5.1.

Almost all the features associated with the $2p^53s^23p4s$ array in Al are well resolved from the features associated with the $2p^53s^23p3d$ and $2p^53s3p^3$ configurations. However, a double and a single transition assigned to a shoulder at 78.91 eV are not resolvable. In the doubles assigned to the $(^3D)\ ^4D_{3/2}$, $(^3P)\ ^4P_{3/2}$ and $(^3P)\ ^2P_{3/2}$ terms at 78.47 eV, 79.02 eV and 79.13 eV, respectively, the upper terms could be assigned to the lower level $^2P_{3/2}$ only as the gf-values associated with the transitions arising from the $^2P_{1/2}$ level are negligible (table 5.1).

In the 5s array in Al, only the $^2P_{1/2} \rightarrow (^3D)\ ^4D_{3/2}$ and $^2P_{1/2} \rightarrow (^1P)\ ^2P_{3/2}$ transitions show non-negligible gf-values. The features predicted by these transitions (table 5.2) are observed at 80.23 eV and 80.70 eV.

In Si^+, where the 2p absorption is dominated by the strong and broad features arising from the $2p^63s^23p \rightarrow 2p^5[3s^23pnd + 3s3p^2np]$ transitions, the ns series members are predicted very weak compared to and degenerate with the strong members of the $2p^53s^23p3d$ and $2p^53s3p^3$ configurations. Only a shoulder measured at 111.34 eV could be assigned to the $^2P_{3/2} \rightarrow 4s(^3D)\ ^2D_{5/2}$ transition. This transition has also been observed as strongest in the 4s array of Al. The predicted energy of this transition is 111.38 eV and the corresponding gf-value is 0.0426. The gf-value of the remaining members are negligible (table 5.1).

The terms belonging to the $2p^53s^23p4s$ array exhibit strong mixing among themselves. However, no significant mixing was observed with the terms belonging to the $2p^53s^23pnd$ Rydberg series members or the $2p^53s3p^2np$ configuration which is analogous to the $2p^53s^2ns$ interaction with the $2p^53s^2nd$ and $2p^53s3pnp$ series along the Mg-sequence in ground state absorption (see chapter 4). In the Mg-sequence, only the $2p^53s^2nd$ and $2p^53s3pnp$ channels interact strongly. The same is observed here in the aluminium sequence where the ns series remains unperturbed. The LS-compositions of the dominant terms remain dominant in moving along the sequence with the exception of the $(^1P)\ ^2P_{3/2}$ and

(^{3}D) $^2D_{3/2}$ terms. In Si^+, these terms appear twice as they become dominant over the (^{3}P) $^4P_{3/2}$ and (^{3}P) $^2P_{3/2}$ terms respectively. The inclusion of the $2p^63s^23d$, $2p^63s3p^2$ and $2s2p^63s^23p^2$ configurations, which account for the core-polarisation effect (Hibbert, 1989) in our configuration-interaction (CI) approach, have shown no significant effect on the term energies of the $2p^53s^23pns$ series. Even the gf-values are not affected to any great extent by the addition of these configurations.

Table 5.1. Measured energies (eV), calculated energies (eV) and gf-values for the $2p^63s^23p\ ^2P \rightarrow 2p^53s^23p4s\ ^{2,4}L$ transitions in Al and Si^+.

			Al						Si+		
Term	J_i	J_f	$E_{calc.}$	$E_{meas.}$	gf	Term	J_i	J_f	$E_{calc.}$	$E_{meas.}$	gf
$(^3S)\ ^4S$	1.5	1.5	77.82		0.0001	$(^3S)\ ^4S$	1.5	1.5	110.38		0.0001
$(^3S)\ ^4S$	0.5	1.5	77.83		0.0000	$(^3S)\ ^4S$	0.5	1.5	110.40		0.0000
$(^3S)\ ^2S$	1.5	0.5	77.97	77.85	0.0048	$(^3S)\ ^2S$	1.5	0.5	110.63	110.49	0.0202
$(^3S)\ ^2S$	0.5	0.5	77.98		0.0028	$(^3S)\ ^2S$	0.5	0.5	110.66		0.0108
$(^3D)\ ^4D$	1.5	2.5	78.38	78.40	0.0042	$(^3D)\ ^4D$	1.5	2.5	111.15		0.0094
$(^3D)\ ^4D$	1.5	1.5	78.43		0.0008	$(^3D)\ ^4D$	1.5	1.5	111.24		0.0004
$(^3D)\ ^4D$	0.5	1.5	78.44	78.47	0.0046	$(^3D)\ ^4D$	0.5	1.5	111.26		0.0103
$(^3D)\ ^2D$	1.5	2.5	78.50	78.53	0.0126	$(^3D)\ ^2D$	1.5	2.5	111.38	111.34	0.0426
$(^3D)\ ^4D$	1.5	0.5	78.53		0.0002	$(^3D)\ ^4D$	1.5	0.5	111.39		0.0007
$(^3D)\ ^4D$	0.5	0.5	78.54		0.0004	$(^3D)\ ^4D$	0.5	0.5	111.42		0.0011
$(^3D)\ ^2D$	1.5	1.5	78.59		0.0031	$(^3D)\ ^2D$	1.5	1.5	111.48		0.0092
$(^3D)\ ^2D$	0.5	1.5	78.60	78.65	0.0061	$(^3D)\ ^2D$	0.5	1.5	111.51		0.0152
$(^3P)\ ^4P$	1.5	2.5	78.69		0.0013	$(^3P)\ ^4P$	1.5	2.5	111.61		0.0002
$(^3P)\ ^2P$	1.5	1.5	78.78		0.0017	$(^3P)\ ^2P$	1.5	1.5	111.76		0.0002
$(^3P)\ ^2P$	0.5	1.5	78.79	78.76	0.0020	$(^3P)\ ^2P$	0.5	1.5	111.79		0.0157
$(^1P)\ ^2P$	1.5	0.5	78.85		0.0001	$(^1P)\ ^2P$	1.5	0.5	111.85		0.0017
$(^1P)\ ^2P$	0.5	0.5	78.86		0.0002	$(^1P)\ ^2P$	0.5	0.5	111.88		0.0032
$(^1P)\ ^2P$	1.5	1.5	78.88		0.0020	$(^1P)\ ^2P$	1.5	1.5	111.88		0.0005
$(^1P)\ ^2P$	0.5	1.5	78.89	78.91	0.0044	$(^1P)\ ^2P$	0.5	1.5	111.91		0.0049
$(^1D)\ 2D$	1.5	2.5	78.93	78.91	0.0034	$(^3P)\ ^4P$	1.5	0.5	111.98		0.0005
$(^3P)\ ^4P$	1.5	0.5	78.95		0.0009	$(^1D)\ ^2D$	1.5	2.5	111.98		0.0000
$(^3P)\ ^4P$	0.5	0.5	78.96		0.0019	$(^3P)\ ^4P$	0.5	0.5	112.00		0.0018
$(^3P)\ ^4P$	1.5	1.5	78.99	79.02	0.0053	$(^1P)\ ^2P$	1.5	1.5	112.05		0.0015
$(^3P)\ ^4P$	0.5	1.5	79.00		0.0016	$(^1P)\ ^2P$	0.5	1.5	112.08		0.0143
$(^3P)\ ^2P$	1.5	1.5	79.06	79.13	0.0054	$(^3D)\ ^2D$	1.5	1.5	112.22		0.0102
$(^3P)\ ^2P$	0.5	1.5	79.07		0.0000	$(^3D)\ ^2D$	0.5	1.5	112.25		0.0894
$(^3P)\ ^2P$	1.5	0.5	79.13		0.0007	$(^3P)\ ^2P$	1.5	0.5	112.28		0.0009
$(^3P)\ ^2P$	0.5	0.5	79.14		0.0001	$(^3P)\ ^2P$	0.5	0.5	112.31		0.0000
$(^1S)\ ^2S$	1.5	0.5	81.72		0.0006	$(^1S)\ ^2S$	1.5	0.5	115.98		0.0003
$(^1S)\ ^2S$	0.5	0.5	81.73		0.0006	$(^1S)\ ^2S$	0.5	0.5	116.01		0.0001

Table 5.2. Measured energies (eV), calculated energies (eV) and gf-values for the $2p^63s^23p\ ^2P \rightarrow 2p^53s^23p5s\ ^{2,4}L$ transitions in Al and Si^+.

			Al						Si+		
Term	J_i	J_f	$E_{calc.}$	Emeas.	gf	Term	J_i	J_f	$E_{calc.}$	$E_{meas.}$	gf
$(^3S)\ ^4S$	1.5	1.5	79.62		0.0002	$(^3S)\ ^4S$	1.5	1.5	114.82		0.0000
$(^3S)\ ^4S$	0.5	1.5	79.63		0.0000	$(^3S)\ ^4S$	0.5	1.5	114.85		0.0000
$(^3D)\ ^4D$	1.5	2.5	80.16		0.0006	$(^3S)\ ^2S$	1.5	0.5	114.91		0.0017
$(^3D)\ ^4D$	1.5	1.5	80.22		0.0002	$(^3S)\ ^2S$	0.5	0.5	114.94		0.0013
$(^3D)\ ^4D$	1.5	2.5	80.23		0.0001	$(^3D)\ ^4D$	1.5	2.5	115.58		0.0057
$(^3D)\ ^4D$	0.5	1.5	80.24	80.23	0.0020	$(^3D)\ ^4D$	1.5	1.5	115.66		0.0011
$(^3D)\ ^4D$	1.5	0.5	80.34		0.0003	$(^3D)\ ^2D$	1.5	2.5	115.68		0.0047
$(^3D)\ ^4D$	0.5	0.5	80.35		0.0003	$(^3D)\ ^4D$	0.5	1.5	115.69		0.0036
$(^3D)\ ^2D$	1.5	1.5	80.36		0.0012	$(^3D)\ ^4D$	1.5	0.5	115.83		0.0003
$(^3D)\ ^2D$	0.5	1.5	80.37		0.0013	$(^3D)\ ^4D$	0.5	0.5	115.86		0.0008
$(^3P)\ ^4P$	1.5	2.5	80.49		0.0002	$(^3D)\ ^2D$	1.5	1.5	115.87		0.0004
$(^1D)\ ^2D$	1.5	1.5	80.51		0.0000	$(^3D)\ ^2D$	0.5	1.5	115.90		0.0052
$(^1D)\ ^2D$	0.5	1.5	80.52		0.0000	$(^3P)\ ^4P$	1.5	2.5	116.05		0.0013
$(^1P)\ ^2P$	1.5	0.5	80.66		0.0003	$(^3P)\ ^2P$	1.5	1.5	116.10		0.0035
$(^1P)\ ^2P$	0.5	0.5	80.67		0.0007	$(^3P)\ ^2P$	0.5	1.5	116.13		0.0011
$(^1P)\ ^2P$	1.5	1.5	80.67		0.0000	$(^1P)\ ^2P$	1.5	0.5	116.28		0.0015
$(^1P)\ ^2P$	0.5	1.5	80.68	80.70	0.0035	$(^1P)\ ^2P$	1.5	1.5	116.31		0.0000
$(^3P)\ ^4P$	1.5	2.5	80.74		0.0013	$(^1P)\ ^2P$	0.5	0.5	116.31		0.0020
$(3P)\ ^4P$	1.5	0.5	80.75		0.0000	$(^1P)\ ^2P$	0.5	1.5	116.34		0.0002
$(^3P)\ ^4P$	0.5	0.5	80.76		0.0018	$(^1D)\ ^2D$	1.5	2.5	116.42		0.0023
$(^3P)\ ^4P$	1.5	0.5	80.77		0.0001	$(^3P)\ ^4P$	1.5	0.5	116.43		0.0013
$(^3P)\ ^2P$	1.5	1.5	80.77		0.0014	$(^3P)\ ^4P$	0.5	0.5	116.46		0.0028
$(^3P)\ ^4P$	0.5	0.5	80.78		0.0001	$(^1D)\ ^2D$	1.5	1.5	116.48		0.0000
$(^3P)\ ^2P$	0.5	1.5	80.79		0.0001	$(^3P)\ ^2P$	1.5	1.5	116.51		0.0031
$(^3P)\ ^4P$	1.5	1.5	80.80		0.0013	$(^1D)\ ^2D$	0.5	1.5	116.51		0.0015
$(^3P)\ ^4P$	0.5	1.5	80.81		0.0006	$(^3P)\ ^2P$	0.5	1.5	116.53		0.0000
$(^3P)\ ^2P$	1.5	0.5	80.84		0.0004	$(^3P)\ ^2P$	1.5	0.5	116.57		0.0006
$(^3P)\ ^2P$	0.5	0.5	80.85		0.0003	$(^3P)\ ^2P$	0.5	0.5	116.60		0.0001
$(^1S)\ ^2S$	1.5	0.5	83.53		0.0003	$(^1S)\ ^2S$	1.5	0.5	120.40		0.0005
$(^1S)\ ^2S$	0.5	0.5	83.54		0.0002	$(^1S)\ ^2S$	0.5	0.5	120.43		0.0004

5.3.2 Transitions to the $2p^5 3s 3p^3$ array

In Al I the terms of the $2p^5 3s 3p^3$ array are smeared out over the entire Rydberg series members and throughout the continuum. Among the 73 possible transitions (table 5.3) associated with this array the energies of 46 transitions are predicted above the $2p^5 3s^2 3p$ (^3S) edge. Out of these 46 transitions in 32 transitions the upper term is ^2L. However, out of the remaining 27 transitions which are predicted below the 2p-limit only 5 transitions have the upper terms of the type ^2L.

The 27 transitions predicted below the $2p^5 3s^2 3p$ (^3S) edge include 11 unresolvable doubles and 5 single transitions. The 7 doubles with upper terms (^4S) $^4P_{1/2,3/2}$, (^2D) $^4D_{1/2,3/2}$, (^2D) $^4F_{3/2}$, (^2P) $^4S_{3/2}$, (^2P) $^4P_{1/2}$ and (^2D) $^4D_{3/2}$ show negligible gf-values. The 4 single transitions having the upper terms (^4S) $^4P_{5/2}$, (^2D) $^4D_{5/2}$, (^2D) $^4F_{5/2}$ and (^2D) $^4F_{5/2}$ also show negligible gf-values. Thus in Al we are left with 3 doubles and one single transition having non-negligible gf-values. These transitions are associated with the (^2D) $^2P_{3/2}$, (^2D) $^2P_{1/2}$, (^2P) $^4D_{1/2}$ and (^2D) $^4P_{5/2}$ upper terms. In our absorption measurements all of these four predicted structures are observed (Figure 6.1). Their assignment is listed in table 5.3. The two doubles assigned to the (^2D) $^2P_{3/2}$ and (^2D) $^2P_{1/2}$ terms, are not resolvable. The same is observed for a feature assigned to the (^2D) $^4D_{1/2}$ term which is degenerate with a very strong and broad structure measured at 79.58 eV. However, a very strong feature measured at 79.37 eV assigned to the (^2D) $^4P_{5/2}$ term is well resolved.

The Si^+ spectrum looks quite different from its isoelectronic partner Al I. It exhibits relatively much more strong features which are divided into sharp and broad structures. The reason is that in Si^+ the whole $2p^5 3s 3p^3$ array drops below the 2p-threshold and gives rise to a number of strong and sharp absorption structures.

In Si^+ there are 12 transitions connected with the upper terms of the type $^4L_{1/2}$, 16 transitions connected with the $^4L_{3/2}$ terms and 7 transitions connected with the $^4L_{5/2}$ terms. Thus we are left with 38 transitions connected with the upper terms of the type ^2L. In Si^+, all these 38 transitions are predicted below the 2p-

threshold. The $^4L_{1/2,3/2}$ terms in Si^+ are not mixed with ^2L terms to any great extent. Consequently, all the doubles connected with upper quartet terms show negligible gf-values. Among the 7 single transitions only the 2 transitions connected with the $(^2P)\ ^4D_{5/2}$ and $(^2P)\ ^4P_{5/2}$ terms show non-negligible gf-values.The 38 transitions which are connected with the upper terms of the type ^2L include 16 unresolvable doubles and 6 single transitions.

In table 5.3 we show a comparison of calculated and measured spectra both for Al and Si^+. The inspection of LS-compositions showed that, in moving from Al to ionic Si^+, most of the dominant terms remained dominant in their LS-compositions along the sequence. But the strong transitions in Al are no longer strong in Si^+ (see table 5.3).

In Al the lower energy region is dominated by the $2p^53s^23p4s$ array. However, in Si^+ it is dominated by the members of the $2p^53s3p^3$ configuration. In moving from Al to Si^+ level crossing of the $2p^53s3p^3$ array takes place with respect to the ns and nd series. Also the level crossing of the nd series occurs with respect to the ns series. Consequently, most of the weak members of the 3s array become degenerate with the strong members of the 3d array. The level crossing of the $2p^53s3p^3$ configuration and the $2p^53s^23pnd$ series with respect to the $2p^53s^23pns$ series has no significant effect on the level structure. However, the level crossing of the members of the $2p^53s3p^3$ array with respect to the $2p^53s3p^3nd$ series gives rise to a number of irregularities along the sequence. The strong features exhibited by the $2p^53s3p^3$ array in Si^+ are associated with the terms which were above the $2p^53s^23p\ (^3S)$ edge in Al.

Table 5.3. Measured energies (eV), calculated energies (eV) and gf-values for the $2p^6 3s^2\ ^2P \rightarrow 2p^5 3s 3p^3\ ^{2,4}L$ transitions in Al and Si^+.

Al						Si^+					
Term	J_i	J_f	$E_{calc.}$	$E_{meas.}$	gf	Term	J_i	J_f	$E_{calc.}$	$E_{meas.}$	gf
$(^4S)\ ^4P$	1.5	0.5	76.83		0.0000	$(^4S)\ ^4P$	1.5	0.5	105.38		0.0000
$(^4S)\ ^4P$	0.5	0.5	76.84		0.0000	$(^4S)\ ^4P$	0.5	0.5	105.41		0.0000
$(^4S)\ ^4P$	1.5	1.5	76.93		0.0000	$(^4S)\ ^4P$	1.5	1.5	105.53		0.0000
$(^4S)\ ^4P$	0.5	1.5	76.94		0.0000	$(^4S)\ ^4P$	0.5	1.5	105.56		0.0000
$(^4S)\ ^4P$	1.5	2.5	77.05		0.0000	$(^4S)\ ^4P$	1.5	2.5	105.71		0.0000
$(^2D)\ ^4D$	1.5	2.5	78.35		0.0013	$(^2D)\ ^4D$	1.5	2.5	107.28		0.0002
$(^2D)\ ^4D$	1.5	1.5	78.38		0.0008	$(^2D)\ ^4D$	1.5	1.5	107.32		0.0039
$(^2D)\ ^4D$	0.5	1.5	78.40		0.0007	$(^2D)\ ^4D$	1.5	0.5	107.34		0.0012
$(^2D)\ ^4D$	1.5	0.5	78.40		0.0004	$(^2D)\ ^4D$	0.5	1.5	107.35		0.0004
$(^2D)\ ^4D$	0.5	0.5	78.41		0.0008	$(^2D)\ ^4D$	0.5	0.5	107.37		0.0028
$(^2D)\ ^4F$	1.5	2.5	78.67		0.0002	$(^2D)\ ^4F$	1.5	2.5	107.66		0.0001
$(^2D)\ ^4F$	1.5	1.5	78.75		0.0004	$(^2D)\ ^4F$	1.5	1.5	107.79	107.77	0.0104
$(^2D)\ ^4F$	0.5	1.5	78.76		0.0010	$(^2D)\ ^4F$	0.5	1.5	107.81		0.0068
$(^2D)\ ^2P$	1.5	1.5	78.83	78.84	0.0131	$(^2D)\ ^2P$	1.5	1.5	107.88	107.89	0.0248
$(^2D)\ ^2P$	0.5	1.5	78.84		0.0017	$(^2D)\ ^2P$	0.5	1.5	107.90		0.0044
$(^2D)\ ^2P$	1.5	0.5	78.90		0.0033	$(^2D)\ ^2P$	1.5	0.5	107.96		0.0058
$(^2D)\ ^2P$	0.5	0.5	78.91	78.91	0.0076	$(^2D)\ ^2P$	0.5	0.5	107.98	108.01	0.0135
$(^2D)\ ^2F$	1.5	2.5	78.99		0.0002	$(^2D)\ ^2F$	1.5	2.5	108.14		0.0010
$(^2P)\ ^4S$	1.5	1.5	79.24		0.0000	$(^2P)\ ^4S$	1.5	1.5	108.65		0.0001
$(^2P)\ ^4S$	0.5	1.5	79.25		0.0000	$(^2P)\ ^4S$	0.5	1.5	108.68		0.0000
$(^2D)\ ^4P$	1.5	2.5	79.32	79.37	0.0082	$(^2D)\ ^4P$	1.5	0.5	108.76		0.0000
$(^2P)\ ^4D$	1.5	0.5	79.63	79.58	0.0077	$(^2D)\ ^4P$	0.5	0.5	108.79		0.0001
$(^2P)\ ^4D$	0.5	0.5	79.64		0.0027	$(^2P)\ ^4D$	1.5	2.5	108.86	108.79	0.0142
$(^2P)\ ^4P$	1.5	0.5	79.66		0.0012	$(^2D)\ ^4P$	1.5	1.5	108.86		0.0003
$(^2P)\ ^4P$	0.5	0.5	79.68		0.0002	$(^2D)\ ^4P$	0.5	1.5	108.89		0.0036
$(^2D)\ ^4D$	1.5	1.5	80.48		0.0002	$(^2P)\ ^4D$	1.5	2.5	108.89		0.0033
$(^2D)\ ^4D$	0.5	1.5	80.49		0.0003	$(^2P)\ ^4D$	1.5	1.5	108.99		0.0016
$(^2P)\ ^4P$	1.5	2.5	81.33		0.0004	$(^2P)\ ^4D$	0.5	1.5	109.02		0.0052
$(^2P)\ ^4P$	1.5	0.5	81.36		0.0002	$(^2P)\ ^4D$	1.5	0.5	109.13		0.0000
$(^2P)\ ^4P$	0.5	0.5	81.37		0.0002	$(^2D)\ ^2D$	1.5	1.5	109.13		0.0134
$(^2P)\ ^4P$	1.5	1.5	81.37		0.0002	$(^2P)\ ^4D$	0.5	0.5	109.15		0.0001
$(^2P)\ ^4P$	0.5	1.5	81.38		0.0002	$(^2D)\ ^2D$	1.5	2.5	109.15	109.02	0.0228
$(^2D)\ ^4P$	1.5	1.5	81.70	81.65	0.0034	$(^2D)\ ^2D$	0.5	1.5	109.16		0.0124
$(^2D)\ ^4P$	0.5	1.5	81.71		0.0000	$(^2P)\ ^4P$	1.5	2.5	109.46		0.0038
$(^2P)\ ^2D$	1.5	2.5	81.73		0.0000	$(^2P)\ ^4P$	1.5	1.5	109.51		0.0004

Continued

Table 5.3. Continued

Al						Si+					
Term	J_i	J_f	$E_{calc.}$	Emeas.	gf	Term	J_i	J_f	$E_{calc.}$	$E_{meas.}$	gf
$(^2D)\ ^4P$	1.5	2.5	81.75		0.0002	$(^2P)\ ^4P$	0.5	1.5	109.53		0.0030
$(^2P)\ ^2P$	1.5	0.5	81.76		0.0001	$(^2P)\ ^4P$	1.5	0.5	109.66		0.0005
$(^2P)\ ^2P$	0.5	0.5	81.77		0.0006	$(^2P)\ ^4P$	0.5	0.5	109.69		0.0006
$(^2P)\ ^2P$	1.5	1.5	81.77		0.0004	$(^2P)\ ^2D$	1.5	1.5	109.70		0.0017
$(^2P)\ ^2P$	0.5	1.5	81.78		0.0002	$(^2P)\ ^2D$	0.5	1.5	109.73	109.68	0.0119
$(^2P)\ ^2S$	1.5	0.5	82.26		0.0014	$(^2P)\ ^4P$	1.5	0.5	109.74		0.0045
$(^2P)\ ^2S$	0.5	0.5	82.27		0.0010	$(^2P)\ ^4P$	1.5	2.5	109.77		0.0230
$(^4S)\ ^2P$	1.5	0.5	83.02		0.0001	$(^2P)\ ^4P$	0.5	0.5	109.77		0.0023
$(^4S)\ ^2P$	0.5	0.5	83.03		0.0001	$(^2P)\ ^4P$	1.5	1.5	109.86		0.0002
$(^4S)\ ^2P$	1.5	1.5	83.10		0.0007	$(^2P)\ ^4P$	0.5	1.5	109.89		0.0001
$(^4S)\ ^2P$	0.5	1.5	83.11		0.0000	$(^2P)\ ^2S$	1.5	0.5	110.89	110.96	0.1001
$(^4S)\ ^4P$	1.5	2.5	83.22		0.0000	$(^2P)\ ^2S$	0.5	0.5	110.92		0.0470
$(^2D)\ ^2F$	1.5	2.5	83.40		0.0009	$(^4S)\ ^4P$	1.5	2.5	113.47		0.0010
$(^4S)\ ^4P$	1.5	1.5	83.46		0.0000	$(^4S)\ ^4P$	1.5	1.5	113.64		0.0061
$(^4S)\ ^4P$	0.5	1.5	83.47		0.0002	$(^4S)\ ^4P$	0.5	1.5	113.67		0.0008
$(^4S)\ 4P$	1.5	0.5	83.56		0.0000	$(^2D)\ ^2P$	1.5	0.5	113.68		0.0000
$(^4S)\ ^4P$	0.5	0.5	83.57		0.0000	$(^2D)\ ^2P$	0.5	0.5	113.70	113.73	0.0064
$(^2D)\ ^2D$	1.5	2.5	83.68		0.0032	$(^4S)\ ^4P$	1.5	1.5	113.99	114.00	0.0074
$(^2D)\ ^2D$	1.5	1.5	83.68		0.0001	$(^4S)\ ^4P$	1.5	0.5	114.01		0.0001
$(^2D)\ ^2D$	0.5	1.5	83.69		0.0024	$(^4S)\ ^4P$	0.5	1.5	114.02		0.0003
$(^2P)\ ^2D$	1.5	2.5	83.95		0.0000	$(^4S)\ ^4P$	0.5	0.5	114.04		0.0009
$(^2D)\ ^2D$	1.5	1.5	84.03		0.0000	$(^2D)\ ^2D$	1.5	1.5	114.50		0.0000
$(^2D)\ ^2D$	0.5	1.5	84.04		0.0019	$(^2D)\ ^2D$	0.5	1.5	114.53	114.47	0.0110
$(^2P)\ ^2D$	1.5	2.5	84.13		0.0064	$(^2D)\ ^2D$	1.5	2.5	114.65		0.0115
$(^2P)\ ^2P$	1.5	1.5	84.21		0.0001	$(^2P)\ ^2D$	1.5	2.5	114.94	114.94	0.0302
$(^2P)\ ^2P$	0.5	1.5	84.22		0.0012	$(^2P)\ ^2P$	1.5	1.5	115.14		0.0059
$(^2P)\ ^2P$	1.5	0.5	84.30		0.0025	$(^2P)\ ^2P$	0.5	1.5	115.17		0.0021
$(^2P)\ ^2P$	1.5	1.5	84.31		0.0005	$(^2P)\ ^2S$	1.5	0.5	115.26		0.0000
$(^2P)\ ^2P$	0.5	0.5	84.31		0.0005	$(^2P)\ ^2S$	0.5	0.5	115.28		0.0004
$(^2P)\ ^2P$	0.5	1.5	84.32		0.0004	$(^2P)\ ^2D$	1.5	1.5	115.42		0.0025
$(^2P)\ ^2D$	1.5	1.5	84.54		0.0032	$(^2P)\ ^2D$	0.5	1.5	115.45		0.0059
$(^2P)\ ^2D$	0.5	1.5	84.55		0.0044	$(^4S)\ ^2P$	1.5	0.5	115.50		0.0066
$(^2P)\ ^2S$	1.5	0.5	84.67		0.0009	$(^4S)\ ^2P$	0.5	0.5	115.53	115.43	0.0133
$(^2P)\ ^2S$	0.5	0.5	84.69		0.0075	$(^4S)\ ^2P$	1.5	1.5	115.79	115.75	0.0749
$(^4S)\ ^2P$	1.5	0.5	85.00		0.0058	$(^4S)\ ^2P$	0.5	1.5	115.82		0.0045
$(^4S)\ ^2P$	0.5	0.5	85.01		0.0034	$(^2D)\ ^2D$	1.5	2.5	116.11	116.05	0.0384
$(^4S)\ ^2P$	1.5	1.5	85.03		0.0202	$(^4S)\ ^2P$	1.5	0.5	116.52		0.0005
$(^4S)\ ^2P$	0.5	1.5	85.04		0.0041	$(^4S)\ ^2P$	0.5	0.5	116.55		0.0010

5.3.3 The $2p^53s^23pnd$ series

The $2p^53s^23pnd$ Rydberg series members are mixed with the $2p^53s3p^3$ $^{2,4}L$ doubly excited states. In Al because of the spreading nature of the $2p^53s3p^3$ configuration the $2p^53s3p^3$ and $2p^53s^23pnd$ mixing is relatively dilute. In Si^+, as the whole $2p^53s3p^3$ array drops below the 2p-threshold a number of its terms become degenerate with the $2p^53s^23pnd$ Rydberg series members and result in relatively more interaction with the Rydberg series members. Consequently, it makes the calculations more difficult for the Si^+ than the less perturbed Al I spectrum. In particular, the interaction between the $2p^53s^23p3d$ and $2p^53s3p^3$ configurations is found to be very strong.

Among the 76 predicted possible transitions associated with arrays of the type $2p^53s^23pnd$ $^{2,4}L$, 58 transitions constitute 29 unresolvable doubles and the remaining 18 single transitions. In the 2p absorption spectrum of Al I all the strongest features exhibit the transitions to the strongly mixed $2p^53s3p^3$ and $2p^53s^23p3d$ configurations. Out of the 29 doubles only 13 doubles, assigned to the $(^3D)\ ^4P_{3/2}$, $(^3D)\ ^2P_{1/2}$, $(^1D)\ ^2D_{3/2}$, $(^3D)\ ^2P_{3/2}$, $(^3D)\ ^4P_{1/2}$, $(^3D)\ ^2P_{3/2}$, $(^3D)\ ^4P_{3/2}$, $(^1D)\ ^2D_{3/2}$, $(^3D)\ ^2S_{1/2}$, $(^1D)\ ^2P_{3/2}$, $(^1D)\ ^2S_{1/2}$, $(^1D)\ ^2P_{3/2}$ and $(^3P)\ ^4D_{3/2}$ terms, exhibit transitions having non-negligible gf-values. Among the remaining 18 are single transitions in which the upper term is associated with J values 5/2 only the 7 transitions, assigned to the $(^3S)\ ^2D$, $(^3P)\ ^4D$, $(^3P)\ ^4P$, $(^3D)\ ^4P$, $(^3P)\ ^4D$, $(^1P)\ ^2D$ and $(^3P)\ ^4P$ terms, show non-negligible gf-values. A strong feature observed at 79.47 eV could be assigned to the two doubles and one single transition associated with the $(^3D)\ ^2P_{1/2}$, $(^1D)\ ^2P_{3/2}$ and $(^3P)\ ^4D_{5/2}$ terms as the predicted values for these terms are 79.47±0.1 eV. A double and a single transition assigned to a strong feature at 79.58 eV is also not resolvable.

In moving from neutral Al to ionic Si^+ dramatic changes occur both in the measured and computed spectra. With the exception of a few terms, having negligible gf-values both in Al and Si^+, almost all the terms change their relative positions (table 5.4). We believe that in Si^+, the whole $2p^53s^23p3d$ $^{2,4}L$ array is strongly perturbed by the doubly excited $2p^53s3p^3$ states. Also in Si^+ the change in LS-composition results in the flipping of most of the terms. The unique

assignment of such a strongly perturbed Rydberg series is meaningless, therefore, here we can provide only tentative assignments.

In Si^+, for the $2p \rightarrow 3d$ transitions, there are 19 unresolvable doubles and 7 single transitions which show negligible values. These doubles and single transitions are associated with the $(^3P)\ ^2P_{1/2}$, $(^3S)\ ^4D_{1/2}$, $(^3S)\ ^4D_{3/2}$, $(^1P)\ ^2D_{3/2}$, $(^3P)\ ^4F_{3/2}$, $(^3D)\ ^2D_{3/2}$, $(^3D)\ ^4S_{3/2}$, $(^1D)\ ^2S_{1/2}$, $(^3D)\ ^2P_{3/2}$, $(^3D)\ ^4D_{3/2}$, $(^3D)\ ^4D_{1/2}$, $(^3D)\ ^4P_{1/2}$, $(^3D)\ ^4P_{1/2}$, $(^3D)\ ^4P_{3/2}$, $(^1D)\ ^2P_{3/2}$, $(^3D)\ ^4D_{1/2}$, $(^3D)\ ^4D_{3/2}$, $(^1D)\ ^2D_{3/2}$, $(^1P)\ 2P_{1/2}$, $(^1P)\ ^2P_{3/2}$, $(^3D)\ ^2S_{1/2}$, $(^1S)\ ^2D_{3/2}$, $(^1P)\ ^2D_{5/2}$, $(^3P)\ ^4F_{5/2}$, $(^3D)\ ^2D_{5/2}$, $(^3D)\ ^4D_{5/2}$, $(^3P)\ ^2D_{5/2}$, $(^3S)\ ^2D_{5/}2$, $(^1D)\ ^2D_{5/2}$, $(^1D)\ ^2D_{5/2}$ and $(^3P)\ ^2F_{5/2}$ upper terms. Their measured energies, calculated energies and gf-values are listed in table 6.4.

The absorption structures observed above 80.00 eV and 115.00 eV are dominated by the $2p^63s^23p \rightarrow 2p^53s^23pn(= 4 \text{ and } 5)d + 2p^53s3p^3$ transitions both in Al and Si^+. The features assigned to the 4d and 5d Rydberg series members are listed in tables 5.5 and 5.6 respectively.

The inclusion of the $2p^63s^23d$ and $2p^63s3p^2$ configurations in the excited state expansion was found to enhance the gf-values of some members of the $2p^53s3p^3$ configuration and the $2p^53s^23pnd$ series very prominently. While the inclusion of $2s2p^63s^23p^2$ configuration leads to redistribution of oscillator strength. Consequently, brings the calculated gf-values in a better visual agreement with the measured spectra.

Table 5.4. Measured energies (eV), calculated energies (eV) and gf-values for the $2p^63s^23p\ ^2P \rightarrow 2p^53s^23p3d\ ^{2,4}L$ transitions in Al and Si^+.

			Al						Si+		
Term	J_i	J_f	$E_{calc.}$	$E_{meas.}$	gf	Term	J_i	J_f	$E_{calc.}$	$E_{meas.}$	gf
$(^3S)\ ^2D$	1.5	2.5	78.93	78.91	0.0033	$(^3P)\ ^2P$	1.5	0.5	110.05		0.0250
$(^3S)\ ^2D$	1.5	1.5	79.00		0.0005	$(^3P)\ ^2P$	0.5	0.5	110.08		0.0536
$(^3S)\ ^2D$	0.5	1.5	79.01		0.0002	$(^3D)\ ^2F$	1.5	2.5	110.16		0.0001
$(^3S)\ ^4D$	1.5	1.5	79.13		0.0003	$(^3S)\ ^4D$	1.5	0.5	110.25		0.0001
$(^3S)\ ^4D$	1.5	2.5	79.13		0.0003	$(^3P)\ ^2P$	1.5	1.5	110.27	109.98	0.0591
$(^3S)\ ^4D$	1.5	0.5	79.14		0.0000	$(^3S)\ ^4D$	0.5	0.5	110.28		0.0002
$(^3S)\ ^4D$	0.5	1.5	79.14		0.0000	$(^3S)\ ^4D$	1.5	1.5	110.30		0.0158
$(^3S)\ ^4D$	0.5	0.5	79.15		0.0002	$(^3P)\ ^2P$	0.5	1.5	110.30		0.0270
$(^3P)\ ^4P$	1.5	0.5	79.22		0.0002	$(^3S)\ ^4D$	0.5	1.5	110.32		0.0173
$(^3P)\ ^4P$	0.5	0.5	79.23		0.0002	$(^3S)\ ^4D$	1.5	2.5	110.36		0.0029
$(^3D)\ ^4P$	1.5	1.5	79.28		0.0005	$(^1P)\ ^2D$	1.5	2.5	110.61	110.49	0.0702
$(^3D)\ ^4P$	0.5	1.5	79.29	79.21	0.0021	$(^1P)\ ^2D$	1.5	1.5	110.66		0.0645
$(^3D)\ ^2P$	1.5	0.5	79.46		0.0061	$(^1P)\ ^2D$	0.5	1.5	110.69		0.0173
$(^3D)\ ^2P$	0.5	0.5	79.47	79.47	0.0116	$(^3D)\ ^4G$	1.5	2.5	110.81		0.0001
$(^1D)\ ^2D$	1.5	1.5	79.47		0.0034	$(^3P)\ ^4F$	1.5	1.5	111.27		0.0006
$(^3P)\ ^4D$	1.5	2.5	79.47	79.47	0.0082	$(^3P)\ ^4F$	0.5	1.5	111.30		0.0112
$(^1D)\ ^2D$	0.5	1.5	79.48	79.47	0.0166	$(^3P)\ ^4F$	1.5	2.5	111.31	111.19	0.0339
$(^3P)\ ^4P$	1.5	2.5	79.53	79.47	0.0080	$(^1P)\ ^2F$	1.5	2.5	111.42		0.0003
$(^3D)\ ^4G$	1.5	2.5	79.56		0.0000	$(^3D)\ ^2D$	1.5	2.5	112.02	111.80	0.3782
$(^3D)\ ^2P$	1.5	1.5	79.56		0.0013	$(^3D)\ ^2D$	1.5	1.5	112.12		0.0493
$(^3D)\ ^2P$	0.5	1.5	79.57		0.0059	$(^3D)\ ^2D$	0.5	1.5	112.15	111.91	0.1279
$(^3D)\ ^4P$	1.5	0.5	79.58		0.0013	$(^3D)\ ^4S$	1.5	1.5	112.46		0.0079
$(^3D)\ ^4P$	0.5	0.5	79.60		0.0034	$(^3D)\ ^4S$	0.5	1.5	112.49		0.0029
$(^3D)\ ^4G$	1.5	2.5	79.60		0.0005	$(^1D)\ ^2S$	1.5	0.5	112.60		0.0017
$(^3D)\ ^2P$	1.5	1.5	79.61	79.58	0.0248	$(^1D)\ ^2S$	0.5	0.5	112.63		0.0115
$(^3D)\ ^2P$	0.5	1.5	79.62		0.0003	$(^3P)\ ^4D$	1.5	2.5	112.64		0.0030
$(^3D)\ ^4P$	1.5	2.5	79.64		0.0304	$(^3D)\ ^2P$	1.5	1.5	112.68	112.43	0.0287
$(^3D)\ ^4P$	1.5	1.5	79.68		0.0009	$(^3P)\ ^4D$	1.5	1.5	112.70		0.0183
$(^3D)\ ^4P$	0.5	1.5	79.69		0.0068	$(^3D)\ ^2P$	0.5	1.5	112.71	112.53	0.0355
$(^3D)\ ^4F$	1.5	1.5	79.79		0.0000	$(^3D)\ ^4P$	1.5	2.5	112.72		0.0000
$(^1P)\ ^2P$	1.5	0.5	79.80		0.0008	$(^3P)\ ^4D$	0.5	1.5	112.73		0.0043
$(^3D)\ ^4F$	0.5	1.5	79.80		0.0001	$(^3D)\ ^4D$	1.5	0.5	112.74		0.0085
$(^3D)\ ^2D$	1.5	2.5	79.81	79.75	0.0003	$(^3D)\ ^4D$	0.5	0.5	112.76		0.0144
$(^1P)\ ^2P$	0.5	0.5	79.81		0.0005	$(^3D)\ ^4P$	1.5	0.5	112.79		0.0104
$(^3D)\ ^4F$	1.5	2.5	79.82		0.0000	$(^3D)\ ^4P$	0.5	0.5	112.82		0.0126
$(^1D)\ ^2D$	1.5	1.5	79.85		0.0051	$(^3D)\ ^4D$	1.5	2.5	112.83	112.65	0.0202
$(^1D)\ ^2D$	0.5	1.5	79.86		0.0011	$(^3D)\ ^4P$	1.5	1.5	112.83		0.0019

Continued

Table 5.4. Continued

Al						Si^+					
Term	J_i	J_f	$E_{calc.}$	$E_{meas.}$	gf	Term	J_i	J_f	$E_{calc.}$	$E_{meas.}$	gf
$(^3D)\,^4P$	1.5	1.5	79.87		0.0000	$(^3D)\,^4P$	0.5	1.5	112.86		0.0038
$(^3D)\,^4P$	0.5	1.5	79.89		0.0005	$(^1P)\,^2D$	1.5	1.5	112.92		0.0024
$(^3D)\,^4G$	1.5	2.5	79.94		0.0005	$(^3D)\,^4P$	1.5	0.5	112.95		0.0066
$(^3P)\,^4D$	1.5	2.5	79.96	79.97	0.0030	$(^1P)\,^2D$	0.5	1.5	112.95		0.0002
$(^3D)\,^2S$	1.5	0.5	79.96	80.01	0.0091	$(^3P)\,^2D$	1.5	2.5	112.97		0.0491
$(^3D)\,^2S$	0.5	0.5	79.98	80.01	0.0034	$(^3D)\,^4P$	0.5	0.5	112.98		0.0255
$(^1P)\,^2D$	1.5	1.5	80.00	80.01	0.0033	$(^3D)\,^4P$	1.5	1.5	113.04	112.84	0.0640
$(^1P)\,^2D$	0.5	1.5	80.01	80.01	0.0055	$(^3D)\,^4F$	1.5	2.5	113.07		0.0051
$(^1P)\,2D$	1.5	2.5	80.01	80.01	0.0020	$(^3D)\,^4P$	0.5	1.5	113.07		0.0026
$(^1D)\,^2S$	1.5	0.5	80.13		0.0019	$(^1D)\,^2P$	1.5	1.5	113.09	112.94	0.0539
$(^1D)\,^2S$	0.5	0.5	80.15		0.0023	$(^1D)\,^2P$	0.5	1.5	113.12		0.0205
$(^3D)\,^2P$	1.5	1.5	80.16		0.0003	$(^3D)\,^2P$	1.5	0.5	113.16		0.0027
$(^3D)\,^2P$	0.5	1.5	80.18		0.0014	$(^3D)\,^2P$	0.5	0.5	113.18		0.0010
$(^3D)\,^4D$	1.5	2.5	80.19		0.0003	$(^3S)\,^2D$	1.5	2.5	113.24		0.0148
$(^3D)\,^4D$	1.5	0.5	80.20		0.0010	$(^3D)\,^4D$	1.5	0.5	113.32		0.0073
$(^3D)\,^4D$	1.5	1.5	80.21		0.0000	$(^3D)\,^4D$	1.5	1.5	113.33		0.0168
$(^3D)\,^4D$	0.5	0.5	80.21		0.0000	$(^3D)\,^4D$	0.5	0.5	113.35		0.0186
$(^3D)\,^4D$	0.5	1.5	80.22		0.0000	$(^3D)\,^4D$	0.5	1.5	113.35		0.0051
$(^3D)\,^4S$	1.5	1.5	80.25		0.0001	$(^3P)\,^4P$	1.5	0.5	113.42		0.0039
$(^3D)\,^4S$	0.5	1.5	80.26		0.0001	$(^3P)\,^2D$	1.5	1.5	113.43		0.0000
$(^3P)\,^4F$	1.5	2.5	80.29		0.0000	$(^1D)\,^2D$	1.5	2.5	113.44		0.0101
$(^1D)\,^2P$	1.5	1.5	80.42	80.38	0.0019	$(^3P)\,^4P$	0.5	0.5	113.44		0.0019
$(^1D)\,^2P$	0.5	1.5	80.43		0.0002	$(^3P)\,^2D$	0.5	1.5	113.46		0.0029
$(^3D)\,^2P$	1.5	0.5	80.45		0.0000	$(^1D)\,^2D$	1.5	1.5	113.53		0.0056
$(^3D)\,^2P$	0.5	0.5	80.46		0.0002	$(^3P)\,^4P$	1.5	1.5	113.55		0.0059
$(^3P)\,^2D$	1.5	2.5	80.52		0.0000	$(^1D)\,^2D$	1.5	2.5	113.55		0.0123
$(^1D)\,^2P$	1.5	0.5	80.55		0.0001	$(^1D)\,^2D$	0.5	1.5	113.55	113.30	0.0195
$(^3P)\,^4D$	1.5	1.5	80.55		0.0014	$(^3P)\,^4P$	0.5	1.5	113.57		0.0000
$(^1D)\,^2P$	0.5	0.5	80.56		0.0010	$(^3P)\,^4P$	1.5	2.5	113.70		0.0086
$(^3P)\,^4D$	0.5	1.5	80.56	80.49	0.0024	$(^1P)\,^2P$	1.5	1.5	113.72	113.45	0.0459
$(^3P)\,^2D$	1.5	1.5	80.60		0.0014	$(^1P)\,^2P$	1.5	0.5	113.72		0.0292
$(^3P)\,^2D$	0.5	1.5	80.61		0.0004	$(^1P)\,^2P$	0.5	1.5	113.74		0.0016
$(^3P)\,^2F$	1.5	2.5	80.67		0.0000	$(^1P)\,^2P$	0.5	0.5	113.75		0.0110
$(^1D)\,^2P$	1.5	0.5	80.69		0.0000	$(^3D)\,^2S$	1.5	0.5	113.86		0.0171
$(^3P)\,^4P$	1.5	2.5	80.69	80.71	0.0022	$(^3D)\,^2S$	0.5	0.5	113.89	113.57	0.0178
$(^1D)\,^2P$	0.5	0.5	80.70		0.0000	$(^3D)\,^2F$	1.5	2.5	114.10		0.0019
$(^1S)\,^2D$	1.5	2.5	82.92		0.0006	$(^3P)\,^2F$	1.5	2.5	114.45		0.0062
$(^1S)\,^2D$	1.5	1.5	82.92		0.0000	$(^1S)\,^2D$	1.5	1.5	117.16		0.0023
$(^1S)\,^2D$	0.5	1.5	82.93		0.0000	$(^1S)\,^2D$	0.5	1.5	117.19	117.19	0.0094

Table 5.5. Measured energies (eV), calculated energies (eV) and gf-values for the $2p^6 3s^2 3p\ ^2P \rightarrow 2p^5 3s^2 3p4d\ ^{2,4}L$ transitions in Al and Si^+.

Al						Si^+					
Term	J_i	J_f	$E_{calc.}$	$E_{meas.}$	gf	Term	J_i	J_f	$E_{calc.}$	$E_{meas.}$	gf
$(^3S)\ ^4D$	1.5	0.5	79.94	79.97	0.0032	$(^3S)\ ^4D$	1.5	0.5	115.00		0.0000
$(^3S)\ ^4D$	1.5	1.5	79.95		0.0001	$(^3S)\ ^4D$	1.5	1.5	115.01		0.0002
$(^3S)\ ^4D$	0.5	0.5	79.95		0.0018	$(^3S)\ ^4D$	0.5	0.5	115.03		0.0000
$(^3S)\ ^4D$	0.5	1.5	79.96		0.0000	$(^3S)\ ^4D$	1.5	2.5	115.03		0.0012
$(^3S)\ ^2D$	1.5	2.5	80.07	80.11	0.0203	$(^3S)\ ^4D$	0.5	1.5	115.04		0.0003
$(^3S)\ ^2D$	1.5	1.5	80.11		0.0004	$(^3S)\ ^2D$	1.5	2.5	115.31	115.33	0.0244
$(^3S)\ ^2D$	0.5	1.5	80.12		0.0116	$(^3S)\ ^2D$	1.5	1.5	115.33		0.0003
$(^3D)\ ^4P$	1.5	0.5	80.39		0.0011	$(^3S)\ ^2D$	0.5	1.5	115.35	115.33	0.0283
$(^3D)\ ^4P$	1.5	2.5	80.40		0.0001	$(^3D)\ ^4G$	1.5	2.5	115.76		0.0010
$(^3D)\ ^4P$	0.5	0.5	80.40		0.0000	$(^3D)\ ^2P$	1.5	0.5	115.77		0.0055
$(^3D)\ ^2D$	1.5	2.5	80.53	80.59	0.0085	$(^3D)\ ^2P$	0.5	0.5	115.80	115.72	0.0120
$(^3D)\ ^2D$	1.5	2.5	80.58	80.59	0.0076	$(^3D)\ ^4S$	1.5	1.5	115.84		0.0000
$(^3D)\ ^2S$	1.5	0.5	80.60	80.59	0.0071	$(^3D)\ ^4P$	1.5	2.5	115.87		0.0000
$(^3D)\ ^2S$	0.5	0.5	80.61		0.0005	$(^3D)\ ^4S$	0.5	1.5	115.87		0.0001
$(^3D)\ ^4G$	1.5	2.5	80.62		0.0013	$(^3D)\ ^4F$	1.5	1.5	115.90		0.0016
$(^3D)\ ^2P$	1.5	0.5	80.63		0.0007	$(^3D)\ ^4P$	1.5	2.5	115.92	116.06	0.0255
$(^3D)\ ^2P$	0.5	0.5	80.64		0.0050	$(^3D)\ ^4F$	0.5	1.5	115.93		0.0166
$(^3D)\ ^2P$	1.5	1.5	80.64		0.0052	$(^3D)\ ^4P$	1.5	0.5	115.94		0.0068
$(^3D)\ ^2P$	0.5	1.5	80.65		0.0000	$(^3D)\ ^4P$	0.5	0.5	115.97		0.0004
$(^3D)\ ^2P$	1.5	1.5	80.71		0.0015	$(^3D)\ ^4D$	1.5	1.5	115.97		0.0001
$(^3D)\ ^2P$	0.5	1.5	80.72		0.0022	$(^3D)\ ^4D$	0.5	1.5	116.00		0.0150
$(^3P)\ ^4P$	1.5	1.5	80.73		0.0008	$(^3D)\ ^4D$	1.5	0.5	116.03		0.0001
$(^3D)\ ^4D$	1.5	2.5	80.73		0.0001	$(^3D)\ ^4D$	0.5	0.5	116.06		0.0115
$(^3P)\ ^4P$	0.5	1.5	80.74		0.0002	$(^3D)\ ^4D$	1.5	2.5	116.08		0.0166
$(^3D)\ ^4F$	1.5	1.5	80.74		0.0001	$(^3D)\ ^4P$	1.5	1.5	116.12		0.0000
$(^3D)\ ^4F$	0.5	1.5	80.76		0.0000	$(^3D)\ ^4P$	0.5	1.5	116.15		0.0020
$(^3D)\ ^4S$	1.5	1.5	80.76		0.0000	$(^3D)\ ^2F$	1.5	2.5	116.16		0.0525
$(^3D)\ ^4S$	0.5	1.5	80.77		0.0008	$(^3D)\ ^2D$	1.5	1.5	116.17		0.0006
$(^3D)\ ^2F$	1.5	2.5	80.79		0.0007	$(^3D)\ ^2D$	0.5	1.5	116.20	116.06	0.0484
$(^3D)\ ^4D$	1.5	0.5	80.79		0.0000	$(^1D)\ ^2P$	1.5	0.5	116.31		0.0005
$(^3D)\ ^4D$	0.5	0.5	80.80		0.0002	$(^3P)\ ^4D$	1.5	2.5	116.33		0.0000
$(^1D)\ ^2D$	1.5	1.5	80.81		0.0000	$(^1D)\ ^2P$	0.5	0.5	116.34		0.0165
$(^3D)\ ^4D$	1.5	2.5	80.81		0.0005	$(^1D)\ ^2P$	1.5	1.5	116.35		0.0271
$(^1D)\ ^2D$	0.5	1.5	80.82		0.0003	$(^3P)\ ^4P$	1.5	0.5	116.38		0.0349
$(^3P)\ ^2P$	1.5	0.5	80.83		0.0005	$(^1D)\ ^2P$	0.5	1.5	116.38		0.0023
$(^3D)\ ^2F$	1.5	2.5	80.83		0.0008	$(^1P)\ ^2F$	1.5	2.5	116.40		0.0000
$(^3P)\ ^2P$	0.5	0.5	80.84		0.0001	$(^3P)\ ^4P$	0.5	0.5	116.40		0.0022

Continued

Table 5.5. Continued

	Al						Si+				
Term	J_i	J_f	$E_{calc.}$	$E_{meas.}$	gf	Term	J_i	J_f	$E_{calc.}$	$E_{meas.}$	gf
$(^3D)\ ^2P$	1.5	1.5	80.84		0.0007	$(^1P)\ ^2D$	1.5	1.5	116.42		0.0097
$(^3D)\ ^2P$	0.5	1.5	80.85		0.0002	$(^1P)\ ^2D$	0.5	1.5	116.44		0.0260
$(^1P)\ ^2P$	1.5	1.5	80.88		0.0002	$(^1D)\ ^2D$	1.5	1.5	116.45		0.0170
$(^1P)\ ^2P$	0.5	1.5	80.89		0.0007	$(^1P)\ ^2D$	1.5	2.5	116.46		0.0171
$(^1D)\ ^2S$	1.5	0.5	80.94	80.91	0.0041	$(^1D)\ ^2D$	0.5	1.5	116.47		0.0017
$(^1P)\ ^2D$	1.5	2.5	80.95		0.0008	$(^1D)\ ^2F$	1.5	2.5	116.58		0.0012
$(^1D)\ ^2S$	0.5	0.5	80.95		0.0010	$(^3P)\ ^4F$	1.5	1.5	116.62		0.0025
$(^3D)\ ^4F$	1.5	1.5	80.97		0.0005	$(^3P)\ ^4F$	0.5	1.5	116.65		0.0008
$(^3D)\ ^4F$	0.5	1.5	80.98		0.0031	$(^1P)\ ^2P$	1.5	1.5	116.67		0.0057
$(^1P)\ ^2F$	1.5	2.5	80.99		0.0020	$(^3P)\ ^4P$	1.5	2.5	116.70		0.0028
$(^1D)\ ^2S$	1.5	0.5	81.00		0.0001	$(^1P)\ ^2P$	0.5	1.5	116.70		0.0000
$(^3P)\ ^4D$	1.5	2.5	81.01		0.0005	$(^3P)\ ^4D$	1.5	0.5	116.71		0.0002
$(^1D)\ ^2S$	0.5	0.5	81.01		0.0014	$(^1D)\ ^2F$	1.5	2.5	116.71		0.0003
$(^1D)\ ^2D$	1.5	1.5	81.03	81.03	0.0027	$(^3P)\ ^4P$	1.5	0.5	116.72		0.0165
$(^1D)\ ^2D$	0.5	1.5	81.04		0.0002	$(^3P)\ ^4D$	0.5	0.5	116.74		0.0175
$(^3P)\ ^2F$	1.5	2.5	81.04		0.0025	$(^3D)\ ^2P$	1.5	1.5	116.75		0.0098
$(^1D)\ ^2P$	1.5	1.5	81.05		0.0009	$(^3P)\ ^4P$	0.5	0.5	116.75		0.0002
$(^1D)\ ^2P$	0.5	1.5	81.06		0.0000	$(^3D)\ ^2P$	0.5	1.5	116.77		0.0026
$(^3P)\ ^2P$	1.5	1.5	81.07		0.0003	$(^3P)\ ^2P$	1.5	1.5	116.78		0.0010
$(^3P)\ ^2P$	0.5	1.5	81.08		0.0001	$(^1D)\ ^2D$	1.5	2.5	116.79		0.0015
$(^3P)\ ^2D$	1.5	2.5	81.08		0.0003	$(^3P)\ ^2P$	0.5	1.5	116.81		0.0007
$(^3P)\ ^4D$	1.5	2.5	81.11		0.0002	$(^3P)\ ^4P$	1.5	1.5	116.81	116.89	0.0133
$(^3P)\ ^4F$	1.5	2.5	81.21		0.0008	$(^3P)\ ^4P$	0.5	1.5	116.84		0.0007
$(^3D)\ ^2P$	1.5	0.5	81.24		0.0005	$(^3P)\ ^4P$	1.5	2.5	116.86		0.0000
$(^3D)\ ^2P$	0.5	0.5	81.25		0.0008	$(^1P)\ ^2P$	1.5	0.5	116.87		0.0034
$(^1P)\ ^2D$	1.5	1.5	81.25		0.0005	$(^1P)\ ^2P$	1.5	1.5	116.88		0.0008
$(^3P)\ ^4F$	1.5	1.5	81.26		0.0001	$(^1P)\ ^2P$	0.5	0.5	116.89	116.96	0.0115
$(^1P)\ ^2D$	0.5	1.5	81.26		0.0000	$(^1P)\ ^2P$	0.5	1.5	116.91		0.0088
$(^3P)\ ^4F$	0.5	1.5	81.27		0.0000	$(^1D)\ ^2S$	1.5	0.5	116.91		0.0087
$(^3P)\ ^4F$	1.5	2.5	81.27		0.0000	$(^3P)\ ^2D$	1.5	2.5	116.92	116.96	0.0295
$(^3P)\ ^4D$	1.5	0.5	81.28		0.0000	$(^1D)\ ^2S$	0.5	0.5	116.94		0.0010
$(^3P)\ ^4D$	0.5	0.5	81.29		0.0002	$(^3P)\ ^2P$	1.5	1.5	117.00		0.0154
$(^1D)\ ^2P$	1.5	0.5	81.31		0.0007	$(^3P)\ ^2P$	0.5	1.5	117.03	117.03	0.0052
$(^3P)\ ^2D$	1.5	1.5	81.31		0.0001	$(^3P)\ ^2D$	1.5	2.5	117.27	117.26	0.0349
$(^1D)\ ^2P$	0.5	0.5	81.32		0.0009	$(^3P)\ ^2P$	1.5	0.5	117.36		0.0034
$(^3P)\ ^2D$	0.5	1.5	81.32		0.0001	$(^3P)\ ^2P$	0.5	0.5	117.38		0.0010
$(^3P)\ ^4P$	1.5	1.5	81.34		0.0011	$(^1S)\ ^2D$	1.5	1.5	120.64		0.0002
$(^3P)\ 2D$	1.5	2.5	81.35	81.37	0.0021	$(^1S)\ ^2D$	1.5	2.5	120.65		0.0015
$(^3P)\ ^4P$	0.5	1.5	81.35		0.0001	$(^1S)\ ^2D$	0.5	1.5	120.67		0.0019

Table 5.6 Measured energies (eV), calculated energies (eV) and gf-values for the $2p^6 3s^2 3p\ ^2P \rightarrow 2p^5 3s^2 3p5d\ ^{2,4}L$ transitions in Al and Si^+.

			Al						Si+		
Term	J_i	J_f	$E_{calc.}$	Emeas.	gf	Term	J_i	J_f	$E_{calc.}$	$E_{meas.}$	gf
$(^3S)\ ^2D$	1.5	2.5	80.33		0.0019	$(^3S)\ ^4D$	1.5	0.5	116.63		0.0001
$(^3S)\ ^2D$	1.5	1.5	80.34		0.0007	$(^3S)\ ^4D$	1.5	1.5	116.65		0.0037
$(^3S)\ ^4D$	1.5	2.5	80.35		0.0000	$(^3S)\ ^4D$	1.5	2.5	116.66		0.0030
$(^3S)\ ^2D$	0.5	1.5	80.35		0.0000	$(^3S)\ ^4D$	0.5	0.5	116.66		0.0008
$(^3S)\ ^4D$	1.5	0.5	80.35		0.0002	$(^3S)\ ^4D$	0.5	1.5	116.68		0.0000
$(^3S)\ ^4D$	1.5	1.5	80.36		0.0000	$(^3D)\ ^2D$	1.5	2.5	117.14		0.0034
$(^3S)\ ^4D$	0.5	0.5	80.36		0.0000	$(^3D)\ ^4P$	1.5	1.5	117.39		0.0000
$(^3S)\ ^4D$	0.5	1.5	80.37		0.0001	$(^3D)\ ^2D$	1.5	1.5	117.39		0.0022
$(^3S)\ ^2D$	1.5	2.5	80.39		0.0025	$(^3D)\ ^4P$	1.5	2.5	117.40		0.0000
$(^3S)\ ^2D$	1.5	1.5	80.42		0.0001	$(^3D)\ ^4P$	0.5	1.5	117.42		0.0001
$(^3S)\ ^2D$	0.5	1.5	80.43		0.0029	$(^3D)\ ^2D$	0.5	1.5	117.42	117.47	0.0180
$(^3D)\ ^2D$	1.5	2.5	80.88		0.0020	$(^3D)\ ^4F$	1.5	2.5	117.44		0.0033
$(^3D)\ ^4P$	1.5	0.5	80.89		0.0007	$(^3D)\ ^4P$	1.5	0.5	117.47		0.0062
$(^3D)\ ^4P$	0.5	0.5	80.90		0.0000	$(^3D)\ ^4D$	1.5	1.5	117.47		0.0093
$(^3D)\ ^2D$	1.5	1.5	80.91	80.91	0.0048	$(^3D)\ ^4P$	0.5	0.5	117.50		0.0001
$(^3D)\ ^2D$	0.5	1.5	80.92		0.0006	$(^3D)\ ^4D$	0.5	1.5	117.50		0.0001
$(^3D)\ ^2D$	1.5	2.5	80.92		0.0009	$(^3D)\ ^4P$	1.5	2.5	117.51		0.0046
$(^3D)\ ^4P$	1.5	1.5	80.95		0.0029	$(^3D)\ ^4F$	1.5	1.5	117.56		0.0004
$(^3D)\ ^4P$	0.5	1.5	80.96		0.0030	$(^3D)\ ^4D$	1.5	0.5	117.57		0.0001
$(^3D)\ ^2S$	1.5	0.5	81.03		0.0019	$(^3D)\ ^4F$	0.5	1.5	117.59		0.0087
$(^3D)\ ^2S$	0.5	0.5	81.04		0.0000	$(^3D)\ ^4D$	0.5	0.5	117.60		0.0160
$(^3D)\ ^4G$	1.5	2.5	81.06		0.0005	$(^3D)\ ^2D$	1.5	2.5	117.62	117.54	0.0201
$(^3D)\ ^4S$	1.5	1.5	81.08		0.0021	$(^3D)\ ^4F$	1.5	2.5	117.65		0.0001
$(^3D)\ ^4D$	1.5	0.5	81.09		0.0007	$(^3D)\ ^2D$	1.5	1.5	117.68	117.74	0.0208
$(^3D)\ ^4S$	0.5	1.5	81.09		0.0014	$(^3D)\ ^4D$	1.5	1.5	117.69		0.0033
$(^3D)\ ^4D$	0.5	0.5	81.10	81.16	0.0060	$(^3D)\ ^2D$	0.5	1.5	117.70		0.0047
$(^3D)\ ^4F$	1.5	1.5	81.10		0.0000	$(^3D)\ ^4D$	0.5	1.5	117.72		0.0092
$(^3D)\ ^4F$	0.5	1.5	81.11		0.0004	$(^3D)\ ^2P$	1.5	0.5	117.73		0.0123
$(^3D)\ ^4D$	1.5	0.5	81.13		0.0004	$(^3D)\ ^2P$	0.5	0.5	117.76		0.0101
$(^3D)\ ^4D$	1.5	1.5	81.13		0.0018	$(^3D)\ ^2D$	1.5	2.5	117.77	117.95	0.0367
$(^3D)\ ^4D$	0.5	0.5	81.14		0.0000	$(^3D)\ ^2S$	1.5	0.5	117.82		0.0325
$(^3D)\ ^4D$	0.5	1.5	81.14		0.0007	$(^3D)\ ^2P$	1.5	1.5	117.83	118.08	0.0472
$(^3D)\ ^4D$	1.5	2.5	81.14		0.0001	$(^3D)\ ^2S$	0.5	0.5	117.85		0.0150
$(^3D)\ ^2P$	1.5	1.5	81.20		0.0013	$(^3D)\ ^2P$	0.5	1.5	117.86		0.0174
$(^3D)\ ^2P$	0.5	1.5	81.21	81.21	0.0024	$(^1D)\ ^2P$	1.5	0.5	117.89		0.0049
$(^1D)\ ^2S$	1.5	0.5	81.21		0.0002	$(^3P)\ ^4D$	1.5	2.5	117.90		0.0016
$(^1D)\ ^2S$	0.5	0.5	81.22		0.0000	$(^3P)\ ^4D$	1.5	1.5	117.91		0.0030

Continued

Table 5.6. Continued

	Al					Si^+					
Term	J_i	J_f	$E_{calc.}$	Emeas.	gf	Term	J_i	J_f	$E_{calc.}$	$E_{meas.}$	gf
$(^3D)\ ^2F$	1.5	2.5	81.24		0.0002	$(^1D)\ ^2P$	0.5	0.5	117.92		0.0000
$(^3P)\ ^2D$	1.5	1.5	81.30		0.0014	$(^3P)\ ^4D$	0.5	1.5	117.93		0.0005
$(^1D)\ ^2F$	1.5	2.5	81.30		0.0006	$(^1D)\ ^2S$	1.5	0.5	118.04		0.0039
$(^3P)\ ^2D$	0.5	1.5	81.31		0.0001	$(^1P)\ ^2F$	1.5	2.5	118.05		0.0013
$(^3P)\ ^4P$	1.5	2.5	81.37		0.0002	$(^1D)\ ^2S$	0.5	0.5	118.07		0.0034
$(^1D)\ ^2S$	1.5	0.5	81.39		0.0006	$(^1P)\ ^2F$	1.5	2.5	118.09		0.0081
$(^1D)\ ^2P$	1.5	1.5	81.39		0.0019	$(^3D)\ ^2P$	1.5	1.5	118.10		0.0002
$(^1D)\ ^2S$	0.5	0.5	81.40		0.0001	$(^3D)\ ^2P$	0.5	1.5	118.12		0.0163
$(^1D)\ ^2P$	0.5	1.5	81.40		0.0001	$(^1P)\ ^2D$	1.5	1.5	118.15		0.0009
$(^3P)\ ^2P$	1.5	1.5	81.40	81.44	0.0026	$(^1P)\ ^2D$	0.5	1.5	118.18		0.0223
$(^3P)\ ^2P$	0.5	1.5	81.42		0.0003	$(^1D)\ ^2F$	1.5	2.5	118.20		0.0027
$(^1P)\ ^2F$	1.5	2.5	81.43		0.0000	$(^3P)\ ^4D$	1.5	1.5	118.21		0.0080
$(^1P)\ ^2P$	1.5	0.5	81.44		0.0002	$(^3P)\ ^4D$	1.5	0.5	118.21		0.0020
$(^1P)\ ^2F$	1.5	2.5	81.44		0.0000	$(^3P)\ ^4D$	0.5	1.5	118.24		0.0001
$(^3P)\ ^4D$	1.5	2.5	81.44		0.0016	$(^3P)\ ^4D$	0.5	0.5	118.24		0.0166
$(^3P)\ ^4D$	1.5	1.5	81.45		0.0000	$(^3P)\ ^4F$	1.5	1.5	118.25		0.0000
$(^1P)\ ^2P$	0.5	0.5	81.45		0.0007	$(^3P)\ ^4F$	1.5	2.5	118.25		0.0028
$(^3P)\ ^4D$	0.5	1.5	81.46		0.0000	$(^3P)\ ^4F$	0.5	1.5	118.28		0.0057
$(^3P)\ ^2P$	1.5	1.5	81.48		0.0000	$(^1D)\ ^2P$	1.5	1.5	118.29		0.0029
$(^3P)\ ^2F$	1.5	2.5	81.49		0.0007	$(^1D)\ ^2D$	1.5	2.5	118.30		0.0000
$(^3P)\ ^2P$	0.5	1.5	81.49		0.0002	$(^3P)\ ^2F$	1.5	2.5	118.31	118.44	0.0191
$(^3P)\ ^4D$	1.5	0.5	81.55		0.0001	$(^1D)\ ^2P$	0.5	1.5	118.32		0.0002
$(^3P)\ ^4D$	1.5	2.5	81.55	81.48	0.0027	$(^1D)\ ^2S$	1.5	0.5	118.33		0.0068
$(^3P)\ ^4D$	0.5	0.5	81.56		0.0003	$(^3P)\ ^2P$	1.5	1.5	118.35		0.0046
$(^1P)\ ^2D$	1.5	1.5	81.56		0.0003	$(^3P)\ ^4P$	1.5	2.5	118.35	118.51	0.0214
$(^1P)\ ^2D$	0.5	1.5	81.57	81.57	0.0020	$(^1D)\ ^2S$	0.5	0.5	118.36		0.0001
$(^3P)\ ^4F$	1.5	1.5	81.57		0.0003	$(^3P)\ ^4P$	1.5	1.5	118.36		0.0210
$(^3P)\ ^4F$	0.5	1.5	81.58		0.0000	$(^1P)\ ^2P$	1.5	0.5	118.37		0.0041
$(^3P)\ ^4D$	1.5	0.5	81.61		0.0000	$(^3P)\ ^2P$	0.5	1.5	118.37		0.0000
$(^3P)\ ^4F$	1.5	2.5	81.62		0.0006	$(^3P)\ ^4P$	0.5	1.5	118.39		0.0000
$(^3P)\ ^4D$	0.5	0.5	81.62		0.0009	$(^1P)\ ^2P$	0.5	0.5	118.40		0.0054
$(^3P)\ ^4P$	1.5	0.5	81.63		0.0017	$(^3P)\ ^2F$	1.5	2.5	118.62	118.90	0.0299
$(^3P)\ ^4P$	0.5	0.5	81.64		0.0002	$(^3P)\ ^2P$	1.5	0.5	118.66		0.0012
$(^3P)\ ^2D$	1.5	1.5	81.64		0.0002	$(^3P)\ ^2P$	0.5	0.5	118.69		0.0048
$(^3P)\ ^2D$	0.5	1.5	81.65		0.0019	$(^3P)\ ^2D$	1.5	1.5	118.70		0.0044
$(^3P)\ ^2F$	1.5	2.5	81.68	81.68	0.0037	$(^3P)\ ^2D$	0.5	1.5	118.73		0.0050
$(^1D)\ ^2D$	1.5	1.5	81.68		0.0000	$(^1S)\ ^2D$	1.5	1.5	122.24		0.0003
$(^1D)\ ^2D$	0.5	1.5	81.69		0.0002	$(^1S)\ ^2D$	1.5	2.5	122.24		0.0021
$(^1S)\ ^2D$	1.5	2.5	84.40		0.0066	$(^1S)\ ^2D$	0.5	1.5	122.26		0.0019

5.4 Conclusions

In this work a comprehensive investigation of the 2p absorption spectra of Al and Si^+, recorded using the dual laser-produced plasma technique, have been carried out . A combination of photoabsorption and theoretical studies along the isoelectronic sequence have been successfully employed for explaining the measured spectra.

The investigations presented in this work are not in agreement with those of Cantu *et al.* (1982) and Daum and Kelly (1976) reported for Al and Si^+ respectively. In the case of Al all the strong features were assigned to the $2p^53s^23p4s$ array by Cantu *et al.* (1982). Though the calculated term energies and relative intensities were in reasonable agreement with the observed features we believe the analysis presented by Cantu and co-workers is not reliable for the following reasons: i) the contribution of 2p → 3d transitions was seriously underestimated, and (ii) no configuration-interaction effects were taken into account in the semi-empirical approach used. In the photoionization calculations of Si^+ (Daum and Kelly 1976), the resonances belonging to the $2p^53s3p^3$ configuration were not included. Our calculations, where almost all significant interactions have been included, predict that the 2p absorption spectra for both Al and Si^+ are dominated by the $2p^63s^23p \rightarrow 2p^53s3p^3 + 2p^53s^23pnd$ transitions and the $2p^63s^23p \rightarrow 2p^53s^23pns$ transitions are relatively very weak which has also been found to be in agreement with the experiment.

5.5 References

Cantu A M and Tozzi G P, 1982, J. Opt. Soc. Am., **72**, 729.

Carroll P K and Kennedy E T, 1977, Phys. Rev. Lett., **38**, 1068.

Costello J T, Evans D, Hopkins R B, Kennedy E T, Kiernan L, Mansfield M W D, Mosnier J-P, Sayyad M H and Sonntag B F, 1992, J. Phys. B: At. Mol. Phys., **25**, 5055.

Daum G R and Kelly H P, 1976, Phys. Rev. A **13**, 715.

Dufton P L, Keenan F P, Hibbert A, Ojha P C and Stafford R P, 1992, The Astophysical Journal, **387**, 414.

Hibbert A, Kinston A E and Tiwary S N, 1982, J. Phys. B: At. Mol. Phys., **15**, L643.

Hibbert A, 1989, Physica Scripta, **39**, 574.

Malutzki R, Watcher A, Schmidth V and Hansen J E, 1987, J. Phys. B: At. Mol. Phys., **20**, 5411.

Martin W C and Zalubas R, 1979, J. Phys. Chem. Ref. Data, **8**, 820.

Martin W C and Zalubas R, 1979, J. Phys. Chem. Ref. Data, **8**, 826.

Martin W C and Zalubas R, 1983, J. Phys. Chem. Ref. Data, **12**, 342.

Martin W C and Zalubas R, 1983, J. Phys. Chem. Ref. Data, **8**, 347.

Martinson I, 1989, Rep. Prog. Phys., **52**, 157.

Mosnier J-P, Costello J T, Kennedy E T, Kiernan L and Sayyad M H, 1994, Phys. Rev. A **49**, 755.

Tayal S S and Burke P G, 1987, J. Phys. B: At. Mol. Phys., **20**, 4715.

Chapter 6

THE GROUND STATE ABSORPTION IN ATOMIC SILICON

The photoabsorption spectrum of atomic Si is reported in the 103 eV to 113 eV region. The absorption features in this region arise from the excitation of 2p electrons. Interpretation for the measured spectrum is provided on the basis of configuration-interaction atomic structure calculations. Comparison is made with the 2p absorption in gas phase SiH_4.

6.1 Introduction

The study of the spectrum involving inner-shell excitations is a valuable tool to establish connections between the behaviour of free atoms and those in molecules, clusters and solids, currently an important thrust of research (see e.g. Connerade *et al.* 1987, Connerade and Karnatak 1990, Costello *et al.* 1991). Most frequently inner-shell excitation in molecules and solids exhibit spectra similar to those of the constituent atoms. For example, inner-shell excitations in molecules and solids exhibit giant resonances if the constituent atoms do so. The persistence of these resonances indicate that the effect originates inside the constituent atoms, where the initial- and final state wavefunctions are only slightly perturbed by the external environment (Brechignac *et al.* 1991). Considerable attention has been paid to the phenomenon of giant resonances and its consequences (Connerade *et al.* 1987 and references therein). The basic mechanism of giant-resonance formation has been explained in terms of a collective oscillation of an electron shell as well as within the framework of an independent particle model (Clark 1987 and references therein). Their formation involves one-electron excitations which have very significant probability in molecules as well as solids. Therefore, they have been observed in the inner-shell spectra of metals and molecules. Close similarities have been observed between the inner-shell spectra of metals, molecules and their constituent atoms exhibiting giant resonances (see e.g. Costello *et al.* 1991) because the transitions take place between the orbits which are deep within the

atom and, therefore, are not influenced by the environment. The 4d and 3p photoabsorption studies in rare-earths (see e.g. Richter *et al.* 1989) and 3d elements (see e.g. Sonntag and Zimmermann 1992), respectively, and their molecules has played a major role not only in establishing relations between the behaviour of these atoms and their molecules but also proved of great value in understanding the various aspects of giant resonances (Connerade *et al.* 1987 and references therein).

For more than two decades second row atoms and their molecules have been the subject of 2p-subshell photoabsorption/photoionization investigations. However, in spite of intense efforts their spectra have not been thoroughly investigated. The 2p-subshell photoabsorption/photoionization measurements have been made in Na (Connerade *et al.* 1971, Wolff *et al.* 1972), Mg (see chapter 4 and references therein) and Al (see chapter 5 and references therein) atoms but to our knowledge corresponding spectra of their molecules have not been reported. On the other hand the 2p-subshell photoabsorption have been studied extensively in the molecules of Si (Hayes *et al.* 1971, Hayes and Brown 1972, de Souza *et al.* 1986, Sutherland *et al.* 1994), P (Hayes and Brown 1972, Ishiguro *et al.* 1987), S (Hayes and Brown 1972, Hudson *et al.* 1993, 1994) and Cl (Hayes and Brown 1972, Aksela *et al.* 1990) but the corresponding spectra of these atoms have not been reported. Therefore, it was not possible to study the behaviour of second row atoms and their molecules in their 2p photoabsorption spectra . With this in mind, the photoabsorption investigations of the 2p-subshell spectrum of atomic Si has been carried out and comparison is made with the gas phase 2p absorption spectrum of SiH_4 reported by Hayes *et al.* (1971, 1972).

The investigations and identification of the 2p photoabsorption spectra of atomic Si will be reported first. Then, comparison will be made with the corresponding photoabsorption spectrum of gas phase SiH_4.

6.2 Results and analysis

The ground configuration $2p^63s^23p^2$ of Si neutral includes the $^3P_{0,1,2}$, $^1D_2$ and $^1S_0$ levels. The $^3P_1$, $^3P_2$, $^1D_2$ and $^1S_0$ levels lie 77.115 cm^{-1}, 223.157 cm^{-1}, 6298.850 cm^{-1}, 15394.370 cm^{-1}, respectively, above the ground state $^3P_0$ and lie lower than the levels of the excited configurations (Martin and Zalubas 1983). Therefore, in the dual laser plasma experiment, optimised for Si neutral, all of

these levels could get populated and significant absorption can result from these levels. The transitions can take place to the Rydberg series $2p^5 3s^2 3p^2(n+1)s$, $2p^5 3s^2 3p^2 nd$ and the doubly excited configuration $2p^5 3s 3p^4$. The various excited levels could fall in the same spectral region and yield a complicated spectrum. In such an overlapped spectrum, without knowing the population of the different levels of the ground configuration, it could be very difficult to distinguish the absorption taking place from different lower levels. The atomic structure calculations could predict everything in agreement with the measurements but assignment of the observed features to some particular configuration seems to be very difficult in this case. If absorption takes place only from ^3P levels then at least it is possible to associate some unique upper level with the lower levels and provide a comparison with the measured and computed spectrum.

The photoabsorption spectrum of atomic Si going to the 2p limit at 107.96 eV is shown in figure 6.1. The energy of the limit has been obtained from the $2p^6 3s 3p^2 \rightarrow 2p^5 3s^2 3p^2$ transition measured at 94.46 eV in the 2p absorption from Si^+ (see chapter 7). The relevant optical energies have been taken from Martin and Zalubas (1983).

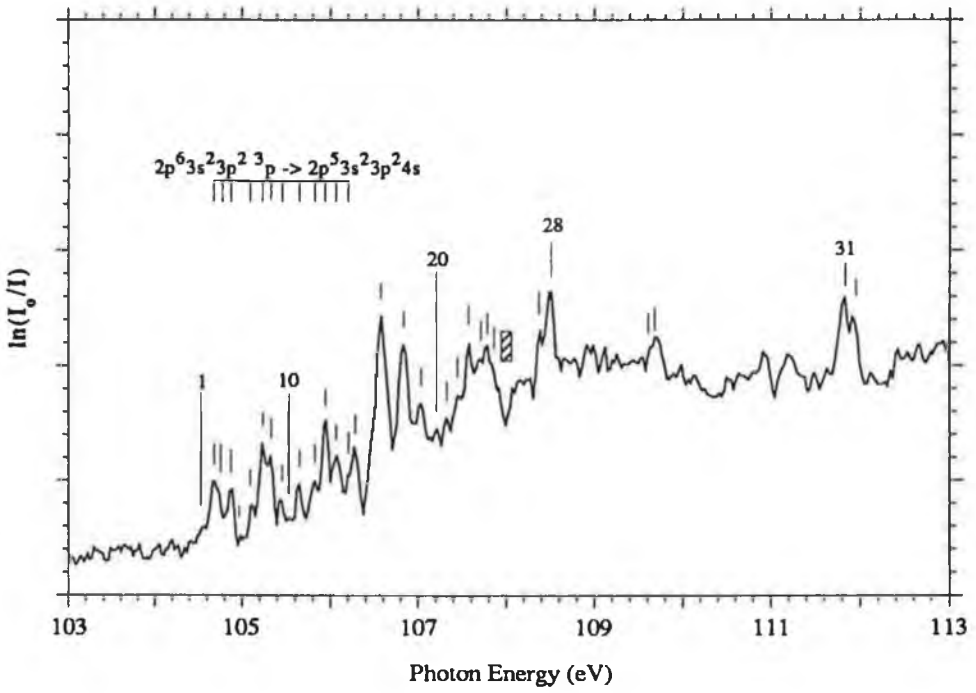

Figure 6.1

The 2p-subshell photoabsorption spectrum of atomic silicon in ground states. The features labelled as 31 and 32 exhibit the strongest transitions of Si^+ (see chapter 5).

The observed Si I energies and their assignments are listed in tables 6.1, 6.2 and 6.3. The assignments are given on the basis of scaled atomic structure calculations (see chapter 2) carried out for the $2p^63s^23p^2 + 2p^63p^4 \rightarrow 2p^5[3s^23p^2(4s + 5s + 6s) + 3s^23p^2(3d + 4d) + 3s3p^4]$ transitions. The HF integrals F^k (i, i), F^k (i, j), G^k (i, j), R^k (i, j) and ξ (i) have been scaled by 15%, 15%, 15%, 25% and 10% respectively. The $2p^63p^4$ configuration has been included to provide configuration-interaction effects in the ground states. No extra configuration-interaction effects have been included in the core-excited states. The core-excited $2p53s^23p^2nd$ series has been found mixed with the doubly excited $2p^53s3p^4$ configuration, however, the mixing is not severe. On the other hand, the $2p^53s^23p^2(n+1)s$ series have been observed not to mix with the $2p^53s^23p^2nd$ series and the $2p^53s3p^4$ configuration.

6.2.1 Transitions from $2p^63s^23p^2\ ^3P_{0,\ 1,\ 2}$ levels

From $^3P_{0,1,\ 2}$ levels transitions to the ^3L terms are expected to appear strongly. Departures from LS coupling will allow transitions to the ^5L and ^1L terms. In the case of the $2p^53s^23p^2(n+1)s$ series significant mixing has been observed between the ^3L and ^5L terms, therefore, strong transitions have been predicted to only the ^3L and ^5L terms (see table 6.1). Transitions to the ^1L terms have been predicted with negligible gf-values and along with the other transitions predicted with negligible gf-values have been deleted in table 6.1. With the exception of the two lowest terms there is excellent agreement between the computed and measured term energies. Analogous to the 2p absorption in atomic Mg (see chapter 4) and atomic Al (see chapter 5) the whole lower energy region is dominated by the $2p \rightarrow 4s$ transition array. The $2p \rightarrow 5s$ and 6s transitions are predicted very weak and degenerate with the very strong transitions resulting from the $2p \rightarrow 3d$ transitions, therefore, their identification here is not possible.

In the case of transitions to $2p^53s^23p^23d$ and $2p^53s^23p^24d$ configurations, out of the total 470 possible transitions (see Appendix C) only 50 transitions have been predicted with non-negligible gf-values and their assignment is given in table 6.2. In the region from 106.44 eV to 106.81 eV, a number of transitions have been predicted. But in this region only the peaks 17 and 18 (Figure 6.1) appear as resolved. These two peaks appear as strongest in the 2p absorption spectrum of atomic Si. The computed energy of the $(^3P)\ ^3P_2 \rightarrow (^1D)\ ^1F_3$ transition predicted as strongest is in agreement with the measured energy of peak 18, therefore, this

transition can be assigned to peak 18. The gf-value of the transition having energy corresponding to the measured energy of the strongest feature (peak 17) has been predicted almost zero and analogous to the 2p absorption in atomic Al (see chapter 5). The gf-value of the transition corresponding to the strongest observed feature in atomic Al was predicted almost zero. In the calculations carried out for the isoelectronic ion Si^+ the same transition was predicted as the strongest and was in agreement with the experiment. Therefore, assignment was given on the basis of isoelectronic comparison of measured and computed spectra. In the present case the calculations carried out for P^+ which is isoelectronic to atomic Si predict the same transition as the strongest. Therefore, we believe the computed gf-values for neutrals are not reliable. The zero gf predicted for the strongest transition in atomic Si could be due to cancellation effects which have been observed frequently (see chapter 2).

The doubly excited $2p^53s3p^4$ configuration has 40 terms (see Appendix C). The transitions to the ^3L terms expected to appear as strong have been predicted far above the 2p threshold. On the other hand, transitions to the ^5L terms which are dipole forbidden in pure LS coupling have been predicted all below the 2p threshold with the exception of transitions to the $(^3P)\ ^5S_1$ term. No significant mixing has been observed between the ^5L terms of the $2p^53s3p^4$ configuration with the terms of $2p^53s^23p^2nd$ series. As the transitions to the doubly excited states borrow strength mainly through mixing with the most favourable transitions to the nd series, therefore, transitions to the doubly excited states have been predicted with negligible gf-values. However, analogous to the Al isoelectronic sequence (see chapter 5), the ^3L terms of the doubly excited configuration in P^+ isoelectronic to Si I will drop below the the 2p threshold. Their mixing with the terms of the $2p^53s^23p^2nd$ series could give rise to some strong transitions to the doubly excited states. Furthermore, the strong interaction between the doubly and singly excited states in P^+ could yield relatively complicated spectrum and make the identification difficult.

Table 6.1. Measured energies (eV), calculated energies (eV) and gf-values for the $2p^63s^23p^2\ ^3P \rightarrow 2p^53s^23p^2[4s + 5s + 6s]\ ^{1,3,5}L$ transitions in atomic Si.

Transition	$E_{calc.}$	gf	$E_{meas.}$	Peak
$^3P_2$ - 4s (^3P) $^3P_2$	104.83	0.0049	106.68	2
$^3P_1$ - 4s (^3P) $^3P_2$	104.85	0.0035	104.75	3
$^3P_2$ - 4s (^3P) $^3P_1$	104.94	0.0021	104.87	4
$^3P_0$ - 4s (^3P) $^3P_1$	104.97	0.0026	104.87	4
$^3P_1$ - 4s (^3P) $^3P_0$	105.00	0.0021	104.98	5
$^3P_2$ - 4s (^3P) $^5D_3$	105.12	0.0038	105.12	6
$^3P_1$ - 4s (^3P) $5D_2$	105.23	0.0027	105.24	7
$^3P_1$ - 4s (^3P) $^3D_1$	105.37	0.0024	105.33	
$^3P_2$ - 4s (^3P) $^3D_3$	105.38	0.0083	105.33	8
$^3P_2$ - 4s (^3P) $^3P_2$	105.43	0.0043	105.46	9
$^3P_1$ - 4s (^3P) $^3D_2$	105.56	0.0026	105.52	10
$^3P_0$ - 4s (^3P) $^5D_1$	105.68	0.0024	105.65	11
$^3P_1$ - 4s (^3P) $^3D_2$	105.83	0.0041	105.80	12
$^3P_2$ - 4s (^3P) $^3D_3$	105.93	0.0084	105.94	13
$^3P_2$ - 4s (^3P) $^3S_1$	106.15	0.0024	106.06	14
$^3P_1$ - 4s (^3P) $^3S_1$	106.16	0.0020	106.21	15
$^3P_2$ - 4s (^3P) $^3S_1$	106.44	0.0023		
$^3P_2$ - 5s (^3P) $^3P_2$	106.60	0.0012		
$^3P_1$ - 5s (^3P) $^3P_0$	106.85	0.0006		
$^3P_2$ - 5s (^3P) $^3D_3$	107.12	0.0029		
$^3P_2$ - 5s (^3P) $^5D_2$	107.23	0.0013		
$^3P_1$ - 5s (^3P) $^3D_1$	107.34	0.0009		
$^3P_0$ - 5s (^3P) $^5D_1$	107.67	0.0006		
$^3P_2$ - 5s (^3P) $^3D_3$	107.96	0.0021		
$^3P_1$ - 6s (^3P) $^3P_2$	107.24	0.0011		
$^3P_2$ - 6s (^3P) $^3D_3$	107.74	0.0016		

Table 6.2. Measured energies (eV), calculated energies (eV) and gf-values for the $2p^6 3s^2 3p^2\ ^3P \rightarrow 2p^5 3s^2 3p^2[3d + 4d]\ ^{1,3,5}L$ transitions in atomic Si.

Transition	$E_{calc.}$	gf	$E_{meas.}$	Peak
$^3P_2$ - 3d (^3P) $^3D_3$	106.10	0.0055	106.06	14
$^3P_1$ - 3d (^3P) $^3D_2$	106.20	0.0038	106.21	15
$^3P_1$ - 3d (^3P) $^3D_1$	106.35	0.0026	106.28	
$^3P_2$ - 3d (^3P) $^5P_2$	106.36	0.0048	106.28	16
$^3P_0$ - 3d (^3P) $^3D_1$	106.36	0.0008	106.57	17
$^3P_2$ - 3d (^3P) $^3S_1$	106.43	0.0029		
$^3P_1$ - 3d (^3P) $^3S_1$	106.44	0.0028		
$^3P_0$ - 3d (^3P) $^3S_1$	106.45	0.0036		
$3P_2$ - 3d (^3P) $^3S_1$	106.63	0.0038		
$^3P_1$ - 3d (^3P) $^3S_1$	106.65	0.0026		
$^3P_2$ - 3d (^3P) $^5F_3$	106.66	0.0033		
$^3P_1$ - 3d (^3P) $^5F_2$	106.67	0.0057		
$^3P_1$ - 3d (^3P) $^5F_1$	106.71	0.0024		
$^3P_0$ - 3d (^3P) $^5F_1$	106.71	0.0047		
$^3P_2$ - 3d (^3P) $^3D_3$	106.74	0.0106		
$^3P_2$ - 3d (^3P) $^3P_1$	106.74	0.0085		
$3P_1$ - 3d (^3P) $^3P_0$	106.74	0.0044		
$3P_1$ - 3d (^3P) $^5G_2$	106.75	0.0096		
$3P_1$ - 3d (^3P) $^3P_1$	106.75	0.0025		
$^3P_2$ - 3d (^1D) $^1D_2$	106.78	0.0040		
$^3P_1$ - 3d (^1D) $^1D_2$	106.80	0.0047		
$^3P_2$ - 3d (^1D) $^1F_3$	106.80	0.0120		
$^3P_2$ - 3d (^3P) $^3P_2$	106.81	0.0192	106.84	18
$^3P_2$ - 3d (^3P) $^3D_3$	106.98	0.0042		

Continued.

Table 6.2. Continued.

Transition	$E_{calc.}$	gf	$E_{meas.}$	Peak
$^3P_2$ - 3d (^3P) $^3P_2$	107.00	0.0055	107.03	19
$^3P_1$ - 3d (^3P) $^5F_1$	107.03	0.0031		
$^3P_2$ - 3d (^3P) $^3F_3$	107.22	0.0035	107.20	20
$^3P_2$ - 3d (^3P) $^5D_1$	107.28	0.0033		
$^3P_1$ - 3d (^3P) $^5D_1$	107.30	0.0042	107.35	21
$^3P_0$ - 3d (^3P) $^3D_1$	107.44	0.0042	107.44	22
$^3P_1$ - 3d (^3P) $^5D_2$	107.47	0.0034		
$^3P_1$ - 3d (^3P) $^3F_2$	107.57	0.0037	107.57	23
$^3P_2$ - 3d (^3P) $^3S_1$	107.79	0.0033	107.78	25
$^3P_1$ - 3d (^3P) $^1D_2$	107.83	0.0031	107.86	26
$^3P_2$ - 4d (^3P) $^3D_3$	107.19	0.0102	107.20	
$^3P_2$ - 4d (^3P) $^3P_2$	107.28	0.0038	107.35	21
$^3P_2$ - 4d (^3P) $^3P_1$	107.57	0.0057		
$^3P_2$ - 4d (^3P) $^5F_3$	107.58	0.0168	107.57	23
$^3P_2$ - 4d (^3P) $^5G_3$	107.61	0.0100		
$^3P_2$ - 4d (^3P) $^3P_2$	107.63	0.0159	107.69	24
$^3P_1$ - 4d (^3P) $^3D_1$	107.67	0.0058		
$^3P_1$ - 4d (^3P) $^5G_2$	107.72	0.0039		
$^3P_2$ - 4d (^3P) $^5D_3$	107.77	0.0082	107.78	25
$^3P_1$ - 4d (^1D) $^3F_2$	107.78	0.0029		
$^3P_2$ - 4d (^3P) $^5P_3$	107.79	0.0028		
$^3P_1$ - 4d (^3P) $^3P_2$	107.80	0.0022		
$^3P_0$ - 4d (^3P) $^5P_1$	107.95	0.0029		
$^3P_0$ - 4d (^3P) $^5F_1$	108.08	0.0033		
$^3P_1$ - 4d (^3P) $^3P_1$	108.37	0.0020		
$^3P_2$ - 4d (^1D) $^1F_3$	108.48	0.0043		
$^3P_2$ - 4d (^3P) $^5D_1$	108.53	0.0032		

6.2.2 Transitions from the $2p^63s^23p^2\ {}^1D_2$ level

The assignments of the transitions resulting from the ^1D level are given in table 6.3. With the exception of transitions assigned to peaks 1 and 28 all other transitions from the ^1D level coincide with the transitions resulting from ^3P levels. As the gf-values corresponding to the transitions assigned to the peaks 1 and 28 have been predicted in agreement with the experiment and no other transitions resulting from ^3P or ^1S levels have been predicted corresponding to their measured energies. Therefore, in the present experiment significant populations of the ^1D levels are present in the absorbing plasma.

Table 6.3. Measured energies (eV), calculated energies (eV) and gf-values for the $2p^63s^23p^2\ {}^1D \rightarrow 2p^53s^23p^2[3d + 4d + 4s]\ {}^{1,3,5}L$ transitions in atomic Si.

Transition	$E_{calc.}$	gf	$E_{meas.}$	Peak
$^1D_2$ - 3d $(^3P)^1D_2$	106.43	0.0031		
$^1D_2$ - 3d $(^1D)^1F_3$	106.47	0.0058	106.57	17
$^1D_2$ - 3d $(^1D)^1P_1$	107.08	0.0052	107.03	19
$^1D_2$ - 3d $(^1D)^3P_2$	107.18	0.0076	107.20	20
$^1D_2$ - 3d $(^1D)^3P_2$	107.31	0.0045		
$^1D_2$ - 3d $(^1D)^1P_1$	107.33	0.0066	107.35	21
$^1D_2$ - 3d $(^1D)^1F_3$	107.39	0.0148	107.44	22
$^1D_2$ - 3d $(^1D)^3G_3$	107.69	0.0102	107.69	24
$^1D_2$ - 3d $(^1S)^1F_3$	108.66	0.0057		
$^1D_2$ - 3d $(^1S)^1P_1$	108.76	0.0028		
$^1D_2$ - 3d $(^3P)^1D_2$	108.88	0.0092		
$^1D_2$ - 3d $(^1S)^3D_2$	109.06	0.0039		
$^1D_2$ - 3d $(^1S)^1D_2$	109.11	0.0101		
$^1D_2$ - 4d $(^1D)^3P_1$	106.85	0.0035		
$^1D_2$ - 4d $(^3P)^3F_3$	106.87	0.0035		
$^1D_2$ - 4d $(^3P)^5D_1$	106.87	0.0075	106.84	18
$^1D_2$ - 4d $(^3P)^3F_3$	106.98	0.0112	107.03	19

Continued.

Table 6.3. Continued.

Transition	$E_{calc.}$	gf	$E_{meas.}$	Peak
$^1D_2$ - 4d $(^3P)^3D_3$	107.02	0.0024		
$^1D_2$ - 4d $(^3P)^1D_2$	107.44	0.0041	107.44	22
$^1D_2$ - 4d $(^1D)^3D_2$	107.61	0.0033	107.57	23
$^1D_2$ - 4d $(^1D)^1F_3$	107.62	0.0028		
$^1D_2$ - 4d $(^1D)^3P_2$	107.67	0.0036		
$^1D_2$ - 4d $(^1D)^3D_1$	107.70	0.0045		
$^1D_2$ - 4d $(^3P)^1F_3$	107.82	0.0046		
$^1D_2$ - 4d $(^3P)^3D_3$	107.86	0.0081	107.86	26
$^1D_2$ - 4d $(^1D)^1F_3$	108.51	0.0111	108.51	28
$^1D_2$ - 4s $(^1D)^1P_1$	104.51	0.0032	104.56	1
$^1D_2$ - 4s $(^1D)^1F_3$	105.36	0.0107	105.33	8
$^1D_2$ - 4s $(^1D)^1F_3$	105.69	0.0082	105.65	11
$^1D_2$ - 4s $(^1D)^1D_2$	106.37	0.0099	106.28	16

6.2.3 Transitions from the $2p^63s^23p^2\ ^1S_0$ level

In principle, from the $^1S_0$ level transitions can take place to the ^1L and ^3L terms. But in the present case most of the ^1L terms have been observed almost pure LS coupled, therefore, strong transitions are expected only to the ^1L terms. In calculations two strong transitions have been predicted to the (^1S) 3d ^1P and (^3P) 3d ^1P terms at 107.92 eV and 108.93 eV respectively. The corresponding gf-values were 0.0153 and 0.0161 respectively. The identification of the $^1S \rightarrow (^1S)\ ^1P$ term is not possible as it falls in the region dominated by the strong ^3P, $^1D \rightarrow$ 4d transitions. However, the predicted position of the $^1S \rightarrow (^3P)\ ^1P$ transition does not coincide with any other transition arising from ^3P or ^1D levels, therefore, if absorption is present from ^1S level then the identification of this transition should not be a problem. But corresponding to this transition a very weak feature is present. Therefore, it is inferred that under the conditions of our experiment the ^1S population is very small relative to the populations of ^3P and ^1D levels.

6.3 Comparison between the 2p absorption in atomic silicon and gas phase silane

The results of 2p absorption in SiH_4 (Hayes *et al.* 1971, Hayes and Brown 1972) reveal two kinds of resonances. One type include a broad structure, observed in the lower energy region, assigned to the excitations of inner-shell 2p electrons into the first empty molecular orbital. This is a typical molecular effect and is not found in the 2p absorption spectrum of atomic Si. The second type of resonances include atomic-like Rydberg series converging to the 2p ionisation thresholds. In order to provide interpretation for the sharp features the united atom approach has frequently been used (Hayes *et al.* 1971, Hayes and Brown 1972, Nenner 1987). In this approach, the distance between the two nuclei is allowed to become zero so that the Hamiltonian for the molecule reduces to that of an atom whose nuclear charge is the sum of the nuclear charges of the atoms composing the molecule. Each molecular orbital then has been labelled by the united-atom orbital into which it degenerates when the nuclei are brought together. The united atom for the SiH_4 is Ar, and the L shell spectrum of argon has been studied by Nakamura *et al.* (1968) and by Watson and Morgan (1969). The electron energy loss spectrum of argon has been reported by King *et al.* (1977).

Two groups of Rydberg series are found in argon, arising from the excitation of a single 2p electron to 4s and higher s levels and to 3d and higher d levels. Therefore, the sharp atomic-like features observed in the photoabsorption spectra of SiH_4, analogous to argon, have been assigned to the (n+1)s and nd Rydberg series. The photoabsorption spectrum of SiH_4 measured by Hayes and Brown (1972), along with the assignments given by them, are shown in figure 6.3. According to Hayes and Brown (1972), the $L_{III, II}$ spectrum of SiH_4 arises from transfer of a single silicon 2p electron to empty molecular-orbital states. The point symmetry of SiH_4 in its ground electronic state is T_d, and in this symmetry s orbitals transform like A_1 and p orbitals like F_2; d orbitals split into a triply degenerate (F_2) and a doubly degenerate (E). The ground configuration of SiH_4 is $1a_1^2\ 2a_1^2\ 1f_2^6\ 3a_1^2\ 2f_2^6$ ($^1A_1$) and allowed electric dipole transitions occur to the underlined F_2 states in the excited configurations listed below:

$$
\begin{aligned}
&1f_2^5\ na_1\ (^{1,3}\underline{F_2})\ n \geq 4 \quad (a),\\
&1f_2^5\ nf_2\ (^{1,3}\underline{F_2},\ ^{1,3}E,\ ^{1,3}A_1)\ n \geq 3 \quad (f),\\
&1f_2^5\ ne\ (^{1,3}\underline{F_2},\ ^{1,3}F_1)\ n \geq 1 \quad (e).
\end{aligned}
\qquad (6.1)
$$

The index n represents the molecular orbital in order of occurrence as a function of energy. For example, n is one or greater in the excitation series (e) because the doublet type e occurs for the first time in the excited configuration (Hayes and Brown 1972). In equation (6.1) series (a) represents the transitions arising from the excitation of a 2p electron to the 4s and higher orbital. Series (f) and (e) correspond to the 2p to 3d and higher d transitions.

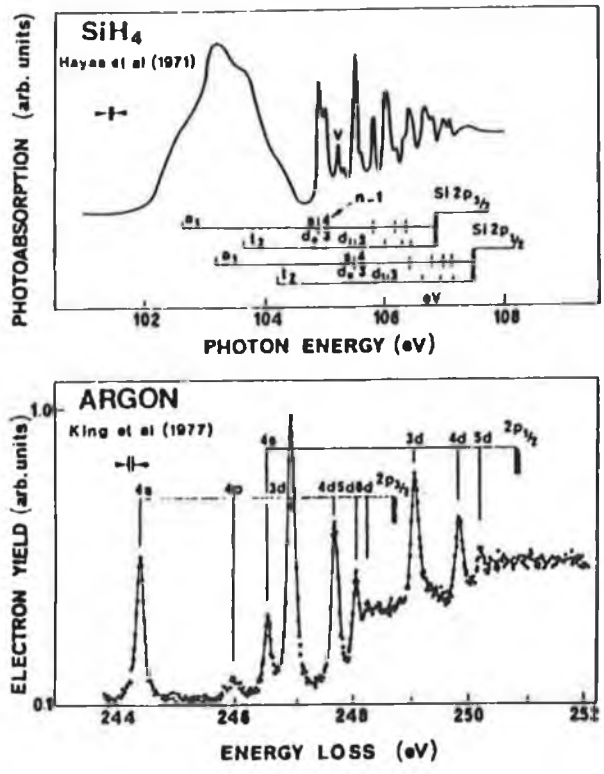

Figure 6.2

Comparison of the 2p photoabsorption spectrum of silane (top) with the electron energy loss spectrum near the Ar 2p edge (bottom) (from Nenner 1987).

The comparison between the 2p photoabsorption spectrum of SiH_4 and the electron energy loss spectrum of Ar has been made by Nenner (Figure 6.2). It was suggested by Nenner (1987) that the molecular field brought by the hydrogen atoms around silicon atom should be very weak. For the H_2S molecule it has been suggested by Brechignac *et al.* (1991) that hydrogen atoms do not perturb appreciably the inner-shell spectra of sulphur. Therefore, the 2p photoabsorption spectrum of SiH_4 may show some similarities with the corresponding spectrum of atomic Si. The comparison between their spectra are shown in figure 6.4. It can be

seen from this comparison that both spectra have a number of discrete transitions in the same energy region. While there is no simple one-to-one correspondence between the spectra the features joined by a sloping line 5 in series (a) of SiH_4 and the peaks 7 and 13 are very similar in appearence and energy positions. In SiH_4 these peaks have been assigned to the 2p → 5s transitions. Their measured energies

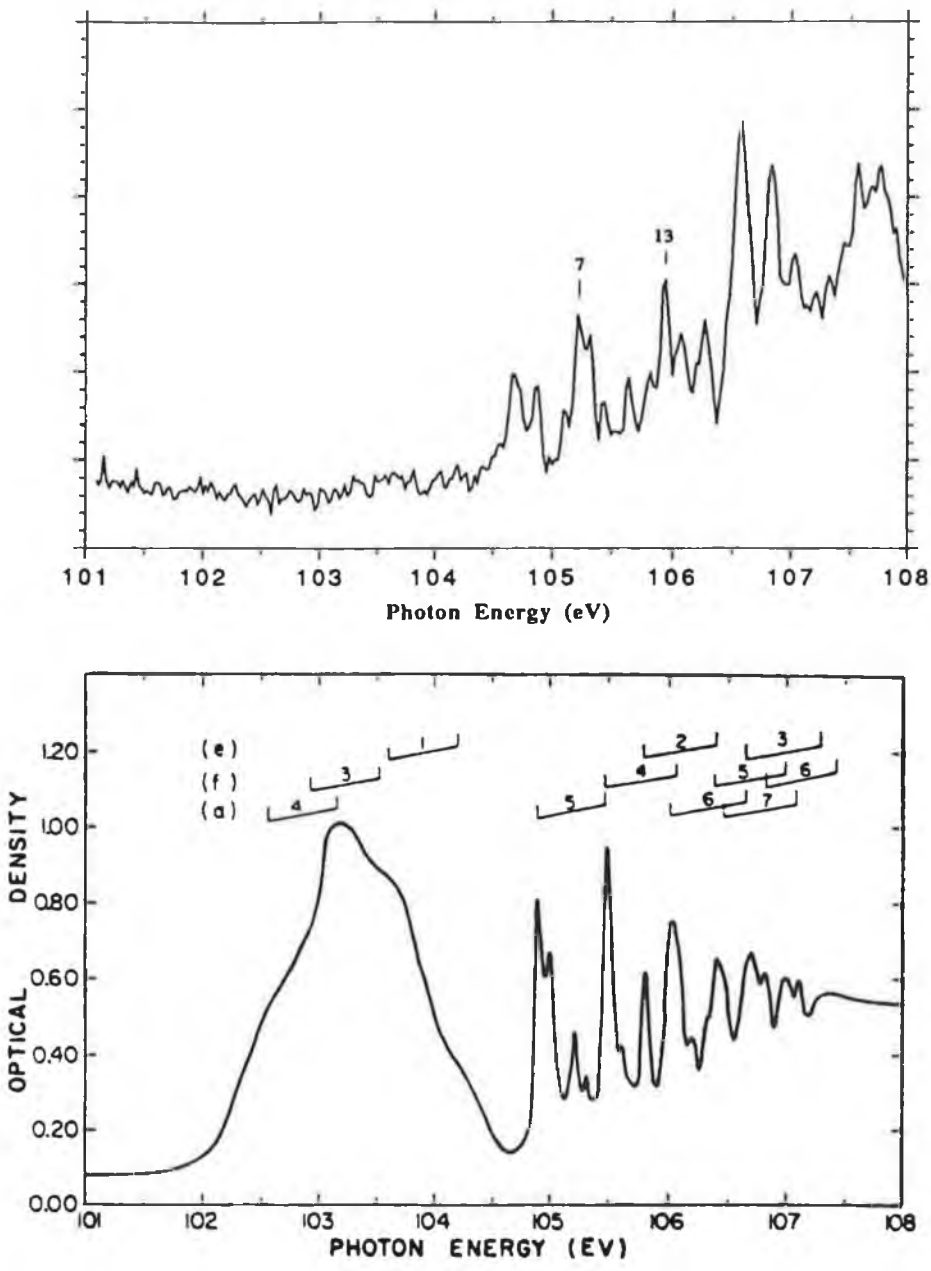

Figure 6.3

Comparison of the 2p photoabsorption spectrum of atomic silicon (top: this work) with the gas phase 2p photoabsorption spectrum of silane (bottom: from Hayes *et al.* 1972).

are 104.92 and 105.52 eV. The measured difference of 0.7 eV between these peaks has been associated with spin-orbit interaction produced due to $2p^5$ core of silicon (Hayes and Brown 1972). The energies of the peaks 7 and 13, assigned to the $2p \rightarrow 4s$ transitions (this work), in the photoabsorption spectrum of atomic Si have been measured at 105.24 eV and 105.94 eV and have a splitting of 0.7 eV which is in agreement with the spin-orbit splitting produced by the $2p^5$ core of silicon in silane. This agreement is suggestive but may be no more than coincidental. It is very difficult to make an overall comparison of the photoabsorption spectra of atomic silicon and silane as the silicon atom in silane is not isoelectronic to the free silicon atom. In order to examine the effects of hydrogen bonding on the inner-shell spectra of second-row atoms more comparisons are required. These comparisons could help to know in which direction the shift in the 2p ionization energies takes place. As the 2p absorption spectra of second-row atoms Na, Mg and Al exhibits strong multiply excited states, therefore, their comparisons with the corresponding spectra of hydrides can help in understanding the probability of multiply excited states in molecules.

6.4 Conclusions

Photoabsorption spectrum of atomic silicon arising from the 2p excitation has been interpreted with the help of configuration-interaction atomic structure calculations. The ground configuration $2p^63s^23p^2$ includes the ^3P, ^1D and ^1S levels. Strong absorption has been observed from the lower ^3P and ^1D levels, however, no significant absorption has been observed from the highest ^1S level.

The 2p absorption in atomic Si is found to exhibit the spectrum arising from the $2p^63s^23p^2 \rightarrow 2p^53s^23p^2$ [nd + (n+1)s, $n \geq 3$] one-electron excitations only. Transitions to the $2p^63s^23p^2 \rightarrow 2p^53s3p^3np$ two-electron series have not been observed which is in contrast with the 2p absorption spectra of Mg and Al neutrals. The $2p^53s^23p^2(n+1)s$ series has been found not to be significantly mixed with the $2p^53s^23p^2nd$ and $2p^53s3p^3np$ series which is analogous to the 2p absorption in Mg and Al neutrals. The interaction between the $2p^53s^23p^2nd$ series and the doubly excited $2p^53s3p^4$ configuration has been found to persist but weak as compared to the Mg and Al cases (see chapters 4 and 5). The lower energy region in atomic Si, analogous to the 2p absorption spectra of the Mg and Al atoms, has been found to be dominated by the $2p \rightarrow 4s$ transition array.

Comparison has been made between the 2p photoabsorption spectra of atomic silicon and gas phase silane. Some of the features observed in the 2p photoabsorption spectrum of SiH_4 and atomic silicon have been found very similar in appearance and energy positions. However, on the whole the members of Ryberg series observed in SiH_4 do not show strong resemblance with that of the atomic silicon spectrum. This is not surprising even if it is assumed that the 2p absorption spectrum of atomic silicon is not influenced to any great extent by the hydrogen atoms in silane. Atomic silicon is an open system and in the present experiment absorption is taking place from various levels of the ground configuration. On the other hand, in silane silicon atom is isoelectronic to argon and is behaving like a closed system. Also in silane absorption is taking from a single well-defined ground level.

6.5 References

Aksela H, Aksela S, Ala-Korpela M, Sairanen O-P, Hotokka M, Bancroft G M, Tan K H and Tulkki J, 1990, Phys. Rev. A **41**, 6000.

Brechignac C, Broyer M, Cahuzac Ph, de Frutos M, Labastie P and Roux J-Ph, 1991, Phys. Rev. Lett. **67**, 1222.

Clark C W, 1987, Phys. Rev. A **35**, 4865.

Connerade J P, Esteva J M and Karnatak R C (eds.), 1987, "*Giant resonances in Atoms, Molecules and Solids*" (NATO ASI Series B) Vol. **151** (New York: Plenum).

Connerade J P, Garton W R S and Mansfield M W D, 1971, Astrophys. J. **165**, 203.

Connerade J P and Karnatak R C, 1990, Comment. At. Mol. Phys. **24**, 1.

Costello J T, Kennedy E T, Sonntag B F and Clark C W, 1991, Phys. Rev. A **43**, 1441.

de Souza G G B, Morin P and Nenner I, 1986, Phys. Rev. A **34**, 4770.

Hayes W, Brown F C and Kunz A B, 1971, Phys. Rev. Lett. **27**, 774.

Hayes W and Brown F C, 1972, Phys. Rev. A **6**, 21.

Hudson E, Shirley D A, Domke M, Remmers G, Puschmann A, Mandel T, Xue C and Kaindl G, 1993, Phys. Rev. A **47**, 361.

Hudson E, shirely D A, Domke M, Remmers G and Kaindl G, 1994, Phys. Rev. **49**, 161.

Ishiguro E, Iwata S, Mikuni A, Suzuki Y, Kanamori H and Sasaki T, 1987, J. Phys. B: At. Mol. Phys. **20**, 4725.

King G C, Tronc M, Read F H and Bradford R C, 1977, J. Phys. B Atom. Molec. Phys. **10**, 2479.

Martin W C and Zalubas R, 1983, J. Phys. Chem. Ref. Data, 12, 323.

Nakamura M, Sasanuma M, Sato S, Watanahe M, Yamashita H, Iguchi Y, Ejira A, Nakai S, Yameguchi S, Sagawa T, Nakai Y and Oghio T, 1968, Phys. Rev. Lett. **21**, 1303.

Nenner I, 1987, "*Giant resonances in Atoms, Molecules and Solids*", eds. Connerade J P, Esteva J M and Karnatak R C (NATO ASI Series B) Vol. **151** (New York: Plenum).

Sutherland D G J, Liu Z F, Bancroft G M and Tan K H, 1994, Nuclear Instruments and Methods in Physics Research B **87**, 183 [Proceedindings of the 16th International Conference on X-RAY AND INNER-SHELL PROCESSES (X' 93) Debrecen, Hungary, July 12-16]

Watson W S and Morgan P J, 1969, J. Phys. B **2**, 277.

Wolff H W, Radler K, Sonntag B and Haensel R, 1972, Zeitschreift fur Physik. **157**, 353.

Chapter 7

PHOTOABSORPTION IN VALENCE-EXCITED ISOELECTRONINC SPECIES

Photoabsorption investigations of species isoelectronic to magnesium and aluminium, prepared in their valence-excited states, have been carried out. Interpretation for the observed spectra is provided on the basis of configuration-interaction atomic structure calculations. In order to obtain insight into the dynamics of excited states a comparison is made with the ejected-electron spectra of the corresponding atomic and ionic species arising from the autoionising and Auger transitions following electron- and photon-impact excitation/ionisation respectively. A qualitative interpretation for the population and depopulation of the valence-excited levels in the laser plasma is given.

7.1 Introduction

The photoabsorption measurements in valence-excited species allow to study the core-excited states which do not connect to the ground state via the electric dipole operator. The experimental data on these states in atoms and ions are required for understanding the many-electron dynamics, laboratory plasmas and astrophysical phenomena (Mosnier *et al.* 1994). In photoabsorption measurements of these states the species of interest are prepared beforehand in a specific valence-excited state. Such experiments were carried out in the inner-shell regime first using photoabsorption spectroscopy (Lucatorto and McIlrath 1977, Sugar *et al.* 1979) and then using photoelectron spectroscopy (Bizau *et al.* 1985). Also, the controllable excitation of a valence electron into higher states offers the unique opportunity to produce gradual modifications in the effective potential of an inner-shell electron (Sonntag *et al.* 1986, Ferray *et al.* 1987). The specific properties of high intensity synchrotron light sources (wigglers, undulators) combined with highly selective excitation mechanisms and detection techniques have initiated measurements on excited atoms providing an ever more complete description of the photoionization process, e.g. resonant photoionization of excited aligned species (Meyer *et al.* 1987), direct photoionization cross-sections of excited atoms

(Cubaynes *et al.* 1989), angular dependence of ejected electrons in the photoionization of excited aligned atoms (Pahler *et al.* 1992).

In all the experiments mentioned above, the excitation technique used was based on the pioneering works of Bradley (1969), Bradley *et al.* (1973), McIlrath (1969), and McIlrath and Carlsten (1973). In this technique a high power tunable dye laser selectively pumps ground state atoms into an excited state. The population density of the excited state thus obtained is large enough so as to make a photoabsorption or a photoelectron spectrum originating from it readily observable. The applicability of the technique to a wide range of atomic species is only limited by the tuning range of the high power dye laser. As the spectral range covered by currently available high power dye lasers is limited to the visible region, excited state studies have been restricted to only a few neutral species to date. The dual laser-produced plasma technique has enabled us (i) to study photoabsorption both in atoms and ions prepared in their valence-excited states, and to extend them along the sequences.

Very little is known about the kinetics of the valence-excited states in the laser-plasmas. The photoabsorption studies reported in this work though carried out from a spectroscopic point of view could be very stimulating for theoretical and experimental studies regarding the modelling of laser-plasmas.

7.2 Magnesium sequence in excited state absorption

As far as we know, no previous results exist for 2p photoabsorption of species isoelectronic to Mg in valence excited states. In the case of ions this may be due to the experimental difficulties in generating the sufficient densities of absorbing species and preparing them in selectively excited states beforehand for absorption measurements. An extensive study of the ejected-electron spectrum of magnesium autoionising levels excited by low-energy electron impact was published some years ago by Pejcev *et al.* (1977). At the low incident electron energies (62, 100 and 400 eV) used by these authors, the $2p^5 3s^2 3p$ autoionising levels are populated via quadrupole excitation of a 2p ground state electron. Although the presence of these levels was mentioned no assignments were given. Recently, a comprehensive study of the Auger spectra of atomic Al following 2p

photoionization has been reported by Malutzki *et al.* (1987). The decay of the $2p^53s^23p\ ^{1,3}L$ levels to the $2p^63s$, 3p and 3d channels have been examined in detail.

7.2.1 Results and term analyses

The 2p-subshell absorption spectra of Mg, Al^+ and Si^{2+} in their valence-excited states are shown in figure 7.1. The spectra are dominated by the $2p^53s^23p$ transition array. The absorption structures of this transition array appear as two groups of lines one originating from the ^3P metastable levels and the other group from the short-lived ^1P level (Figure 7.1). The $3s3p\ ^1P$ (^3P) levels (neglecting fine structure) in Mg, Al^+ and Si^{2+} are located approximately 4.3 eV (2.7eV), 7.4 eV (4.6 eV) and 10.3 eV (6.5 eV) above the ^1S ground state (Martin and Zalubas, 1979, 1980, 1983). We note that the higher energy lines associated with the ^3P initial states are in each case more intense than the lower energy lines associated with the ^1P initial state (see Figure 7.1). We also note that in the experimental conditions of figure 7.1 the gross features of the three spectra remain similar, thereby indicating similar plasma dynamics and atomic physics for all three species. A strong pair of resonances is also present on the short wavelength side of each spectrum. These lines are easily recognised as the $2p^63s\ ^2S_{1/2} \rightarrow 2p^53s^2\ ^2P_{1/2,3/2}$ transitions in the sodium-like structure (Esteva and Mehlman, 1974; Mosnier *et el.* 1987) and indicate that in the conditions of figure 7.1 a large fraction of ions exist in the ground state of the Na-like species.

Line measurements together with term assignments are listed in table 7.1. The computed transition energies and corresponding gf-values were obtained with the help of configuration-interaction atomic structure calculations (see chapter 2). The $2p^63s3p$ and $2p^63p3d$ configurations were included in the initial states expansion while $2p^53s^23p$, $2p^53s3p3d$ and $2p^53p3d^2$ configurations were included in the final states expansion. With these expansions the predicted term energies were found almost in agreement with the measured ones. Therefore, no scaling of the various F, G and R integrals and spin-orbit parameters was necessary which is in contrast with our calculations carried out for the same sequence in ground state absorption (see Chapter 4). In the calculations carried out for the spectra from ground state absorption, it was not possible to include all the possible significant interactions. To provide an approximate allowance for the neglected weak

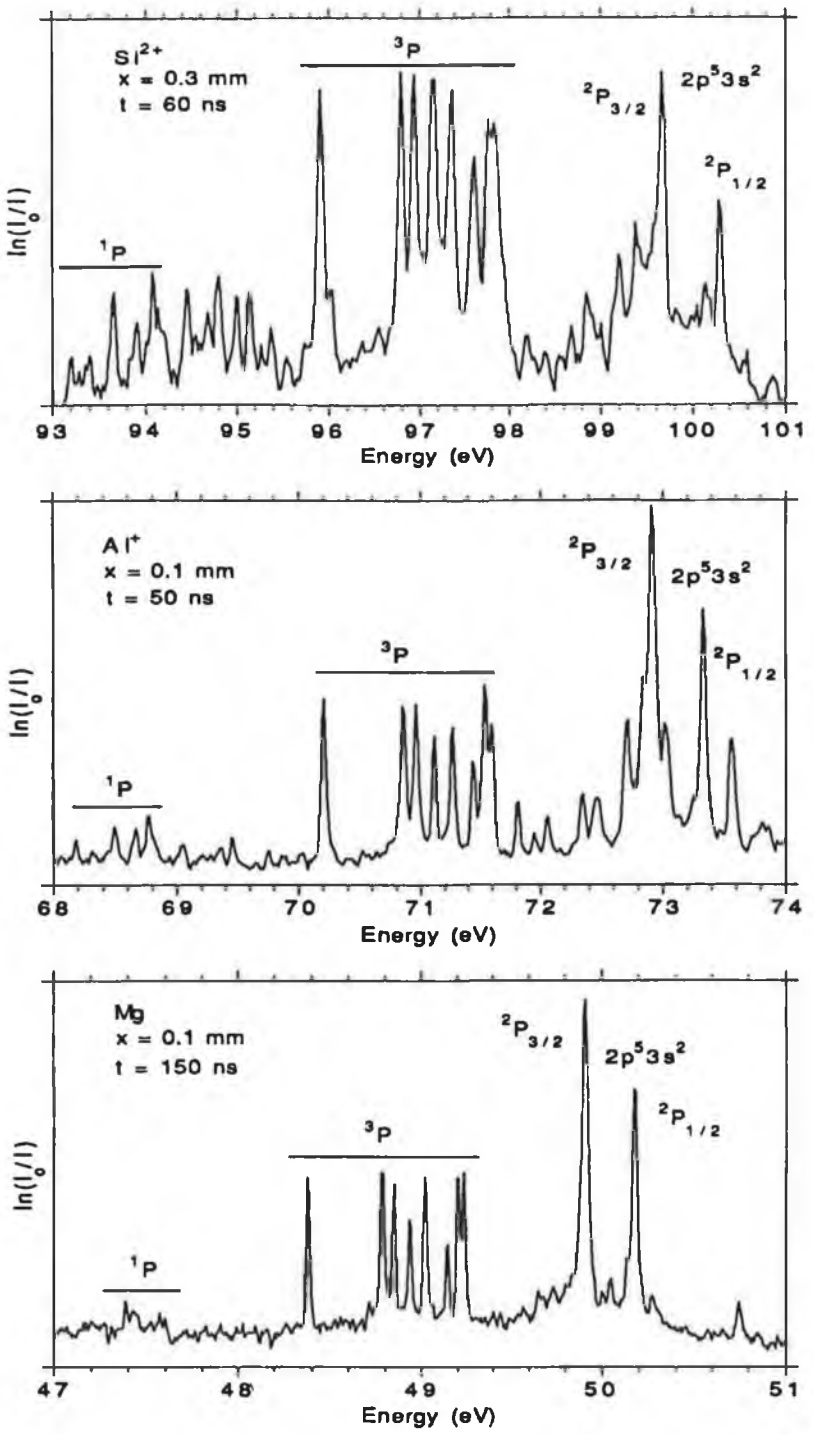

Figure 7.1

The relative photoabsorption spectra of Mg (a), Al^+ (b) and Si^{2+} (c) in the region of the $2p^63s3p\ ^{3,1}P$ -> $2p^53s^23p\ ^{3,1}L$ transition array as obtained with the DLPP technique. The optimum values for the position of the absorbing target (x) and time delay (t) between the two laser pulses are indicated on each spectrum. The spectral intervals for the transitions having $2p^63s3p\ ^3P$ or ^1P as initial state are delineated in each spectrum. Also marked in each spectrum are the $2p^53s^2\ ^2P_{1/2,3/2}$ resonances in the sodium-like ion.

configuration-interaction effects the various Slater integrals were reduced by suitable amounts for which the calculated term energies and distribution of oscillator strength was found in very good agreement with the measured level structure. In the case of excited state absorption the interactions included were found sufficient enough to reproduce the observed structure, in particular for term energies; therefore, there was no need for scaling the Slater integrals.

In the case of transitions from ^3P as initial states, line assignments are straightforward as the computed values are in very good agreement with the measured values. In the case of transitions having ^1P initial state, it was found that the *ab initio* computed transition energies differed from the measured values by a constant amount roughly equal to 0.5 eV in all three spectra. This is due to an overestimation of the $G^1(3s,3p)$ exchange integral. Although an abundant literature is available on the subject of the precise calculation of the optical levels in the magnesium series (see e.g. Martin and Zalubas, 1979, 1980, 1983), it was found sufficient for the purpose of assigning inner-shell transitions to apply a constant correction factor to the relevant transition energies. The value of the correction is equal to the amount that must be added to the *ab initio* energy value of $2p^63s3p\ ^1P$ in order to make the ^3P - ^1P energy interval exactly equal to its tabulated value (Martin and Zalubas, 1979, 1980, 1983). This factor is equal to 5796 cm^{-1} (Mg), 4845 cm^{-1} (Al^+) and 4462 cm^{-1} (Si^{2+}). This simple constant shifting procedure brings the calculated values in good agreement with the measured ones; the only exception being the $^1P_1$ - $^1S_0$ transitions which are not present in our spectra . In view of the general good agreement previously observed for all levels except $2p^53s^23p\ ^1S_0$, we surmise that our *ab initio* unscaled calculations provide only a mediocre description of the wavefunction of the latter. Thus, the corresponding transition energies and strengths quoted in table 7.1 are only indicative. This view is supported by the interpretation of the photoinduced 2p Auger spectrum of atomic aluminium by Malutzki *et al.* (1987) in which similar difficulties are reported and discussed in the case of the calculation of the Auger decay rate of $2p^53s^23p\ ^1S_0$.

In a pure LS coupling picture, the $2p^63s3p \rightarrow 2p^53s^23p$ spectrum exhibits the characteristic $^{3,1}P \rightarrow {}^{3,1}S$, $^{3,1}P, {}^{3,1}D$ structure with cross-system transitions being forbidden. However, the observed spectra are more complex than suggested by this picture as a number of strong lines must be assigned to LS forbidden transitions (see Table 7.1). Comparison with the 2p valence excited photoabsorption spectra in the sodium sequence provides a straightforward explanation for this observation. In effect, it has been reported by several authors

(Froese-Fisher, 1986; Brilly *et al.* 1990) that the structure of the $2p^63p \rightarrow 2p^53s3p$ spectrum is due mostly to large spin-orbit mixing of different terms of the upper configuration produced by the $2p^5$ open core. It is plain that the addition of an extra electron in the 3s subshell should only be marginal in this respect and we therefore expect strong departure from LS coupling for some of the terms of the $2p^53s^23p$ configuration. Wavefunction composition of the relevant triplet and singlet states in Mg, Al^+ and Si^{2+} is given in table 7.2 in increasing order of energy. Correlation mixing with $2p^53s3p3d$ amounts to 1.5% at most and therefore has a minor influence over the energy level structure of the $2p^53s^23p$ configuration. On the other hand, when one considers autoionization /Auger decay, it is well known that such configuration effects play an essential role in the understanding of the origin of satellite features attributed to electron correlations (see below for further discussion). The $^3S_1$, $^3D_3$ and $^1S_0$ terms have been omitted from this table as they are all 95% or more pure LS. Complete breakdown of LS coupling is exemplified by the almost complete mixing between $^3P_2$ and $^1D_2$. In view of the rather arbitrary nature of LS labelling in these cases, we simply designate a state by considering only the leading eigenvector, hence the double appearance of the $^3P_2$ state in table 7.2. Also, the $^1P_1$ state is placed below $^3P_1$ as a result of strong mixing between them.

Following our previous conclusions regarding the relative intensity patterns in figure 7.1, we infer from figure 7.1 and table 7.2 that on going from Mg to Si^{2+} , the dominant effect remains spin-orbit mixing due to the open core since the increase in nuclear charge has little influence on the restructuring of the energy level system of the $2p^53s^23p$ configuration. This is in sharp contrast with the behaviour of the $2p^53s^23d$ configuration observed in photoabsorption along the same isoelectronic sequence (see chapter 4).

Table 7.1. Measured energies, calculated energies and gf - values for the $2p^6 3s3p\ ^{3,1}P \rightarrow 2p^5 3s^2 3p\ ^{3,1}L$ transitions in Mg, Al^+ and Si^{2+}.

Transition	Mg			Al^+			Si^{2+}		
	Meas. (eV)	Calc. (eV)	gf	Meas. (eV)	Calc. (eV)	gf	Meas. (eV)	Calc. (eV)	gf
$^1P_2$-$^3S_1$		48.202	0.0324	70.21	70.211	0.0315	95.99	95.964	0.0298
$^3P_1$-$^3S_1$	48.38	48.406	0.0317		70.223	0.0314		95.993	0.0316
$^3P_0$-$^3S_1$		48.407	0.0132		70.231	0.0133		96.008	0.0138
$^3P_2$-$^3D_3$	48.79	48.752	0.191	70.86	70.812	0.206	96.80	96.803	0.2157
$^3P_2$-$^3D_2$		48.812	0.0110		70.905	0.0115		96.924	0.0105
$^3P_1$-$^3D_2$	48.85	48.816	0.102	70.97	70.917	0.1155	96.95	96.954	0.1226
$^3P_2$-$^3D_1$		48.907	0.0004		71.052	0.0004		97.144	0.0007
$^3P_1$-$^3D_1$		48.911	0.0125		71.064	0.0152		97.175	0.0147
$^3P_0$-$^3D_1$	48.94	48.912	0.0547	71.12	71.072	0.0613	97.16	97.182	0.0651
$^3P_2$-$^3P_2$	49.02	48.993	0.0429	71.27	71.223	0.0542	97.36	97.388	0.0653
$^3P_1$-$^3P_2$		48.996	0.0358		71.235	0.0370		97.419	0.0391
$^3P_2$-$^1P_1$		49.129	0.0147		71.416	0.0182		97.664	0.0205
$^3P_1$-$^1P_2$	49.14	49.133	0.0290	71.44	71.428	0.0307	97.62	97.688	0.0340
$^3P_0$-$^1P_1$		49.135	0.0009		71.432	0.0001		97.703	0.0002
$^3P_2$-$^3P_2$	49.20	49.177	0.0879	71.54	71.498	0.0975	97.77	97.803	0.1016
$^3P_1$-$^3P_2$		49.180	0.0001		71.511	0.0000		97.826	0.0000
$^3P_1$-$^3P_0$		49.193	0.0286		71.527	0.0336		97.826	0.0369
$^3P_2$-$^3P_1$	49.22	49.226	0.0340	71.60	71.577	0.0371	97.84	97.904	0.0400
$^3P_1$-$^3P_1$		49.229	0.0085		71.589	0.0104		97.927	0.0112
$^3P_0$-$^3P_1$		49.231	0.0141		71.593	0.0166		97.934	0.0176
$^3P_1$-$^1S_0$		50.973	0.0001		75.097	0.0001		102.349	0.0002
$^1P_1$-$^3S_1$	46.766		0.0005		67.415	0.0004		92.271	0.0004
$^1P_1$-$^3D_2$	47.20	47.175	0.0236	68.19	68.139	0.0229	93.20	93.229	0.0252
$^1P_1$-$^3D_1$	47.31	47.270	0.0133	68.44	68.440	0.0098	93.40	93.447	0.0095
$^1P_1$-$^3P_2$	47.39	47.355	0.0618	68.49	68.458	0.0726	93.65	93.694	0.0749
$^1P_1$-$^1P_1$	47.52	47.493	0.0348	68.67	68.648	0.0330	93.92	93.971	0.0294
$^1P_2$-$^3P_2$	47.57	47.540	0.0525	68.77	68.732	0.0647	94.08	94.106	0.0741
$^1P_1$-$^3P_0$		47.553	0.0002		68.751	0.0002		94.106	0.0003
$^1P_1$-$^3P_1$	47.60	47.588	0.0254	68.81	68.812	0.0246	94.14	94.206	0.0237
$^1P_1$-$^1S_0$		49.333	0.0345		71.913	0.0554		98.628	0.0714

Table 7.2. Calculated purity of some of the terms (in increasing order of energy) of the $2p^5 3s^2 3p$ configuration in Mg, Al^+ and Si^{2+}. Term labeling (left -hand side column) is obtained by considering the leading component only.

Term	$^3D_2$			$^3D_1$			$^3P_2$			$^3P_1$			$^1D_2$			$^1P_1$		
	Mg	Al^+	Si^{2+}	Mg	Al^+	Si^{2+}	Mg	Al^+	Si^{2+}	Mg	Al^+	Si^{2+}	Mg	Al^+	Si^{2+}	Mg	Al^+	Si^{2+}
$^3D_2$	78	79	78										17	14	14			
$^3D_1$				70	74	73				10	8	10				18	14	15
$^3P_2$							51	51	54				44	44	41			
$^1P_1$				27	22	24				25	27	27				46	47	46
$^3P_2$	17	16	17				43	42	39				37	39	41			
$^3P_1$										62	59	59				33	35	36

7.2.2 Decay of the levels of $2p^53s^23p$ configuration

A detailed study of the decay of $2p^53s^23p$ configuration has been carried out in Al^+ by Malutzki *et al.* (1987). In this study the levels of $2p^53s^23p$ configuration were populated following 2p photoionization of atomic Al and Auger spectra were measured. The observed decay is mainly into the $2p^63p\varepsilon l$ and the $2p^63s\varepsilon' l''$ continua, respectively. The decay to the final states $2p^63s$, 3p and 3d are about 46%, 39% and 15% respectively. Decay to the $2p^63d$ final states is through electron correlations (Mosnier *et al.* 1994). The autoionisation of the levels of $2p^53s^23p$ configuration has been observed in the ejected-electron spectra of atomic Mg following electron-impact excitation.

In order to predict the kinetic energies of the electrons ejected upon autoionization and Auger decay, and compare our photoabsorption data, we have performed calculations for the $2p^63p$, $2p^63s$ and $2p^63d$ final states of the decay in Mg^+ and Al^{2+}. The values of the optical energy levels have been taken from Martin and Zalubas (Mg and Mg^+: 1980; Al^+ and Al^{2+}:1979). The results are summarised in tables 7.3 and 7.4 for Mg and Al^+ respectively.

From table 7.3, we observe that there is an excellent agreement (within 0.02 eV) between our predicted data and the ejected-electron lines numbered 26, 27, 29, 30, 31 and 32 in Pejcev *et al.* (1977) (see Figures 7.2 and 7.3) (Mosnier *et al.* 1994). Also we note that the intensity of this group of lines is stronger at lower incident electron energy (see Figure 7.3). We therefore conclude that this group of lines is due to the autoionising decay of the $2p^53s^23p$ $^{3,1}P,^{3,1}D$ states into the corresponding $2p^63p\varepsilon l$ continua. In the case of the decay $2p^53s^23p$ $^3S_1 \rightarrow$ $2p^63p$, we predict an energy of 39.02 eV for the ejected electron. No such line is present in Pejcev *et al.* (1977). Therefore, assuming statistical population of the initial states by electron impact, the autoionization transition probability of the $2p^53s^23p$ $^3S_1$ state into the $2p^63p\varepsilon l$ continuum appears to be substantially smaller than that of the $2p^53s^23p$ $^{3,1}P,^{3,1}D$ states into the corresponding $2p^63p\varepsilon l$ continua and the ejected-electron line is therefore too weak to be observed in the experimental conditions of Pejcev *et al.* (1977). We note that the same situation is also encountered in the 2p Auger spectrum of atomic aluminium (Malutzki *et al.* 1987).

It was suggested in Pejcev *et al.* (1977) that the lines numbered 43, 44 and

45 (the intensities of which exhibit the same pattern of behaviour as lines 26, 27, 29, 30, 31 and 32 when the energy of the incident electron beam is varied) appear to be due to the excitation of non-optical Mg I states which subsequently decay to $2p^63s$. This is confirmed by our photoabsorption measurements, the agreement in energy being within 0.02 eV for the three lines.The corresponding decays are: $2p^53s^23p\ ^3D_{1,2,3} \rightarrow 2p^63s$.

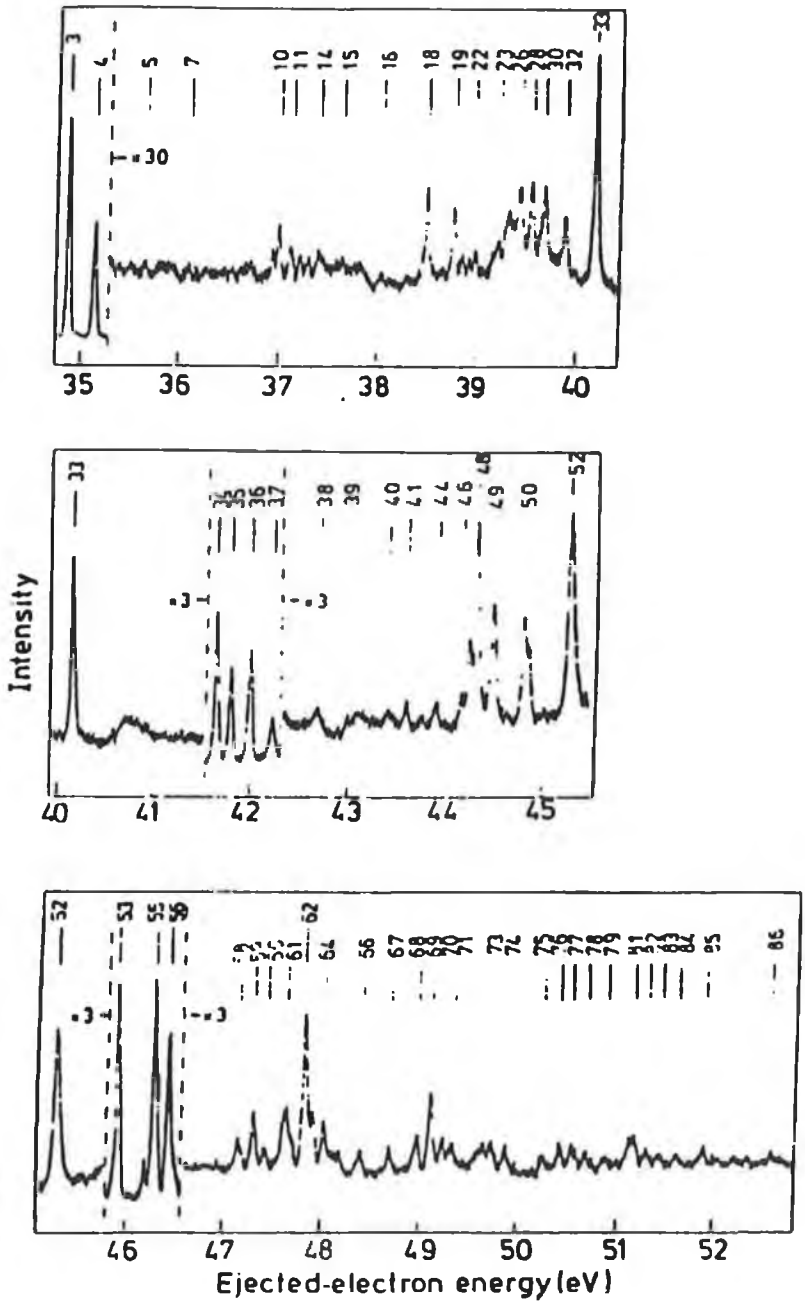

Figure 7.2

Ejected-electron spectrum of magnesium vapour following excitation by a 400 eV incident electron beam (from Pejcev *et al.* 1977)

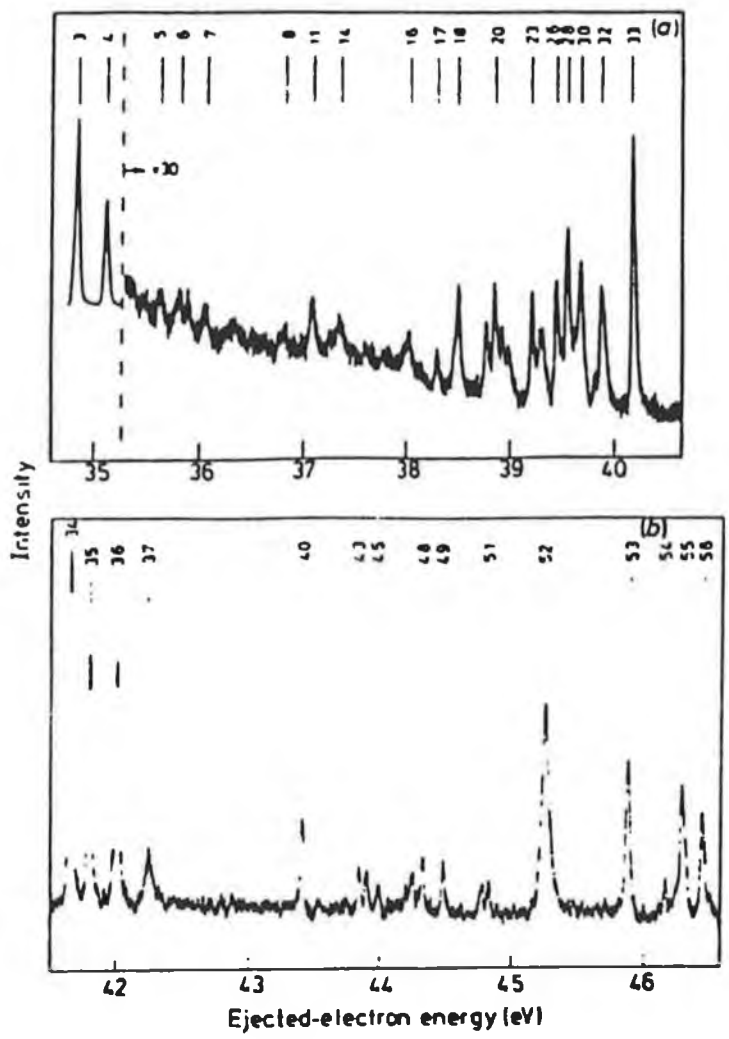

Figure 7.3

Ejected-electron spectrum of magnesium vapour following excitation by a 100 eV incident electron beam (from Pejcev *et al.* 1977)

The dependence of the intensity of the ejected-electron line numbered 40 (43.41 eV) in Pejcev *et al.* (1977) upon the energy of the low-energy incident electron beam suggests the assignment $2p^53s^23p\ {}^3S_1 \rightarrow 2p^63s$ for the corresponding autoionizing decay (see table 7.3). The ejected-electron lines numbered 46 (44.17 eV), 47 (44.25 eV) and 48 (44.32 eV) are possible candidates for the decay of the $2p^53s^23p$ states having dominant ^3P or ^1P character (table 7.3). The assignments are considered less definite in these cases for the dependence on incident energy differ appreciably for the three lines as discussed in Pejcev *et al.* (1977).

According to our data autoionisation decays of $2p^53s^23p$ to $2p^63d$ (16.510 eV) and $2p^64p$ (17.643 eV) -entirely due to electron correlations- would give rise to ejected-electrons with kinetic energies in the 34.585-35.44 eV and 33.452-34.311 eV ranges respectively. In the first case the presence of the very intense

$L_{2,3}M_1M_1$ Auger lines at 34.86 eV and 35.13 eV make the identification of the corresponding ejected-electron lines impossible in the spectrum of Pejcev *et al.* (1977). A different experimental technique would be required in this case to clarify this important point, *i.e.* the strength of electron correlations which result in $2p^63d$ as the final state of the autoionizing decay of $2p^53s^23p$. There is no evidence in Pejcev *et al.* (1977) for the presence of ejected electrons with kinetic energies corresponding to the second type of decay ($2p^64p$ final state) for which a possible class of correlation effects would be $3p \rightarrow 4p$ shake up excitation. We note that in the case of the photoinduced 2p Auger spectrum of atomic aluminium (Malutzki *et al.* 1987), the $2p^63d$ exit channel contributes about 15% of the overall intensity whereas $2p^64p$ has a negligible contribution.

Finally, we point out that in the spectrum of Pejcev *et al.* (1977) the group of lines we assigned to the $2p^53s^23p \rightarrow 2p^63p$ decay is stronger than the group of lines we assigned to the $2p^53s^23p \rightarrow 2p^63s$ decay, with, however, the notable exception of the lines corresponding to the decay of $2p^53s^23p\ ^3S_1$ in which case the opposite situation is observed. This seems to suggest that the 3p electron chiefly remains a spectator during the autoionizing decay of the $2p^53s^23p\ ^{3,1}P,^{3,1}D$ states resulting in $2p^63p\varepsilon l$ as a preferential decay channel.

Table 7.3. Energies of the electrons ejected upon autoionisation decay of the $2p^5 3s^2 3p\ ^{3,1}L$ states in magnesium.

		Ejected-electron energy (eV)	
E[a] (eV)	Autoionising Transition	Predicted[b]	Pejcev[c]
51.95	$2p^5 3s^2 3p\ ^3P_1$ - $2p^6 3s\ ^2S$	44.31[d]	
51.92	$^3P_0$	44.28	
51.91	$^3P_2$	44.27	
51.86	$^1P_1$	44.21	
51.73	$^3P_2$	44.09	
51.65	$^3D_1$	44.00	43.97 (45)
51.56	$^3D_2$	43.92	43.90 (44)
51.50	$^3D_3$	43.85	43.85 (43)
51.09	$^3S_1$	43.45	43.41 (40)
	$2p^5 3s^2 3p\ ^3P_1$ - $2p^6 3p\ ^2P$	39.88	39.86 (32)
	$^3P_0$	39.85	39.86 (32)
	$^3P_2$	39.84	39.86 (32)
	$^1P_1$	39.79	39.80 (31)
	$^3P_2$	39.66	39.67 (30)
	$^3D_2$	39.49	39.50 (27)
	$^3D_1$	39.58	39.60 (29)
	$^3D_3$	39.43	
	$^3S_1$	39.02	
	$2p^5 3s^2 3p\ ^3P_1$ - $2p^6 3d\ ^2D$	38.15	
	$^3P_0$	38.12	
	$^3P_2$	38.11	
	$^1P_1$	38.06	
	$^3P_2$	37.93	
	$^3D_2$	37.76	
	$^3D_1$	37.85	
	$^3D_3$	37.70	
	$^3S_1$	37.29	

[a] Energy obtained from the measurement of $2p^6 3s3p\ ^3P \rightarrow 2p^5 3s^2 3p\ ^{3,1}L$ transitions.

[b] Obtained from the Excited State Energy column and the optical energy levels of Mg and Mg^+ given in Martin and Zalubas (1980).

[c] The number in brackets is the line number as labeled in Pejcev *et al.* (1977).

[d] Tentative assignment.

Table 7.4. Energies of the electrons ejected upon autoionisation decay of the $2p^5 3s^2 3p\ ^{3,1}L$ states in Al^+.

		Ejected-electron energy (eV)	
E^a (eV)	Autoionising Transition	Predicted[b]	Malutzki
71.60	$2p^5 3s^2 3p\ ^3P_1$ - $2p^6 3s\ ^2S$	57.41	
71.54	$^3P_0$	57.35	
71.54	$^3P_2$	57.35	57.35
71.44	$^1P_1$	57.25	
71.27	$^3P_2$	57.08	57.05
71.12	$^3D_1$	56.93	
70.97	$^3D_2$	56.78	56.75
70.86	$^3D_3$	56.67	
70.21	$^3S_1$	56.02	56.05
	$2p^5 3s^2 3p\ ^3P_1$ - $2p^6 3p\ ^2P$	50.75	
	$^3P_0$	50.69	
	$^3P_2$	50.69	50.68
	$^1P_1$	50.59	
	$^3P_2$	50.42	50.38
	$^3D_2$	50.27	
	$^3D_1$	50.12	50.08
	$^3D_3$	50.01	
	$^3S_1$	49.36	49.38
	$2p^5 3s^2 3p\ ^3P_1$ - $2p^6 3d\ ^2D$	43.03	
	$^3P_0$	42.97	
	$^3P_2$	42.97	42.98
	$^1P_1$	42.87	
	$^3P_2$	42.70	42.68
	$^3D_1$	42.55	
	$^3D_2$	42.40	42.38
	$^3D_3$	42.29	
	$^3S_1$	41.64	

[a] Energy obtained from the measurement of $2p^6 3s3p\ ^3P \rightarrow 2p^5 3s^2 3p\ ^{3,1}L$ transitions.

[b] Obtained from the Excited State Energy column and the optical energy levels of Al^+ and Al^{2+} given in Martin and Zalubas (1979).
The energies of $2p^6 3s3p$, $2p^6 3s$, $2p^6 3p$ and $2p^6 3d$ from $2p^6 3s^2$ were taken as 4.64 eV, 18.83 eV, 20.85 eV and 28.57 eV respectively.

7.2.3 Absorption from metastable and dipole allowed levels

In a laser produced plasma, a complex combination of various collisional and recombination processes result in a spatial and temporal distribution of ions among the different ionisation stages in their ground state and various excitation states which include both optically accessible and inaccessible states from the ground state. Using the dual laser-produced plasma technique, by suitably regulating the laser power density on the absorbing target, the distance between the optical axis and the absorbing target, and the time delay between the absorbing plasma and the background continuum pulse one can optimise the absorbing species of one particular ionisation stage for absorption measurements. The versatility of this selective nature of the dual laser produced plasma technique, which exploits temporal and spatial evolution of laser plasmas, for the ground state absorption is evident from the space and time-resolved studies reported in chapter 3. However, in the case of excited state absorption, the optimisation of some particular initial state belonging to some specific ionisation stage is an extremely difficult task and is well exhibited in the photoabsorption measurements from the valence excited configuration $2p^63s3p$ in Mg, Al^+ and Si^{2+}. In all these cases the absorption features associated with the ^1P levels are relatively very weak compared to the absorption features associated with the ^3P levels. After a number of experiments we were hardly able to see the features associated with the ^1P levels although the calculated gf-values for the transitions arising both from the ^1P and ^3P levels were predicted of the same order with a few exceptions. We believe that in our photoabsorption measurements, made always during the cooling phase of the laser plasma, the relative populations of the ^1P levels was much less than the ^3P levels. A quantitative interpretation for the relative populations of ^1P and ^3P would only be obtained with the help of extensive modelling of the laser plasma. However, a qualitative interpretation for the relative population of initial states in the laser plasma can be provided by examining the mechanisms of their population/depopulation. Experimentally some information about the mechanisms of population/depopulation of these levels can be obtained by looking at the optical emission spectra of the laser plasma or by examining the time and space history of the initial states and taking into account the plasma conditions. The time and space history can be obtained with the help of time and space-resolved photoabsorption measurements of the absorbing plasma. Both these studies can provide some clues

regarding the relative population of ^3P levels but the temporal resolution of our system (≈ 10-15 ns) as determined by the continuum pulse was not suitable for investigating the time history of the dipole allowed ^1P levels which have life times less than 2 nano seconds. The time history of the nonmetastable as well as metastable levels can only be investigated together if the temporal resolution of the experimental system is at least less than the decay time of the nonmetastable levels. Therefore, on the basis of our time and space-resolved studies for the ^3P levels and space-resolved studies only for the ^1P levels, carried out during our photoabsorption measurements, we will examine the mechanisms of populations of these levels.

7.2.3(a) Kinetics of ^1P and ^3P populations

The kinetics of ^1P and ^3P levels are shown in Figure 7.2. In our absorption studies the plasma plume was probed during its cooling phase. Also the plasma plume was optimised for the Mg and Na-like absorbing species. No absorption from higher ion stages was present. Therefore, under such conditions, the collisional ionisation and excitation processes from the excited states should be negligible.

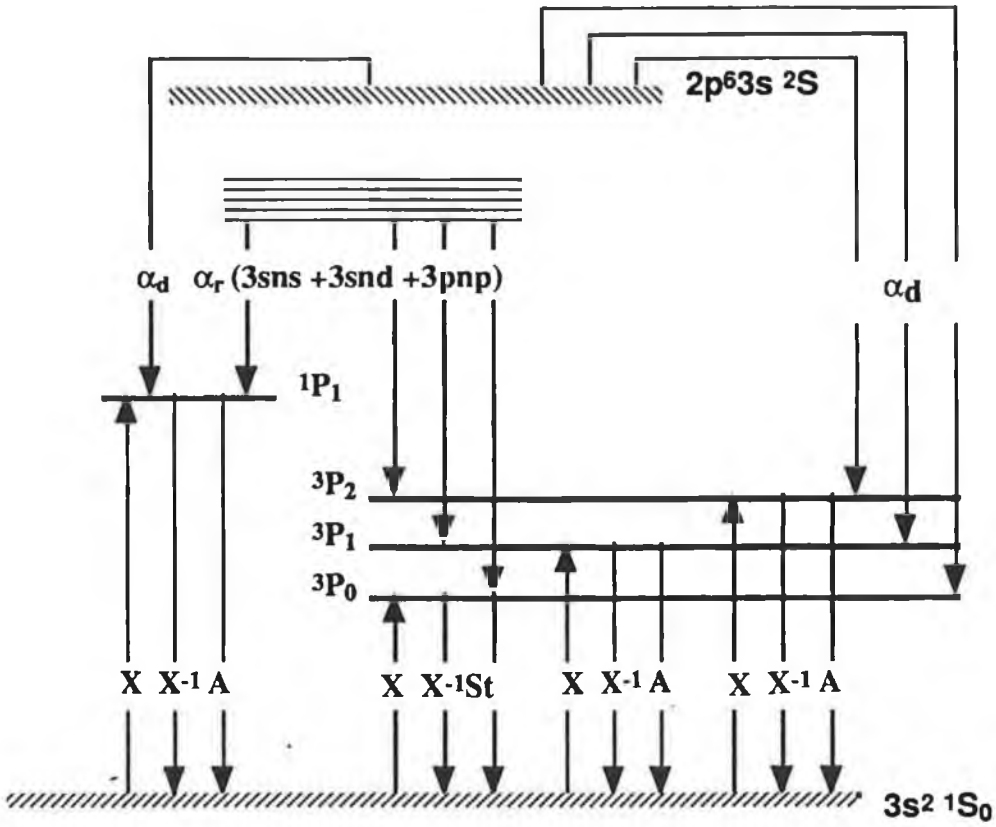

Figure 7.4

Energy - level diagram showing different atomic processes that are involved in the population and depopulation of ^1P and ^3P levels.

X	:	collisional excitation
X^{-1}	:	collisional deexcitation
A	:	spontaneous radiative decay
S_t	:	stimulated emission
α_d	:	dielectronic recombination
α_r	:	emission from the higher excited states

7.2.3(b) Population of ^3P levels

A photoabsorption spectrum of a dye-laser produced aluminium plasma was recorded on a photographic plate with inter-plasma time delays of 0.8 μs, 1.0 μs, 1.4 μs and 1.8 μs (not shown in this work). In that spectrum, absorption features associated with the ^3P levels were observed at time delays of 0.8 μs and 1.0 μs only. These are delays at which absorption from the ground state of Al^{2+}, in addition to the ground state absorption of Al^{+}, was also present. Although at a longer time delay of 1.4 μs the ground state absorption in Al^{+} was present no absorption from ^3P levels was observed at this delay. A similar situation is exhibited in the absorption spectra of Al plasma shown in figure 3.7.

Figure 7.5 shows a space-resolved photoabsorption spectra of ruby-laser produced aluminium plasma recorded 0.1 mm, 0.2 mm, 0.3 mm, 0.4 mm, 0.5 mm, 0.6 mm, 0.7 mm, 0.8 mm and 0.9 mm from the target surface at a fixed time delay of 50 ns. These spectra exhibit strong absorption both from the ground and excited states of Al^{2+}. As the plasma is scanned starting with $\Delta x = 0.1$ mm to $\Delta x =$ 0.9 mm away from the target surface, the intensities of absorption both in Al^{+*} and Al^{2+} decrease. However, the relative intensities of the features associated with the ^3P level of Al^{+*} and those associated with the ground state absorption of Al^{2+} remain the same. These time and space-resolved studies suggest that the dominant mechanism through which the ^3P levels get populated could be the dielectronic recombination and radiative decay proceeding as follows:

$$e + Al^{+2}(3s) \rightarrow Al^{+**}(3pml) \rightarrow Al^{+}(3snl) + h\upsilon$$

$$\downarrow$$

$$Al^{+*}(3s3p) + h\upsilon$$

In general,

$$e + X^{+n}(3s) \rightarrow X^{+(n-1)**}(3pml) \rightarrow X^{+(n-1)}(3snl) + h\upsilon$$

$$\downarrow$$

$$X^{+(n-1)}(3s3p) + h\upsilon$$

The process of dielectronic recombination (DR) in ions is often the dominant cooling path for hot plasmas (Duabau and Volonte, 1980). In a photoabsorption experiment (Bradley *et al.* 1973) from the laser-pumped 3s3p ^{1}P level it was suggested that the selective pumping beam at λ = 285.2 nm tuned to the 3s^2 ^{1}S $\rightarrow$ 3s3p ^{1}P resonance line in atomic magnesium will also cause ionisation from the 3s3p ^{1}P state and recombination can leave the Mg atom in one of the excited 3s3p ^{3}P levels. Experimentally, the dielectronic recombination in Mg^+ has been observed by Belic *et al.* (1983) with the use of crossed beams of electrons and Mg^+ ions.

The radiative decay could be confirmed from the photoabsorption experiment of Bradley *et al.* (1973) which shows very strong emission lines, terminating in 3s3p ^{3}P levels, from the 3sns ^{3}S, 3snd ^{3}D and 3p^2 ^{3}P excited levels. These emission lines are superimposed on the strong absorption features arising from the laser-pumped 3s3p ^{1}P levels of atomic magnesium.

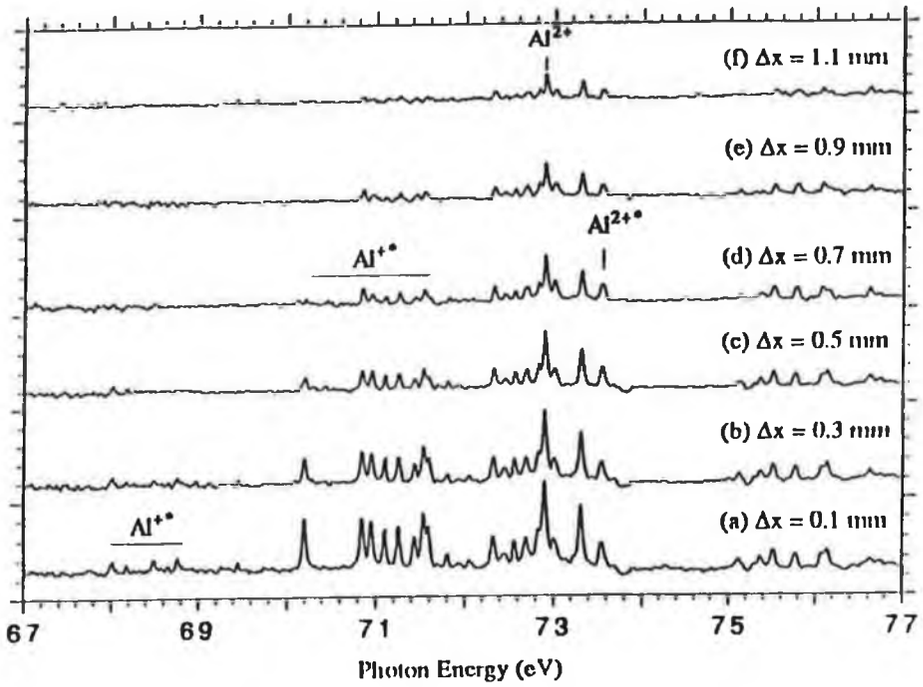

Figure 7.5

Space-resolved photoabsorption spectra of ruby laser generated Al plasmas recorded in the 2p-subshell region of Al^+ in excited states. The plasmas were probed 0.1 mm, 0.3 mm, 0.5 mm, 0.7 mm and 0.9 mm from the target surface after a fixed inter-plasma time delay of 50 ns.

In our assignment, the transitions from different $^3P_{0,1,2}$ levels have been associated with a single core excited level. This is because of the negligible resolution of our system as far the separation of ^3P levels is concerned. The photoabsorption studies from the laser-pumped excitation, tuned to the intercombination line $3s^2\ ^1S_o \rightarrow 3s3p\ ^1P_1$ can complement our studies and help us to some extent in assigning the upper state to some particular initial state which in turn tell us about the presence of different ^3P levels in the laser plasmas. Also there is need to do more experiments with the dual laser plasma technique because they could also be of great help in assigning the upper state to some particular initial state. This is evident from the space-resolved photoabsorption spectra shown in figure 7.5. A feature at 70.21 eV associated with the $^3P_{0,1,2} \rightarrow {}^3S_1$ transition in Al^+ is gone in the space-resolved spectra at $\Delta x = 0.7$ mm.

7.2.3(c) Population of ^1P levels

In our experiments (Figure 7.1) absorption from the ^1P levels has been observed close to the target surface at relatively shorter time delays where both the plasma temperature and electron density are relatively higher. In this region due to the high electron density the collisional processes should be more important than the radiative decay. On the other hand, away from the target surface the electron density as well as the density of absorbing species decreases. Consequently, the radiative decay should become the dominant process and should result in less population of the ^1P levels. This is evident from the space-resolved photoabsorption scans shown in figure 5.5. In going from $\Delta x = 0.1$ mm to $\Delta x = 0.4$ mm away from the target surface the absorption strength of the features associated with the ^1P levels goes on decreasing and at $\Delta x = 0.5$ mm all these features are gone.

7.3 Aluminium sequence in excited state absorption

As far as we know 2p photoabsorption from the valence-excited configuration of species isoelectronic to Al sequence has not been reported before. The photoabsorption data reported here could be very useful for future complementary studies which are very difficult to carry out without the photoabsorption data available. The odd parity configuration $2p^5 3s^2 3p^2$ is the lowest core-excited configuration in Si^+. Therefore, levels of the higher even parity $2p^5 3s^2 3pnl$ configurations can decay radiatively to the levels of the $2p^5 3s^2 3p^2$ configuration. The emission spectra arising from this decay can be studied in beam-foil spectroscopy similar to the studies carried out for Mg^+ (Gaardsted *et al.* 1988) and Al^{2+} (Gaardsted *et al.* 1990), and the levels of the $2p^5 3s^2 3pnl$ type configurations in Si^+ can be resolved which were not possible in our XUV photoabsorption study (see chapter 5).

Also our results from the valence-excited state of Si^+ should be very helpful for the study of Auger spectra of atomic silicon vapour following 2p photoionization similar to the one carried out for atomic Al vapour by Malutzki *et al.* (1987). This kind of study can provide deep insight into the dynamics of the states of the $2p^5 3s^2 3p^2$ configuration.

7.3.1 Results and discussion

The photoabsorption spectrum from the valence-excited states of Si^+ is shown in figure 7.6. There is strong absorption present from the valence-excited states of Si^{2+} (section 7.2), showing that along with Si^+ a large quantity of the higher ion stage Si^{2+} was also present in the absorbing plasma.

The absorption structures due to the valence-excited states of Si^+ exhibit $2p^6 3s 3p^2 \rightarrow 2p^5 3s^2 3p^2$ transitions. The initial configuration $2p^6 3s 3p^2$ includes the ^4P, ^2D, ^2P and ^2S levels. The metastable ^4P levels are lower in energy than the dipole-allowed ^2L levels (see Martin and Zalubas 1983) which is analogous to the levels of the valence-excited configuration $2p^6 3s 3p$ in the Mg sequence (see Martin and Zalubas 1980), Al^+ (see Martin and Zalubas 1980) and Si^{2+} (see Martin and Zalubas 1983). In our photoabsorption measurements from the valence-excited species isoelectronic to Mg (see section 7.2) strong absorption was observed from the metastable $2p^6 3s 3p\ ^3P$ levels, however, absorption from the short-lived dipole

allowed $2p^63s3p\ ^1P$ levels was observed to be very weak. The same situation is expected in the photoabsorption measurements made from the valence-excited states of the Al isoelectronic sequence, with the exception of Al neutral. Our photoabsorption studies of the laser plasmas, carried out during the cooling phase of the plasma, exhibit significant absorption only from the lowest valence-excited levels of the absorbing species. In atomic aluminium the lowest valence-excited configuration is $2p^63s^24s$ (see Martin and Zalubas 1979), therefore, it would be very difficult to measure the absorption from the valence-excited states of the higher $2p^63s3p^2$ configuration.

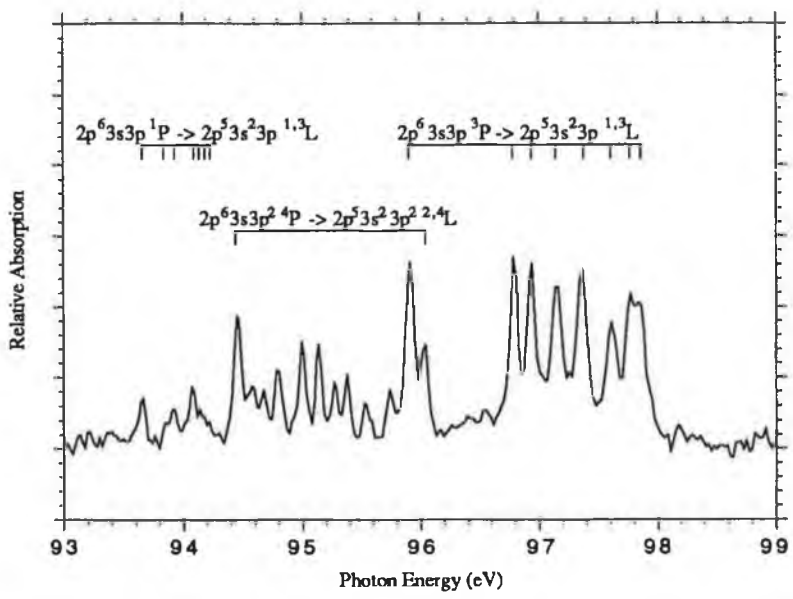

Figure 7.6

Photoabsorption measurements 2p absorption from the valence-excited states of Si^+. Along with absorption from the $2p^63s3p^2$ valence-excited configuration of Si^+ a strong absorption from the valence-excited configuration $2p^63s3p$ of Si^{2+} is also present.

The levels of the core-excited configuration $2p^53s^23p$ in Mg sequence have been reported unperturbed (see section 7.2) as no significant mixing was observed with levels of other core-excited configurations. For such a pure configuration, the *ab initio* calculated term energies were found in excellent agreement with the measured spectrum. As the levels of the $2p^53s^23p^2$ configuration do not overlap with the levels of any other odd parity core-excited configuration in Si^+, therefore,

their level structure should not be affected significantly by the other weakly interacting configurations. So the $2p^53s^23p^2$ configuration in Si^+ should behave similar to the $2p^53s^23p$ configuration in the Mg sequence.

In order to investigate the origin of the absorption features, assess the role of electron-correlations and provide identification for the spectrum *ab initio* atomic structure calculations have been carried out. The calculations, performed with the Cowan's Configuration-Interaction Hartree-Fock (CIHF) code (see chapter 2), include $2p^63s3p^2$, $2p^63d3p^2$, $2p^53s^23p^2$, $2p^53s^23d^2$ and $2p^53s3p^23d$ configurations. A comparison of the measured and computed energies is listed in table 7.5. The percent LS compositions of observed terms of the core-excited configuration $2p^53s^23p^2$ are given in table 7.6. In table 7.5 the calculated energies are given only for the observed transitions which according to the calculations are arising from the ^4P levels only. The transitions having negligible predicted gf-values are also deleted in table 7.5. The gf-values for the transitions arising both from ^4L and ^2L were predicted to be of the same order. In the experiment we have observed absorption only from the metastable $2p^63s3p^2$ ^4P levels but not from the short-lived dipole allowed ^2L levels. This is analogous to the 2p absorption observed from the valence-excited states in Mg sequence (see section 7.2). In order to provide interpretation for the mechanisms of population and depopulation of valence-excited states of species in laser plasmas there is need to study experimentally as well theoretically the temporal and spatial behaviour of these species during both heating and cooling phases of the laser plasmas.

Eigenvectors of the ^2L and ^4L levels (see table 7.6) show that the ^4L levels of the $2p^53s^23p^2$ configuration are almost pure LS-coupled with the exception of the $^4D_{5/2,\ 3/2,\ 1/2}$ terms. Unlike the $2p^53s^23p$ configuration observed in photoabsorption of Si^{2+} (Mosnier *et al.* 1994), the spectrum of $2p^53s^23p^2$ is simpler. In $2p^53s^23p$ configuration the mixing among the ^1L and ^3L levels was very significant. For a number of terms complete breakdown of the LS-coupling was exhibited, therefore, some strong features were assigned to LS forbidden transitions. Because of the strong mixing some of the terms were assigned twice. However, in the present case the mixing of the ^2L and ^4L levels is observed very dilute, therefore, the assignments presented in table 7.5 are unambiguous.

Table 7.5. Measured energies (eV), calculated energies (eV) and gf-values for the $2p^6 3s 3p^2\ {}^4P \rightarrow 2p^5 3s^2 3p^2\ {}^{2,4}L$ transitions in Si^+.

Transition	Meas.	Calc.	gf
$(^2S)\ {}^4P_{5/2} - (^3P)\ {}^4P_{5/2}$	94.46	94.65	0.0778
$(^2S)\ {}^4P_{3/2} - (^3P)\ {}^4P_{5/2}$		94.67	0.0796
$(^2S)\ {}^4P_{5/2} - (^3P)\ {}^4P_{3/2}$	94.78	94.76	0.0244
$(^2S)\ {}^4P_{3/2} - (^3P)\ {}^4P_{3/2}$		94.77	0.0090
$(^2S)\ {}^4P_{1/2} - (^3P)\ {}^4P_{3/2}$		94.78	0.0712
$(^2S)\ {}^4P_{3/2} - (^3P)\ {}^4P_{1/2}$		94.87	0.0353
$(^2S)\ {}^4P_{1/2} - (^3P)\ {}^4P_{1/2}$		94.88	0.0146
$(^2S)\ {}^4P_{5/2} - (^3P)\ {}^4D_{7/2}$	95.05	95.09	0.2297
$(^2S)\ {}^4P_{5/2} - (^3P)\ {}^4D_{5/2}$	95.19	95.20	0.0626
$(^2S)\ 4P_{3/2} - (^3P)\ {}^4D_{5/2}$		95.21	0.0774
$(^2S)\ {}^4P_{5/2} - (^3P)\ {}^4D_{3/2}$	95.31	95.29	0.0050
$(^2S)\ {}^4P_{3/2} - (^3P)\ {}^4D_{3/2}$		95.31	0.0542
$(^2S)\ {}^4P_{1/2} - (^3P)\ {}^4D_{3/2}$		95.32	0.0146
$(^2S)\ {}^4P_{3/2} - (^3P)\ {}^4D_{1/2}$	95.58	95.59	0.0104
$(^2S)\ {}^4P_{1/2} - (^3P)\ {}^4D_{1/2}$		95.60	0.0370
$(^2S)\ {}^4P_{5/2} - (^3P)\ {}^2D_{3/2}$	95.75	95.74	0.0065
$(^2S)\ {}^4P_{3/2} - (^3P)\ {}^2D_{3/2}$		95.75	0.0233
$(^2S)\ {}^4P_{1/2} - (^3P)\ {}^2D_{3/2}$		95.76	0.0126
$(^2S)\ {}^4P_{5/2} - (^3P)\ {}^2D_{5/2}$		95.86	0.0220
$(^2S)\ {}^4P_{3/2} - (^3P)\ {}^2D_{5/2}$		95.88	0.0115
$(^2S)\ {}^4P_{5/2} - (^3P)\ {}^4S_{3/2}$	96.06	96.03	0.0832
$(^2S)\ {}^4P_{3/2} - (^3P)\ {}^4S_{3/2}$		96.05	0.0313
$(^2S)\ {}^4P_{1/2} - (^3P)\ {}^4S_{3/2}$		96.06	0.0113

Table 7.6. LS compositions of the terms of the $2p^5 3s^2 3p^2$ configuration in Si^+.

Term	%LS - composition
$(^3P)\ ^4P_{5/2}$	$3s^2 3p^2$ [91.93% $(^3P)\ ^4P$ - 3.58% $(^3P)\ ^4D$ + 0.68% $(^3P)\ ^2D$] + $3s3p^2 3d$ [- 0.95% $(^1D)\ ^4P$ + 0.88% $(^1D)\ ^4P$]
$(^3P)\ ^4P_{3/2}$	$3s^2 3p^2$ [8.46% $(^3P)\ ^4P$ - 3.65% $(^3P)\ ^4D$ - 1.94% $(^3P)\ ^4S$ + 1.24% $(^3P)\ ^2P$] + $3s3p^2 3d$ [- 0.91% $(^1D)\ ^4P$]
$(^3P)\ ^4P_{1/2}$	$3s^2 3p^2$ [89.03% $(^3P)\ ^4P$ - 3.29% $(^3P)\ ^2S$ - 1.73% $(^3P)\ ^4D$ + 1.19% $(^3P)\ ^2P$] + $3s3p^2 3d$ [- 0.92% $(^1D)\ ^4P$]
$(^3P)\ ^4D_{7/2}$	$3s^2 3p^2$ [96.06% $(^3P)\ ^4D$] + $3s3p^2 3d$ [- 1.23% $(^1D)\ ^4D$ + 0.70% $(^1D)\ ^4D$ - 0.70% $(^3P)\ ^4D$]
$(^3P)\ ^4D_{5/2}$	$3s^2 3p^2$ [77.22% $(^3P)\ ^4D$ + 16.89% $(^3P)\ ^2D$ + 1.91% $(^3P)\ ^4P$] + $3s3p23d$ [- 0.88% $(^1D)\ ^4D$]
$(^3P)\ ^4D_{3/2}$	$3s^2 3p^2$ [60.46% $(^3P)\ ^4D$ + 27.06% $(^3P)\ ^2D$ - 2.73% $(^3P)\ ^2P$ + 2.60% $(^3P)\ ^4P$ + 2.24% $(^1D)\ ^2P$]
$(^3P)\ ^4D_{1/2}$	$3s^2 3p^2$ [76.86% $(^3P)\ ^4D$ - 11.67% $(^1D)\ ^2P$ + 7.04% $(^3P)\ ^2P$ + $3s3p^2 3d$ [- 0.98% $(^1D)\ ^4D$ + 0.56% $(^1D)\ ^4D$]
$(^3P)\ ^2D_{3/2}$	$3s^2 3p^2$ [55.30% $(^3P)\ ^2D$ - 31.58% $(^3P)\ ^4D$ + 4.39% $(^1D)\ ^2P$ - 3.19 (3P) ^2P - 1.10% $(^3P)\ ^4P$]
$(^3P)\ ^2D_{5/2}$	$3s^2 3p^2$ [77.19% $(^3P)\ ^2D$ - 15.24% $(^3P)\ ^4D$ - 2.34% $(^3P)\ ^4P$ + 1.31% $(^1D)\ ^2D$] + $3s3p^2 3d$ [- 0.72% $(^1D)\ ^2D$]
$(^3P)\ ^4S_{3/2}$	$3s^2 3p^2$ [87.63% $(^3P)\ ^4S$ + 3.32% $(^1D)\ ^2P$ + 3.00% $(^3P)\ ^4P$ + 1.44% $(^3P)\ ^2P$] + $3s3p^2 3d$ [- 1.92% $(^1D)\ ^4S$]

Correlation mixing with the $2p^5 3s3p^2 3d$ and $2p^5 3p^2 3d^2$ configurations amounts to less than 2% at most and therefore they have a minor influence over the energy level structure of the $2p^5 3s^2 3p^2$ configuration. This is analogous to the mixing of the $2p^5 3s^2 3p$ configuration with the $2p^5 3s3p3d$ configuration in Mg sequence. In both cases the significant interaction is observed only within the complex. In contrast to the Mg sequence in ground state absorption which is observed strongly perturbed by the doubly excited states (see chapter 4, Costello *et al.* 1992), the absorption spectra of valence-excited states of Mg sequence are observed almost unperturbed (see section 7.2). In moving along the Mg sequence dramatic changes are observed in the ground state absorption spectra, however, no irregularities have been observed in the absorption from valence-excited states.

In the 2p absorption along the Al sequence in ground state, moving from Al neutral to singly ionised Si a number of irregularities have been observed (see chapter 5). However, the levels of the core-excited configuration $2p^5 3s^2 3p^2$ have been observed unperturbed - analogous to the $2p^5 3s^2 3p$ configuration in Mg sequence (Mosnier *et al.* 1994) -, therefore, its structure and behaviour is expected same in the other isoelectronic species.

7.4 Conclusions

Inner-shell photoabsorption investigations of the core-excited states which do not connect to the ground state via the electric dipole operator are presented along the magnesium isoelectronic sequence for Mg, Al^+ and Si^{2+}, and for Si^+. The results show the powerful potential of the DLP technique for the study of photoabsorption from the valence-excited states along an isoelectronic which has not been achieved before.

Photoabsorption spectra reported along the magnesium sequence exhibits the $2p^6 3s3p \rightarrow 2p^5 3s^2 3p$ transitions. In moving along the sequence, spectra remain similar in appearance, with the exception of transition energy shifts, which rules out the presence of any perturbers. This is in contrast with the ground state absorption reported along this sequence. The behaviour of the core-excited configuration $2p^5 3s^2 3p^2$ in Si^+ has been shown same to the $2p^5 3s^2 3p$ configuration in magnesium sequence.

In case of atomic magnesium the photoabsorption data has been used to interpret its ejected-electron spectrum (Pejcev *et al.* 1977) excited by low-energy electron impact corresponding to the autoionization decay of $2p^5 3s^2 3p$ states. In the case of Al^+ the decay dynamics of this core-excited configuration has already been described in detail by Malutzki *et al.* (1987), therefore, only comparison is shown with their data.

As the measurements were made during cooling phase of the laser plasma, strong absorption has been observed only from the metastable states both in magnesium and aluminium sequences.

7.5 References

Belic D S, Dunn G H, Morgan T J, Mueller D W and Timmer C, 1983, Phys. Rev. Lett., **50**, 339.

Bizau J M, Wuillemier F, Ederer D L, Keller J C, LeGouet J L, Picque J.-L, carre B and Koch P M, 1985, Phys. Rev. Lett. **55**, 1281.

Bradley D J, 1969, Appl. Opt. **8**, 1957.

Bradley D J, Ewart P, Nicholas J V, Shaw J R D and Thompson D G, 1973, Phys.Rev.Lett., **31**, 263.

Brilly J, Kennedy E T and Mosnier J -P, 1990, Phys. Scr. **41**, 30.

Costello J T, Evans D, Hopkins R B, Kennedy E T, Kiernan L, Mansfield M W D, Mosnier J P, Sayyad M H and Sonntag B F, 1992, J. Phys.B: At. Mol. Phys., **25**, 5055.

Cowan R D, 1981, The Theory of Atomic Structure and Spectra, University of California Press.

Cubaynes D, Bizau J M, Wuilleumier F J, Carre B and Gounand F, 1989, Phys. Rev. Lett. **63**, 2460.

Dubau J and Volonte S, 1980, Rep. Prog. Pysic. **43**, 199.

Esteva J M and Mehlman G, 1974, Ap.J., **193**, 747 (1974).

Ferray M, Gounand F, D'Oliveira P, Fournier P R, Cubaynes D, Bizau J M, Morgan T J and Wuilleumier F J, 1987, Phys. Rev. Lett. **59**, 2040.

Froese-Fisher C, 1986, Phys. Rev. A **34**, 1667.

Gaardsted J O, Andersen T, Sonnek D, Mannervik S and Short R T, 1988, Physica Scripta, **38**, 27.

Gaardsted J O, Brage, Froese Fischer C and Sonnek D, 1990, Physica Scripta, **42**, 543.

Lucatorto T B and McIlrath T J, 1977, Phys. Rev. Lett. **38**, 1390.

Malutzki R, Wachter A, Schmidt V and Hansen J E, 1987,J. Phys.B: At. Mol. Phys., **20**, 5411.

Martin W C and Zalubas R, 1979, J. Phys. Chem. Ref. Data, **8**, 817.

Martin W C and Zalubas R, 1980, J. Phys. Chem. Ref. Data, **9**, 1.

Martin W C and Zalubas R, 1983, J. Phys. Chem. Ref. Data, **12**, 323.

McIlrath T J, 1969, Appl.Phys.Lett., **15**, 41.

McIlrath T J and Carlsten J L, 1973, J.Phys.B: Atom. Molec.Phys., **6**, 697.

Meyer M, Muller B, Nunnemann A, Prscher Th, Raven R v, Richter M, Schmidt M, Sonntag B and Zimmermann P, 1987, Phys. Rev. Lett. **59**, 2040.

Mosnier J -P, Brilly J and Kennedy E T, 1987, J.Physique, **48**, C9-219 (1987).
Mosnier J P, Costello J T, Kennedy E T, Kiernan L and Sayyad M H, 1994, Phys. Rev. A **49**, 755.

Pahler M, Lorenz C, Raven E v, Ruder J, Sonntag B, Baier S, Muller B R, Schulze M, Staiger H, Zimmermann P and Kabachnik N M, 1992, Phys. Rev. Lett. **68**, 2285.

Pejcev V, Ottley T W, Rassi D and Ross K J, 1977, J.Phys.B: Atom. Molec. Phys., **10**, 2389

Sonntag B F, Cromer C L, Bridges J M, McIlrath T J and Lucatorto T B, 1986, in *Short Wavelength Coherent Radiation: Generation and Applications* (Monterey, California, March 24-26, 1986), edited by Attwood D T and Bokor J, AIP Conf. Proc. No. 147 (AIP, New York), p. 412.

Sugar J, Lucatorto T B, McIlrath T J and Weiss A W, 1979. Opt. Lett. **4**, 109.

APPENDIX A

THE SODIUM ISOELECTRONIC SEQUENCE IN GROUND STATE ABSORPTION

Photoabsorption spectrum of Na-like Si^{3+} has been recorded in the 2p-subshell region. The results of the measurements made in the regions of $2p^63s\ ^2S \rightarrow 2p^53s^2\ ^2P$ and $2p^63s\ ^2S \rightarrow 2p^5[3snd + 3s(n+1)s + 3pnp,\ n \geq 3]$ resonances are shown in figures A-1(a) and A-1(b) respectively. The Si^{3+} spectrum is dominated by the $2p \rightarrow 3d$ transitions and the remaining Rydbergs are relatively very weak.

In order to do isoelectronic comparison, the photoabsorption spectra of Na-like ions Mg^+ and Al^{2+} have also been recorded. In figure A-2 the results are shown in the regions of $2p \rightarrow 3p^2 + 3s3d$ and 3s4s transitions for the isoelectronic species Mg^+, Al^{2+} and Si^{3+}. In moving from Mg^+ to Si^{3+}, the 3d contraction and level crossings result in dramatic changes in the spectra. In the case of Mg^+, the spectrum shown is only due to the $2p \rightarrow 3p^2 + 3s3d$ and 3s4s transitions and in this region no significant absorption has been observed from its valence-excited states. In the cases of Al^{2+} and Si^{3+}, relatively more absorption features are observed which are arising from the $2p^63p \rightarrow 2p^53p3d$ transitions.

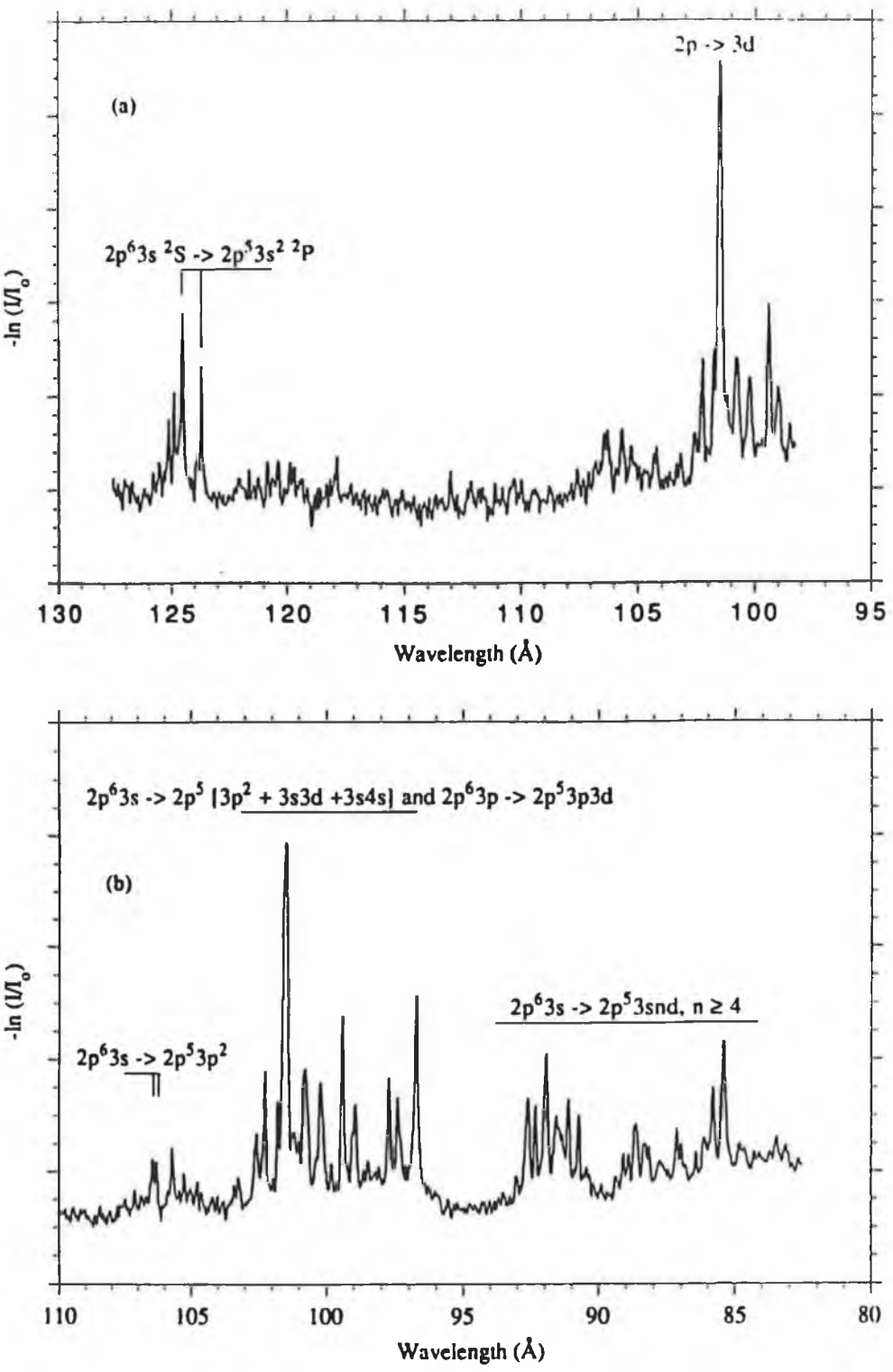

Figure A-1

Photoabsorption spectrum of Na-like Si^{3+} recorded in the regions of (a) $2p^63s \rightarrow 2p^53s^2$, and (b) $2p^63s \rightarrow 2p^5[3snd + 3s(n+1)s + 3pnp, n \geq 3]$ resonances.

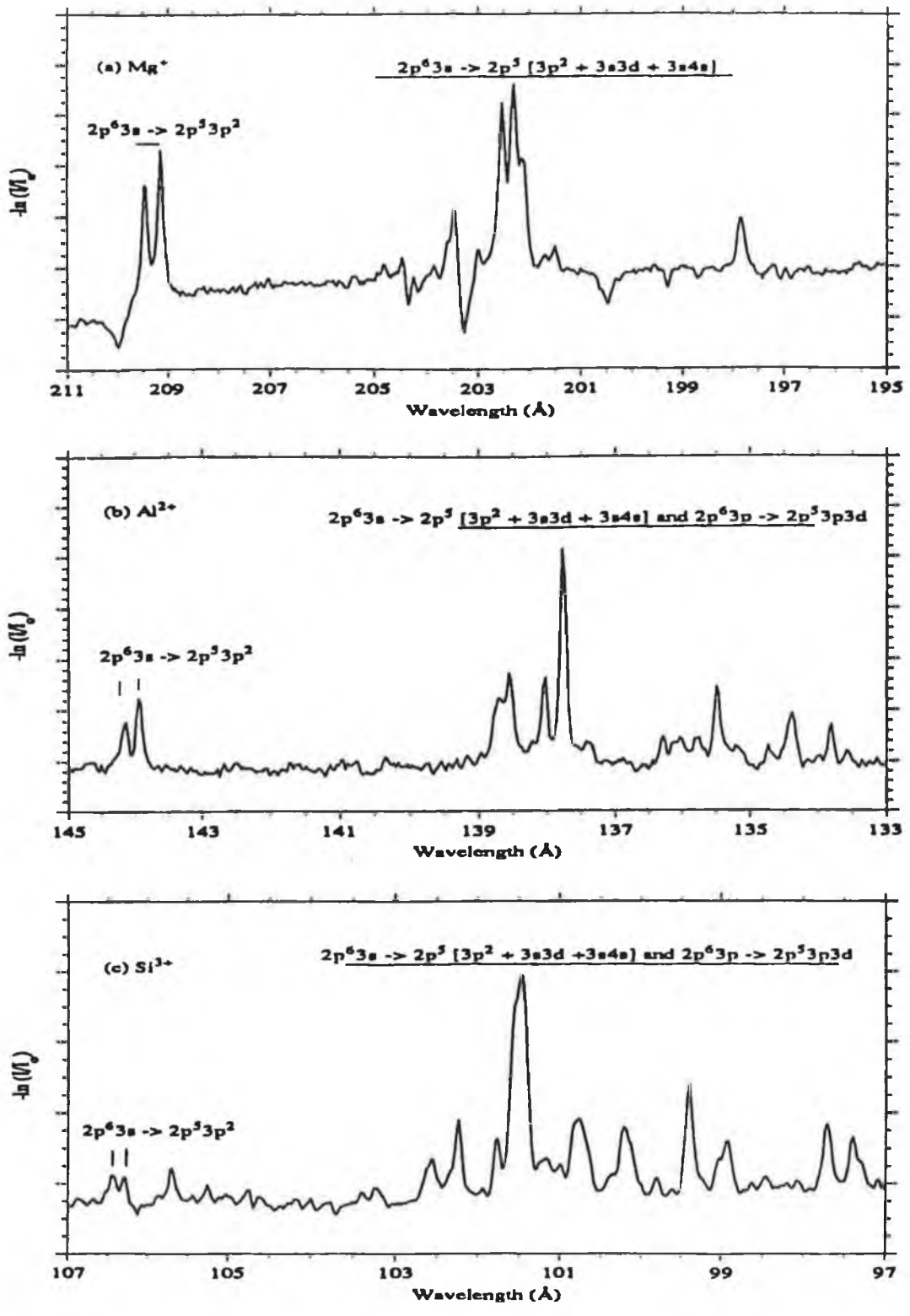

Figure A-2

Photoabsorption spectra of the isoelectronic species (a) Mg^{+}, (b) Al^{2+} and (c) Si^{3+} in the regions of the $2p^63s \rightarrow 2p^5[3p^2 + 3snd + 3s(n+1)s, n \geq 3]$ resonances.

APPENDIX B

THE SODIUM ISOELECTRONIC SEQUENCE IN EXCITED STATE ABSORPTION

Using the dual laser-produced plasma technique the 2p-subshell photoabsorption spectra have been measured for the Na-like ions Mg^{+}, Al^{2+} and Si^{3+} prepared in valence-excited states. The results are shown in figure B-1. In these spectra, along with the absorption from Mg^{+}, Al^{2+} and Si^{3+} in valence-excited states $2p^{6}3p\ ^{2}P_{1/2,\ 3/2}$, the absorption structures which include the resonances arising from the $2p^{6}3s\ ^{2}S_{1/2} \rightarrow 2p^{5}3s^{2}\ ^{2}P_{3/2,1/2}$ (Na-like ground state state absorption) and the transition arrays arising from the $2p^{6}3s3p \rightarrow 2p^{5}3s^{2}3p$ (Mg-like excited state absorption) are also present.

In the $2p^{5}3s3p$ excited configuration the parent configuration 3s3p couples through the exchange interaction to form $^{1,3}P$ terms. These two terms in turn couple with the $2p^{5}\ ^{2}P_{3/2,1/2}$ core to form terms of the type $^{2,4}D$, $^{2,4}P$, and $^{2,4}S$ and form two groups of excitation states.

In moving along the sequence from Mg^{+} to Si^{3+}, no significant change can be observed which rules out the presence of any perturbation. This is analogous to the photoabsorption spectra measured along Mg sequence prepared in the valence-excited $2p^{6}3s3p$ configuration (see chapter 5).

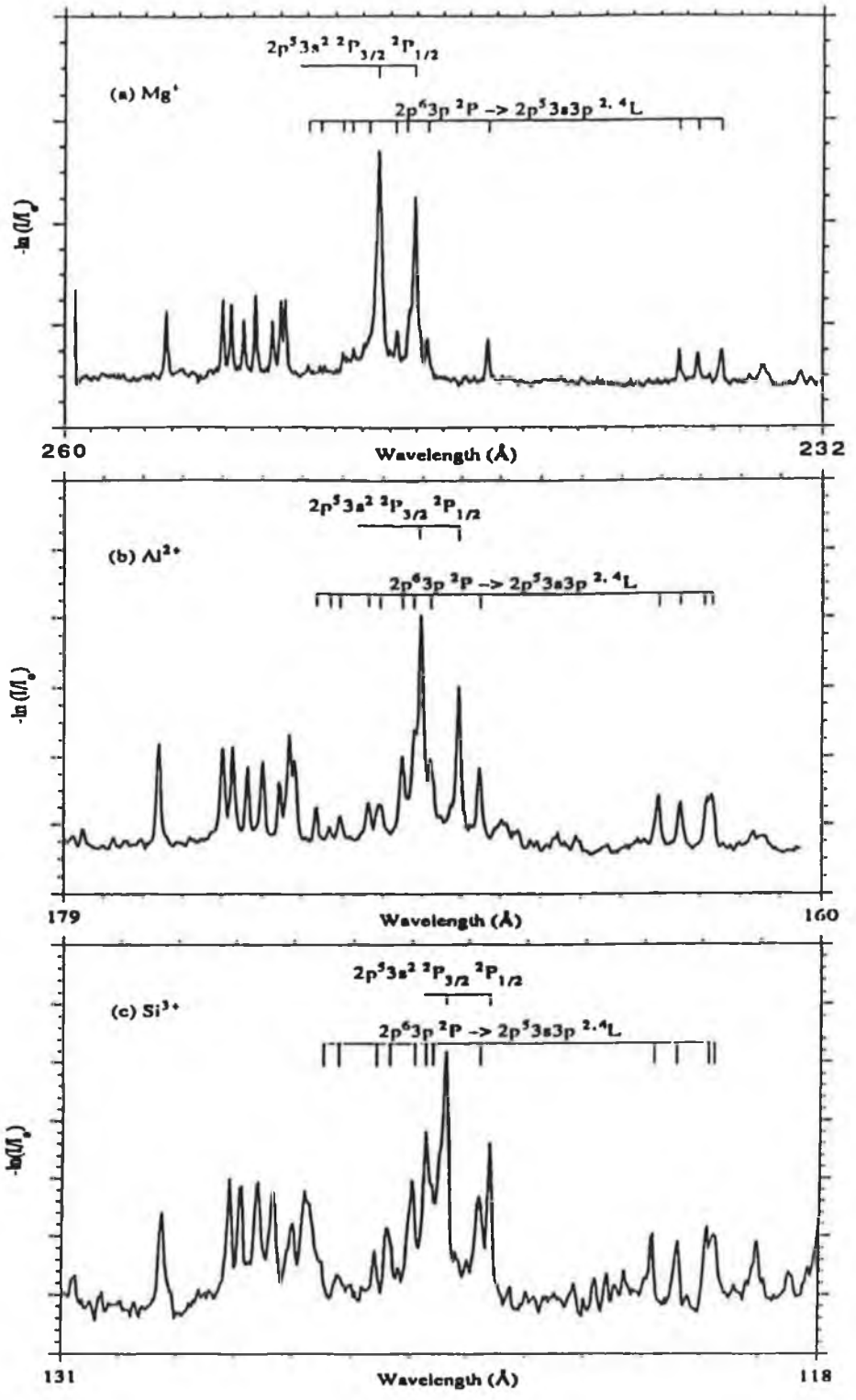

Figure B-1

The relative photoabsorption spectra of (a) Mg^{+}, (b) Al^{2+} and (c) Si^{3+} in the region of the $2p^63p\ ^2P \rightarrow 2p^53s3p\ ^{2,4}L$ transitions.

APPENDIX C

DETAILS OF THE TRANSITIONS IN ATOMIC SILICON ABSORPTION

Possible terms of the $2p^5 3s^2 3p^2 s$ type configuration which could combine with the ground configuration.

J =	3	2	1	0
	$(^3P)\ ^5D$	$(^3P)\ ^5D$	$(^3P)\ ^5D$	$(^3P)\ ^5D$
	$(^3P)\ ^3D$ (2)	$(^3P)\ ^3D$ (2)	$(^3P)\ ^3D$ (2)	$(^3P)\ ^3P$ (2)
	$(^3P)\ ^5P$	$(^3P)\ ^5P$	$(^3P)\ ^5P$	$(^3P)\ ^1S$
	$(^1D)\ ^3F$	$(^3P)\ ^3P$ (2)	$(^3P)\ ^3P$ (2)	$(^1D)\ ^3P$
	$(^1D)\ ^1F$	$(^3P)\ ^5S$	$(^3P)\ ^3S$ (2)	$(^1S)\ ^3P$
	$(^1D)\ ^3D$	$(^3P)\ ^1D$	$(^3P)\ ^1P$	
		$(^1D)\ ^3F$	$(^1D)\ ^3D$	6
	7	$(^1D)\ ^3D$	$(^1D)\ ^3P$	
		$(^1D)\ ^1D$	$(^1D)\ ^1P$	
		$(^1D)\ ^3P$	$(^1S)\ ^3P$	
		$(^1S)\ ^3P$	$(^1S)\ ^1P$	
		13	14	

Transitions from $^3P_0$ level = 14

Transitions from $^3P_1$ level = 33

Transitions from $^3P_2$ level = 34

Total tarnsitions from $^3P_{0,1,2}$ levels = 111

Transitions from $^1D_2$ level = 34

Transitions from $^1S_0$ level = 14

Possible terms of the $2p^5 3s^2 3p^2 d$ type configuration which could combine with the ground configuration.

J = 3	J = 2	J = 1	J = 0
$(^3P)\ ^5G$	$(^3P)\ ^5G$	$(^3P)\ ^5F$ (2)	$(^3P)\ ^5D$ (3)
$(^3P)\ ^5F$ (2)	$(^3P)\ ^5F$ (2)	$(^3P)\ ^5D$ (3)	$(^3P)\ ^3P$ (4)
$(^3P)\ ^5D$ (3)	$(^3P)\ ^5D$ (3)	$(^3P)\ ^5P$ (2)	$(^3P)\ ^1S$
$(^3P)\ ^5P$ (2)	$(^3P)\ ^5P$ (2)	$(^3P)\ ^3D$ (6)	$(^1D)\ ^3P$ (3)
$(^3P)\ ^3G$ (2)	$(^3P)\ ^5S$	$(^3P)\ ^3P$ (4)	$(^1D)\ ^1S$
$(^3P)\ ^3F$ (4)	$(^3P)\ ^3F$ (4)	$(^3P)\ ^3S$ (2)	$(^1S)\ ^3P$
$(^3P)\ ^3D$ (6)	$(^3P)\ ^3D$ (6)	$(^3P)\ ^1P$ (2)	———
$(^3P)\ ^1F$ (2)	$(^3P)\ ^3P$ (4)	$(^1D)\ ^3D$ (3)	13
$(^1D)\ ^3G$ (2)	$(^3P)\ ^1D$ (3)	$(^1D)\ ^3P$ (3)	
$(^1D)\ ^3F$ (3)	$(^1D)\ ^3F$ (3)	$(^1D)\ ^1P$ (3)	
$(^1D)\ ^3D$ (3)	$(^1D)\ ^3D$ (3)	$(^1D)\ ^3S$	
$(^1D)\ ^1F$ (3)	$(^1D)\ ^3P$ (3)	$(^1S)\ ^3D$	
$(^1S)\ ^3F$	$(^1D)\ ^1D$ (3)	$(^1S)\ ^3P$	
$(^1S)\ ^3D$	$(^1S)\ ^3F$	$(^1S)\ ^1P$	
$(^1S)\ ^1F$	$(^1S)\ ^3P$	———	
———	$(^1S)\ ^1D$	34	
36	———		
	42		

Transitions from $^3P_0$ level = 34

Transitions from $^3P_1$ level = 89

Transitions from $^3P_2$ level = 111

Total tarnsitions from $^3P_{0,1,2}$ levels = 234

Transitions from $^1D_2$ level = 111

Transitions from $^1S_0$ level = 34

Possible terms of the $2p^5 3s 3p^4$ configuration which could combine with the ground configuration.

J =	3	2	1	0
	$(^3P)\ ^5D$	$(^3P)\ ^5D$	$(^3P)\ ^5D$	$(^3P)\ ^5D$
	$(^3P)\ ^5P$	$(^3P)\ ^5P$	$(^3P)\ ^5P$	$(^3P)\ ^3P$ (2)
	$(^3P)\ ^3D$ (2)	$(^3P)\ ^5S$	$(^3P)\ ^3D$ (2)	$(^3P)\ ^1S$
	$(^1D)\ ^3F$	$(^3P)\ ^3D$ (2)	$(^3P)\ ^3P$ (2)	$(^1D)\ ^3P$
	$(^1D)\ ^3D$	$(^3P)\ ^3P$ (2)	$(^3P)\ ^3S$ (2)	$(^1S)\ ^3P$
	$(^1D)\ ^1F$	$(^3P)\ ^1D$	$(^3P)\ ^1P$	
	7	$(^1D)\ ^3F$	$(^1D)\ ^3D$	6
		$(^1D)\ ^3D$	$(^1D)\ ^3P$	
		$(^1D)\ ^3P$	$(^1S)\ ^3P$	
		$(^1S)\ ^3P$	$(^1D)\ ^1P$	
		$(^1D)\ ^1D$	$(^1S)\ ^1P$	
		13	14	

Transitions from $^3P_0$ level = 14

Transitions from $^3P_1$ level = 33

Transitions from $^3P_2$ level = 34

Total tarnsitions from $^3P_{0,1,2}$ levels = 81

Transitions from $^1D_2$ level = 34

Transitions from $^1S_0$ level = 14

Acknowledgements

First of all I would like to thank Professor Eugene T Kennedy for providing me with the opportunity to carry out research in the Physics Department, School of Physical Sciences. Without his inspiration, encouragement and kindness this work would never have been completed.

The efforts of the respected staff of LPGROUP -my supervisor, Dr. John T Costello and Dr. Jean-Paul Mosnier- and the contribution of the fellow postgraduates in developing an excellent facility which enabled me to carry out the research reported in this thesis are very much appreciated. I am also grateful to the staff for keeping open for me the doors of all kinds of assistance and guidance throughout this period.

I am grateful to Dr. John T Costello for numerous discussions which proved very stimulating and helpful in writing chapter 4. I would also like to thank Dr. Jean-Paul Mosnier for his time and help during discussions on various topics of spectroscopy and acknowledge his help in providing the comparison of photoabsorption data with the ejected-electron spectra reported in chapter 5.

I wish to thank Martin G O'Mullane of UCC for help in installing and running Cowan' s code on the DCU VAX which has been used for the atomic structure calculations reported in this work.

The co-operation and help of the technical and administrative school staff on various occasions are very much appreciated.

I would also like to take this opportunity to thank very much Dr. R J A Bradley on his very sympathetic efforts in getting visas for me and my family.

The time passed in extra-circular activities with fellow postgraduates, particularly, Dave, Bruce, Matthew, Martin, Laurence and Ulrich will never be forgotten.

Finally I would also like to thank my family members who allowed me to go for studies and showed a great patience. I am also grateful to my brother Muhammad Hussain and in-laws who shared my family responsibilities during this difficult period.